Computational Atomic Structures Toward Heavy Element Research

ECOLE
POLYTECHNIQUE
DE BRUXELLES

Computational Atomic Structures Toward Heavy Element Research

by Sacha Schiffmann

LUND UNIVERSITY

ULB UNIVERSITÉ LIBRE DE BRUXELLES

Thesis for the degree of
Doctor of Philosophy in Physics from Lund University and
Docteur en Sciences de l'ingénieur et technologie de l'Université libre de Bruxelles

Thesis advisors: Tomas Brage and Per Jönsson (Lund U.)
Michel Godefroid and Nathalie Vaeck (ULB)

Faculty opponent: José Paulo Santos

To be presented, with the permission of the Faculty of Sciences of Lund University and of École polytechnique de Bruxelles de l'Université libre de Bruxelles, for public criticism in the Rydberg Hall at the Physics Department on Wednesday, the 12th of May 2021 at 13:00.

Organization	Document name
LUND UNIVERSITY Department of Mathematical Physics Box XYZ SE–221 00 LUND Sweden	**DOCTORAL DISSERTATION** Date of disputation 2021-05-12 Sponsoring organization
Author(s) Sacha Schiffmann	

Title and subtitle

Computational Atomic Structures Toward Heavy Element Research

Abstract

We are interested in complex electronic structures of various atomic and ionics systems. We use an *ab initio* approach, the multiconfigurational Dirac-Hartree-Fock (MCDHF), to compute atomic structures and properties. We contribute in three main ways to the already existent literature: by developing and implementing original computer programs, by investigating possibilities of alternative computational methodologies and strategies, and finally by performing accurate atomic structure calculations to support other research fields, i.e., nuclear physics, astrophysics or experimental physics, through the theoretical estimation of relevant atomic data.

We raise questions about the choice of the optimal orbital basis by considering finite basis sets, MCDHF orbital bases and *natural-orbital* bases. We demonstrate the promising potential of the latter in the context of hyperfine structures and hope that others will find interest in pursuing our analysis. Ultimately, our work put forward some weaknesses of the traditional optimization strategy based on the layer-by-layer optimization strategy.

We also perform large-scale calculations to determine accurate atomic properties such as energy levels, hyperfine structures, isotope shifts, transition parameters, radiative lifetimes and Landé g factors. We show through the variety of atomic properties and atomic systems studied, the difficulty of describing, in the relativistic framework, the correlation between the spatial position of electrons due to their Coulomb repulsion.

This thesis is organized in two main parts. The first one is dedicated to the theoretical and computational backgrounds that are needed to understand the theoretical models and the interpretation of our results. The second part presents and summarizes our articles and manuscripts. They are separated in four groups, A, B, C, and D, around the themes of the atomic orbital bases, the applications to nuclear physics, the applications to astrophysics, and investigations of negative ions.

Key words

atoms, electron correlation, relativity, quantum mechanics, calculations, natural orbitals, isotope shifts, hyperfine structures, transition parameters, Landé g factors

Classification system and/or index terms (if any)

Supplementary bibliographical information	Language
	English
ISSN and key title	ISBN
	978-91-7895-777-4 (print) 978-91-7895-778-1 (pdf)
Recipient's notes	Number of pages: 410 / Price
	Security classification

ECOLE
POLYTECHNIQUE
DE BRUXELLES

Computational Atomic Structures Toward Heavy Element Research

by Sacha Schiffmann

LUND
UNIVERSITY

ULB UNIVERSITÉ LIBRE DE BRUXELLES

A doctoral thesis at a university in Sweden takes either the form of a single, cohesive research study (monograph) or a summary of research papers (compilation thesis), which the doctoral student has written alone or together with one or several other author(s).

In the latter case the thesis consists of two parts. An introductory text puts the research work into context and summarizes the main points of the papers. Then, the research publications themselves are reproduced, together with a description of the individual contributions of the authors. The research papers may either have been already published or are manuscripts at various stages (in press, submitted, or in draft).

Cover illustration front: *Atomes et lumières* © Gecko

Funding information: The thesis work was financially supported by a FRIA grant of the Belgian Fund for Scientific Research F.R.S.-FNRS.

Lund University, Faculty of Sciences, Department of Mathematical Physics
Université libre de Bruxelles, École polytechnique de Bruxelles, Spectroscopy, Quantum Chemistry and Atmospheric Remote Sensing (SQUARES)

ISBN: 978-91-7895-777-4 (print)
ISBN: 978-91-7895-778-1 (pdf)

Printed in Sweden by Media-Tryck, Lund University, Lund 2021

vous vous débattiez dans des problèmes si effroyablement compliqués
que même le jeune homme candide et optimiste
que vous étiez alors dut parfois,
comme ses camarades d'infortune,
maudire le jour où il avait eu l'idée saugrenue
de se mêler de physique atomique

Le principe - Jérôme Ferrari [Extrait]

Acknowledgements

This thesis started in September 2017 and ended in May 2021 and during these four years I was lucky enough to share my time between Brussels (ULB) and Lund (LU). However, I spent most of last 12 months in my bedroom in the strangest of times, in lockdown because of COVID19. I was also very lucky, unlike many other PhD students, that my work could be performed entirely remotely, which allows me to finish my thesis as planned. That is of course not the only reason and I should thank all the people that have contributed to make that happened.

First, I would like to warmly thank Michel Godefroid for his constant support and encouragements throughout these four years. It is his communicative passion and enthusiasm for research in general, and atomic physics in particular, that motivated me to start a thesis. He brings the perfect balance between tutoring and friendship and so makes the working environment of his PhD students and co-workers a real treat. I am also extremely grateful that he voluntarily (or maybe not) continued to supervise my work after his retirement. Finally, I can not thank him enough for accepting the adventure of a double degree in partnership with Lund University and for his dedicated help with all the administrative paperwork needed to finally reach an agreement between the two universities.

Second, I would like to express my profound gratitude to Tomas Brage and Per Jönsson. They always made me feel welcome in Sweden and it was a great pleasure to share my time between Lund and Malmö. This unique experience could not have been possible without their help. I also thank them for the passionate discussions we had about physics and atoms. Many thanks to Tomas for inviting me to his famous midsummer parties and to Per for showing me the millions-years-old volcanoes of Skåne. I am also grateful to Per for taking the time to guide me into all GRASP subroutines.

Then, I would like to thank Nathalie Vaeck for accepting to take Michel's place after his retirement. Because of that, she received countless administrative emails regarding the preparation of the double degree agreement.

I gratefully thank Jörgen Ekman for all the discussions we had about nuclear physics and natural orbitals and for the considerate interest he always had in my work.

I also wish to thank my colleagues both in Belgium and in Sweden. A thesis is, in many aspects, more than a solitary work and so it has been an extreme pleasure to be part of two departments. First, the CQP/SQUARES members, who made these four years such an easy road. I want to thank Antoine, Jimmy and Gilles, my desk mates, for all the good times we had together. From the long lunches at Ninja House to the endless ping-pong games, it was a real pleasure to spend these years with them. I should also not forget Thibaut, Andrew and Nico who welcomed me to the department. The number of friday's afterwork definitely dropped after they left. I also want to thank the PhD students from the other side of the hallway, Hélène, Nico and Thibault for

the fun moments we shared everyday. It was a real pleasure to have you with us. I also wish to express my gratitude to all other members of the department, especially Julie, Pierre-François and Jean, for their help and support. Finally, I thank Ran and Kai. It was such a pleasure to form together a small atomic physics research group during their stays in Brussels.

I am also thankful to my Swedish friends and colleagues in Lund and Malmö. I wish to thank Asimina for showing me around in Lund and Malmö. It was so nice to work with her on our 'tin' project (even though it kept us busy for over 2 years) and I always felt very lucky that we were both doing a thesis on computational atomic structures at the same time (and defending 5 days apart!). I also want to thank Madeleine for her kindness and her friendship. Thanks to her I swam in the Baltic sea, so cool ! I am of course not forgetting LUMCAS members, Betül, Wenxian, Brian, Henrik, Hampus, and all the others. Finally, I wish to acknowledge all the people at the mathematical physics department in Lund, especially Katarina who has helped me countless times.

I also want to take the opportunity to thank the CompAS community. It was a priviledge to be a part of this fantastic international collaboration. Our annual meetings are without a doubt the highlight of the years. I would like to specifically thank Jon for the great energy he always brings. I also address my most grateful thanks to Charlotte, Gediminas, Jacek, Alan, Ian, and all others for their guidance and their thoughtfulness.

There are also many people outside of the world of physics without whom I could not have done this. I think first to my roommates that have supported me on a daily basis. First Clara, Milena and Maroussia of course. What a year of fun and laughters we have had together. Thanks you for all the precious moments we shared. And also thank you for (not) accepting my messiness. Then of course I want to thank Noé, Julien, Michaël and all the people that have lived 'Chez Gab' during the last 2 years. It is definitely a challenge to write a thesis stuck at home with 5 roommates, but they made it so easy. Thank you for the movie nights on our giant screen, the countless board game nights, and more simply for all the discussions, laughs, dinners or drinks that we share every day. I also would like to thank my childhoods friends Noé, Manjit and Totti for visiting me in Lund (almost twice!). Thank you also for the nice walks we had this last winter, it definitely helped me get through the writing of my thesis. Finally, I want to thank Antonin for the great illustration he made for the cover page, it could not have been any better.

Last but not least, my parents, who are always there for me. They have always supported me in my choices and encouraged me to do what I wanted. I also want to thank my brother and sister, Simon and Elsa, for the nicest time we had when they visited me in Lund. This first parents-free trip together was most definitely the first of many! Many thanks to Elsa for shooting the back cover picture. Finally, I wish to thank the rest of my small family, my grandfather, my aunts and my cousins.

Popular summary

The world we live in is fascinating. Extraordinary is our ability to describe and communicate about any observed phenomenon with a single, universal language: mathematics. Throughout centuries humanity has developed models and theories to understand almost everything we witness. From the microscopic, infinitely small world to the macroscopic, infinitely large Universe, atoms are some of the most basic constituents we know. For long, atoms were believed to be unbreakable, so that by combining atoms we could explain the constitution of all matter. Nowadays, the existence of subatomic particles is established, revealing the compound nature of atoms. Each atom is composed of a small nucleus made of protons and neutrons and an electron cloud extending far out from the nucleus (the nucleus is 10 000 smaller than the atom).

We are interested in the properties of these atoms, and in particular we aim to understand and describe the collective behaviour of electrons. For that, we combine two of the most well-known theories of the 20th century: quantum mechanics and general relativity. The former is intricate with the infinitesimal nature of electrons and atoms, that results in a duality of characters –corpuscular and wave-like– for all matter, while the latter deals with high energy phenomenon and supplanted classical mechanics. Nevertheless, the dynamical systems formed by electrons and nuclei are extremely difficult to apprehend, and large computer resources are required to predict their properties.

Atoms and ions are immense sources of information thanks to the light they produce or absorb. Because of their quantum nature, electrons bound by the nucleus can only take discrete energy values, so that by jumping from one energy level to another, they emit or absorb light, revealing the corresponding atomic spectra. These atomic spectra are valuable to analyze the light incoming from e.g., distant stars, revealing the presence of certain elements and contributing to explain the origins of matter in the Universe. On a much smaller scale, these transitions help to characterize the atomic nuclei, their shapes, their sizes, etc.. In order to extract this useful information, theoretical calculations are required to predict accurately the electronic energy levels, transition energies and transition rates, including effects such as the interaction with the electromagnetic field of the nucleus or the influence of adding (or subtracting) neutrons in the nucleus (isotope dependence). The goals of this thesis are therefore to perform atomic structure calculations for a set of systems of interest and to contribute to the developments of computational methodologies and state-of-the-art atomic codes.

Contents

List of publications

This thesis is based on the following publications, that are organized in four thematic groups. Within each group, they are referred to by their Roman numerals:

Group A: on the orbital basis

A$_{\text{I}}$ **Natural orbitals in multiconfiguration calculations of hyperfine structure parameters**

S. Schiffmann, M. Godefroid, J. Ekman, P. Jönsson, and C. Froese Fischer
Phys. Rev. A **101** 062510 (2020)

A$_{\text{II}}$ **Coulomb (Velocity) Gauge Recommended in Multiconfiguration Calculations of Transition Data Involving Rydberg Series**

A. Papoulia, J. Ekman G. Gaigalas, M. Godefroid, S. Gustafsson, H. Hartman, Henrik, W. Li, L. Radžiūtė, P. Rynkun, **S. Schiffmann**, K. Wang and P. Jönsson
Atoms 7 106 (2019)

A$_{\text{III}}$ **Relativistic Electron Density Functions and Natural Orbitals from GRASP2018**

S. Schiffmann, J. G. Li, J. Ekman, G. Gaigalas, M. Godefroid, P. Jönsson
To be submitted to *Comput. Phys. Commun.* (2021)

A$_{\text{IV}}$ **Relativistic semiempirical-core-potential calculations in Ca^+, Ba^+ and Sr^+ ions on Lagrange meshes.**

L. Filippin, **S. Schiffmann**, J. Dohet-Eraly, D. Baye and M. Godefroid
Phys. Rev. A **97** 012506 (2018)

A$_{\text{V}}$ **POLALMM: A program to compute polarizabilities for nominal one-electron systems using the Lagrange-mesh method.**

S. Schiffmann, L. Filippin, D. Baye and M. Godefroid
Comput. Phys. Commun. **256** 107402 (2020)

Group B: Nuclear physics applications

B$_{\mathrm{I}}$ **New structural trends in atomic nuclei from laser spectroscopy of tin**

D. T. Yordanov, L. V. Rodriguez, D. L. Balabanski, J. Bieroń, M. L. Bissell, K. Blaum, B. Cheal, J. Ekman, G. Gaigalas, R. F. Garcia Ruiz, G. Georgiev, W. Gins, M .R. Godefroid, C. Gorges, Z. Harman, H. Heylen, P. Jönsson, A. Kanellakopoulos, S. Kaufmann, C. H. Keitel, V. Lagaki, S. Lechner, B. Maass, S. Malbrunot-Ettenauer, W. Nazarewicz, R. Neugart, G. Neyens, W. Nörtershäuser, N. S. Oreshkina, A. Papoulia, P. Pyykkö, P.-G. Reinhard, S. Sailer, R. Sánchez, **S. Schiffmann**, S. Schmidt, L. Wehner, C. Wraith, L. Xie, Z.-Y. Xu and X.-F. Yang
Commun. Phys. **3** 107 (2020)

B$_{\mathrm{II}}$ ***Ab initio* electronic factors of the A and B hyperfine structure constants for the $5s^2 5p 6s\ ^{1,3}P^{\mathrm{o}}_1$ states in Sn I**

A. Papoulia[1], **S. Schiffmann**[1], J. Bieroń, G. Gaigalas, M. Godefroid, Z. Harman, P. Jönsson, N. S. Oreshkina, P. Pyykkö and I. I. Tupitsyn
Phys. Rev. A **103** 022815 (2021)

B$_{\mathrm{III}}$ **In-gas-cell laser resonance ionization spectroscopy of ^{196,197,198}Ir**

M. Mukai, Y. Hirayama, Y. X. Watanabe, **S. Schiffmann**, J. Ekman M. Godefroid I. Hamamoto, P. Schury, Y. Kakiguchi, M. Oyaizu, M. Wada, S. C. Jeong, J. Y. Moon, J. H. Park, H. Ishiyama, S. Kimura, H. Ueno, M. Ahmed, A. Ozawa, H. Watanabe, S. Kanaya and H. Miyatake
Phys. Rev. C **102** 054307 (2020)

B$_{\mathrm{IV}}$ **Electronic isotope shift factors for the Ir $5d^7 6s^2\ ^4F_{9/2} \rightarrow$ (odd, $J = 9/2$) line at 247.587 nm.**

S. Schiffmann and M. Godefroid
J. Quant. Spectrosc. Radiat. Transfer **258** 107332 (2021)

[1] Both authors have contributed equally.

Group C: Astrophysics applications

C$_{\text{I}}$ **Atomic structure calculations of Landé g factors of astrophysical interest with direct applications for solar coronal magnetometry**

S. Schiffmann, T. Brage P. Judge, A. Paraschif, and K. Wang
To be submitted to *Astrophys. J.* (2021)

C$_{\text{II}}$ **Benchmarking Atomic Data from Large-scale Multiconfiguration Dirac–Hartree–Fock Calculations for Astrophysics: S-like Ions from Cr IX to Cu XIV**

K. Wang, C. X. Song, P. Jönsson, G. Del Zanna, **S. Schiffmann**, M. Godefroid, G. Gaigalas, X. H. Zhao, R. Si, C. Y. Chen, and J. Yan
Astrophys. J., Suppl. Ser. **239** 30 (2018)

Group D: Negative ions

D$_{\text{I}}$ **Experimental and theoretical studies of the excited states of Ir^-**

M. K. Kristiansson, **S. Schiffmann**, J. Grumer, J. Karls, N. de Ruette, G. Eklund, V. Ideböhn, D. Gibson, T. Brage, H. Zettergren, D. Hanstorp and H. T. Schmidt.
Submitted to *Phys. Rev. A*

D$_{\text{II}}$ **Ab initio MCDHF calculations of the In and Tl electron affinities and their isotope shifts**

R. Si, **S. Schiffmann**, K. Wang, C. Y. Chen, and M. Godefroid
Submitted to *Phys. Rev. A*

Fundamental constants[1]

Bohr radius	$a_0 = 5.29177210903(80) \times 10^{-11}$ m
Bohr magneton	$\mu_B = 9.274\,010\,0783(28) \times 10^{-24}$ J T^{-1}
Electron mass	$m_e = 9.109\,383\,7015 \times 10^{-31}$ kg
Electron g factor	$g_s = -2.002\,319\,304\,362\,56$
Elementary charge	$e = 1.602\,176\,634 \times 10^{-19}$ C
Fine-structure constant	$\alpha = 7.297\,352\,5693 \times 10^{-3}$
Free space permeability	$\mu_0 = 1.256\,637\,062\,12(19) \times 10^{-6}$ N A^{-2}
Free space permittivity	$\varepsilon_0 = 8.854\,187\,8128(13) \times 10^{-12}$ F m^{-1}
Hartree energy	$E_h = 4.359\,744\,722\,2071 \times 10^{-18}$ J
Planck constant	$h = 6.626\,070\,15 \times 10^{-34}$ J Hz^{-1}
Reduced Planck constant	$\hbar = 1.054\,571\,817\ldots \times 10^{-34}$ J Hz^{-1}
Rydberg constant	$R_\infty = 10\,973\,731.568\,160$ m^{-1}
Speed of light	$c = 299\,792\,458$ m s^{-1}

[1] Values taken from E. Tiesinga, P. J. Mohr, D. B. Newell, and B. N. Taylor (2020), "The 2018 CODATA Recommended Values of the Fundamental Physical Constants" (Web Version 8.1). Database developed by J. Baker, M. Douma, and S. Kotochigova. Available at http://physics.nist.gov/constants, National Institute of Standards and Technology, Gaithersburg, MD 20899.

List of acronyms

AL	Average level
AS	Active set
ASF	Atomic state function
a.u.	Atomic units
CC	Core-core
CFP	Coefficients of fractional parentage
CFGP	Coefficients of fractional grandparentage
CSF	Configuration state function
CSCO	Complete set of commuting observables
CV	Core-valence
D	Double
DC	Dirac-Coulomb
DCB	Dirac-Coulomb-Breit
DHF	Dirac-Hartree-Fock
EAL	Extended average level
EOL	Extended optimal level
FS	Field shift
HF	Hartree-Fock
HFS	Hyperfine structure
HUM	Hylleraas-Undheim-MacDonald
IS	Isotope shift
ITO	Irreducible tensor operator
LBL	Layer-by-layer
LHS	Left-hand-side
MCHF	Multiconfiguration Hartree-Fock
MCDHF	Multiconfiguration Dirac-Hartree-Fock
MS	Mass shift
MBPT	Many-body perturbation
MR	Multireference
NMS	Normal mass shift
OL	Optimal level
PCFI	Partitioned correlation function interaction
PSE	Periodic system of elements
PTE	Periodic table of elements
Q	Quadruple
QED	Quantum electrodynamics
RCI	Relativistic configuration interaction
RHS	Right-hand-side
rFS	Reformulated field shift
rms	Root mean square
S	Single

SCF	Self-consistent field
SE	Self-energy
SMS	Specific mass shift
SR	Singlereference
T	Triple
UHF	unrestricted Hartree-Fock
VC	vector coupling coefficients
VV	Valence-valence
WE	Wigner-Eckart
ZF	Zero-first order method

Part I

Theoretical and computational backgrounds

Chapter 1

Introduction

1.1 Historic perspective

When starting to write my thesis, I came across an interview of Etienne Klein, french physicist and philosopher of sciences.[1] He discussed the idea that *"nous avons une mauvaise connaissance de nos connaissances"*, literally, we have poor knowledge of our knowledge, that is, we have a tendency to forget how a particular knowledge became knowledge and how it overcame the arguments against it from people that had opposite believes at the time. Taking the example of the spherical shape of the earth, well established in the popular opinion since the first pictures were taken from space in 1956, he questioned: *"Comment a-t'on su que la terre était ronde? Et quand ? [...] avec quels arguments [...] à opposer à ceux qui pensaient que la terre était plate?* (How did we know that the earth was round ? And when ? [...] what were the arguments [...] to oppose to those who believed that the earth was flat?). Even as a scientist myself, my answers to these questions were only partial.

These small, destabilizing questions were enough to push myself to interrogate how our conception of the atom evolved through time and how the modern theory of the atom–a quantum atom made of a nucleus and a cloud of wave-like electrons–was established and universally accepted. To guide our thoughts, we follow two books that provide an interesting historic perspective about the modern atomic theory [1, 2].

[1] Étienne Klein : Éthique et philosophie des sciences, le rôle des scientifiques ? (video available since 17/01/2018 at https://www.youtube.com/watch?v=KIwtT8cAAKI)

1.1.1 From the Greeks to the acceptance of the atomic theory

It is often heard that the concept of an atom comes from ancient Greek time. It was indeed most likely born in the atomist school of Abdera under the teaching of the famous Democritus (460–370 BC)[2] and his predecessor, Leucippus (5th century BC)[3]. The name *atom* itself is Greek for indivisible. The doctrine taught by Democritus and Leucippus was based on two basic constituents, atoms and void. However, *"a collection of the terms of the preceding atomist quotations points out that one of the two most basic constituents, atom, is called the full, compact, being, the solid; while the other principal ingredient, the void, is called the empty, nothing, nonbeing and elsewhere in opposition to compact, the rare. [...] the void is as real as the atom"*. [1, p.10]. Their philosophy therefore aims to explain "the all", for which they postulate an infinite number of atoms of infinite different forms, which were compact objects constantly moving and free of void (*"what is not"*); *"their substance was full"* [1, p.3]. The difficulty to assess that it is indeed at that time and place that the concept of an atom was born arises from the lack of anterior writing and the very few pieces from Democritus' work that reached us through the centuries.

Most of what we know about the early atomist doctrine actually comes from Aristotle (384–322 BC) who merely overlapped with Democritus and who was powerfully opposed to the nature indivisible of any physical body. A more complete analysis of Aristotle criticism is presented in the book by McDonnell [1, p.44]. Besides the writing of Aristotle and Democritus himself, the only other ancient source is Lucretius (99–55 BC) in his *De Rerum Natura*, that reinstated the atomist theory. The question asked by McDonnell is therefore to understand whether the atom imagined by the physicists of the 19th century led by Dalton (1766–1844) is the same *thing* or simply possesses the same *name* that the one meant by Democritus. The relevance of such an interrogation is obvious when considering the famous relation

$$\textit{1 atom of A plus 1 atom of B = 1 atom of C, binary} \tag{1.1}$$

from Dalton's theory [3, p. 213], which is in clear contradiction with the indivisible character of Democritus' atoms. The answer to the above question is resumed by McDonnell as follows: *"Some influence, yes; identity, no"* [1, p.117]. That the name *atom* was inherited from Democritus goes without question, passed through time mostly thanks to the fierce opposition of Aristotle, but *"the content of the name changed radically"* [1, p.117] and concluding *"This means then that Dalton's gravimetric atom-concept was new! None of Dalton's fellow scientists turned to the ancient doctrine to find confirmation or explication of Dalton's operations. Essentially the new atom simply does not equal the ancient atom. If this be true then those who equalize the two without distinction, do a disservice to the truth. An unequivocal*

[2] The dates of birth and death are given for each scientist in parenthesis.

[3] Note that the dates of birth and death of ancient Greek philosophers are approximate.

identification of the two, an equating of the ancient and the new, whether in book, lecture or oratory does baneful and unscientific disservice to the facts." [1, p.118–119].

It is still worth following the major steps in the evolution of atomic theory from the definition given by the Greek philosophers to the chemists of the 19th century. One might also be surprised that atoms were 'known' for about two millennia when 're-discovered' by Dalton, Lavoisier and others. Van Melsen highlights in his book two reasons why the supporters of atomism were very few in the Middle Ages: *"In the first place, Democritus' system suffered from an hereditary infection of anti-Christian materialism...Secondly, the Aristotelian minima theory offered at least as many possibilities as atomism."* [4, p.178]. It is Newton (1642–1727) himself, following the corpuscular philosophy of Gassendi (1592–1655) and Boyle (1627–1691) who laid the ground work for the renewal of atomic physics with his study on elastic fluids (i.e., gas) by postulating the hypothesis that gases are constituted of repelling particles. Lavoisier (1740–1794) made important contributions by redefining 'elements' as *"the notion of the ultimate entity arrived at by analysis; all substances that we have not yet decomposed by any means, we consider elements."* [2, p.197], hereby invalidating Aristotle four elements (earth, water, air, fire) and establishing the law of conservation of matter, that would be the cornerstone for all future research in atomic physics. The conditions were then optimal for Proust (1754–1826) and Dalton (1766–1844) to discover the gravimetric laws: the law of constant proportion and the law of simple multiple proportions, respectively. *"The first state that two elements always combine in invariant ratios of weight, and the second specifies that when two elements can combine in several different ways, their relative weights in the resulting combinations form simple ratios, that is to say, rational numbers."* [2, p.198] These laws turn out to be crucial for Dalton to establish his table of relative weights for a number of elements such as hydrogen or oxygen. Unfortunately, Dalton's constant use of the word atom to refer to compound systems added confusion until the works of Gay-Lussac (1778–1850) and Avogadro (1776–1850) who introduced the concept of molecules.

The use of the gravimetric laws to understand e.g., how the basic constituents of water combines, were at the time not accepted by all. In fact, a number of French chemists led by Dumas (1800–1884) attacked vigorously the newly created atomic theory, proclaiming that *"whether ancient or modern, chemists insist on seeing with the eyes of the body, not with those of the mind; they are interested in developing theories of facts, not searching for facts supporting preconceived theories"* [2, p.205]. This criticism that no-one ever *sees* a gas molecule or an atom was recurrent at the time. We are as far as possible from modern considerations that led us to e.g., build the Large Hadron Collider (LHC) to find a particle, the Higgs boson, almost 60 years after its theoretical prediction! Regardless of the attacks against atomic theory, the evidences continued to mount, finally allowing Mendeleev (1834–1907) in 1869 to propose his first version of the *periodic table of elements*. The arrangement of the

known elements according to their atomic weight revealed a periodic structure of their chemical properties. Furthermore, the strength of the periodic table was to predict the existence of new, unknown elements by leaving empty slots in the table. Still, the lack of irrefutable evidences left the scientific community split until the important work of Perrin (1879–1955) who determined Avogadro's constant in multiple ways. His book *Les atomes* published in 1913 can be considered as the decisive victory of the atomic theory. Even Poincaré (1854–1912), who remained sceptical until the very end, acknowledged the existence of atoms right before his death at a conference of the French Physical Society by admitting: *"the atomic hypothesis has recently acquired enough credence to cease being a mere hypothesis. Atoms are no longer just a useful fiction; we can rightfully claim to see them, since we can actually count them"* [2, p.256].

1.1.2 The modern atom

In the beginning of the 20th century, major advances in atomic theory occurred, following the acceptance of atoms. An important turning point is the discovery by Thomson (1856–1940) in 1897 of a negatively charged particle: the electron. In his study on electrical discharges in low-density gases, he was able to demonstrate that electrons were detected independent of what gas was used in the experiment. He rightfully concluded *"Since electrons can be produced by all chemical elements, we must conclude that they enter in the constitution of all atoms."* [2, p.257]. The neutral character of atoms, however, forced scientists to postulate the existence of a positive charge in atoms to counterbalance the negative charge carried by the electrons. The first ever model of the atom was proposed in 1902 by Kelvin (1824–1907) and Thomson, in which they describe atoms as made of negatively charged particles, the electrons, and a *uniformly distributed positive electrical cloud* [2, p.258]. The major problem encountered with this model, besides the peculiar difference of treatment–discrete and continuous–of the negative and positive charges, is the origin of the atomic mass, largely superior to that of the electron.

Rutherford (1871–1937) overcame the question of the atomic mass thanks to his famous experiment. He bombarded thin layers of gold with α particles and observed their scattering. His observations led him to propose the planetary model of the atom in 1911, in which he postulated the existence of a *nucleus*, that is carrying a positive charge equal to the sum of the negative charges carried by all electrons and accounting for most (almost all) of the atomic mass and that is of dimensions 10^{-5} smaller than the atom itself, to explain the measured scattering distribution. In his model, the electrons are rotating around the nucleus thanks to the Coulomb forces, much like planets are orbiting around the Sun thanks to the gravitational force. However, himself was aware that his model was not viable, as it is well-known from classical electrodynamics, since such electrons would continuously

lose energy, hence progressively falling onto the nucleus. The main feature of the model is therefore the discovery of the nucleus, and later of the *proton*, identified as the elementary positively charged particle and 2000 times heavier than an electron.

The shortcomings of the planetary model proposed by Rutherford led Bohr (1885–1962) to propose his own model of the atom a few years later (1913) (see Sec. 2.1). He was guided by the original theory of light quanta by Planck (1858–1947) and Einstein (1879–1955) and by the empirical relation observed by Balmer (1825–1898) in his work on atomic spectra of hydrogen. To resolve the inadequation of theory–experiment on the blackbody radiation distribution, Planck postulated that matter emits and absorbs light in discrete "packages", that are multiple of elementary quantum of light (1900). The existence of light quanta strongly opposed to the believe that energy was exchanged continuously. Einstein's work on the photoelectric effect a few years later (1905) established the corpuscular nature of light. Light is composed of elementary particles called *photons*, that have energies equal to the fundamental light quanta introduced by Planck. Bohr's brilliant idea was to combine the planetary model of Rutherford with the theory of light quanta. His model brought the satisfactory result to explain Balmer's formula, which describes atomic spectra using simple integers. Bohr suggested that every atomic system possesses a discrete number of possible states, each associated to a different energy, and that the frequency of the emitted light is fixed by the change in energy. This implies that electrons move in certain selected orbits with constant energy and have the possibility to jump to another orbit by emitting (or absorbing) a quantum of light with an energy equal to the energy difference between the two orbits $h\nu = E_1 - E_2$. Bohr's model of the atom opened the door to quantum mechanics as we know it.

The recurrent use of integers already appearing in Balmer's formula and inherited from the theory of quanta in Bohr's model was the first step toward the wave-like behaviour of matter. Indeed, integers are frequent in all physics phenomena that deal with waves, such as acoustics or optics. Standing waves for example are characterized by their number of nodes (0,1,2,...). It is therefore not so surprising to imagine that electrons could (partly) behave as waves. Moreover, as discussed earlier, light, that was always considered a wave, had just acquired particle-like character. This duality was made explicit by de Broglie (1892–1987) who, inspired by Einstein's formula $E = mc^2$, i.e., to any particle of mass m is associated an energy $E = mc^2$, assigned to any particle a frequency ν and an energy $E = h\nu$. de Broglie went one step further by establishing another relation, $\lambda = h/p$, which associates to any particle with the momentum p a wave of wavelength λ. These relations establish the dual nature –corpuscular and wave-like– of any material. *And so does quantization lose its mystery; it becomes a natural consequence of the standing wave character of electrons in an atom.* [2, p.275]

Acknowledging the wave character of matter, Schrödinger (1887–1961) derived the wave equation that carries his name, the *Schrödinger equation*. The mathematical details are discussed further in later sections, but its main features are the following. The solution of the time-independent equation provides a *wave function*, that describes the particle in a particular state of energy E. The interpretation of what the wave function really *is* led the physicists to considerable debates. As an example Schrödinger himself considered the wave function as real property of the electrons, just as real as acoustic or optic waves. A very different interpretation was proposed by Born (1882–1970) and is widely accepted today: *"The square of the module of the wave function Ψ at any given point and any given instant is a measure of the probability that the corresponding particle be found at that point and at that instant."* [2, p.278] . This interpretation changed radically our perceptions of the atom and electrons: there is no certainty about an electron position. Only a certain probability to find it in a certain volume of space. Nevertheless, an electron could be detected experimentally e.g., by scintillation on a fluorescent screen, and its position resolved and known. How conciliate that a spread-out wave-electron suddenly concentrate in a given point of space ? The *collapse* of the wave function is obviously a difficult phenomenon to interpret. The best explanation is that the wave function collapses due to our own intervention, i.e., by doing the measurement.

We here stop our historical perspective on atomic theory, leaving out important aspects due to their increasing mathematical complexity. Some are discussed in great details in later sections. Nevertheless, it is important to cite the names of Dirac (1902–1984), who proposed another wave equation for the electron a few years after Schrödinger that revealed the existence of the *positron*, anti-particle of the electron, and therefore *anti-matter* in general, Pauli (1900–1958), who took advantage of the discovery of the electron *spin* to establish his *exclusion principle*, Heisenberg (1901–1976) and his *uncertainty principle* or Einstein (1879–1955) and the theory of relativity. Finally, we should at the very least mention Curie (1867–1934), who's work on radioactivity proofed wrong Democritus and Leucippius once and for all: atoms are not indivisible.

1.2 The periodic system of elements

The periodic table of elements (PTE) is the playground of atomic physicists (see Fig. 1.1), although it might be more faithful to introduce atoms as forming a *periodic system of elements* (PSE) graphically displayed in tables such as the iconic PTE (see e.g., [5]). The PTE as we know it is based on the observation of similarities of chemical properties of groups of elements. Based on the graphical display of the PTE, Wang and Schwarz [6] list "vertical" groups such as Li–K or He–Rn, "horizontal" groups such as Cr–Cu or La–Lu, but also "diagonal" groups as Be–Al that were observed prior to the PTE. Finally, smaller groups are

formed by pairs of elements sharing interesting properties such as Ag-Tl ("knight's move pair"), Ru-Pt ("connected fields") or Al-Fe ("distant pair"). Interestingly, the large variety of atomic and chemical properties, such as atomic radii, number of electrons in valence shells, dominant valence numbers, electronegativity, reactivities, ..., are best ordered according to the nuclear charge Z. Any attempts to classify elements according to another quantity was unsuccessful: it is the nuclear charge that determines fully the ordering of the elements and reveals the periodicities of chemical properties.

The origin of these periodicities is most likely centred around the noble gases and the closure of the $1s^2$ and np^6 shells. Together with elements belonging to the previous group (group 17; halogens) and the next group (group 1; alkali metals) they are the backbone of the PSE [6]. Most of the other elements are therefore defined with their distance from the noble gases. Their extraordinary stability is due to the large energy gap above, that makes the extra electron of their successor elements loosely bound and correspondingly these elements are electropositive while their predecessors have valence-active p-holes; they are electronegative. The understanding of the chemical properties of elements belonging to groups 3 to 12, corresponding to the filling of the d-shells is more difficult. Group 10 (Ni-Pd-Pt) is particularly interesting. The ground configurations of the bound free atoms are $3d^8 4s^2$, $4d^{10} 5s^0$ and $5d^9 6s$, respectively, that make it not easy to relate them with chemical trends. Extraordinarily, the Ni atom in a compound such as $Ni(CO)_4$ and the free-atom Ni are dissimilar. Their ground configurations are $4d^{10}$ for the compound Ni and $3d^8 4s^2$ for the free atom: they significantly differ. When inserted in contact with its environment, the atomic valence s orbital overlaps with s orbitals of other atoms, that destabilizes the atomic orbitals and leads to a much lower energy for the nd orbital compared to the $(n+1)s$ orbital [6]. In this thesis, we exclusively focus on free atoms, and consider only the influence of external electromagnetic fields on the electronic structure.

The PTE is an excellent tool to predict chemical properties thanks to the observed trends along elements of a given group or period. However these trends start to be broken toward the end of the PTE. This is explained by the growing influence of relativity that perturbs considerably the electronic atomic structures. The *relativistic effects* are somewhat hard to define precisely. Pyykkö and Desclaux [7] define the relativistic effects as the differences observed when using an infinite value for c, the speed of light, and its actual finite value. That ambiguity is also raised by Froese Fischer *et al.*, that refer to relativistic effects as the difference between the Schrödinger and Dirac equations [8, §7]. With the latter definition, the correction to the Coulomb operator known as the Breit interaction is not a relativistic effect. Following Pyykkö and Desclaux we discuss three main relativistic effects: orbital contractions, spin-orbit splitting and relativistic self-consistent expansions [7]. The orbital contractions affect mostly the s and $p_{1/2}$ orbitals, that are pulled toward the nucleus. Because these orbitals are contracted, they provide a more efficient screening of the nuclear charge, which explains the expansion of the $p_{3/2}$ and higher l-angular momenta

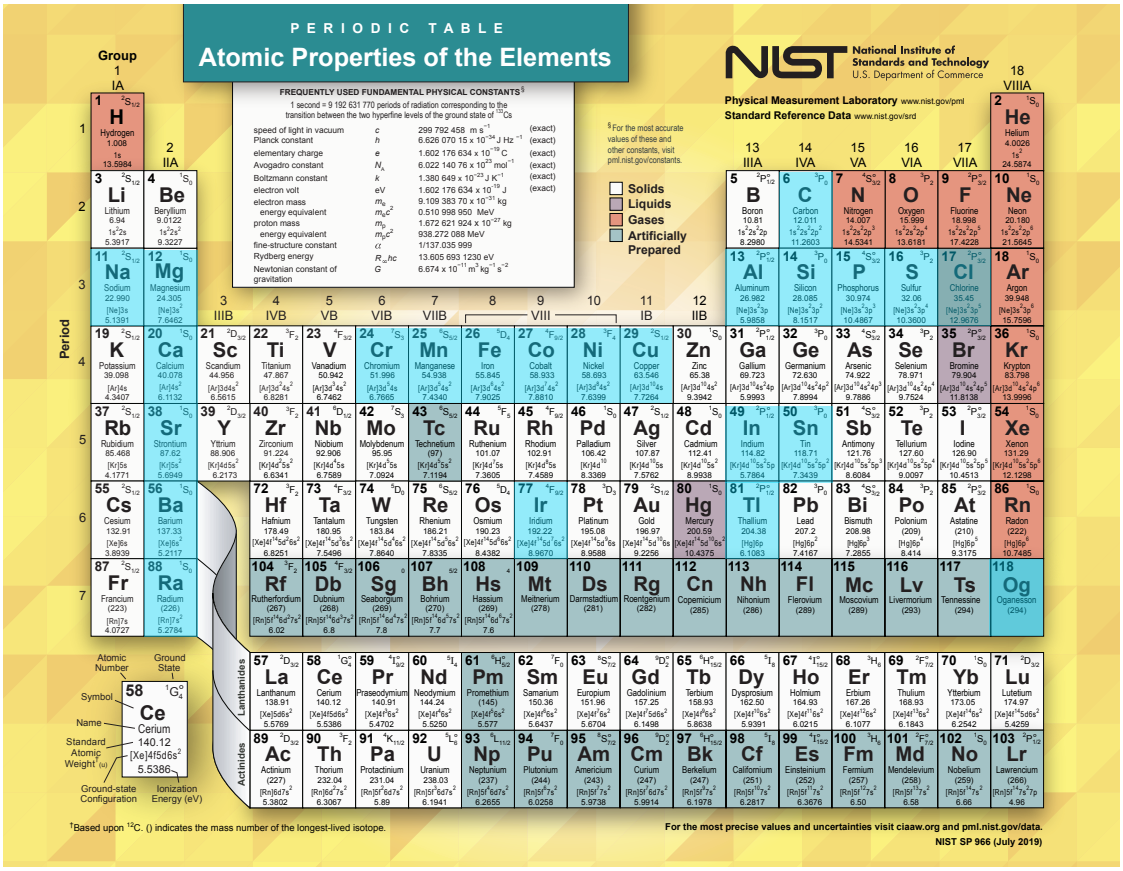

Figure 1.1: Periodic table of elements taken from NIST [9]. The elements in light blue correspond to the atomic systems studied in this thesis.

orbitals, i.e., the effective charge of the nucleus is lesser and they are less tightly bound. The spin-orbit coupling results from the coupling of the orbital angular momentum and the electron spin. Spectacular consequences of these effects are observed in e.g., the Au-Hg pair, that is mostly due to the contraction of the $6s$ orbital. Because of that contraction, Hg, with its $[\mathrm{Xe}]4f^{14}5d^{10}6s^2$ closed shell structure, behaves almost as an inert noble gas element. Toward the end of the PTE, in the region of the super-heavy elements (SHEs) with $Z > 103$, the relativistic effects make the chemical properties even less predictable. Because these SHEs already deviate substantially from the trends expected from their lighter homologous, one can expect the complete break down of the PTE in the 8th row [6]. A striking example is Og ($Z = 118$), the heaviest element ever recognized. Although predicted as a noble gas, it has drastically different chemical properties e.g., it is not inert, due to a combination of the three relativistic effects listed above: the contraction of the $7s$ and $7p_{1/2}$ orbitals followed by the expansion of the $7p_{3/2}$ orbital, hence the large fine-structure splitting between the $7p_{1/2}$ and $7p_{3/2}$ orbitals, explain the different chemical nature of Og.

1.3 Motivation

Turning to our specific research work, we have chosen a title, *Computational Atomic Structures Toward Heavy Element Research*, that is intentionally broad and unspecific so that it leaves some room for interpretation. In our introduction we will decompose and justify each of its elements to provide a clearer context in which this thesis is written. Essentially, it conveys the guiding principle that connects the different projects conducted over the last four years.

First, and above all, this is a thesis about atoms and their electronic structure. Throughout this manuscript, we aim to study how electrons interact with each other and with the nucleus. *Atomic Structures* refer broadly to the energy level positioning and the transition characteristics between two energy levels. Atomic transitions are of the greatest importance in the understanding of observed spectra, that consist of the frequency decomposition of e.g., incoming light. Probably one of the most studied spectra comes from the light emitted by the Sun and reaching Earth after it has passed through our atmosphere. Actually, most of the information we have about stellar objects consist of spectra. The *spectral* analysis consisting of the frequency decomposition of the incoming light is therefore of prime importance to characterize the light source, i.e., the presence of certain elements, their abundance, and ultimately it provides information about the birth of the Universe and the production of all known elements. However, these observations rely greatly on theoretical support and predictions. The literature is over-abundant on the theoretical aspects as attests the following books and papers, *The Theory of Complex Spectra* (1929) [10], *The Theory of Atomic Spectra* (1935) [11], *Theory of Complex Spectra. I-IV* (1942–1947) [12, 13, 14, 15], *Atomic Spectra* (1964) [16], *The theory of atomic structure and spectra* (1981) [17], *Theoretical Atomic Spectroscopy* (1997) [18], *Computational Atomic Structure* (1997) [8], *Operator Techniques In Atomic Spectroscopy* (1998) [19] or *Atomic Structure Theory* (2007) [20], to cite a few. This research area is still very active at the beginning of the 21th century (see e.g., [21, 22, 23, 24, 25, 26]), as also supported by our research papers and manuscripts.

The theoretical treatment of atomic systems from first principles is a complex task. So much that the equations that characterize the state of a system can be solved analytically only in the simplest cases, that are atomic and ionic systems with a single electron. The Coulomb repulsion that arises between two electric charges of the same sign is such that He-like systems, i.e., two-electron systems, have no analytical solutions to their differential equations. That is why we turn to *Computational* methods that solve numerically (and approximately) the many-electron equations. It should then become clear that this thesis focuses on *Computational Atomic Structures*: the method of calculations itself is our guiding principle. We are using throughout this thesis variational methods, and, in particular, the *multiconfigurational Dirac-Hartree-Fock* (MCDHF) method [27, 28] as implemented in the *general-purpose relativistic atomic structure program* (Grasp) [29, 30]. Nevertheless, it

is worth mentioning the MCDFGME code that is also based on the MCDHF method [31, 32, 33]. Other many-body approaches exist, but will not be discussed in the following. Whereas the MCDHF method takes advantage to the variational principle to generate the basis functions that minimize the energy, other methods like the *many-body perturbation theory* (MBPT) and *coupled cluster* (CC) methods employ perturbation theory and define effective Hamiltonians [34, 35, 36]. Numerous programs are available to perform either MBPT or CC calculations such as the FAC code [37], the DIRAC19 program [38], the CI-MBPT program [39], the AMBiT program [40] or the RCCPAC program [41]. Each of these programs has its own specificities and therefore might be more suitable than the others depending on the application at hand.

The concept of *Heavy Element* is defined in the nuclear physics context and is directly related to the mass of the nucleus. Unfortunately, the limits of the heavy nuclei group are somewhat unclear. Although there is little doubt that e.g., Pb ($Z = 82$) should be considered as heavy or C ($Z = 6$) as light, nuclei in the middle-range such as Fe ($Z = 26$) are more subject to interpretation. Furthermore, discussing whether an element is heavy or not based on the sole atomic number is somewhat biased and the nuclear physicists would rather use the mass number A that combines the number of protons and neutrons. That way, isotopes, which are nuclei with the same atomic number but different neutron number, are also included. Looking toward the end of the periodic table, however, the group of super-heavy elements (SHEs) is quite well defined. Numerous papers refer to SHEs as the elements with $Z > 103$, which then correspond exactly to the *transactinides* [42, 43, 44]. Still Oganessian refers to SHE as elements with $Z > 113$ based on nuclear physics considerations [45]. Grevesse *et al.* provide a clearer definition of heavy elements as the elements with $29 \leq Z \leq 90$ (from copper to thorium) and even defines medium elements as elements with $Z > 8$, i.e., heavier than oxygen. Other examples are e.g., Quinet who refers to heavy elements as those with $Z \geq 37$ (Rb and above) [46], Indelicato and Lindroth who refer to medium to very heavy elements to elements with $31 \leq Z \leq 100$ (Ga to Fm) [47] or Thielemann *et al.* who defines heavy elements as heavier than Fe [48]. The concept of very heavy elements is also used by Dorvaux *et al.* as the elements heavier than Pb ($Z = 82$) [49]. Impressive is the number of papers mentioning heavy elements without giving an explicit definition, most likely relying on some implicit common knowledge. Striking examples are the papers *Quantum Electrodynamics of Heavy Ions and Atoms* by Shabaev *et al.* [50] or *On the accuracy of valence–shell computations for heavy and super–heavy elements* by Fritzsche [51].

In atomic physics, however, the sole nuclear charge is not enough to assess the complexity of a system. For example, the U^{91+} ion is heavy without a doubt, but the corresponding Dirac equation can be solved analytically. Two effects are competing when describing complex atomic systems: the *electron correlation* and the *relativistic effects* (and quantum electrodynamics (QED) effects). The challenges faced in computational atomic structure directly depend on the relative importance of these two aspects. The former is obviously

related to the number of electrons, i.e., neutral and anionic systems are the most sensitive, while the latter is related to the nuclear charge. We will show later that the key parameter for relativistic and QED effects is αZ where $\alpha \approx 1/137$ in atomic units (see Sec. 2.1). A somewhat still fuzzy definition is therefore to consider an element as heavy when Z becomes 'comparable' to $1/\alpha$ [50]. In highly charged heavy ions, the relativistic and QED effects completely dominate over the electron correlation. These atomic systems are therefore often studied to improve our understanding of these effects and their separate different small contributions (see e.g., [52, 53]). These systems are also used to investigate the effect of nuclear polarizations or finite nuclear size corrections [54, 55]. On the other hand, light neutral systems are dominated by electron correlation and one might perform accurate calculations in the non-relativistic framework.

In our work, *Heavy Element* refer to atomic systems for which both electron correlation and relativistic effects are large. That is why we almost exclusively focus on neutral and near-neutral atomic systems, except in our study of highly charged ions of astrophysical interest. In the framework of the MCDHF method, electron correlation is included by expanding the wave function over a large set of many-electron basis functions generated by electron substitutions while relativistic effects are taken into account by solving the many-body Dirac-Coulomb equations. Except for the increasing number of orthogonality constraints, the complexity of the latter is independent of the number of electrons: there is no *additional* difficulty to solve the equations for a larger number of electrons. However, the description of electron correlation crucially depends on the number of electrons and the corresponding occupied shells. From a computational atomic structures perspective, the occupation of the first d-shell can be considered as a pivotal point. When the $3d$-shell is part of the core (neutral atoms with $Z \geq 37$), an accurate description of the correlation within the atomic core is already challenging, so that we can consider as heavy all elements with more than 37 electrons. Nevertheless, we contextualized our work *Toward* heavy elements, which adds even more fuzziness to our title, as we perform atomic calculations not only targeting heavy systems, but also finding efficient ways to achieve accuracy in their description. This explains why we also consider atomic structure calculations for some lighter elements, as useful benchmarks, keeping in mind the road to heavy elements.

The need for improving codes and computational methodologies is motivated by many well-known ongoing research topics that somehow rely on atomic data. Notorious examples include the search of an island of stability around $N = 184$ that drives the calculations for SHEs (see e.g., [44, 56, 57, 22, 58]) or cosmochronometry of ultra-poor metal stars for which the determination of the abundances of Th or U crucially depends of the knowledge on the transition frequencies and their associated oscillator strengths (see e.g. [21, 59]). There are also vast interests in nuclear physics to determine e.g., nuclear shapes and deformations (see e.g., [60, 61, 62, 63] or the shape-staggering effect in Hg [64, 65]). Other examples include astrophysical purposes to analyse observed spectra by computing tran-

sition properties over a wide frequency range (see e.g., [66, 67, 68, 69, 70, 71]) or the determination of solar magnetic field using magnetic-induced transitions (see e.g., [72, 73, 74, 75, 76, 77]). Finally, atomic physics plays a role in the search for "new physics" that would induce unexpected effects such as non-linearities in King plots (see e.g. [78, 79]) or the variation in space and time of universal constants like the fine-structure constant α [80, 81].

In this thesis, we therefore aim to present the results of our work *Computational Atomic Structures Toward Heavy Element Research*. In the first part, that is dedicated to the theoretical and computational backgrounds, we first describe the basic mathematical concepts of atomic structure theory by considering one-electron systems (Chap. 2), for which we decided to follow the original chronological steps taken by the physicists of the beginning of the 20th century. In Chap. 3, we outline the mathematical and computational tools that we use to investigate the atomic structures of complex, many-body systems. In the second part, we present our original scientific results by commenting and summarizing our manuscripts and published papers. We divided them in four thematic groups labelled A, B, C and D, that have different foci. The first one, Group A (Chap. 4), is dedicated to an intensive study of the role of the orbital basis in variational methods. The second one, Group B (Chap. 5), gathers our studies relevant to nuclear physics, while the third one, Group C (Chap. 6), focuses on works oriented to astrophysical applications. Finally, the last chapter preceding the concluding remarks, Group D (Chap. 7), is entirely dedicated to negative ions. The choice of the studied systems depends on external criteria such as ongoing experiments that require atomic data, unresolved discrepancies between theory and experiment or exploratory work of lesser known atomic systems. The large variety of studied systems in this thesis is illustrated on Fig. 1.1, in which we have highlighted in light blue all studied elements in the PTE. Although it is clear that both the nuclear charge and the number of electrons are required to define unequivocally an atomic system of interest, we have decided to only display the studied elements according to their nuclear charge for practical reasons.

Chapter 2

Quantum theory of the hydrogen-like atom

The theoretical background required to understand modern atomic physics is vast. It relies on a complex mathematical formalism and a high level of abstraction. Quantum mechanics is at the heart of every single step we take. Various paths exist to introduce the most up-to-date atomic models and computational methods atomic physicists are employing in the beginning of the 21th century. Countless textbooks exist on quantum mechanics in general and atomic physics in particular, and we follow in this work a couple of them [27, 82, 17, 83]. In this thesis, we aim to provide a brief introduction to quantum mechanics and the quantum theory of atoms by following the original chain of thoughts of the early quantum physicists until the establishment of the one-electron Dirac equation.

2.1 Bohr's model

Bohr's model of the atom is an excellent starting point to dive into the description of atomic structure theory. We already discussed in the introduction how the human understanding of an atom evolved through time and presented the beginning of the 20th century as a turning point in our perception of the atoms.

The discovery that each element emits light with a discrete number of frequencies different from the others culminated with the derivation of the empirical formula of Balmer in 1885,

$$\tilde{\nu}_{ab} = R_\infty \left(\frac{1}{n_a^2} - \frac{1}{n_b^2} \right) ; \quad n_a = 2; \quad n_b > n_a \, , \tag{2.1}$$

where $\tilde{\nu}_{ab} = \nu_{ab}/c$ is the wave number corresponding to the frequency ν_{ab} of the observed

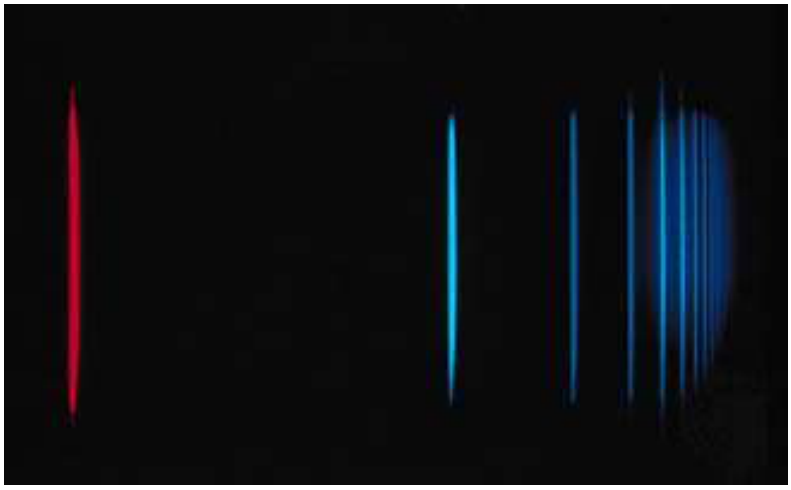

Figure 2.1: Portion of the hydrogen spectrum observed by a low-resolution spectrometer corresponding to the Balmer series. https://www.britannica.com/science/spectroscopy/Basic-properties-of-atoms

line, n_a and n_b are positive integer with $n_b > n_a$, c is the speed of light and R_∞ is the Rydberg constant. Balmer made this important first step thanks to his observations of the hydrogen visible spectrum (see e.g., Fig. 2.1).

The scientific effervescence following the theory of light quanta suggested by Planck and pursued by Einstein led Bohr to propose his model of the atom. Its major success was to reproduce Balmer's formula from theoretical considerations. Bohr introduced the following series of postulates to overcome the limitation of the classical planetary vision of the atom [84]:

1. The electron moves around the nucleus in a circular orbit.
2. The number of accessible orbits is countable, each corresponding to a different energy E_n.
3. An atom only radiates, or emits a photon of energy $h\nu_{ab}$, when an electron jumps from an orbit b to another orbit a, establishing the well-known *frequency relation*

$$h\nu_{ab} = E_b - E_a \ , \tag{2.2}$$

   where $E_b > E_a$.
4. The electron has an angular momentum that can only take discrete values $L = nh/2\pi = n\hbar$, where $\hbar = h/2\pi$ is the reduced Planck constant.

Since the electron is moving around the infinite-mass nucleus on its orbit with a constant velocity v at the distance r, the attractive electric force between the electron and the nucleus

of charge Ze, where Z is the number of protons and e is the electric charge of the proton, equals the product of m, the mass of the electron, and v^2/r the centripetal acceleration or

$$\frac{Ze^2}{4\pi\varepsilon_0 r^2} = \frac{mv^2}{r} \,, \tag{2.3}$$

where ε_0 is the universal constant for the free space's permittivity that appears in the electromagnetic interaction formula. The second equation derived by Bohr relates the classical angular momentum $L = mvr$ and its quantized counterpart $L = n\hbar$,

$$mvr = n\hbar \,, \qquad n = 1, 2, \ldots \,. \tag{2.4}$$

Solving the system of equations (2.3) and (2.4) for v and r, one finds

$$v = \frac{Ze^2}{4\pi\varepsilon_0 \hbar n} \,, \tag{2.5}$$

$$r = \frac{4\pi\varepsilon_0 \hbar^2 n^2}{Ze^2 m} \,. \tag{2.6}$$

Using the classical expression of the kinetic energy, $T = mv^2/2$, and the potential energy $V = -Ze^2/4\pi\varepsilon_0 r$ and knowing that the total energy of the system is given by their sum, Bohr derived

$$E_n = T + V = -\frac{m}{\hbar^2}\left(\frac{Ze^2}{4\pi\varepsilon_0}\right)^2 \frac{1}{n^2} \,. \tag{2.7}$$

Considering the simplest case of the hydrogen atom ($Z = 1$), the frequency of the photon emitted by the jump $b \to a$ between two energy levels a and b is given by

$$\tilde{\nu}_{ab} = \frac{m}{4\pi\hbar^3 c}\left(\frac{e^2}{4\pi\varepsilon_0}\right)^2 \left(\frac{1}{n_a^2} - \frac{1}{n_b^2}\right) \,, \tag{2.8}$$

which reproduces the empirical formula of Balmer (2.1) if the Rydberg constant is identified as $R_\infty = \frac{m}{4\pi\hbar^3 c}\left(\frac{e^2}{4\pi\varepsilon_0}\right)^2$.

Bohr's model of the atom was revolutionary as it is the first ever model able to explain the discrete character of the observed spectra. It also provides the key to define an alternative system of units to the *International System of units* called *atomic units* (a.u.) and widely used in the present days by all atomic physicists. Consider the hydrogen atom ($Z = 1$) with its single electron in its lowest energy level ($n = 1$) as the reference. From equations (2.5) and (2.6), the unit of length a_0, called the Bohr radius, is derived to be $a_0 = 4\pi\varepsilon_0\hbar^2/e^2 m$ and the unit of velocity v_0 to be $v_0 = e^2/4\pi\varepsilon_0\hbar$, respectively. Equivalently, we can set $e = \hbar = m = 4\pi\varepsilon_0 = 1$, that define the unit of electric charge as the absolute value of the electron charge, the unit of angular momentum as $\hbar$, the unit of mass as the electron

mass and the unit of length as the Bohr radius. Finally, the unit of energy $E_h = 2hcR_\infty$, the Hartree, corresponds to $27.211\ 386\ 988(53) \simeq 27.2$ eV.

Ultimately, this model provides the fundamentals to discuss the importance to include–or not–the theory of relativity in our quantum description of the atom. Any object is said to be *relativistic* when its velocity approaches $c = 299\ 792\ 458$ m s^{-1}, the speed of light in vacuum. It is therefore useful to rewrite the velocity of Bohr's first orbit as

$$v_0 = \alpha c \tag{2.9}$$

where $\alpha = 7.297\ 352\ 5693(11) \times 10^{-3} \simeq 1/137$, as the speed of light is, in a.u., $c \simeq 137$, is called the dimensionless *fine structure constant*. The Bohr velocity of an hydrogenic system with nuclear charge Z is therefore simply given by $v = \alpha Z c$. The product αZ thus provides information about the relativistic character of the electron.

2.2 Schrödinger equation

Bohr's model for the atom was unsatisfactory for multiple reasons e.g., that it can not deal with systems with more than one electron, the arbitrary choice of circular orbits, the lack of any method to calculate transition rates and its inability to describe unbound systems [84]. These limitations engaged other scientists to propose their own quantum theory of the atom, Schrödinger leading the way. The source of his inspiration goes back to the roots of classical mechanics known since the integral calculus of Newton and Leibnitz and the equations of motion of Lagrange and Hamilton. Newton's second law of motion,

$$\boldsymbol{F} = m\boldsymbol{a} = \frac{\partial \boldsymbol{p}}{\partial t} = m\frac{\partial^2 \boldsymbol{x}}{\partial t^2}\ , \tag{2.10}$$

where $\boldsymbol{p} = m\boldsymbol{v}$ is the momentum of an object of mass m and velocity $\boldsymbol{v}$, is still an important starting point. Indeed, Schrödinger was strongly influenced by classical mechanics when he imagined his quantum wave theory. The duality wave–particle was postulated by de Broglie with the relations

$$E = \hbar w\ , \qquad \boldsymbol{p} = \hbar \boldsymbol{k}\ , \tag{2.11}$$

where E refers to the energy of the wave–particle, w is the angular frequency associated with the propagating wave, $\boldsymbol{k}$ is the propagation vector and $\hbar$ is the reduced Planck constant. These relations were well known from acoustics and optics, as they are intimately related to the classical wave equation

$$\boldsymbol{\nabla}^2 \Psi(\boldsymbol{r}, t) = \frac{1}{v^2}\frac{\partial^2 \Psi(\boldsymbol{r}, t)}{\partial t^2} \tag{2.12}$$

where $\psi(\boldsymbol{r},t)$ is a wave function of the spatial coordinates x,y,z and the time t and v is its velocity. The plane waves,

$$\psi(\boldsymbol{r},t) = A\exp[\mathrm{i}(\boldsymbol{k}\cdot\boldsymbol{r} - wt)] \ , \tag{2.13}$$

where A is a real number, are trivially solutions of Eq. (2.12) if $v^2 = w^2/\boldsymbol{k}^2$ since

$$\boldsymbol{\nabla}^2\psi(\boldsymbol{r},t) = -\boldsymbol{k}^2\psi(\boldsymbol{r},t) \ , \tag{2.14}$$

$$\frac{\partial^2\Psi}{\partial t^2} = -w^2\psi(\boldsymbol{r},t) \ . \tag{2.15}$$

The genius of de Broglie was to associate to any free particle of mass m and energy $E = \boldsymbol{p}^2/2m$ a wave character. Using relations (2.11) and inserting the standard expression of the energy, he found the following *dispersion relation*,

$$w = \frac{\hbar\boldsymbol{k}^2}{2m} \ . \tag{2.16}$$

In his original work, Schrödinger wrote: "*[...] the wave-phenomena must in this case be studied in detail. This can only be done using an "equation of wave propagation". Which one is this to be ? In the case of a single material point moving in an external field of force, the simplest way is to try to use the ordinary wave equation.*" [85]. He proposed a wave equation,

$$\mathrm{i}\hbar\frac{\partial\psi(\boldsymbol{r},t)}{\partial t} = \frac{-\hbar^2}{2m}\boldsymbol{\nabla}^2\psi(\boldsymbol{r},t) \ , \tag{2.17}$$

for which planes waves are solutions satisfying the relation Eq. (2.16). The identifications

$$E \leftrightarrow \mathrm{i}\hbar\frac{\partial}{\partial t} \qquad \boldsymbol{p} \leftrightarrow -\mathrm{i}\hbar\boldsymbol{\nabla} \tag{2.18}$$

were derived from building the wave equation. The strong postulate of quantum mechanics is to assume that these relations hold for non-plane wave solutions, e.g., when a potential is added

$$\mathrm{i}\hbar\frac{\partial\Psi(\boldsymbol{r},t)}{\partial t} = \left[\frac{-\hbar^2}{2m}\boldsymbol{\nabla}^2 + V(\boldsymbol{r},t)\right]\psi(\boldsymbol{r},t) \ . \tag{2.19}$$

If the potential is time-independent, one can solve the wave equation by separating the spatial and time coordinates. The wave function is therefore written as

$$\psi(\boldsymbol{r},t) = \phi(\boldsymbol{r})\exp[-\mathrm{i}Et/\hbar] \tag{2.20}$$

where $\phi(\boldsymbol{r})$ only depends on radial coordinates and $\exp[-\mathrm{i}Et/\hbar]$ completely defines the evolution of the system over time. $\phi(\boldsymbol{r})$ is solution of the stationary eigenvalue problem or time-independent Schrödinger equation

$$\mathcal{H}\phi(\boldsymbol{r}) = E\phi(\boldsymbol{r}) \ , \tag{2.21}$$

where $\mathcal{H} = \left[\frac{-\hbar^2}{2m}\boldsymbol{\nabla}^2 + V(\boldsymbol{r})\right]$ is the Hamiltonian of the system. Although Schrödinger designed his wave theory having in mind *real* waves that would physically vibrate, the adopted interpretation of the wave function is probabilistic. The quantity

$$\phi^*(\boldsymbol{r})\phi(\boldsymbol{r})d\boldsymbol{r} = |\phi(\boldsymbol{r})|^2 d\boldsymbol{r} \tag{2.22}$$

is associated to the probability of finding the massive particle, e.g., an electron, in the element of volume $d\boldsymbol{r}$. The normalization condition,

$$\int_{R^3} \phi^*(\boldsymbol{r})\phi(\boldsymbol{r})d\boldsymbol{r} = 1\ , \tag{2.23}$$

trivially corresponds to a probability of 1 to find the particle somewhere in space (R^3).

In the case of hydrogenic atoms, the single electron is well described by the stationary Schrödinger equation assuming a Coulomb potential $V = -Ze^2/4\pi\epsilon_0|\boldsymbol{r}|$. Schrödinger identified two types of solutions: with $E > 0$ or $E < 0$. The solutions of positive energy can take any value of E, i.e., there is a continuum of solutions, corresponding to unbound systems. The solutions of negative energy only exist for discrete, quantized values of the energy, corresponding to the energies provided by Balmer's formula and Bohr's model. Schrödinger himself was aware of the limitations of his model as he wrote: *"[...]the undelatory theory of mechanics has been developed without reference to two very important things, viz. (1) the relativity modifications of classical mechanics, (2) the action of a magnetic field on the atom"* [85]. The disagreement of his model with the experimentally measured fine structure of hydrogen and of its Zeeman components, leading to half-integer quantum numbers, *"must be intimately connected with Uhlenbeck-Goudsmit's theory of the spinning electron. But in what way the electron spin has to be taken into account in the present theory is yet unknown."* [85].

2.3 One-electron Dirac equation

2.3.1 The spinning electron

The Schrödinger equation is revolutionary in many aspects and is still one of the fundamental relation taught in all quantum mechanics classes. However, it fails to provide an understanding of the Stern-Gerlach experiment, which was designed to measure the electron's magnetic moment. Stern and Gerlach were studying the influence of external magnetic fields on electrons, when they observed that electrons were deflected in two different preferential directions [86]. This demonstrated the quantization of the magnetic moment of

the electron. To resolve the theory–experiment disagreement, the *spin* or *proper momentum* of the electrons was introduced.

The consequences of introducing the electron spin were studied by Pauli in his analysis of the spectrum of earth alkaline atoms. He wrote: *"For instance, the ground state of the alkaline earths in which the two valence electrons are equivalent corresponds to a singlet S-term*[1] *, while in those stationary states of the atom which belong to the triplet system the valence electrons are never bound equivalently, as the lowest triplet S-term*[1] *has a principal quantum number exceeding that of the ground state by unity."* [87], that already announces Pauli's famous *exclusion principle* proposed further in the same paper. In a subsequent paper [88], he established the mathematical tools to deal with the electron spin. More specifically, he promoted it as an independent variable with the components s_x, s_y and s_z. He further suggested the use of two-components wave functions or *spinors* to account for the two observed values of the magnetic momentum, $+\hbar/2$ and $-\hbar/2$.

Let us dive into more technical considerations, as the mathematical treatment of the spin is relevant both for the understanding of angular algebra in general, but also for the derivation of the Dirac equation. The spin, as any other angular momentum, satisfies the important commutation relations

$$[s_x, s_y] = \mathrm{i}\hbar s_z \quad \text{and} \quad [s_z, \boldsymbol{s}^2] = 0 \,, \tag{2.24}$$

and their cyclic permutations, where the commutator of two operators A and B is defined as $[A, B] = AB - BA$. These relations are easily derived for the orbital angular momentum $\boldsymbol{L} = \boldsymbol{r} \times \boldsymbol{p}$ by computing the commutator explicitly.[2] The spin eigenfunctions, χ_{s,m_s}, simultaneously satisfy the eigenvalue equations

$$\boldsymbol{s}^2 \chi_{s,m_s} = s(s+1)\hbar^2 \chi_{s,m_s} \tag{2.25}$$

and

$$s_z \chi_{s,m_s} = m_s \hbar \chi_{s,m_s} \,, \tag{2.26}$$

where m_s is the spin projection alongside the z-axis. For an electron, $m_s = \pm 1/2$ and $s = 1/2$. Since there are only two possible eigenfunctions, we can denote them $\chi_{1/2,+1/2}$

[1] The singlet and triplet states refer to systems of two electrons with anti-parallel and parallel spins, respectively.

[2] Starting with the classical orbital angular momentum $\boldsymbol{L} = \boldsymbol{r} \times \boldsymbol{p}$ and inserting the replacement $\boldsymbol{p} \to -\mathrm{i}\hbar\boldsymbol{\nabla}$, we find the three components of $\boldsymbol{L}$ to be $L_x = -\mathrm{i}\hbar\left(y\frac{\partial}{\partial z} - z\frac{\partial}{\partial y}\right)$, $L_y = -\mathrm{i}\hbar\left(z\frac{\partial}{\partial x} - x\frac{\partial}{\partial z}\right)$ and $L_z = -\mathrm{i}\hbar\left(x\frac{\partial}{\partial y} - y\frac{\partial}{\partial x}\right)$. From there one finds that $[L_x, L_y] = L_x L_y - L_y L_x = \hbar^2\left((y\frac{\partial}{\partial z} - z\frac{\partial}{\partial y})(z\frac{\partial}{\partial x} - x\frac{\partial}{\partial z})\right) - \hbar^2\left((z\frac{\partial}{\partial x} - x\frac{\partial}{\partial z})(y\frac{\partial}{\partial z} - z\frac{\partial}{\partial y})\right)$, and by remembering that e.g., $y\frac{\partial}{\partial z}z\frac{\partial}{\partial x} = y\frac{\partial}{\partial x} + yz\frac{\partial^2}{\partial z \partial x}$, the previous expression reduces to $\hbar^2\left(y\frac{\partial}{\partial x} - x\frac{\partial}{\partial y}\right) = i\hbar L_z$, since all double derivatives cancel out.

and $\chi_{1/2,-1/2}$. One can readily find the matrix representation of $\boldsymbol{s}^2$ and s_z to be

$$\boldsymbol{s}^2 = \frac{3}{4}\hbar^2 \begin{pmatrix} 1 & 0 \\ 0 & 1 \end{pmatrix} \tag{2.27}$$

$$s_z = \frac{\hbar}{2} \begin{pmatrix} 1 & 0 \\ 0 & -1 \end{pmatrix} . \tag{2.28}$$

The details of the derivation of the s_x and s_y matrices can be found elsewhere [84]. However the final result important to highlight here is the matrix definition of the spin vector as

$$\boldsymbol{s} = \frac{\hbar}{2}\boldsymbol{\sigma} \tag{2.29}$$

where

$$\sigma_x = \begin{pmatrix} 0 & 1 \\ 1 & 0 \end{pmatrix} \qquad \sigma_y = \begin{pmatrix} 0 & -\mathrm{i} \\ \mathrm{i} & 0 \end{pmatrix} \qquad \sigma_x = \begin{pmatrix} 1 & 0 \\ 0 & -1 \end{pmatrix} \tag{2.30}$$

are the well-know Pauli matrices. The latter have important properties that will be useful in the following, which are

$$\sigma_x^2 = \sigma_y^2 = \sigma_z^2 = I_{2\times 2} \ , \quad \{\sigma_x, \sigma_y\} \equiv \sigma_x\sigma_y + \sigma_y\sigma_x = O_{2\times 2} \ , \quad [\sigma_x, \sigma_y] = \mathrm{i}\sigma_z \tag{2.31}$$

and their cyclic permutations, where the anticommutator of two operators A and B is defined as $\{A, B\} = AB + BA$ and $I_{2\times 2}$ and $O_{2\times 2}$ are the 2×2 identity and zero matrices, respectively. If an electron is neither in one of the eigenstates $\chi_{1/2,+1/2}$ or $\chi_{1/2,-1/2}$, its spin is described by using the two-component spinor

$$\chi = \begin{pmatrix} \chi_+ \\ \chi_- \end{pmatrix} \qquad \text{or} \qquad \chi = \chi_+ \left(\chi_{1/2,+1/2}\right) + \chi_- \left(\chi_{1/2,-1/2}\right) , \tag{2.32}$$

where χ_+ and χ_- are the spin components along $\chi_{1/2,+1/2}$ and $\chi_{1/2,-1/2}$, respectively. However, the artificial introduction of these spinors in the non-relativistic theory of Schrödinger by considering relativistic and magnetic corrections to his wave equation was unexplained. Pauli himself was conscious that the spin of the electron and the spinor wave function, i.e., two-components wave function, should emerge naturally from the wave equation as he wrote: *"the theory that is formulated here is to be regarded as only provisional, since one must demand of an ultimate theory that it be formulated in a relativistically-invariant way."* [88].

2.3.2 Relativity

The theory of relativity was first introduced by Einstein. The experimental fact that the speed of light was the same in all reference frames was in obvious violation of the theorem

of addition of velocities. The change of frame of reference that would preserve both the laws of physics and the speed of light's invariance are described by Lorentz's transformations in the framework of special relativity. From this theory it follows that objects moving with a velocity close to the speed of light were subject to time dilatation and distance contraction. Within that theory, time and space form a four-dimensional spacetime, called the Minkowski space, that suppresses the special character of the time dimension relatively to the three spatial dimensions. Time dilatation and distance contraction are then explained by rotations in the four-dimensional spacetime, allowing time and space to mix with each other.

The derivation of the Dirac equation, however, requires the knowledge of useful concepts of general relativity. The theory of general relativity imagined by Einstein overruled the "classical" Newton laws of motion, showing disagreement mostly in the high-energy domain. It was only a matter of time for quantum mechanics–the mechanics of the infinitely small–and relativity–the mechanics of high energies–to be unified.

In the relativity theory, four-components vectors, $x^\mu = \{x^0, x^1, x^2, x^3\}$, are defined in their *contravariant* form or, $x_\mu = \{x_0, x_1, x_2, x_3\}$, in their *covariant* form. The transformation from the covariant form to the contravariant form is performed by using the metric tensor

$$g_{\mu\nu} = \begin{pmatrix} 1 & 0 & 0 & 0 \\ 0 & -1 & 0 & 0 \\ 0 & 0 & -1 & 0 \\ 0 & 0 & 0 & -1 \end{pmatrix} , \tag{2.33}$$

which is identical in its covariant and contravariant forms, $g_{\mu\nu} = g^{\mu\nu}$. The transformation from one form to the other is made explicit by the lowering or highering of indices

$$x^\mu = g^{\mu\nu} x_\nu , \qquad x_\mu = g_{\mu\nu} x^\nu . \tag{2.34}$$

As an example the four-component spacetime coordinate vector is $x^\mu \equiv (ct, x, y, z)$ in its contravariant form and $x_\mu \equiv (ct, -x, -y, -z)$ in its covariant form. Similarly we define the usual four-momentum vector

$$p^\mu = \{p^0, p^1, p^2, p^3\} = \{E/c, p^x, p^y, p^z\} \tag{2.35}$$

and the four-potential vector of the electromagnetic field

$$a^\mu = \{A^0, A^1, A^1, A^1\} = \{\Phi, cA^x, cA^y, cA^z\} . \tag{2.36}$$

The components of the four-momentum vector can be written using the Lorentz factor $\gamma(v) = 1/\sqrt{1 - v^2/c^2}$ where $v = |\boldsymbol{v}|$ as

$$p^0 = E/c = mc\gamma(v) , \qquad \boldsymbol{p} = m\boldsymbol{v}\gamma(v) . \tag{2.37}$$

Expanding the above expressions in series of (v/c), we easily derive

$$E = mc^2 + \frac{mv^2}{2} + \frac{3mv^4}{8c^2} + \dots \ , \qquad \boldsymbol{p} = m\boldsymbol{v}\left(1 + \frac{v^2}{2c^2} + \dots\right) \ , \tag{2.38}$$

which reduce to first order to their classical expression $E - mc^2 = mv^2/2$ and $\boldsymbol{p} = m\boldsymbol{v}$, respectively [27, p.11]. The inner product associated to four-components vectors is defined as

$$x \cdot x = x^\mu x_\mu = x^0 x_0 + x^1 x_1 + x^2 x_2 + x^3 x_3 = x_0^2 - \boldsymbol{x}^2 \tag{2.39}$$

using Einstein's notation $x^\mu x_\mu = \sum_{\mu=0}^{3} x^\mu x_\mu$.

A first wave equation was proposed by Klein [89] and Gordon [90] who considered the relativistic relation

$$p^\mu p_\mu = E^2/c^2 - \boldsymbol{p}^2 = m_0^2 c^2 \ , \tag{2.40}$$

where m_0 is the rest mass of the considered particle, and made the replacement inspired by Schrödinger (see Eq. 2.18))

$$p^\mu \to \mathrm{i}\hbar \frac{\partial}{\partial x_\mu} \ .^{[1]} \tag{2.41}$$

They obtain the *Klein-Gordon equation* for a free particle described by a wave function $\psi(x) \equiv \psi(\boldsymbol{r}, t)$,

$$p^\mu p_\mu \psi(x) = m_0^2 c^2 \psi(x) \tag{2.42}$$

or

$$\left(\frac{\partial^2}{c^2 \partial t^2} - \boldsymbol{\nabla}^2 + \frac{m_0^2 c^2}{\hbar^2}\right)\psi(x) = 0 \ . \tag{2.43}$$

The success of this equation was limited. Even though it is Lorentz-invariant, the second derivative with respect to time forbids the usual probabilistic interpretation of the wave function. Moreover, it means that the wave function not only depends on the wave function itself but also on its first derivative. The Klein-Gordon equation, however, is well suited for the description of the motion of spin-0 particle such as pions and kaons that were unknown at the time. It was therefore logical to search for an alternative.

Since it became obvious that the wave equation had to be linear with respect to the first derivative of time, Dirac suggested that it should also be linear with respect to the first derivative of space so that the symmetry between time and space required by relativity is recovered. He then postulated that the form of the wave equation had to be

$$(p_0 + \alpha_1 p_1 + \alpha_2 p_2 + \alpha_3 p_3 + \beta)\psi(x) = 0 \ , \tag{2.44}$$

[1] Note the importance of the contravariant and covariant indices, which provide the correct negative sign when the four components are written explicitly (see Eq. (1.11) in Ref. [91])

where the operators $\alpha_1, \alpha_2, \alpha_3$ and β are independent of $\boldsymbol{r}$ and $\boldsymbol{p}$. Following Dirac chain's of thoughts [92], Eq. (2.44) leads us to

$$\begin{aligned} 0 &= (-p_0 + \alpha_1 p_1 + \alpha_2 p_2 + \alpha_3 p_3 + \beta)(p_0 + \alpha_1 p_1 + \alpha_2 p_2 + \alpha_3 p_3 + \beta)\psi(x) \\ &= \left[-p_0^2 + \sum \alpha_1^2 p_1^2 + \sum(\alpha_1\alpha_2 + \alpha_2\alpha_1)p_1 p_2 + \beta^2 + \sum(\alpha_1\beta + \beta\alpha_1)p_1\right]\psi(x) \end{aligned} \tag{2.45}$$

where $\sum$ represents the cyclic permutations of the indices 1,2,3. Dirac's idea was that Eq. (2.45) should be equal to the Klein-Gordon equation (2.43). This is only possible if (putting $\beta = \alpha_4 mc$)

$$\alpha_\mu^2 = 1 \quad \text{and} \quad \alpha_\mu\alpha_\nu + \alpha_\nu\alpha_\mu = 0 \ (\mu \neq \nu) \ , \qquad \mu, \nu = 1, 2, 3, 4 \ , \tag{2.46}$$

which are quite similar to the relations (2.31) satisfied by Pauli's matrices. However, in order to find 4 matrices that satisfy the conditions (2.46), one must extend the dimensions of Pauli's matrices from 2 to 4. The Dirac matrices then take the form

$$\alpha_i = \begin{pmatrix} O_{2\times2} & \sigma_i \\ \sigma_i & O_{2\times2} \end{pmatrix} \ i = 1, 2, 3 \qquad , \qquad \alpha_4 = \begin{pmatrix} I_{2\times2} & O_{2\times2} \\ O_{2\times2} & -I_{2\times2} \end{pmatrix} \ . \tag{2.47}$$

The one-electron Dirac equation then becomes

$$(p_0 + \boldsymbol{\alpha} \cdot \boldsymbol{p} + \alpha_4 mc)\,\psi(x) = 0 \ . \tag{2.48}$$

Interestingly, this first version of Dirac's equation is not explicitly Lorentz-invariant. However, Dirac demonstrated that the above equation could be re-written in a form which is more convenient to prove the Lorentz's invariance required by relativity [92]. Grant [27, p.121] provides the explicit proof of its invariance starting from

$$(\gamma^\mu p_\mu - mc)\,\psi(x) = 0 \tag{2.49}$$

where γ^μ are 4×4 matrices that can be built by applying canonical transformations to the Dirac matrices.

In the presence of an external electromagnetic field represented by its four-vector a^μ, Dirac equation becomes

$$\left[p_0 - \frac{e}{c}\Phi_0 + \boldsymbol{\alpha} \cdot (\boldsymbol{p} + e\boldsymbol{A}) + \alpha_4 mc\right]\psi(x) = 0 \ . \tag{2.50}$$

In the case of an time-independent electromagnetic field, the time dependence of the wave function is carried by a time dependent phase factor, similarly as in the non-relativistic theory of Schrödinger (see Eq. (2.20)). One can therefore build the time-independent one-electron Dirac equation by looking for the Hamiltonian $\mathcal{H}_\mathrm{D}$ such that

$$(\mathcal{H}_\mathrm{D} - E)\phi(\boldsymbol{r}) = 0 \tag{2.51}$$

where $\phi(\boldsymbol{r}) = \psi(x)\exp\left[\mathrm{i}Et/\hbar\right]$ only depends on spatial coordinates.

2.3.3 Relativistic orbitals and quantum numbers

The one-electron Dirac equation is crucial to provide the tools to understand and derive the equations of the N_e–electron atomic systems that are studied in this thesis. The case of the hydrogenic atoms ($N_e = 1$), in which there is no external electromagnetic field and the potential reduces to the Coulomb potential between the nucleus and the electron, is the cornerstone on which more complex systems are built. We therefore follow the book of Grant [27] up to the radial Dirac equation, giving along the way the important definition of the relativistic orbitals and their associated quantum numbers.

The Dirac Hamiltonian for an electron in a central potential is simply (with $r = |\boldsymbol{r}|$)

$$\mathcal{H}_{\rm D} = c\boldsymbol{\alpha}\cdot\boldsymbol{p} + \beta' mc^2 + V(r) \tag{2.52}$$

where, $\beta' \equiv \alpha_4$ to follow Grant's notations. In order to find the appropriate set of quantum numbers and the suitable structure of the four-component spinors $\phi_{n\kappa m}(\boldsymbol{r})$ (the meaning of the quantum numbers $n\kappa m$ or equivalently $nljm$ will naturally appear later), we should identify the operators that commute with $\mathcal{H}_{\rm D}$. Together they form what is called a *Complete Set of Commuting Observables*[2] (CSCO). It is well-known from basic quantum mechanics that two operators that commute have the same set of eigenfunctions [83].[3] The Dirac Hamiltonian commutes with the total angular momentum $\boldsymbol{J} = \boldsymbol{L} + \boldsymbol{S}$, including its projection on the z-axis, J_z. However, it does not commute with $\boldsymbol{L}$ nor $\boldsymbol{S}$, even though $[\mathcal{H}_{\rm D}, \boldsymbol{L}] = -[\mathcal{H}_{\rm D}, \boldsymbol{S}]$, so that $[\mathcal{H}_{\rm D}, \boldsymbol{J}]$ is indeed equal to 0. Furthermore, since $[J_i, J_j] \neq 0$ ($i \neq j$), two different components of $\boldsymbol{J}$ can not be part simultaneously of our CSCO. The latter commutation relations were already discussed for the spin operator in Eq. (2.24) and translate for the total angular momentum $\boldsymbol{J}$ as

$$[\boldsymbol{J}, \boldsymbol{J}] = i\hbar\boldsymbol{J} \quad \text{and} \quad [J_z, \boldsymbol{J}^2] = 0\,. \tag{2.53}$$

It follows naturally that $[\mathcal{H}_{\rm D}, \boldsymbol{J}^2] = 0$.[4]

The parity-operator P, acting on a function $f(\boldsymbol{r})$ such that $Pf(\boldsymbol{r}) = f(-\boldsymbol{r})$, does not commute with $\mathcal{H}_{\rm D}$. The alternative form for the parity-operator $\mathcal{P} = \beta P$ does, however,

[2] The appellation "observable" designates any operator for which its expectation value is a measurable quantity.

[3] Let us consider two commuting operators A and B such that $[A, B] = 0$. Assuming that we know the non-degenerate complete set of eigenfunctions ψ_n of the operator A such that $A\psi_n = a_n\psi_n$, we have $BA\psi_n = Ba_n\psi_n = a_nB\psi_n$ and $BA\psi_A = AB\psi_n$ using $[A, B] = 0$. Therefore we obtain the important result that $AB\psi_n = a_nB\psi_n$, which means that $B\psi_n$ is also eigenfuntion of A with the eigenvalue a_n. Since the set of eigenfunctions is non-degenerate, it means that $B\psi_n$ has to differ from ψ_n by a multiplicative constant, namely, b_n: $B\psi_n = b_n\psi_n$. It follows that ψ_n is simultaneously eigenfunction of A and B with the eigenvalue a_n and b_n, respectively.

[4] Using the mathematical relation $[A, BC] = [A, B]C + B[A, C]$, we find that $[\mathcal{H}_{\rm D}, \boldsymbol{J}^2] = [\mathcal{H}_{\rm D}, \boldsymbol{J}\cdot\boldsymbol{J}] = [\mathcal{H}_{\rm D}, \boldsymbol{J}]\boldsymbol{J} + \boldsymbol{J}[\mathcal{H}_{\rm D}, \boldsymbol{J}] = 0$ since $[\mathcal{H}_{\rm D}, \boldsymbol{J}] = 0$.

commutes with $\mathcal{H}_{\rm D}$. The CSCO is therefore composed of $\{\mathcal{H}_{\rm D}, \boldsymbol{J}^2, J_z, \mathcal{P}\}$ and $\phi_{n\kappa m}(\boldsymbol{r})$ is simultaneous eigenfunction of these four operators and can be therefore associated to a definite energy, a total angular momentum and its projection, and a parity.

The form of the one-electron wave function or *relativistic orbitals* $\phi_{n\kappa m}(\boldsymbol{r})$ highly depends on the four-component nature of the Dirac equation. Due to the structure of the $\boldsymbol{\alpha}$ and β matrices (see Eq. (2.47)), the generic form of the four-component spinor is

$$\phi_{n\kappa m}(\boldsymbol{r}) = \frac{1}{r}\begin{pmatrix} P_{n\kappa}(r)\Omega_{\kappa m}(\theta,\varphi) \\ \mathrm{i}Q_{n\kappa}(r)\Omega_{-\kappa m}(\theta,\varphi) \end{pmatrix} \tag{2.54}$$

where the radial and angular parts are separated and (r, θ, φ) are the usual spherical coordinates. $P_{n\kappa}(r)$ and $Q_{n\kappa}(r)$ are the large and small components,[5] respectively, and $\Omega_{\kappa m}(\theta,\varphi)$ are spin-angular two-spinors. The latter are eigenfunctions of $\tilde{\boldsymbol{j}}^2, \tilde{j}_z, \tilde{\boldsymbol{l}}^2$ and $\tilde{\boldsymbol{s}}^2$, where the tilde is introduced to emphasize that these operators act on two-dimensional spinors instead of four-component spinors. They verify the eigenvalue equations, in a.u.,

$$\tilde{\boldsymbol{j}}^2\Omega_{\kappa m}(\theta,\varphi) = j(j+1)\Omega_{\kappa m}(\theta,\varphi) \tag{2.55}$$
$$\tilde{j}_z\Omega_{\kappa m}(\theta,\varphi) = m\Omega_{\kappa m}(\theta,\varphi) \tag{2.56}$$
$$\tilde{\boldsymbol{l}}^2\Omega_{\kappa m}(\theta,\varphi) = l(l+1)\Omega_{\kappa m}(\theta,\varphi) \tag{2.57}$$
$$\tilde{\boldsymbol{s}}^2\Omega_{\kappa m}(\theta,\varphi) = \frac{3}{4}\Omega_{\kappa m}(\theta,\varphi)\ , \tag{2.58}$$

where j is a positive half-integer, $m = -j, -j+1, \cdots, j-1, j$, and $l = j \pm 1/2$. Their most efficient classification requires the definition of the operator $\tilde{K}$ as

$$\tilde{K} = -\left[1 + \tilde{\boldsymbol{j}}^2 - \tilde{\boldsymbol{l}}^2 - \tilde{\boldsymbol{s}}^2\right] = -(1 + \boldsymbol{\sigma}\cdot\tilde{\boldsymbol{l}})\ , \tag{2.59}$$

that immediately follows the definition of the total angular momentum $\tilde{\boldsymbol{j}} = \tilde{\boldsymbol{l}} + \tilde{\boldsymbol{s}}$. The two-spinors are also eigenfunctions of $\tilde{K}$

$$\tilde{K}\Omega_{\kappa m}(\theta,\varphi) = \kappa\Omega_{\kappa m}(\theta,\varphi)\ , \tag{2.60}$$

where κ is the relativistic angular quantum number[6] that takes the values

$$\kappa = \pm(j+1/2) \quad \text{when} \quad l = j \pm 1/2\ . \tag{2.61}$$

[5] In Ref. [93], Grant comments that the labels 'large' and 'small' are defined in the case of states of positive energy. It is not hard to imagine that the situation is 'reverse' for negative energy states, i.e., $P_{n\kappa}(r)$ and $Q_{n\kappa}(r)$ would be 'small' and 'large', respectively.

[6] Note that for each non-relativistic orbital characterized by its angular quantum number $l \neq 0$, two relativistic orbitals exist with total angular momentum $j = l \pm 1/2$. Following the non-relativistic notation $s(l=0), p(l=1), d(l=2), f(l=3), \ldots$, the relativistic orbitals are identified by the couple of quantum number l_j instead of κ as $s_{1/2}(\kappa=-1), p_{1/2}(\kappa=1), p_{3/2}(\kappa=-2), d_{3/2}(\kappa=2), d_{5/2}(\kappa=-3), \ldots$.

The two-spinors are eigenfunctions of both the spin and the orbital angular momentum. They can therefore be expanded over direct products of the spin and orbital angular momentum eigenfunctions. We already saw in Sec. 2.3.1 that the spin eigenfunctions are $\chi_{1/2,1/2}$ and $\chi_{1/2,-1/2}$, which, in their matrix representations, are

$$\chi_{1/2,1/2} = \begin{pmatrix} 1 \\ 0 \end{pmatrix} \quad \text{and} \quad \chi_{1/2,-1/2} = \begin{pmatrix} 0 \\ 1 \end{pmatrix} . \tag{2.62}$$

The eigenfunctions of the orbital angular momentum are the well-known spherical harmonics $Y_l^{m_l}(\theta,\phi)$, $m_l = -l, -l+1, \cdots, l-1, l$ associated to the eigenvalues $l(l+1)$ and m_l for the square of the orbital angular momentum operator and its projection on the z-axis. The two-spinors are then constructed using the general formula

$$\Omega_{\kappa m}(\theta,\varphi) = \sum_{m_s=-1/2,1/2} (l, m-m_s, 1/2, m_s | l, 1/2, j, m) Y_l^{m-m_s}(\theta,\varphi) \chi_{1/2,m_s} , \tag{2.63}$$

where $(l, m-m_s, 1/2, m_s | l, 1/2, j, m)$ are Clebsch-Gordan coefficients [82] (see also Sec. 3.4.4) and $l = j \pm 1/2$ depending on the sign of κ (see Eq (2.61)). Their expression is finally given by

$$\Omega_{+|\kappa|m}(\theta,\varphi) = \begin{pmatrix} -\left(\frac{j+1-m}{2j+2}\right)^{1/2} Y_{j+1/2}^{m-1/2}(\theta,\varphi) \\ \left(\frac{j+1+m}{2j+2}\right)^{1/2} Y_{j+1/2}^{m+1/2}(\theta,\varphi) \end{pmatrix} \tag{2.64}$$

$$\Omega_{-|\kappa|m}(\theta,\varphi) = \begin{pmatrix} \left(\frac{j+m}{2j}\right)^{1/2} Y_{j-1/2}^{m-1/2}(\theta,\varphi) \\ \left(\frac{j-m}{2j}\right)^{1/2} Y_{j-1/2}^{m+1/2}(\theta,\varphi) \end{pmatrix} . \tag{2.65}$$

These two-spinors, just as the spherical harmonics, form an orthonormal basis, such that the scalar product between two different two-spinors is simply given by

$$(\Omega_{\kappa m}(\theta,\varphi) | \Omega_{\kappa' m'}(\theta,\varphi)) = \delta_{\kappa\kappa'}\delta_{mm'} , \tag{2.66}$$

which corresponds to an angular integration over the unit sphere:

$$(\Omega_{\kappa m}(\theta,\varphi) | \Omega_{\kappa' m'}(\theta,\varphi)) \equiv \int_0^\pi \sin\theta d\theta \int_0^{2\pi} \Omega_{\kappa m}^\dagger(\theta,\varphi) \Omega_{\kappa' m'}(\theta,\varphi) d\phi . \tag{2.67}$$

Thanks to this relation, one can associate to the *probability density*

$$\rho_{n\kappa m}(\boldsymbol{r}) = |\phi_{n\kappa m}(\boldsymbol{r})|^2 \tag{2.68}$$

a radial density

$$D_{n\kappa}(r) = |P_{n\kappa}(r)|^2 + |Q_{n\kappa}(r)|^2 . \tag{2.69}$$

The quantity $D_{n\kappa}(r)dr$ is therefore the probability to find the electron in the radial interval $[r, r+dr]$ away from the nucleus, regardless of the direction.

2.3.4 Radial equation

In the previous sections, we defined (almost) everything that is needed to derive the radial one-electron Dirac equation. Remaining is the treatment of the $\boldsymbol{\alpha} \cdot \boldsymbol{p}$ operator. An important relation is given in [27, §3.2.3],

$$\boldsymbol{\sigma} \cdot \boldsymbol{p} = -\mathrm{i}\sigma_r \left(\partial_r + \frac{K+1}{r} \right) , \tag{2.70}$$

where the operator σ_r (anti-)commutes with $\tilde{\boldsymbol{j}}(P)$ and acts on the 2-spinors as

$$\sigma_r \Omega_{\kappa m}(\theta, \varphi) = -\Omega_{-\kappa m}(\theta, \varphi) , \tag{2.71}$$

which connects basis functions of opposite sign of κ. The derivation of the radial Dirac equations is then straightforward,

$$\begin{aligned}
0 &= (\mathcal{H}_\mathrm{D} - E_{n\kappa})\phi_{n\kappa m}(\boldsymbol{r}) \\
&= (c\boldsymbol{\alpha} \cdot \boldsymbol{p} + \beta' mc^2 + V(r) - E_{n\kappa}) \frac{1}{r} \begin{pmatrix} P_{n\kappa}(r)\Omega_{\kappa m}(\theta,\varphi) \\ \mathrm{i}Q_{n\kappa}(r)\Omega_{-\kappa m}(\theta,\varphi) \end{pmatrix} \\
&= \begin{pmatrix} mc^2 + V(r) - E_{n\kappa} & -\mathrm{i}c\sigma_r \left(\partial_r + \frac{K+1}{r}\right) \\ -\mathrm{i}c\sigma_r \left(\partial_r + \frac{K+1}{r}\right) & -mc^2 + V(r) - E_{n\kappa} \end{pmatrix} \frac{1}{r} \begin{pmatrix} P_{n\kappa}(r)\Omega_{\kappa m}(\theta,\varphi) \\ \mathrm{i}Q_{n\kappa}(r)\Omega_{-\kappa m}(\theta,\varphi) \end{pmatrix} \\
&= \frac{1}{r} \begin{pmatrix} \left\{ (mc^2 + V(r) - E_{n\kappa})P_{n\kappa}(r) + c\left(-\frac{dQ_{n\kappa}(r)}{dr} + \frac{\kappa}{r}Q_{n\kappa}(r) \right) \right\} \Omega_{\kappa m}(\theta,\varphi) \\ \left\{ c\left(\frac{dP_{n\kappa}(r)}{dr} + \frac{\kappa}{r}P_{n\kappa}(r) \right) + (-mc^2 + V(r) - E_{n\kappa})Q_{n\kappa}(r) \right\} \Omega_{-\kappa m}(\theta,\varphi) \end{pmatrix} ,
\end{aligned} \tag{2.72}$$

leading to the coupled system of radial equations

$$\begin{aligned}
(mc^2 + V(r) - E_{n\kappa})P_{n\kappa}(r) + c\left(-\frac{dQ_{n\kappa}(r)}{dr} + \frac{\kappa}{r}Q_{n\kappa}(r) \right) &= 0 \\
c\left(\frac{dP_{n\kappa}(r)}{dr} + \frac{\kappa}{r}P_{n\kappa}(r) \right) + (-mc^2 + V(r) - E_{n\kappa})Q_{n\kappa}(r) &= 0 .
\end{aligned} \tag{2.73}$$

2.3.5 Discussion

Relativistic wave equations, opposed to non-relativistic Schrödinger-like equations, have interesting properties that follow directly from a relativistic treatment. Considering Eq. (2.40), the energy of the relativistic particle is

$$E_{n\kappa} = \pm c\sqrt{\boldsymbol{p}^2 + m^2c^2} , \tag{2.74}$$

which admits positive and negative solutions. Greiner [91, § 2.1] provides an interesting alternative derivation of this result starting from $\mathcal{H}_{\rm D}$ for a free particle ($V(r) = 0$). Keeping the operator $\boldsymbol{\sigma} \cdot \boldsymbol{p}$ in its vectorial form, the coupled system of equations admits non-zero solutions for $\phi_{n\kappa m}(\boldsymbol{r})$ only if

$$\begin{vmatrix} E_{n\kappa} - mc^2 & -c\boldsymbol{\sigma} \cdot \boldsymbol{p} \\ -c\boldsymbol{\sigma} \cdot \boldsymbol{p} & E_{n\kappa} + mc^2 \end{vmatrix} = 0 \, . \tag{2.75}$$

This determinant is exactly zero only if Eq. (2.74) is verified. The existence of negative solutions was revolutionary when Dirac established his equation. Their interpretation is discussed further in this section.

First, it is worth discussing the hydrogenic case, for which the potential is the pure Coulomb potential, $V(r) = -Z/r$, assuming a point-like nucleus. Seeking squared-integrable, bound solutions, i.e., that the radial density $D_{n\kappa}(r)$ (2.69) must be finite on $0 \leq r \leq \infty$, we should investigate the behaviour of the wave functions for the two limits $r \to 0$ and $r \to \infty$. Inserting $V(r)$ in Eq. (2.73) and assuming first $r \to \infty$, the system of equations resumes to, in matrix notations,

$$\begin{pmatrix} mc^2 - E_{n\kappa} & -c\frac{d}{dr} \\ c\frac{d}{dr} & -mc^2 - E_{n\kappa} \end{pmatrix} \begin{pmatrix} P_{n\kappa}(r) \\ Q_{n\kappa}(r) \end{pmatrix} \to 0 \tag{2.76}$$

Extracting Q_{E_κ} from the second equation and inserting it into the first one, we find

$$\frac{d^2 P_{n\kappa}(r)}{dr^2} + (E_{n\kappa}^2/c^2 - m^2c^2) P_{n\kappa}(r) = 0 \, . \tag{2.77}$$

It is easy to see that the above equation accept solutions of the type $\exp[\pm\lambda r]$, where $\lambda^2 = (m^2c^2 - E_{n\kappa}^2/c^2)$. Similar reasoning is applied to $Q_{n\kappa}(r)$ and the same result can be found. We identify two energy regimes with strongly different implications. Either $-mc^2 \leq E_{n\kappa} \leq mc^2$ or $mc^2 < |E_{n\kappa}| < \infty$.

In the first scenario, λ is real and the solutions of $P_{n\kappa}(r)$ and $Q_{n\kappa}(r)$ behave like $\exp[\pm|\lambda|r]$. The positive solutions obviously diverge. This is obvious when we consider the integration of the radial density over (R, ∞)

$$\int_R^\infty D_{n\kappa}(r) dr \, , \tag{2.78}$$

where $D_{n\kappa}(r)$ is given by Eq. (2.69). Oppositely, the negative solutions imply that $P_{n\kappa}(r)$, $Q_{n\kappa}(r) \to 0$ for $r \to \infty$ and the expression (2.78) remains finite. They correspond to *bound states*.

In the second scenario, $mc^2 < |E_{n\kappa}| < \infty$, λ is pure imaginary. Taking $\lambda = -i\tilde{\lambda}$ when $E_{n\kappa} > 0$, we have $\tilde{\lambda}^2 = E^2/c^2 - m^2c^2$. $P_{n\kappa}(r)$ and $Q_{n\kappa}(r)$ then behave like

$\exp[\pm \mathrm{i}|\tilde{\lambda}|r]$, corresponding to progressive or standing waves. In any case, the integration of the radial density (2.78) diverges.

We can now look at the case $r \to 0$, for which the $P_{n\kappa}(r)$ and $Q_{n\kappa}(r)$ are developed in power series of r as $r^{\pm\gamma}\{1 + O(r)\}$ with $\gamma^2 = \kappa^2 - \alpha^2 Z^2$ where $\alpha^2 = 1/c^2$ is the fine-structure constant introduced in Sec. 2.1. The solutions must be bounded close to the origin, more precisely,

$$\int_0^{R'} D_{n\kappa}(r) dr \tag{2.79}$$

must remain between 0 and say M_1, some real finite number. This condition implies that $\pm 2\gamma > -1$, since $D_{n\kappa}(r)$ is $\propto r^{\pm 2\gamma}$ for $r \to 0$. Considering the most limiting case where $|\kappa| = 1$ or $j = 1/2$, the atomic number Z is limited by $Z < c\sqrt{3}/2 \approx 118.6$ so that Eq. (2.79) remains finite. This limit is further extended to $Z = 137$ when considering the finite expectation value of the Coulomb potential. This result is crucial, it means that there are no bound solutions for hydrogenic atoms with $Z > 137$. However, going beyond the point-like nucleus assumption and hence replacing the Coulomb potential $-Z/r$ by some potential $V_{nuc}(r)$ extends further the range of solutions to $Z > 137$. These conditions on the wave functions are derived from the squared-integrability requirement of bound solutions, as summarized by Grant in his *Proposition 1* and *Proposition 2* [93] and later demonstrated in the same paper.

Details of the calculations of the bound and continuum states are given by Grant [27, §3.3.2]. We hereby only introduce a few quantities relevant in the following. When seeking for bound state solutions, the definitions of N, n and n_r, which are the *apparent principal quantum number*, the *principal quantum number* and the *inner quantum number*, respectively, naturally appear. The latter is associated with the number of nodes of the large radial component while

$$N = \left[n^2 - 2n_r(|\kappa| - \gamma)\right]^{1/2} \tag{2.80}$$

and

$$n = n_r + |\kappa| \,. \tag{2.81}$$

The corresponding bound relativistic energy can be computed algebraically and is given by [91]

$$E_{n\kappa} = mc^2 \left\{ \left[1 + \frac{Z^2\alpha^2}{[n - |\kappa| + \sqrt{(|\kappa|^2 - Z^2\alpha^2)}]^2} \right]^{-1/2} \right\} . \tag{2.82}$$

The latter not only depends on the principal quantum number n as in the non-relativistic theory but also on the relativistic quantum number κ. This resolved the theory–experiment discrepancy due to the experimentally measured fine structure spectrum, which removes the

n-degeneracy obtained in non-relativistic theory. Nevertheless, the Dirac model leaves degenerate states with same n and $|\kappa|$, or equivalently, n and j, e.g., $2s_{1/2}$ and $2p_{1/2}$. Years after the establishment of Dirac theory, Lamb and Retherford proposed an experiment that put forward a small frequency shift between the $2s_{1/2}$ and $2p_{1/2}$ states of hydrogen of about a 1000 MHz, removing the degeneracy obtained with the Dirac equation in spite of a fully relativistic model of the electron [94]. This frequency shift, nowadays well-know as the *Lamb shift*, is the starting point of a chain of thoughts that would end with the *quantum electrodynamics* (QED) theory. 'Radiative corrections' are added to Dirac theory to account for the interaction of the electron with the quantized electromagnetic field. The theoretical developments are beyond the scope of this thesis, but an original interpretation presented by Welton [95] is as follows (see also Bransden and Joachain [84, §5.4]). The quantization of the radiation field showed that even in the vacuum there are fluctuations, which interact with electrons, causing rapid oscillations. Therefore when the electron is subject to the non-uniform electric field of the nucleus, it will experience a potential that is slightly different than that at its mean position. The electrons that are the closest to the nucleus will then be more affected, which explains why the s-states exhibit the largest Lamb shifts. The result is that the $2p_{1/2}$ state is more tightly bound than the $2s_{1/2}$, in the hydrogen atom (see Fig. 5.7 of Ref [84] for an illustration).

Up to now we only briefly discussed the existence and the meaning of the negative energy continuum. It is worth coming back to its interpretation as its discovery shook the scientific community of the beginning at the 20th century. The most commonly accepted interpretation is that of Dirac sea or the *hole theory*, in which only the solutions with positive energy $E > mc^2$ are associated to real electrons. The discovery of negative-energy particles contradicted the foundations of quantum mechanics, which assume that any atom has a state of lowest energy, i.e., the ground state. If negative solutions were available to electrons, they would continuously lose energy, forming unstable systems. The hole theory [91, §12] is based on the hypothesis that all states of negative energy are already occupied by electrons. Thanks to Pauli's principle an electron is forbidden to fall into the negative continuum by emitting radiation. The negative-energy electrons however, if they absorb a radiation quantum with an energy larger than $2mc^2$ can reach a state in the positive continuum, leaving a hole in the Dirac sea. This hole behaves just as an electron of charge $+e$ as Dirac wrote *"an electron with negative energy moves in an external field as though it carries a positive charge."* [96]. Although Dirac misidentified them as protons (his paper is entitled "*A Theory of Electrons and Protons.*"), they were later defined as the electron's antiparticle, the positron and the energy $2mc^2$ is nowadays well-known as the minimal amount of energy required for the creation of electron-positron pairs.

2.3.6 Non-relativistic limit

Atomic physics is often taught and learned starting from the non-relativistic Schrödinger equation. Most of the textbooks dedicated to education are focused on non-relativistic quantum mechanics [84, 17, 8], and only briefly mention the existence of the Dirac equation derived from a fully relativistic treatment. The reason is most likely of pedagogical nature since relativistic effects may be approached through the addition of ad-hoc relativistic corrections (derived by Foldy and Wouthuysen [97]) to the non-relativistic Hamiltonian using perturbation theory with the non-relativistic eigenfunctions of the Schrödinger equation as zeroth-order wave functions. The results so obtained are indeed in good agreement with those calculated from Dirac equation, at least for light systems.

Most of our work is based on the fully relativistic Dirac equation. Nevertheless it is interesting to present some aspects of the non-relativistic and quasi-relativistic theories as they correspond to a more natural way of interpreting our results.

For now, let us consider briefly the Pauli approximation, as presented by Froese Fischer *et al.* [8]. In order to compare non-relativistic and relativistic theories, it is common to define $\varepsilon = E - mc^2$, so that the relativistic energies coincide with non-relativistic ones. Redefining the four-spinors (2.54) as (dropping all $n\kappa m$ indices)

$$\phi(\boldsymbol{r}) = \begin{pmatrix} \xi(\boldsymbol{r}) \\ \eta(\boldsymbol{r}) \end{pmatrix} , \tag{2.83}$$

the Dirac coupled equations reads

$$\varepsilon\xi(\boldsymbol{r}) = c(-\mathrm{i}\hbar\boldsymbol{\sigma}\cdot\boldsymbol{\nabla})\eta(\boldsymbol{r}) + V(r)\xi(\boldsymbol{r}) \tag{2.84}$$

$$(\varepsilon + 2mc^2)\eta(\boldsymbol{r}) = c(-\mathrm{i}\hbar\boldsymbol{\sigma}\cdot\boldsymbol{\nabla})\xi(\boldsymbol{r}) + V(r)\eta(\boldsymbol{r}) . \tag{2.85}$$

Extracting $\eta(\boldsymbol{r})$ from Eq. (2.84) and inserting it into Eq. (2.85) leads to an inadequate definition of the probability density

$$\rho(\boldsymbol{r}) = |\xi(\boldsymbol{r})|^2 + |\eta(\boldsymbol{r})|^2 , \tag{2.86}$$

as pointed out by Froese Fischer *et al.* [8, §B.2.3]. Indeed, the probability density can not be rewritten as $\rho(\boldsymbol{r}) = |\psi(\boldsymbol{r})|^2$, where $\psi(\boldsymbol{r})$ would be a two-spinor, as expected from non-relativistic theory. However, the transformation

$$\psi(\boldsymbol{r}) = \left(1 - \frac{\hbar^2}{8m^2c^2}\boldsymbol{\nabla}^2\right)\xi(\boldsymbol{r}) \tag{2.87}$$

restores the appropriate form of the probability density. Skipping the mathematical details, the Pauli Hamiltonian satisfying the eigenvalue equation

$$\mathcal{H}_{\rm P}\psi(\boldsymbol{r}) = \varepsilon\psi(\boldsymbol{r}) \,, \tag{2.88}$$

is given by

$$\mathcal{H}_{\rm P} = -\frac{\hbar^2}{2m}\boldsymbol{\nabla}^2 + V(r) - \frac{\hbar^4}{8m^3c^2}\boldsymbol{\nabla}^4 + \frac{1}{2m^2c^2}\frac{1}{r}\frac{dV}{dr}\boldsymbol{l}\cdot\boldsymbol{s} + \frac{\hbar^2}{8m^2c^2}\boldsymbol{\nabla}^2 V \,. \tag{2.89}$$

The two first terms are easily identified as the Schrödinger Hamiltonian of Eq. (2.21), while the others are the relativistic mass correction, the spin–orbit interaction and the one-body Darwin term, respectively. Each of these corrections induces an energy shift with respect to the non-relativistic $\varepsilon_n = -Z^2/2n^2$ hydrogenic energy derived in Bohr's model and confirmed by Schrödinger equation. The total energy is then given by

$$\varepsilon_{nj} = \varepsilon_n\left[1 + \frac{(Z\alpha)^2}{n^2}\left(\frac{n}{j+1/2} - \frac{3}{4}\right)\right] \,, \tag{2.90}$$

that now depends on n and j, which agrees with the Dirac fully relativistic energy of Eq. (2.82) to second order in $(\alpha Z)^2$. Hence, we show explicitly that the relativistic corrections are expanded in powers of (αZ) as already announced in Sec. 2.1.

Relativistic effects have direct, measurable consequences.[7] Especially, we observe that the relativistic density distributions are more compact than non-relativistic ones. The mean radii are $\langle r_{n\kappa}\rangle < \langle r_{nl}\rangle$, such that their relative difference is of the order of $(\alpha Z)^2$. Furthermore, Dirac electrons are more tightly bound than Schrödinger's, according to their individual energies $\varepsilon_{n\kappa} < \varepsilon_{nl}$, with the spin-orbit splitting beeing such that $\varepsilon_{n,\kappa=l} < \varepsilon_{n,\kappa=-l-1} < \epsilon_{nl}$, i.e., the $p_{1/2}$ is more tightly bound than the $p_{3/2}$ [27, p.17]. Radial contractions are important and well-known effects going from non-relativistic to relativistic theory [98]. It has sensitive consequences in very heavy elements for which αZ is close to unity. The most recent example is the case of oganesson that, although classified in the periodic table as a rare noble gas, has the possibility to capture an extra electron [99, 56]. This issue is discussed in more details in our paper $\mathrm{A_V}$.

[7] Note that since v is inversely proportional to the orbital angular momentum, we expect the orbitals with the lowest l to be affected by relativistic effect the strongest [27, p.10].

Chapter 3

Many-body systems

The periodic table was recently extended to include elements with the number of protons $Z \geq 110$, hence completing its seventh row (see e.g. [100, 101, 45, 102, 44] for reviews). The very last element of the periodic table, the oganesson, belongs to the noble gas column with its 118 protons, its electrons filling up completely 19 non-relativistic orbitals from the $1s$ to the $7p$ or equivalently the 31 relativistic orbitals from the $1s_{1/2}$ to the $7p_{3/2}$. The one-electron Dirac equation only describes systems with a single electron, whatever nucleus is considered and therefore is inadequate to describe more complex systems. This chapter aims to provide the details of the theoretical and computational methods used for the determination of atomic properties of He-like (2 electrons) to Og-like (118 electrons) atomic systems, spanning the entire range of the periodic table of elements, including both positive and negative ions.

We follows here a 'classical' way to present many-body systems rather than chronologically as it is done in the previous Chapter. It will allow us to be more direct and to establish from the start the scientific vocabulary and mathematical tools that are in use nowadays. We will continue to present our quantum theory in the fully relativistic scheme. However, since many physics interpretations and computational strategies rely on arguments from non-relativistic theory, we will often switch from one framework to the other, assuming that our conclusions in the non-relativistic context still apply in the relativistic context. Since we only describe here the fully-relativistic theory, we refer the reader to a series of textbooks and review papers that focus on the non-relativistic counterpart of what we present here such as the books of Cowan [17], Bransden and Joachain [84] and Froese Fischer *et al.* [8] as well as to the review paper by Froese Fischer *et al.* [28].

3.1 Many-body Hamiltonian

Thanks to our understanding of the one-electron Dirac equation, we can move on to the description of the actual problem studied in this thesis: the many-electron systems, i.e. any atomic system with more than one electron. Starting from the time-independent Dirac Hamiltonian $\mathcal{H}_\mathrm{D}$ of Eq. (2.52), in which $V(r)$ is the nuclear potential $V_\mathrm{nuc}(r)$, we build

$$\mathcal{H}_\mathrm{DC} = \sum_{i=1}^{N_e} \mathcal{H}_\mathrm{D}(i) + \sum_{i<j=1}^{N_e} \frac{1}{r_{ij}} \,, \tag{3.1}$$

the many-body Dirac-Coulomb (DC) Hamiltonian. The latter is simply a sum of one-electron Dirac Hamiltonians for the N_e electrons plus the Coulomb repulsion $1/r_{ij} = 1/|\boldsymbol{r}_i - \boldsymbol{r}_j|$ for each pair of electrons. The introduction of the electron-electron repulsion potential has tremendous consequences, as we will discuss later, since $1/r_{ij} \to \infty$ when two electrons are getting closer to each other. We are then looking for wave functions $\Psi(\boldsymbol{r}_1, \boldsymbol{r}_2, \ldots, \boldsymbol{r}_{N_e})$ that are solutions of the eigenvalue problem

$$\mathcal{H}_\mathrm{DC}\Psi(\boldsymbol{r}_1, \boldsymbol{r}_2, \ldots, \boldsymbol{r}_{N_e}) = E\Psi(\boldsymbol{r}_1, \boldsymbol{r}_2, \ldots, \boldsymbol{r}_{N_e}) \,, \tag{3.2}$$

where E is the total energy of the system. Grant [27, §6.4] discusses in details the *retardation* effects arising from the finite value of the speed of light in quantum electrodynamics (QED) theory. We hereby only recall the most important corrections added to $\mathcal{H}_\mathrm{DC}$. We introduce the long wavelength approximation of the transverse photon interaction,

$$\mathcal{H}_\mathrm{Breit} = -\sum_{j>i=1}^{N_e} \frac{1}{2r_{ij}} \left[(\boldsymbol{\alpha}_i \cdot \boldsymbol{\alpha}_j) + \frac{(\boldsymbol{\alpha}_i \cdot \boldsymbol{r}_{ij})(\boldsymbol{\alpha}_j \cdot \boldsymbol{r}_{ij})}{r_{ij}^2} \right] \,, \tag{3.3}$$

which is then called the Breit interaction that is a relativistic correction to the Coulomb interaction. Note that the interaction between two charged particles, which includes retardation effects as the lowest order relativistic correction, can be derived in classical electrodynamics as discussed by Jackson [103, §12.6]. Adding (3.3) to $\mathcal{H}_\mathrm{DC}$ gives the Dirac-Coulomb-Breit (DCB) Hamiltonian

$$\mathcal{H}_\mathrm{DCB} = \mathcal{H}_\mathrm{DC} + \mathcal{H}_\mathrm{Breit} \,. \tag{3.4}$$

Further QED corrections are included such as the self-energy (SE) correction,

$$\Delta E_\mathrm{SE} = \left(\frac{\alpha}{\pi}\right) \frac{\alpha^2 Z^4}{n^3} F(nlj, Z\alpha) \,, \tag{3.5}$$

which arises from the electron interaction with its own electromagnetic field[1], or the vacuum polarization arising from the creation and annihilation of virtual electron–positron

[1] The electron interaction with its own magnetic field is directly related to the interpretation of the Lamb shift given in Sec. 2.3.5 by considering quantum fluctuations of the radiation field that affects the electron's mean position, as demonstrated by Welton [95]. Note that the same expression of the self-energy was also computed non-relativistically by Bethe [104] and Bethe and Salpeter [105, §19].

pairs [28]. Note that the expression of the SE correction given above is only valid for one-electron systems and that the function $F(nlj, Z\alpha)$ is slowly varying with $Z\alpha$ [106]. Its implementation for more complex atomic systems is given by Grant [27, §7.11]. The 'best' Hamiltonian we deal with is therefore

$$\mathcal{H}_{\mathrm{DCB+QED}} = \mathcal{H}_{\mathrm{DCB}} + \mathcal{H}_{\mathrm{SE}} + \mathcal{H}_{\mathrm{VP}} \; . \tag{3.6}$$

3.2 Configuration state functions

The eigenfunction solutions to Eq. (3.2) are built based on solutions to the *central field* approximation of the $\mathcal{H}_{\mathrm{DC}}$ Hamiltonian,

$$\mathcal{H}_{\mathrm{DC}} \approx \tilde{\mathcal{H}}_{\mathrm{DC}} = \sum_{i=1}^{N_e} \left[H_{\mathrm{D}}(i) + u_i(r_i) \right] \; , \tag{3.7}$$

in which each electron is described in a central field potential $u_i(r_i)$ that accounts for the electron–electron interactions. $\tilde{\mathcal{H}}_{\mathrm{DC}}$ is separable, and all product functions of the type

$$\Psi(\boldsymbol{r}_1, \boldsymbol{r}_2, \ldots, \boldsymbol{r}_{N_e}) = \phi_{\alpha_1}(\boldsymbol{r}_1)\phi_{\alpha_2}(\boldsymbol{r}_2) \ldots \phi_{\alpha_{N_e}}(\boldsymbol{r}_{N_e}) \; , \tag{3.8}$$

where $\phi_{\alpha_i}(\boldsymbol{r}_i)$ are four-spinors (2.54) and α_i represents the quadruplet $(nljm)$ of quantum numbers, are solutions of

$$\tilde{\mathcal{H}}_{\mathrm{DC}}\Psi(\boldsymbol{r}_1, \boldsymbol{r}_2, \ldots, \boldsymbol{r}_{N_e}) = E\Psi(\boldsymbol{r}_1, \boldsymbol{r}_2, \ldots, \boldsymbol{r}_{N_e}) \tag{3.9}$$

with $E = \sum_{i=1}^{N_e} \varepsilon_{\alpha_i}$, ε_{α_i} being the individual energy of the relativistic orbital ϕ_{α_i}. These solutions are however unsatisfactory as such. Indeed, since the Hamiltonian $\mathcal{H}_{\mathrm{DC}}$ is invariant under the exchange of two electrons, which is inherited from the indistinguishability character of electrons, the probability density $|\Psi(\boldsymbol{r}_1, \boldsymbol{r}_2, \ldots, \boldsymbol{r}_{N_e})|^2$ should therefore also be invariant with the exchange of two electrons. Explicitly,

$$|\Psi(\boldsymbol{r}_1, \ldots, \boldsymbol{r}_i, \ldots, \boldsymbol{r}_j, \ldots, \boldsymbol{r}_{N_e})|^2 = |\Psi(\boldsymbol{r}_1, \ldots, \boldsymbol{r}_j, \ldots, \boldsymbol{r}_i, \ldots, \boldsymbol{r}_{N_e})|^2 \; , \tag{3.10}$$

which defines two general families of solutions

$$\Psi(\boldsymbol{r}_1, \ldots, \boldsymbol{r}_i, \ldots, \boldsymbol{r}_j, \ldots, \boldsymbol{r}_{N_e}) = +\Psi(\boldsymbol{r}_1, \ldots, \boldsymbol{r}_j, \ldots, \boldsymbol{r}_i, \ldots, \boldsymbol{r}_{N_e}) \; , \tag{3.11}$$

$$\Psi(\boldsymbol{r}_1, \ldots, \boldsymbol{r}_i, \ldots, \boldsymbol{r}_j, \ldots, \boldsymbol{r}_{N_e}) = -\Psi(\boldsymbol{r}_1, \ldots, \boldsymbol{r}_j, \ldots, \boldsymbol{r}_i, \ldots, \boldsymbol{r}_{N_e}) \; . \tag{3.12}$$

The former are *symmetric* solutions with respect to the interchange of coordinates $(\boldsymbol{r}_i, \boldsymbol{r}_j)$ while the latter are *antisymmetric* solutions. According to Cowan [17, § 4.5], "*it is a strong*

postulate of quantum mechanics that Ψ *be antisymmetric upon interchange of two electrons"*, so that

$$\Psi(\boldsymbol{r}_1, \ldots, \boldsymbol{r}_i, \ldots, \boldsymbol{r}_j, \ldots, \boldsymbol{r}_{N_e}) = -\Psi(\boldsymbol{r}_1, \ldots, \boldsymbol{r}_j, \ldots, \boldsymbol{r}_i, \ldots, \boldsymbol{r}_{N_e}) \tag{3.13}$$

are the only acceptable physical solutions. For simple systems, the easiest solution is to build the total wave function as a *Slater determinant*,

$$\Psi(\boldsymbol{r}_1, \boldsymbol{r}_2, \cdots, \boldsymbol{r}_{N_e}) = \frac{1}{\sqrt{N_e!}} \begin{vmatrix} \phi_{\alpha_1}(\boldsymbol{r}_1) & \phi_{\alpha_1}(\boldsymbol{r}_2) & \cdots & \phi_{\alpha_1}(\boldsymbol{r}_{N_e}) \\ \phi_{\alpha_2}(\boldsymbol{r}_1) & \phi_{\alpha_2}(\boldsymbol{r}_2) & \cdots & \phi_{\alpha_2}(\boldsymbol{r}_{N_e}) \\ \vdots & \vdots & \ddots & \vdots \\ \phi_{\alpha_{N_e}}(\boldsymbol{r}_1) & \phi_{\alpha_{N_e}}(\boldsymbol{r}_2) & \cdots & \phi_{\alpha_{N_e}}(\boldsymbol{r}_{N_e}) \end{vmatrix} , \tag{3.14}$$

which automatically ensures the antisymmetry of the wave function and satisfies the Pauli exclusion principle. Indeed, assuming that two electrons occupy the same relativistic orbital, e.g., $\alpha_1 = \alpha_2$, then the two first rows are identical, which leads automatically to a vanishing wave function thanks to the properties of determinants.

Just as in the one-electron case, the many-body wave function is a simultaneous eigenfunction of a set of operators that commute with the Hamiltonian. These operators are $\boldsymbol{J}^2$, J_z and $\mathcal{P}$, corresponding to the square of the total angular momentum, its projection and the parity. The wave function should therefore satisfy the following eigenvalue equations

$$\begin{aligned} &\mathcal{P}\Psi(\boldsymbol{r}_1, \boldsymbol{r}_2, \cdots, \boldsymbol{r}_{N_e}) = \pi\Psi(\boldsymbol{r}_1, \boldsymbol{r}_2, \cdots, \boldsymbol{r}_{N_e}) , \qquad \pi = (-1)^{l_1+\cdots+l_{N_e}} , \\ &\boldsymbol{J}^2\Psi(\boldsymbol{r}_1, \boldsymbol{r}_2, \cdots, \boldsymbol{r}_{N_e}) = J(J+1)\Psi(\boldsymbol{r}_1, \boldsymbol{r}_2, \cdots, \boldsymbol{r}_{N_e}) , \\ &J_z\Psi(\boldsymbol{r}_1, \boldsymbol{r}_2, \cdots, \boldsymbol{r}_{N_e}) = M_J\Psi(\boldsymbol{r}_1, \boldsymbol{r}_2, \cdots, \boldsymbol{r}_{N_e}) , \end{aligned} \tag{3.15}$$

where M_J takes the values $-J, -J+1, \ldots, J$. However, the Slater determinant wave function (3.14) is usually not an eigenfunction of $\boldsymbol{J}^2$ and the most general case therefore requires to generate the wave function as a linear combination of Slater determinants. Then, the wave function is also an eigenfunction of $\boldsymbol{J}^2$.

Multiple ways exist to couple angular momenta [17, §4.17, §9] to form the total angular momentum $\boldsymbol{J}$. The jj intermediate coupling naturally arises from the relativistic treatment of the electron, for which the orbital and spin angular momenta are coupled in the total one-electron angular momentum, i.e., $\boldsymbol{l} + \boldsymbol{s} = \boldsymbol{j}$. In jj coupling, the total angular momentum is simply

$$\boldsymbol{J} = \sum_{i=1}^{N_e} \boldsymbol{j}_i = \sum_{i=1}^{N_e} (\boldsymbol{l}_i + \boldsymbol{s}_i) \ . \tag{3.16}$$

Another coupling, still widely used, even in fully relativistic theories, is the approximate LS coupling. The latter arises naturally from the non-relativistic theory, in which the total

angular and spin momenta are defined as

$$\boldsymbol{L} = \sum_{i=1}^{N_e} \boldsymbol{l}_i \; ; \quad \boldsymbol{S} = \sum_{i=1}^{N_e} \boldsymbol{s}_i \tag{3.17}$$

that couples into the total angular momentum as $\boldsymbol{J} = \boldsymbol{L} + \boldsymbol{S}$.[2] The habits of non-relativistic theory to refer to LS terms, noted as ${}^{2S+1}L$, are still well anchored in today's notations. Other coupling schemes exist, which might be relevant depending on the relative strength of the Coulomb interaction and the spin–orbit coupling. Transformation matrices exist to switch from one representation to another, as describe by Cowan [17, §9]. Nevertheless, these recoupling matrices are only available for the simplest systems. For more complex studies, computational tools are required such as the ones developed by Gaigalas and co-workers in the framework of the GRASP package [107, 30, 108].

Instead of following a Slater determinant based approach, we follow another equivalent route that is computationally more tractable. We introduce the concept of *relativistic electron configuration* that is fully justified starting from the central field approximation (3.7). In this approximation indeed, the one-electron energies are independent of the magnetic quantum numbers and we can associate the relativistic electron configuration

$$(n_1\kappa_1)^{w_1}(n_2\kappa_2)^{w_2}\ldots(n_m\kappa_m)^{w_x} \; , \tag{3.18}$$

to the total energy

$$E = \sum_{i=1}^{x} w_i \varepsilon_{n_i\kappa_i} \tag{3.19}$$

where w_i is the occupation number of the subshell $(n_i\kappa_i)$ $i = 1, \ldots, x$, so that $\sum_{i=1}^{x} w_i = N_e$. Due to the strong heritage from non-relativistic theory, the configurations are usually still written in their equivalent non-relativistic form as

$$(n_1 l_1)^{\tilde{w}_1}(n_2 l_2)^{\tilde{w}_2}\ldots(n_{m'} l_{m'})^{\tilde{w}_{x'}} \tag{3.20}$$

where $\tilde{w}_i$ is the occupation number of the non-relativistic subshell $(n_i l_i)$. To the w relativistic equivalent electrons, having the same κ-value, i.e. $(n\kappa)^w$, we associate the subshell wave function

$$\Phi((n\kappa)^w \alpha\nu J M_J) \equiv |(n\kappa)^w \alpha\nu J M_J)\rangle \equiv |(nlj)^w \alpha\nu J M_J)\rangle \; , \tag{3.21}$$

where we used the *ket* notation of Dirac $|\cdot\rangle$ and α and ν are additional quantum numbers to uniquely define the wave function besides the total angular momentum J and its

[2] Note that the wave functions built from the coupling $\boldsymbol{L} + \boldsymbol{S}$ and $\boldsymbol{S} + \boldsymbol{L}$ differ by the phase factor $(-1)^{L+S-J}$.

projection M_J (see [28] and references therein for more details). The antisymmetry of the wave function is achieved through the use of *coefficients of fractional parentage* (CFPs), which provides the appropriate coupling between the additional electron and the $(w_i - 1)$ electrons already coupled to form an antisymmetric wave function

$$|(nlj)^w \alpha J M_J)\rangle = \sum_{\bar{\alpha}\bar{J}} |((nlj)^{w-1}\bar{\alpha}\bar{J}, nlj)\alpha J M_J\rangle \, ((lj)^{w-1}\bar{\alpha}\bar{J}|\}(lj)^w \alpha J) \quad (3.22)$$

where $((lj)^{w-1}\bar{\alpha}\bar{J}|\}(lj)^w\alpha J)$ is the CFP associated to the parent $|(nlj)^{w-1}\bar{\alpha}\bar{J}\bar{M}_{\bar{J}}\rangle$. This recurrence relation is used until $w = 1$, for which there is no antisymmetric requirement.[3] The coupling procedure followed in this work is therefore to first couple equivalent electrons within each subshell and then progressively couple subshells to finally build the total wave function of appropriate $\pi J M_J$ symmetry.[4] The resulting wave function is known as a *relativistic configuration state function* (CSF), written as

$$|\gamma\pi J M_J\rangle \qquad \text{or} \qquad |\gamma\pi J\rangle \quad (3.23)$$

where γ represents all additional information such as the configuration and its angular coupling tree with the complete quantum numbers information. The projection of the total angular momentum $\boldsymbol{J}$, M_J, is often omitted since the $2J+1$ levels with total angular momentum J and projection $M_J = -J, -J+1, J-1, J$ are degenerate in the absence of external fields.

3.3 The variational principle and the Dirac-Hartree-Fock method

The definition of the CSF provides the angular structure of the many-body wave function. However, the set of radial functions $\{P_a, Q_a\}$ are still to be determined.[5] We focus in this work on variational methods to compute the radial parts of the orbitals.

Within the family of variational methods, the computations rely on the Rayleigh-Ritz's *variational principle*, which is a fundamental tool used in quantum mechanics. An energy functional is defined as

$$\mathcal{F}[\Psi] = \frac{\langle\Psi|\mathcal{H}|\Psi\rangle}{\langle\Psi|\Psi\rangle} \quad (3.24)$$

[3] The equivalent electron wave function can also be described within the quasispin angular theory as $|(n\kappa)\alpha Q J M_Q M_J)\rangle$, where Q is the quasispin as defined in Ref. [28] (see Sec. 3.4.4).

[4] The parity π was consciously taken out of the recoupling formula to lighten the notations. Nevertheless they are of crucial importance in the following and one should not forget it when defining the CSFs of interest.

[5] To lighten the notations, the radial components of the Dirac orbitals are noted P_a and Q_a instead of $P_{nlj}(r)$ and $Q_{nlj}(r)$ or $P_{n\kappa}(r)$ and $Q_{n\kappa}(r)$.

where $\mathcal{H}$ can be either of the Hamiltonians presented in Sec. 3.1 for our purposes. We use here again the standard Dirac notation according to which

$$\langle \Psi | \mathcal{O} | \Psi \rangle = \int \Psi^* \mathcal{O} \Psi d\boldsymbol{r} \ , \tag{3.25}$$

where $d\boldsymbol{r}$ represent the integration over space coordinates, is the expectation value of an operator $\mathcal{O}$ and

$$\langle \Psi | \Psi \rangle = \int \Psi^* \Psi d\boldsymbol{r} \tag{3.26}$$

corresponds to the norm of $|\Psi\rangle$. In the framework of the variational principle, it can be demonstrated that there is an equivalence between solving the eigenvalue problem

$$\left(\mathcal{H} - \mathcal{F}[\Psi]\right) |\Psi\rangle = 0 \ , \tag{3.27}$$

and looking for solutions $|\Psi\rangle$ such that the energy functional (3.24) is stationary to first order with any variation $|\delta\Psi\rangle$ of the wave function [8, §1.5]. The general idea behind variational methods is therefore to seek for wave functions $|\Psi\rangle$ such that

$$\delta\mathcal{F} = 0 \qquad \forall\, \delta\Psi \ . \tag{3.28}$$

In the case where $|\Psi\rangle$ is a single CSF, $|\delta\Psi\rangle$ represents all variations with respect to the radial components of the orbitals, $|\delta\Psi\rangle \equiv \{\delta P_a, \delta Q_a\}$. When the Hamiltonian is the Dirac-Coulomb Hamiltonian, the variational principle applied to

$$\mathcal{F}(\{P\}, \{Q\}; \gamma\pi J) = \langle \gamma\pi J | \mathcal{H}_{\mathrm{DC}} | \gamma\pi J \rangle + \sum_{a,b} \delta_{\kappa_a,\kappa_b} \lambda_{ab} \mathcal{C}_{ab} \tag{3.29}$$

is the core of the Dirac-Hartree-Fock (DHF) method. The above energy functional enforces the orthonormality for all pairs of orbitals (a, b) (where a or b is a short notation for all quantum numbers to uniquely identify an orbital) belonging to the same κ–symmetry through the use of Lagrange multipliers. These constraints take the following form

$$\mathcal{C}_{ab} \equiv \int \left[P_a(r)P_b(r) + Q_a(r)Q_b(r)\right] dr - \delta_{n_a n_b} = 0 \ , \tag{3.30}$$

which combine the orthogonality condition when $n_a \neq n_b$ with the normalization condition for $n_a = n_b$. The other term in Eq. (3.29) is the expectation value of $\mathcal{H}_{\mathrm{DC}}$. The latter is usually expressed as a sum over one-body contributions and two-body contributions,

$$\langle \gamma\pi J | \mathcal{H}_{\mathrm{DC}} | \gamma\pi J \rangle = \sum_a w_a I(a,a) + \sum_{abk} \Big[f_{abk} F^k(ab) + g_{abk} G^k(ab) \Big] \ , \tag{3.31}$$

where $I(a,b)$ is, in all generality,

$$I(a,b) = \delta_{\kappa_a\kappa_b}\int\left\{P_a(r)V_{\rm nuc}(r)P_b(r) - cP_a(r)\left(\frac{d}{dr}-\frac{\kappa_a}{r}\right)Q_b(r)\right.$$
$$\left. + cQ_a(r)\left(\frac{d}{dr}+\frac{\kappa_a}{r}\right)P_b(r) + Q_a(r)(V_{\rm nuc}(r)-2c^2)Q_b(r)\right\}dr\ . \quad (3.32)$$

The two-body part of Eq. (3.31) is a weighted sum of Slater integrals

$$R^k(ab,cd) = \int\left[P_a(r)P_c(r)+Q_a(r)Q_b(r)\right]\frac{1}{r}Y^k(bd;\ r)dr\ , \quad (3.33)$$

where

$$Y^k(ab;\ r) = r\int\frac{r_<^k}{r_>^{(k+1)}}\left[P_a(s)P_b(s)+Q_a(s)Q_b(s)\right]ds \quad (3.34)$$

as inspired by the non-relativistic work of Hartree [109]. $F^k(ab) = R^k(ab,ab)$ and $G^k(ab) = R^k(ab,ba)$ are known as the *direct* and *exchange* contributions. They arise from the development in Legendre polynomials of the electron–electron interaction

$$\frac{1}{r_{ij}} = \sum_k \frac{r_<^k}{r_>^{k+1}}\ P_k(\cos\theta)\ , \quad (3.35)$$

where $r_< = \min(r_i,r_j)$, $r_> = \max(r_i,r_j)$ and θ is the angle between $\boldsymbol{r}_i$ and $\boldsymbol{r}_j$. The latter expression is often given in its tensorial form as

$$\frac{1}{r_{ij}} = \sum_k \frac{r_<^k}{r_>^{k+1}}\ \mathbf{C}^{(k)}(\theta_i,\phi_i)\cdot\mathbf{C}^{(k)}(\theta_j,\phi_j)\ , \quad (3.36)$$

where $\mathbf{C}^{(k)}$ is the tensor of order k (see Sec. 3.4.4 for more information about tensor operators) corresponding to renormalized spherical harmonics [27, §B.3]. The coefficients f_{abk} and g_{abk} appearing in Eq. (3.31) are pure angular coefficients as shown by Grant [27, §6.4].

In the relativistic many-body theory, the variational principle requires to vary the radial part of all orbitals. For each orbital, the variation $|\delta\Psi\rangle$ consists in the simultaneous variation of the small and large components. Considering the perturbation on the orbital a, we have

$$\begin{cases} P_a \to P_a + \delta P_a \\ Q_a \to Q_a + \delta Q_a\ . \end{cases} \quad (3.37)$$

The stationary condition $\delta\mathcal{F} = 0$ with respect to the above perturbations leads to the following system of equations, called the DHF equations,

$$w_a\begin{pmatrix} V(a;\ r) & -c\left[\frac{d}{dr}-\frac{\kappa_a}{r}\right] \\ c\left[\frac{d}{dr}+\frac{\kappa_a}{r}\right] & V(a;\ r)-2c^2\end{pmatrix}\begin{pmatrix}P_a(r)\\ Q_a(r)\end{pmatrix} = \sum_b \varepsilon_{ab}\delta_{\kappa_a\kappa_b}\begin{pmatrix}P_b(r)\\ Q_b(r)\end{pmatrix} \quad (3.38)$$

where $V(a;\ r) = V_{\rm nuc}(r) + Y(a;\ r) + \bar{X}(a;\ r)$. $Y(a;\ r)$ and $\bar{X}(a;\ r)$ are the direct and exchange potentials made of the accumulated contribution from the variation of the energy contributions from F and G integrals, respectively. The latter is defined as

$$w_a \bar{X}(a;\ r) P_a(r) = \sum_{bk} g_{abk} \left(\frac{Y^k(ab;\ r)}{r} \right) P_b(r) \ , \tag{3.39}$$

which means that $P_a(r)$ and $Q_a(r)$ are part of an integrand. Therefore, one needs to solve the coupled integro-differential equations iteratively, updating the radial orbitals at each step. Such a system of equations is derived for all occupied orbitals of the DHF CSF and therefore the DHF equations form a complex system of coupled equations to solve. Since the evaluation of the direct and exchange potentials requires the knowledge of the radial orbitals, one needs to start with trial functions so that the potentials can be determined and the system of equations solved for the energies ε_{ab} and the updated radial orbitals. The potentials are then re-evaluated with these new radial orbitals and the radial equations are solved again. As Löwdin wrote in the non-relativistic context of the Hartree–Fock (HF) method *"The process is carried on until it becomes self-consistent, i.e., until two successive approximations agree within the accuracy desired, and the procedure is therefore called the 'self-consistent-field' method"* [110].

Remarks

The derivation of the DHF equations using the variational principle requires some additional comments.

The biggest concern about this method is probably related to the potential *variational collapse* of the wave function, which refers to the fall of bound states into the negative continuum when seeking for the minimum of the energy functional. The discussion varies depending on the numerical method used to solve the DHF equations. Grant [93] discusses this issue using finite-basis methods, which are relevant to our papers using the Lagrange-mesh method (see Sec. 4.1.1) as presented in later sections. Although most of our calculations are performed using the GRASP packages, which are based on the finite-difference method, hence solving the DHF coupled equations for one state at the time, the discussion about the variational collapse proposed by Grant using finite-basis methods is still an interesting one to understand the difficulties raised by the negative energy continuum.

He demonstrated that the $2N$ solutions arising from the choice of N basis functions are well split into two disjoint sets of N solutions. One is associated to the bound states and the positive continuum, that corresponds to the Schrödinger spectrum in the non-relativistic limit, and another one associated to the negative continuum.[6] He wrote *"[...] we can ignore*

[6] More information about finite-basis methods are given in Sec. 4.1.1 and in papers A_{IV} and A_V.

the lower continuum when constructing bound states, as it is well known that the imposition of suitable boundary conditions is all that is required for their existence. The traditional approach to Dirac-Fock theory can thus be justified." [93]. He further provided the demonstration that the N eigenvalues corresponding to positive energy states are bounded from below, preventing them to fall into the negative energy continuum. Just as in the non-relativistic theory, these eigenvalues are variational upper bound to the exact energies. This is very well summarized by his Theorem 1 in Ref. [93]. Finally, one should realize the importance of the original debate, in which some physicists suggested the use of projectors (to separate the negative energy states and positive energy states), while others argued that it was not needed if the theory was established in the QED framework [111, 112]. Later, Desclaux would write that *"the variational principle gives only a stationary solution and not a minimum even for the ground state. In practice this does not introduce any numerical difficulty"* [31]. Additional information about the variational collapse using finite basis sets can be found in Refs. [27, §5.5] and [112].

Another interesting feature of the DHF method is the assumption that radial orbitals are independent of the electron spin. An investigation about the $1s2s\ ^3S$ and the $1s2s\ ^1S$ He-like levels showed that these two levels should be treated differently, as discussed by Froese Fischer in the non-relativistic framework [113]. When these two electrons are equivalent, the usual way to write the configuration is $1s^2$, assuming then that the radial components of two $1s$ relativistic orbitals are identical. The removal of this condition, leading to non-orthogonalities and hence a more complex derivation of the HF equations, leads to the so-called *unrestricted Hartree-Fock* (UHF) method. Froese Fischer argued that although the overlap between two s electrons ns and $n's$ is usually small, it can be close to 1 for equivalent electrons $1s1s'$, which can lead to severe numerical instabilities. Furthermore, the UHF method is subject to *spin-contamination*, i.e., the total wave function is no longer an eigenvalue of $\boldsymbol{S}^2$ [114]. Nevertheless it is not surprising that the UHF method improves the energy (gives a lower total energy) compared to the standard HF method since it increases the flexibility of the method. However, because the gain obtained with the UHF method was shown to decrease with Z, other methods, such as those presented in the next sections, are therefore more widely used. The introduction of non-orthogonalities is interesting in spite of a heavier mathematical treatment as discussed in Sec. 3.4.4 and Chap. 4.

3.4 Multiconfiguration methods

3.4.1 Electron correlation

The DHF method and its non-relativistic counterpart, the HF method [115], are key in any atomic structure theories. However, it fails to describe the *correlation* in the movement of the electrons properly. The strong assumption of the DHF method that the total wave function can be built as a linear combination of products of individual relativistic orbitals as in Eqs. (3.8) and (3.14) is directly related to the independent-particle model of the atom. Indeed, the Coulomb repulsion $1/r_{ij}$ is left out when discussing the general form of the wave function. However, the value of this potential increases rapidly when the two electrons i and j are close to each other. It tends to keep these particles apart, and since this correlation is completely neglected when forming the determinant wave function (3.14), the corresponding energy is called the *correlation energy* [116] and

$$E_{\text{corr}} = E_{\text{exact}} - E_{\text{DHF}} \tag{3.40}$$

where E_{exact} corresponds to the exact energy of the many-electron Dirac-Coulomb equation. It was pointed out by Löwdin in the non-relativistic context that the Pauli principle prevents two electrons with the same spin (and the same other quantum numbers) to be close to each other. He further wrote *"The antisymmetry on the wave function therefore acts as if there would be a strong repulsion between particles with the same spin at small distances"* [116], which means that, in a way, part of the electron correlation is already included.

The evaluation of the electron correlation effects on atomic properties is therefore one of the main goals of the atomic structure methods nowadays. In our work we used two *ab initio* methods to capture electron correlation beyond the DHF approximation, the relativistic configuration interaction (RCI) method and the multiconfiguration Dirac-Hartree-Fock (MCDHF) method, and one semiempirical method based on the definition of a semiempirical core potential. The *ab initio* methods are described in Sec. 3.4.2 and 3.4.3, respectively, while the semiempirical method is described in A$_{\text{IV}}$. Both *ab initio* methods result from the variational principle and therefore belong to the families of *variational methods*. The latter are often opposed to the many-body perturbation (MBPT) methods [36, 34, 39] that take advantage of a perturbative approach. We will not discuss MBPT methods in details as we solely used variational methods in this thesis. Nevertheless, it is interesting to point out that even the MBPT methods rely on DHF calculations, at least to compute the orbitals of the configuration of interest.

3.4.2 Relativistic configuration interaction

The relativistic configuration interaction method relies on the description of the total wave functions or *atomic state functions (ASFs)* as

$$|\Gamma \pi J\rangle = \sum_{\alpha=1}^{N_{\rm CSF}} c_\alpha^\Gamma \, |\gamma_\alpha \pi J\rangle \quad \text{with} \quad \sum_{\alpha=1}^{N_{\rm CSF}} (c_\alpha^\Gamma)^2 = 1, \tag{3.41}$$

where c_α are real numbers known as the *expansion coefficients* or *mixing coefficients*, $\{|\gamma_\alpha \pi J\rangle\}$ is the CSF basis set and Γ specifies the targeted state among all possible states represented by the set of CSFs. In the 'pure' RCI method, the basis functions, i.e., the CSFs, are known and fixed, and form, thanks to the orthonormaliy constraints of the radial parts of the orbitals, an orthonormal set such that $\langle \gamma_\alpha \pi J | \gamma_\beta \pi J \rangle = \delta_{\alpha\beta}$ (see Sec. 3.4.4). This means that when applying the variational principle according to Eq. (3.28), the perturbations of the ASF consist in perturbing the mixing coefficients

$$\delta\Psi = \delta c_\alpha^\Gamma \qquad \alpha = 1, \ldots, N_{\rm CSF} \, . \tag{3.42}$$

The energy functional is

$$\begin{aligned}
\mathcal{F}(\{c_\alpha^\Gamma\}; \Gamma\pi J) &= \langle \Gamma\pi J | \mathcal{H} | \Gamma\pi J \rangle - E_\Gamma \sum_{\alpha=1}^{N_{\rm CSF}} (c_\alpha^\Gamma)^2 \\
&= \sum_{\alpha\beta=1}^{N_{\rm CSF}} c_\alpha^\Gamma c_\beta^\Gamma \, \langle \gamma_\alpha \pi J | \mathcal{H} | \gamma_\beta \pi J \rangle - E_\Gamma \sum_{\alpha=1}^{N_{\rm CSF}} (c_\alpha^\Gamma)^2 \\
&= \sum_{\alpha=1}^{N_{\rm CSF}} (c_\alpha^\Gamma)^2 \, \langle \gamma_\alpha \pi J | \mathcal{H} | \gamma_\alpha \pi J \rangle + \sum_{\alpha\neq\beta=1}^{N_{\rm CSF}} c_\alpha^\Gamma c_\beta^\Gamma \, \langle \gamma_\alpha \pi J | \mathcal{H} | \gamma_\beta \pi J \rangle \\
&\quad - E_\Gamma \sum_{\alpha=1}^{N_{\rm CSF}} (c_\alpha^\Gamma)^2
\end{aligned} \tag{3.43}$$

where E_Γ is the Lagrange multiplier associated to the normalization condition and corresponds to the total energy. $\mathcal{H}$ is any of the Hamiltonians presented in Sec. 3.1. The stationary condition $\delta\mathcal{F} = 0 \;\; \forall \, \delta c_\alpha^\Gamma$ leads easily to the eigenvalue problem

$$(\mathbf{H}^{N_{\rm CSF}} - E_\Gamma \mathbf{I}) \mathbf{c}^\Gamma = 0 \, , \tag{3.44}$$

that is written in matrix notation for simplicity, and where $\mathbf{c}^\Gamma$ is the vector column of dimension $N_{\rm CSF}$ containing the c_α^Γ expansion coefficients, $\mathbf{I}$ is the $N_{\rm CSF} \times N_{\rm CSF}$ identity matrix and $\mathbf{H}^{N_{\rm CSF}}$ is the $N_{\rm CSF} \times N_{\rm CSF}$ *interaction matrix*. Note that since the CSFs $|\gamma_\alpha \pi J\rangle$ and $|\gamma_{\alpha'} \pi' J'\rangle$ are two different solutions of the same Hermitian operator, they

have no interaction, i.e., $\langle \gamma_\alpha \pi J | \mathcal{H} | \gamma_{\alpha'} \pi' J' \rangle \propto \delta_{JJ'} \delta_{\pi\pi'}$ and the interaction matrix is therefore (J, π)-block diagonal. The matrix elements of the interaction matrix are defined by

$$H_{\alpha\beta} = \langle \gamma_\alpha \pi J | \mathcal{H} | \gamma_\beta \pi J \rangle \ . \tag{3.45}$$

The eigenvalue problem (3.44) is solved by diagonalizing the interaction matrix, and we thus obtain a set of $N_{\rm CSF}$ eigenvalues and their corresponding eigenvector. The expansion (3.41) therefore represents $N_{\rm CSF}$ different and orthogonal ASFs, hence the need to precise which ASF is of interest with Γ. To each ASF $|\Gamma \pi J\rangle$, we therefore associate one root of the Hamiltonian with the eigen-energy[7]

$$E_\Gamma = (\mathbf{c}^\Gamma)^T \ \mathbf{H}^{N_{\rm CSF}} \mathbf{c}^\Gamma \ , \tag{3.46}$$

and the corresponding mixing coefficients $\mathbf{c}^\Gamma = \left(c_1^\Gamma, \ c_2^\Gamma, \ldots, \ c^\Gamma\right)^T$.

A crucial theorem related to the RCI method was demonstrated by Hylleraas and Undheim [117] and MacDonald [118], namely the Hylleraas–Undheim–MacDonald (HUM) interleaving theorem. This theorem states that a relationship exists between the eigenvalues of the interaction matrix of sizes M an $M+1$ such that

$$\ldots \ E_{\Gamma-1}^M \leq E_\Gamma^{M+1} \leq E_\Gamma^M \ \ldots \ . \tag{3.47}$$

A schematic representation of it is presented in Fig. 3.1. Observing a particular root, say the Γth root, we see that its energy progressively decreases for an increasing size of the system $E_\Gamma^M \geq E_\Gamma^{M+1} \geq E_\Gamma^{M+2} \geq E_\Gamma^{M+3} \geq \ldots$. This has determining consequences since according to the Rayleigh–Ritz method, these energies are upper bound to the exact energy. So that by increasing the size of the system, i.e., adding CSFs to the basis set, the computed energy converges toward the exact energy. We have thus improved the computed energies.

We used intensively the RCI method in this thesis, as attests its presence in most of our published papers. More specifically, the HUM theorem proved to be helpful in our study on the isotope shift of Ir (see $\rm B_{IV}$), which led us to a rigorous detection of a root-flipping (see Sec. 5.2). Furthermore, the case of the 2×2 CI matrix was developed in our paper on g-factors (see $\rm C_I$) following Ref. [28] to illustrate the importance of relativistic mixing.

3.4.3 Multiconfiguration Dirac–Hartree–Fock methods

The multiconfiguration Dirac–Hartree–Fock (MCDHF) method is described following the same reasoning than the DHF method, with the important difference that the ASF is

[7] The notations are usually lightened by dropping the number of CSF. The expression for the energy is therefore $E_\Gamma = (\mathbf{c}^\Gamma)^T \mathbf{H} \mathbf{c}^\Gamma$.

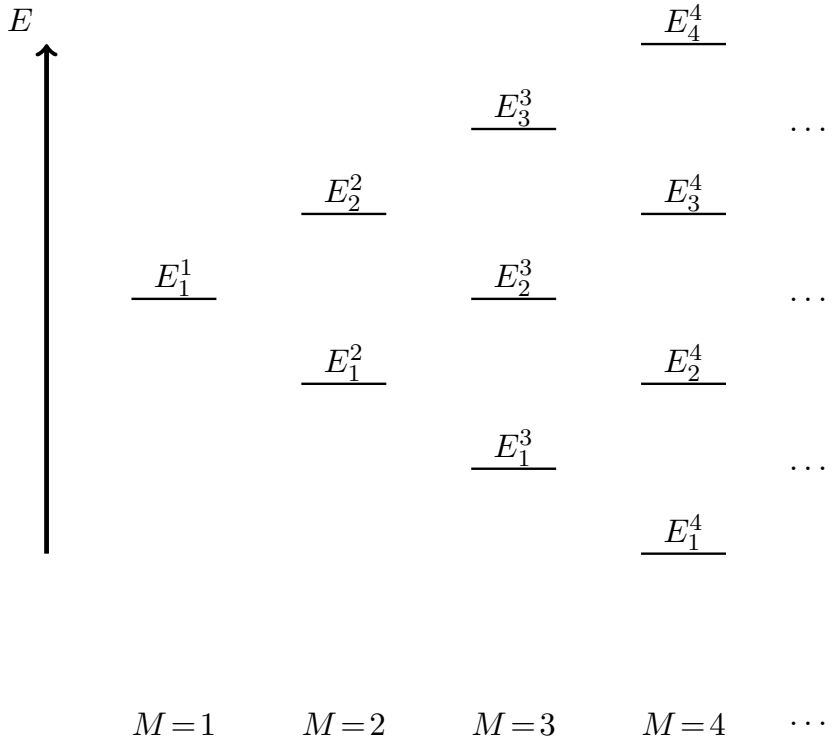

Figure 3.1: Schematic illustration of the interleaving HUM theorem [84, p.135], which displays the energy eigenvalues E_Γ^M for all roots $\Gamma = 1, \ldots, M$ of the interaction matrix of dimension $M = 1, 2, 3, 4$.

now defined according to Eq. (3.41). The trivial case with $N_{\rm CSF} = 1$ reduces to the DHF method. As in the case of the DHF and RCI methods, we start by building the energy functional, that takes the following form

$$\mathcal{F}(\{c_\alpha^\Gamma\}, \{P_a\}, \{Q_a\}; \Gamma\pi J) = \langle \Gamma\pi J | \mathcal{H}_{\rm DC} | \Gamma\pi J \rangle + \sum_{a,b} \delta_{\kappa_a,\kappa_b} \lambda_{ab} \mathcal{C}_{ab} \tag{3.48}$$

which resembles a mix between the DHF energy functional and the RCI energy functional. In the framework of the Grasp package the Hamiltonian is always the Dirac–Coulomb Hamiltonian. Just as in the DHF method, orthogonality constraints are added through the use of Lagrange multipliers λ_{ab} for all pairs of orbitals of the same κ-symmetry. The constraints C_{ab} are identical to those in the DHF method. However, since the ASF is now expanded as a linear combination of CSFs, the present energy functional not only depends on the radial functions $\{P_a\}$ and $\{Q_a\}$, but also on the mixing coefficients $\{c_\alpha^\Gamma\}$. The determination of the radial functions is obtained by solving the MCDHF radial equations derived by seeking the stationary solutions of the energy functional with respect to the perturbations $\{\delta P_a\}$ and $\{\delta Q_a\}$, for a given set of mixing coefficients. The main difference with the DHF method is that the expectation value of the Hamiltonian now writes

$$\langle \Gamma\pi J | \mathcal{H}_{\rm DC} | \Gamma\pi J \rangle = \sum_{ab} t_{ab} I(a,b) + \sum_{abcd;k} \nu_{abcd;k} R^k(ab,cd) \ , \tag{3.49}$$

where

$$t_{ab} = \sum_{\alpha\beta} t_{ab}^{\alpha\beta} c_\alpha^\Gamma c_\beta^\Gamma \quad \text{and} \quad \nu_{abcd;k} = \sum_{\alpha\beta} \nu_{abcd;k}^{\alpha\beta} c_\alpha^\Gamma c_\beta^\Gamma \,. \tag{3.50}$$

The coefficients $t_{ab}^{\alpha\beta}$ and $\nu_{abcd;k}^{\alpha\beta}$ are pure angular coefficients, as in the DHF method. However, the above expression does not reduce only to $I(a,a)$, $F^k(ab)$ and $G^k(ab)$ integrals and the general expressions of $I(a,b)$ and $R^k(ab,cd)$ are needed. The coefficients t_{ab} correspond to the generalized occupation number when $ab = aa$ and $t_{aa} = w_a$ is simply the coefficient to the $I(a,a)$ integral. The MCDHF radial equations have the same form as Eq. (2.73), considering that the direct and exchange potentials include contributions from both diagonal and off-diagonal $\langle \gamma_\alpha \pi J | \mathcal{H} | \gamma_\beta \pi J \rangle$ matrix elements.

The solutions of the MCDHF equations provide the radial components of the orbitals. This step is followed by a RCI calculation to determine the updated mixing coefficients, which are then re–injected in the MCDHF equations. The sequence of solving the MCDHF equations and solving the RCI eigenvalue problem is performed until self-consistency.

Often, more than one state is of interest, and therefore the definition of the energy functional (3.48) should be extended. In extreme cases, the calculations are performed targeting hundreds of states distributed over various total angular momenta and/or parities (see e.g., C_{II}). When n_L states are targeted simultaneously, the energy functional is

$$\mathcal{F}(\{\boldsymbol{c}\}, \{P\}, \{Q\}) = \sum_{\alpha,\beta=1}^{N_{\text{CSF}}} d_{\alpha\beta} H_{\alpha\beta} + \sum_{a,b} \delta_{\kappa_a,\kappa_b} \lambda_{ab} \mathcal{C}_{ab} \tag{3.51}$$

where $H_{\alpha\beta} = \langle \gamma_\alpha \pi_\alpha J_\alpha | \mathcal{H}_{\text{DC}} | \gamma_\beta \pi_\beta J_\beta \rangle$ in all generality and

$$d_{\alpha\beta} = \sum_{i=1}^{n_L} (2J_i + 1) c_\alpha^i c_\beta^i \Big/ \sum_{i=1}^{n_L} (2J_i + 1) \,. \tag{3.52}$$

Since the n_L ASFs are eigenvectors of the same Hamiltonian, they are orthonormal so that

$$(\boldsymbol{c}^i)^T \boldsymbol{c}^j = \delta_{ij} \tag{3.53}$$

in matrix notation. According to Grant [27, §7.3] the first term of the right-hand side of Eq. (3.51) can be interpreted as the weighted sum over the n_L eigenvalues

$$\sum_{\alpha,\beta=1}^{N_{\text{CSF}}} d_{\alpha\beta} H_{\alpha\beta} = \sum_{i=1}^{n_L} (2J_i + 1) E_i \Big/ \sum_{i=1}^{n_L} (2J_i + 1) \,, \tag{3.54}$$

remembering the expression of the energy E_i from Eq. (3.46). When only one state is targeted, Eq. (3.51) trivially reduces to Eq. (3.48). These two optimisation schemes are

defined as the *extended optimal level* (EOL) mode and the *optimal level* (OL), respectively [119]. Two additional modes exist: the *average level* (AL) mode that defines the weights $d_{\alpha\beta} = \delta_{\alpha\beta}(2J_\alpha + 1)/\sum_{r=1}^{N_{\rm CSF}}(2J_r + 1)$, which are independent of the mixing coefficients, i.e., each CSF is weighted according to its J value and the *extended average level* (EAL), in which the weights are chosen arbitrarily.

3.4.4 Angular algebra

The theory of angular algebra and tensor operators is the key for whoever wants to perform many-body atomic calculations. In Secs. 3.2, 3.3 and 3.4, the full derivations of the presented equations were intentionally left out due to their high complexity. The calculations of matrix elements are discussed in countless books and papers. In 1935, only a decade after the birth of quantum wave mechanics, Condon and Shortley wrote *"The Theory of Atomic Spectra"* [11], which stresses how fast the needed theoretical and mathematical developments occurred. Quickly scientists realized that the atomic theory needed efficient and uniform ways to deal with systems of increasing complexity. We should here mention the early work of Slater [10] and, even more importantly, the work of Racah [12, 13, 14, 15] and Fano [120]. Racah's pioneer work in the theory of tensor operators and angular algebra is now well established and known as the Racah or Racah-Fano algebra. Their theory simplified greatly the calculations of matrix elements, avoiding or reducing the need of long tables. It is straightforward for any non-specialist to check that angular integration requires complicated formulas by opening the books of Judd [19], Brink and Satchler [121] or Rudzikas [18], to cite a few. Still, the theory of angular algebra is far from being complete, as attests the more recent series of papers by Gaigalas and co-workers [122, 123, 124, 125, 126, 108, 127], which are of the highest importance in the fully relativistic context of the MCDHF method, as implemented in GRASP. The complexity of the angular algebra is often hidden in "simple" coefficients like $t_{ab}^{\alpha\beta}$ or $v_{abcd;k}^{\alpha\beta}$, which arise from the evaluation of the matrix elements of $\mathcal{H}_{\rm DC}$ (see e.g., Sec. 3.4.3). The aim of the present section is to give to the reader an insight in the theory of angular algebra, revealing the atomic theory in its full complexity.

3.4.4.1 Orthogonalities in one- and two-body operators matrix elements

The orthogonality between two one-electron orbitals has tremendous implications. Consider the well-known decomposition of the Hamiltonian in sums of one-electron operators and two-electron operators,

$$H = F + G = \sum_{i=1}^{N_e} f(i) + \frac{1}{2}\sum_{i\neq j=1}^{N_e} g(ij)\ . \tag{3.55}$$

Slater [10] and Condon and Shortley [11, §7[6]] showed that the matrix elements of the operators F and G between determinant wave functions (3.14) vanish if the two determinants differ by more than one relativistic orbital and more than two relativistic orbitals for F and G, respectively. This strong simplification is only due to the orthogonality between two relativistic orbitals (2.54)

$$\langle \phi_\alpha | \phi_\beta \rangle = \delta_{\alpha\beta} \ . \tag{3.56}$$

It also allows, for example, to reduce the diagonal matrix elements

$$\langle \Psi | F | \Psi \rangle = \langle \Psi | \sum_{i=1}^{N_e} f(i) | \Psi \rangle = \sum_\alpha \langle \phi_\alpha(1) | f(1) | \phi_\alpha(1) \rangle \tag{3.57}$$

to a sum over one-electron matrix elements of individual relativistic orbitals.

Similar simplifications occur for matrix elements of two-body operators

$$\begin{aligned} \langle \Psi | G | \Psi \rangle &= \langle \Psi | \sum_{i<j} g(ij) | \Psi \rangle \\ &= \frac{1}{2} \sum_{\alpha\beta} \Big(\langle \phi_\alpha(1) \phi_\beta(2) | g(12) | \phi_\alpha(1) \phi_\beta(2) \rangle \\ &\qquad - \langle \phi_\alpha(1) \phi_\beta(2) | g(12) | \phi_\beta(1) \phi_\alpha(2) \rangle \Big) \ . \end{aligned} \tag{3.58}$$

To measure the impact of the condition (3.56) on the evaluation of matrix elements between CSFs, we refer to the Appendix of Ref. [128] and to Ref. [129] that explicitly illustrate the effects of relaxing these orthogonality constraints on the Racah-Wigner-Fano algebra.

3.4.4.2 Clebsch-Gordan coefficients

In Sec. 3.2, we presented the coupling of angular momenta (3.16) without discussing its consequences. However, from basic considerations, e.g., the coupling of two angular momenta $\boldsymbol{J}_1 + \boldsymbol{J}_2 = \boldsymbol{J}$, important relations can be found. In the atomic physics context, $\boldsymbol{J}_1$ and $\boldsymbol{J}_2$ could be individual total angular momenta $\boldsymbol{J}_1 = \boldsymbol{j}_1$ and $\boldsymbol{J}_2 = \boldsymbol{j}_2$, individual spin $\boldsymbol{J}_1 = \boldsymbol{s}$ and orbital momenta $\boldsymbol{J}_2 = \boldsymbol{l}$ or even the total spin $\boldsymbol{J}_1 = \boldsymbol{S}$ and total orbital momentum $\boldsymbol{J}_2 = \boldsymbol{L}$. Going from the uncoupled basis $|j_1 m_1\rangle\,|j_2 m_2\rangle$ to the coupled basis $|j_1 j_2 j m_j\rangle$ defines the well-known Clebsch-Gordan coefficients or vector coupling (VC) coefficients. Their definition is given in all quantum mechanics textbooks (see e.g., [82, §6.10]).

The functions $|j_1 m_1\rangle$ and $|j_2 m_2\rangle$ are simultaneously eigenfunctions of $\boldsymbol{J}_i^2$ and J_{zi}, $i = 1, 2$. Their direct product is therefore eigenfunction of $\boldsymbol{J}_1^2$, $\boldsymbol{J}_2^2$, J_{z1} and J_{z2}. However,

since $\boldsymbol{J}^2$ does not commute with J_{1z} nor J_{2z}, the product function $|j_1 m_1\rangle\,|j_2 m_2\rangle$ is not an eigenfunction of $\boldsymbol{J}^2$, and one must seek for the common eigenfunctions of $\boldsymbol{J}^2$, J_z, $\boldsymbol{J}_1^2$ and $\boldsymbol{J}_2^2$, that are denoted $|j_1 j_2 j m_j\rangle$. Both bases of eigenfunctions, i.e., the 'product' basis $|j_1 m_1\rangle\,|j_2 m_2\rangle = |j_1 m_1 j_2 m_2\rangle$ and the 'coupled' basis $|j_1 j_2 j m_j\rangle$, form respectively a complete orthonormal set. The two are therefore related by a unitary transformation

$$|j_1 j_2 j m_j\rangle = \sum_{m_1 m_2} \langle j_1 m_1 j_2 m_2 | j m_j\rangle\,|j_1 m_1 j_2 m_2\rangle \tag{3.59}$$

where $\langle j_1 j_2 m_1 m_2 | j m_j\rangle$ are the Clebsch-Gordan coefficients. Their expression is given explicitly in e.g., [19, §1.5]. It follows directly from $J_z = J_{1z} + J_{2z}$ that $\langle j_1 m_1 j_2 m_2 | j m_j\rangle = 0$ if $m_1 + m_2 \neq m_j$. The Clebsch-Gordan coefficients are related to the Wigner $3j$-coefficients as [18, §6.1]

$$\langle j_1 m_1 j_2 m_2 | j\, -m_j\rangle = (-1)^{j_1 - j_2 - m_j}\sqrt{2j+1}\begin{pmatrix} j_1 & j_2 & j \\ m_1 & m_2 & m_j \end{pmatrix}. \tag{3.60}$$

The Wigner $3j$-coefficients have the advantage of an easier display of the symmetry relations of interchanging angular momenta. We also have that the following selection rules have to be fulfilled for the coefficients to be non-zero: $m_1 + m_2 + m_j = 0$ and $\delta(j_1, j_2, j)$, where $\delta(j_1, j_2, j)$ represents the triangular relation between the angular momenta j_1, j_2 and j. The Wigner $3j$-coefficients and the Clebsch-Gordan coefficients also satisfy important orthonormality conditions such as

$$\sum_{m_1 m_2} \begin{pmatrix} j_1 & j_2 & j \\ m_1 & m_2 & m_j \end{pmatrix}\begin{pmatrix} j_1 & j_2 & j' \\ m_1 & m_2 & m_{j'} \end{pmatrix} = (2j+1)^{-1}\delta_{jj'}\,, \tag{3.61}$$

which derives directly from the orthonormality conditions

$$\begin{aligned} \langle j_1 m_1 j_2 m_2 | j_1 m_1' j_2 m_2'\rangle &= \delta_{m_1 m_1'}\delta_{m_2 m_2'}\,, \\ \langle j_1 j_2 j m_j | j_1 j_2 j' m_{j'}\rangle &= \delta_{jj'}\delta_{m_j m_{j'}}\,. \end{aligned} \tag{3.62}$$

The Clebsch-Gordan coefficients rewritten in terms of $3j$-coefficients are the building blocks to describe the coupling of large numbers of angular momenta, as we will see in the next section.

3.4.4.3 $3nj$-coefficients

The coupling of more than two coefficients is more complex, as there are more than one coupling scheme available. The latter involves higher order coefficients, called $3nj$-coefficients. Let us consider the coupling of three angular momenta $\boldsymbol{J}_1$, $\boldsymbol{J}_2$ and $\boldsymbol{J}_3$. Straightforwardly,

we can build the product basis $|j_1 m_1\rangle\,|j_2 m_2\rangle\,|j_3 m_3\rangle = |j_1 m_1 j_2 m_2 j_3 m_3\rangle$ that is simultaneous eigenfunction of $\boldsymbol{J}_1^2,\ \boldsymbol{J}_2^2,\ \boldsymbol{J}_3^2,\ J_{z1},\ J_{z2}$ and J_{z3}. However, to build the total angular momentum

$$\boldsymbol{J} = \boldsymbol{J}_1 + \boldsymbol{J}_2 + \boldsymbol{J}_3 \tag{3.63}$$

we could chose between the following schemes

$$\boldsymbol{J} = \boldsymbol{J}_1 + \boldsymbol{J}_{23} \tag{3.64}$$

$$\boldsymbol{J} = \boldsymbol{J}_{12} + \boldsymbol{J}_3 \tag{3.65}$$

$$\boldsymbol{J} = \boldsymbol{J}_{13} + \boldsymbol{J}_2 \tag{3.66}$$

where $\boldsymbol{J}_{12},\ \boldsymbol{J}_{23}$ and $\boldsymbol{J}_{13}$ are intermediate couplings for which the angular coupling rules detailed in the previous section can be applied. A successive use of formula (3.59) gives

$$\begin{aligned}|(j_1 j_2) j_{12}, j_3, j m_j\rangle = \sum_{m_{12}, m_3, m_1, m_2} &\langle j_1 m_1 j_2 m_2 | j_1 j_2 j_{12} m_{12}\rangle\,\langle j_{12} m_{12} j_3 m_3 | j_{12} j_3 j m_j\rangle \\ &\times |j_1 m_1 j_2 m_2 j_3 m_3\rangle\end{aligned} \tag{3.67}$$

where $\langle j_1 m_1 j_2 m_2 | j_1 j_2 j_{12} m_{12}\rangle$ and $\langle j_{12} m_{12} j_3 m_3 | j_{12} j_3 j m_j\rangle$ are Clebsch-Gordan coefficients for coupling the angular momenta $\boldsymbol{J}_1$ and $\boldsymbol{J}_2$ to $\boldsymbol{J}_{12}$ and the angular momenta $\boldsymbol{J}_{12}$ and $\boldsymbol{J}_3$ to $\boldsymbol{J}$. However, one could equivalently build the state $|j_1, (j_2 j_3) j_{23}, j m_j\rangle$ using the same Eq. (3.67). The relation between the states in the two coupling schemes is given by

$$|j_1, (j_2 j_3) j_{23}, j m_j\rangle = \sum_{j'_{12}} \langle (j_1 j_2) j'_{12}, j_3, j m | j_1, (j_2 j_3) j_{23}, j m_j\rangle\,|(j_1 j_2) j'_{12}, j_3, j m_j\rangle \tag{3.68}$$

where the coefficients

$$\begin{aligned}\langle (j_1 j_2) j'_{12}, j_3, j m_j | j_1, (j_2 j_3) j_{23}, j m_j\rangle = &\sqrt{(2j'_{12}+1)(2j_{23}+1)}(-1)^{j_1+j_2+j_3+j} \\ &\times \begin{Bmatrix} j_3 & j & j'_{12} \\ j_1 & j_2 & j_{23}\end{Bmatrix}\end{aligned} \tag{3.69}$$

are expressed in terms of $6j$-coefficients [19, §3]. The latter are highly symmetric under exchanges of certain rows and or columns, as described by Judd [19, §3]. The most important feature is that they contain four triangular relations that can be made explicit by expressing the $6j$-coefficient in term of $3j$-coefficients. They are usually represented as

$$\begin{Bmatrix} & \circ & \\ \circ & & \circ\end{Bmatrix}\ \begin{Bmatrix} \circ & \circ & \circ \\ & & \end{Bmatrix}\ \begin{Bmatrix} & & \circ \\ \circ & \circ & \end{Bmatrix}\ \begin{Bmatrix} \circ & & \\ & \circ & \circ\end{Bmatrix}. \tag{3.70}$$

It then becomes obvious that the coupling of n angular momenta will require the knowledge of $3nj$-coefficients. The increasing complexity to find the appropriate formula led scientists to develop graphical approaches [130, 131, 132].

3.4.4.4 Irreducible tensor operators and the Wigner-Eckart theorem

The theory of irreducible tensor operators (ITOs) is mostly due to Racah and Fano [133]. A rigorous presentation of ITOs is usually made in the framework of group theory. This is far beyond the scope of this thesis, and we will rather use the original definition proposed by Racah in 1942 [13]: "*We may therefore define as 'irreducible tensor operator of the degree k' each operator $\mathbf{T}^{(k)}$ whose $2k+1$ components $T_q^{(k)}(q=-k,-k+1,\ldots,k-1,k)$ satisfy the same commutation rule with respect to $\boldsymbol{J}$ as the spherical-harmonics Y_k^q; [...] and is*

$$\begin{aligned}\left[(J_x \pm \mathrm{i}J_y), T_q^{(k)}\right] &= \sqrt{(k \mp q)(k \pm q + 1)}T_{q\pm 1}^{(k)} \ , \\ \left[J_z, T_q^{(k)}\right] &= qT_q^{(k)} \ .\end{aligned} \tag{3.71}$$

Using the formula (3.71), Racah showed that the dependence on q of the matrix elements of $T_q^{(k)}$ could be entirely represented by a single Wigner $3j$-coefficient. This is the well-known Wigner-Eckart (WE) theorem

$$\langle \alpha j m_j | T_q^{(k)} | \alpha' j' m_{j'} \rangle = (-1)^{j-m_j} \begin{pmatrix} j & k & j' \\ -m_j & q & m_{j'} \end{pmatrix} \langle \alpha j || T^{(k)} || \alpha' j' \rangle \ , \tag{3.72}$$

which connects the matrix elements that depend on q to $\langle \alpha j || T^{(k)} || \alpha' j' \rangle$, the *reduced matrix elements*[8], which are independent of q, m_j and $m_{j'}$. This has the advantage that the reduced matrix element should be computed only once to evaluate the corresponding matrix elements for all values of m_j, $m_{j'}$ and q.

The algebra of ITOs is rich and one of its main features is the tensorial product of two ITOs, $\mathbf{T}^{(k_1)}$ and $\mathbf{U}^{(k_2)}$, which is defined as

$$X_q^{(k)} = \left[\mathbf{T}^{(k_1)} \times \mathbf{U}^{(k_2)}\right]_q^{(k)} = \sum_{q_1 q_2} T_{q_1}^{(k_1)} U_{q_2}^{(k_2)} (-1)^{k_1 - k_2 + q} \sqrt{2k+1} \begin{pmatrix} k_1 & k_2 & k \\ q_1 & q_2 & -q \end{pmatrix} . \tag{3.73}$$

Well-known examples are the cases $k=0$, for which Eq. (3.73) reduces to

$$(-1)^k \sqrt{2k+1} \left[\mathbf{T}^{(k)} \times \mathbf{U}^{(k)}\right]_0^{(0)} = \sum_q (-1)^q T_q^{(k)} U_{-q}^{(k)} \tag{3.74}$$

where $Q = (\mathbf{T}^{(k)} \cdot \mathbf{U}^{(k)}) = \sum_q (-1)^q T_q^{(k)} U_{-q}^{(k)}$ is the scalar product of two ITOs, and $k = k_1 = k_2 = 1$ where $\left[\mathbf{T}^{(1)} \times \mathbf{U}^{(1)}\right]_q^{(1)}$ is the usual vector product of the two operators (up to a factor $\mathrm{i}/\sqrt{2}$).

[8] Several definitions of reduced matrix elements exist, that lead to different versions of the WE theorem. This can lead to confusing inconsistencies, as pointed out by Godefroid and Gaigalas [134].

The strength of Racah algebra is to enable the calculation of the matrix elements of the resulting ITO $X_q^{(k)}$. According to the WE theorem, we have

$$\langle \gamma j_1 j_2 j m_j | X_q^{(k)} | \gamma' j_1' j_2' j' m_{j'} \rangle = (-1)^{j-m_j} \begin{pmatrix} j & k & j' \\ -m_j & q & m_{j'} \end{pmatrix} \langle \gamma j_1 j_2 j || X^{(k)} || \gamma' j_1' j_2' j' \rangle \ , \tag{3.75}$$

where the subscript 1 and 2 refers to that the operators $\mathbf{T}^{(k_1)}$ and $\mathbf{U}^{(k_2)}$ act on two different parts of the system, e.g., the orbit and the spin, each on the electrons of a given pair (e.g., the Coulomb repulsion) or the nuclear and atomic parts (see Secs. 3.5.1 and 3.5.2). Then by uncoupling the basis $|\gamma j_1 j_2 j m_j\rangle$ using Eq. (3.59) and after some algebraic manipulations, one finds [19, §3.6]

$$\begin{aligned} \langle \gamma j_1 j_2 j || X^{(k)} || \gamma' j_1' j_2' j' \rangle = \sum_{\gamma''} & \langle \gamma j_1 || T^{(k_1)} || \gamma' j_1' \rangle \langle \gamma j_2 || U^{(k_2)} || \gamma' j_2' \rangle \\ & \times \sqrt{[j,k,j']} \begin{Bmatrix} j_1 & j_1' & k_1 \\ j_2 & j_2' & k_2 \\ j & j' & k \end{Bmatrix} \ , \end{aligned} \tag{3.76}$$

which introduces the $9j$-coefficient and where $[j,k,j'] = (2j+1)(2k+1)(2j'+1)$.

Thanks to the use of formula such as the ones presented above, the calculations of matrix elements elements can be performed in three steps, as summarized by Judd [19, §4.1]: "

1. *The contribution to the Hamiltonian is expressed in tensorial operator form.*
2. *The angular parts of the matrix elements are calculated by means of the formula [presented in this section].*
3. *The radial integrals are considered, and the theory is compared with experiment."*

3.4.4.5 Seniority and quasispin

In Sec. 3.2, we discussed how the CSFs are built using an approach based on the CFPs. However, one should be aware of the degree of complexity that the latter approach requires. As an example, the antisymmetrization of the wave function of atomic systems with multiple open shells is far from being trivial (see Ref. [120]). Another example is the non-uniqueness of the states labelled by the sole J and π quantum numbers. It is rather easy to understand that, the addition of two electrons in an open shell can, among other possibilities give the same LS term. Whether we consider the LSJ- or jj-coupling scheme, the coupling of two equivalent electrons will always lead to, at least, one ${}^1S_0$ or $(jj)_0$ term. Since it has all quantum numbers equal to 0 (either $L = S = J = 0$ or

simply $J = 0$), its coupling with the w already coupled equivalent electron leads to the exact same term. This does not happen in the s nor p shells. It is however a key concept for the description of d shells and, more dramatically, for the f-shells. Indeed, taking the example of the d^3 configuration, the $d^1\ ^2D$ term is coupled to the additional $d^2\ ^1S$, which leads to $d^3\ ^2D$. Therefore one needs an additional quantum number to differentiate the ^2D term originating from the d^1 and d^3 configurations. Racah introduced the concept of *seniority* to overcome this issue [14].

By rewriting Eq. (3.22) in terms of coefficients of fraction grandparentage (CFGP) as

$$|(nlj)^w \alpha J M_J)\rangle = \sum_{\bar{\alpha}\bar{J}\bar{J}'} |((nlj)^{w-2}\bar{\alpha}\bar{J}, (nlj)^2\bar{J}')\alpha J M_J\rangle\, ((lj)^{w-2}\bar{\alpha}\bar{J}|\}(lj)^w \alpha J)\ , \tag{3.77}$$

the seniority appeared naturally (see Rudzikas [18, §9.3]). Although the complete derivation of the seniority can be done in the framework of group theory [135], a more comprehensive and direct definition can be given based on the above example. The idea is to add a subscript ν to the ^{2S+1}L term as $^{2S+1}_{\ \nu}L$ where ν is the seniority number. The common way to define it is to seek for the occupation number of the shell of interest when a given term is generated for the first time. Going back to our example, the first ^2D arises from the d^1 configuration and will therefore be noted ^2_1D while the second ^2D arises from the d^3 configuration and will therefore be noted ^2_3D.

Starting from a group-theoretical interpretation, it is possible to show that the operator

$$Q = \frac{1}{2}\left(\frac{2j+1}{2} - \nu\right) \tag{3.78}$$

will have the same transformation and commutations as the spin angular momentum. That is why Q is usually called the *quasispin*. Its projection is given by

$$M_Q = \frac{1}{2}\left(w - \frac{2j+1}{2}\right) \tag{3.79}$$

and so the information about the number of equivalent electrons in a given shell is embedded in the definition of M_Q. The theory of quasispin therefore follows the general rules of angular algebra and, in particular, satisfies the WE theorem. In quasispin space, the latter is

$$\begin{aligned}\langle j^w\ \alpha Q J M_Q||A^{(k_q k)}_{m_q}||j^{w'}\ \alpha' Q' J' M_{Q'}\rangle =& (-1)^{Q-M_Q}\begin{pmatrix} Q & k_q & Q' \\ -M_Q & m_q & M_{Q'}\end{pmatrix} \\ &\times \langle j\ \alpha Q J|||A^{(k_q k)}|||j^{w'}\ \alpha' Q' J'\rangle\end{aligned} \tag{3.80}$$

where $A^{(k_q k)}_{m_q}$ is any tensorial operator of rank k_q and projection m_q in quasispin space, $\langle j^w\ \alpha Q J M_Q||A^{(k_q k)}_{m_q}||j^{w'}\ \alpha' Q' J' M_{Q'}\rangle$ is the reduced matrix elements of $A^{(k_q k)}_{m_q}$ with

respect to J and $\langle j^w\ \alpha QJ|||A^{(k_q k)}|||j^{w'}\ \alpha' Q' J'\rangle$ is the *completely* reduced matrix elements [125]. The concept of *completely* reduced matrix elements decreases tremendously the size of the required tables and the number of elements to be computed. The use of quasispin formalism is usually closely related to the second quantization formalism [135, 122, 125], in which the creation and annihilation operators in quasispin space are used. Although we do not provide explicit details, the secondly quantized theory and quasispin space are, in practice, employed in the framework of the GRASP package.

3.5 Atomic properties

The strength of the many-body methods is their ability to compute a large variety of atomic properties. In variational approaches, their determination relies on the prior knowledge of the atomic wave function, the definition of the corresponding operators and the angular algebra described in the previous section. In the context of the MCDHF method, their estimation does not modify the wave function itself, neither the mixing coefficients nor the radial orbitals. The expectation value of any operator $\mathcal{O}$ is therefore computed as

$$\langle \Psi | \mathcal{O} | \Psi \rangle \ . \tag{3.81}$$

Some properties connect two different atomic states and they are therefore computed as

$$\langle \Psi | \mathcal{O} | \Psi' \rangle \ . \tag{3.82}$$

In this section, we introduce the operators of the atomic properties relevant for discussing our contributions to the scientific literature (see Part II).

3.5.1 Hyperfine structures

The hyperfine structure results from the electronic interaction between the electromagnetic moments of the nucleus and the electrons. The interaction leads to a coupling of the total electronic angular momentum $\boldsymbol{J}$ and the nuclear spin $\boldsymbol{I}$ to a total angular momentum

$$\boldsymbol{F} = \boldsymbol{J} + \boldsymbol{I} \ , \tag{3.83}$$

and to energy splittings of the fine structure levels. According to the angular theory developed in Sec. 3.4.4, such angular coupling defines the coupled atomic-nuclear wave function $|\Gamma JIF\rangle$ using the Clebsh-Gordan coefficients (3.59) and products $|JM_J\rangle\,|IM_I\rangle$ of atomic and nuclear wave functions. The contribution of the hyperfine interaction to the Hamiltonian is represented by the following multipole expansion

$$\mathcal{H}_{\mathrm{HFS}} = \sum_k \mathbf{T}^{(k)} \cdot \mathbf{M}^{(k)} \ , \tag{3.84}$$

where $\mathbf{T}^{(k)}$ and $\mathbf{M}^{(k)}$ are ITOs acting on the atomic and nuclear wave functions, respectively [136]. The above expansion is usually truncated to its two lowest orders, which consist of the magnetic dipole interaction ($k = 1$) and the electric quadrupole interaction ($k = 2$). Commonly, only the diagonal contribution to the energy is considered, and the corresponding energy shift induced by the hyperfine interaction is simply given by Eq. (3.81) or, more specifically,

$$\langle \Gamma J I F M_F | \mathcal{H}_{\rm HFS} | \Gamma J I F M_F \rangle \ . \tag{3.85}$$

In extreme cases, however, the hyperfine interaction is too strong to be considered as a perturbation, which then requires to evaluate the off-diagonal elements

$$\langle \Gamma J I F M_F | \mathcal{H}_{\rm HFS} | \Gamma' J' I F M_F \rangle \tag{3.86}$$

that couples different electronic fine-structure levels, and to diagonalize the hyperfine interaction matrix [137, 138].

The diagonal contribution to the energy of the magnetic dipole interaction and electric quadrupole interaction are considered separately according to

$$E_{\rm HFS} = \langle \Gamma J I F M_F | \mathcal{H}_{\rm HFS} | \Gamma J I F M_F \rangle = E^{(1)}_{\rm HFS} + E^{(2)}_{\rm HFS} \ . \tag{3.87}$$

In practice, experimental and theoretical studies of hyperfine structures rather discuss the *hyperfine structure constants* A and B, which are related to the energy splittings as

$$\begin{aligned} E^{(1)}_{\rm HFS} &= \frac{1}{2} A C \ , \\ E^{(2)}_{\rm HFS} &= B \ \frac{\frac{3}{4} C(C+1) - J(J+1) I(I+1)}{2I(2I-1)J(2J-1)} \ , \end{aligned} \tag{3.88}$$

where $C = F(F+1)J(J+1)I(I+1)$ [17, §17.9]. Thanks to Racah algebra, the A and B constants can be evaluated using formula such as Eq. (3.76). They are

$$\begin{aligned} A =& \frac{\mu_I}{I} \frac{1}{\sqrt{J(2J+1)(J+2)}} \langle \Gamma \pi J || \mathbf{T}^{(1)} || \Gamma \pi J \rangle \ , \\ B =& 2Q \sqrt{\frac{J(2J-1)}{(J+1)(2J+1)(2J+3)}} \langle \Gamma \pi J || \mathbf{T}^{(2)} || \Gamma \pi J \rangle \ , \end{aligned} \tag{3.89}$$

were μ_I and Q are the nuclear magnetic dipole moment and nuclear quadrupole electric moment, respectively. The latter are related to the reduced matrix elements of the nuclear operators $\mathbf{M}^{(1)}$ and $\mathbf{M}^{(2)}$. The electronic ITOs are given by

$$\mathbf{T}^{(1)} = -\mathrm{i}\alpha \sum_{i=1}^{N_e} \left(\boldsymbol{\alpha}_i \cdot \mathbf{l}_i \ \mathbf{C}^{(1)}(i) \right) \frac{1}{r_i^2} \ , \tag{3.90}$$

$$\mathbf{T}^{(2)} = -\sum_{i=1}^{N_e} \mathbf{C}^{(2)}(i) \frac{1}{r_i^3} \ , \tag{3.91}$$

where $\mathbf{C}^{(1)}$ and $\mathbf{C}^{(2)}$ are the renormalized spherical harmonics of rank 1 and 2, respectively. Due to the spin-angular structure of the odd operator $\mathbf{T}^{(1)}$ [27, §6.2], its radial dependence scales as as $1/r_i^3$, which then agrees with its non-relativistic limit (see also Sec. 5.1.3). In our paper $\mathrm{B_{II}}$, we proposed the definition of purely electronic quantities A_{el} and B_{el} by removing the dependence of A and B on the nuclear parameters:

$$A_{\mathrm{el}} = A\left(\frac{I}{\mu_I}\right) \quad \text{and} \quad B_{\mathrm{el}} = B/Q \; . \tag{3.92}$$

3.5.2 Isotope shifts

Isotope shifts also combine nuclear and atomic physics. An isotope shift quantifies the observed frequency (or equivalently energy) shift of a given transition line between two isotopes [139]. Consider the transition k of frequency ν_k connecting an upper atomic level u to a lower atomic level l for two isotopes of mass A and A'. The associated isotope shift is defined as

$$\delta\nu_{\mathrm{IS},k}^{AA'} = \nu_k^A - \nu_k^{A'} \; . \tag{3.93}$$

The latter is usually decomposed into two contributions. One arises from the different masses of the isotopes, namely the *mass shift* (MS), while the other arises from the change in the nuclear charge density and is known as the *field shift* (FS) so that

$$\delta\nu_{\mathrm{IS},k}^{AA'} = \delta\nu_{\mathrm{MS},k}^{AA'} + \delta\nu_{\mathrm{FS},k}^{AA'} \; . \tag{3.94}$$

The mass shift,

$$\delta\nu_{\mathrm{MS},k}^{AA'} = \left(\frac{1}{M} - \frac{1}{M'}\right)\frac{\Delta K_{\mathrm{MS},k}}{h} \; , \tag{3.95}$$

is the product of a mass-factor $(M' - M)/MM'$, where M, M' are the respective masses of isotopes A, A', and $\Delta K_{\mathrm{MS},k} = K_{\mathrm{MS},u} - K_{\mathrm{MS},l}$ that is the difference between nuclear recoil corrected level parameters. The latter are defined in terms of expectation values of operators [140, 141] defining the *normal mass shift* (NMS) and *specific mass shift* (SMS), including the relativistic formulation of the nuclear recoil [142, 143, 144].

We rather focus on the FS, which becomes dominant for heavy systems due to the fast decrease of the mass factor with the nuclear mass. The differences in the nuclear charge densities, which result in the FS, can be evaluated by performing separate calculations for different sets of nuclear parameters [145]. However this approach is model-dependent and prevents us from having a high flexibility for the parametrization of the nuclear charge density (see Sec. 5.2). Therefore, a perturbative approach is often preferred, defining the FS as

$$\delta\nu_{\mathrm{FS},k}^{AA'} = -\frac{1}{h}\int \left[V_{\mathrm{nuc}}^{A}(\boldsymbol{r}) - V_{\mathrm{nuc}}^{A'}(\boldsymbol{r})\right]\Delta\rho_k^e(\boldsymbol{r})d\boldsymbol{r} \; , \tag{3.96}$$

where $V^A_{\rm nuc}(\boldsymbol{r})$ is the nuclear potential arising from the nuclear charge density associated to the nucleus with mass number A and $\Delta\rho^e_k(\boldsymbol{r}) = \rho^e_u(\boldsymbol{r}) - \rho^e_l(\boldsymbol{r})$ is the change in electronic density between u and l, the two atomic levels involved in the transition k. The definition of the many-electron electronic density is given in Refs [141, 146]. Extensive details are provided in the non-relativistic context of the MCHF method in Ref. [147] to demonstrate how the spherical symmetry of the density is restored when considering its average over magnetic components. Second quantization theory is used for the demonstration and so the details are left to the papers. Nevertheless, we present some its most fundamental features here.

The electronic density of an atomic state described by the ASF $|\Gamma\pi JM_J\rangle$[9],

$$\rho(\boldsymbol{r})^{JM_J} = \sum_{\alpha\beta} c_\alpha c_\beta \, \langle \gamma_\alpha \pi JM_J | \delta(\boldsymbol{r}) | \gamma_\beta \pi JM_J \rangle \ , \tag{3.97}$$

is the expectation value of the one-electron operator $\delta(\boldsymbol{r}) = \sum_{i=1}^{N_e} \delta(\boldsymbol{r} - \boldsymbol{r}_i)$. The spherical symmetry of the electron density, however, is only achieved by taking the average

$$\rho^e(\boldsymbol{r}) = \frac{1}{2J+1} \sum_{J=-M_J}^{M_J} \rho(\boldsymbol{r})^{JM_J} \ , \tag{3.98}$$

over the $2J+1$ magnetic components M_J.

An easier way of getting an electron density of spherical symmetry is to start from the radial operator $\delta(r) = \sum_{i=1}^{N_e} \delta(r - r_i)$ whose expectation value $\langle \delta(r) \rangle$ leads to

$$\rho^e(r) = \sum_{\alpha\beta} c_\alpha c_\beta \, \langle \gamma_\alpha \pi JM_J | \delta(r) | \gamma_\beta \pi JM_J \rangle \ , \tag{3.99}$$

from which the radial density function $D(r)$ can be defined

$$D(r) = r^2 \rho^e(r) = 4\pi r^2 \rho^e(\boldsymbol{r}) \ . \tag{3.100}$$

Note that this electron density is normalized to the number of electrons, so that

$$\int_0^\infty D(r) dr = \int_0^\infty r^2 \rho^e(r) dr = N_e \ . \tag{3.101}$$

This definition of the radial density does not require to average over the magnetic components to recover the spherical symmetry. The operator $\delta(r)$ being radial, i.e. a scalar invariant under rotations, its expectation value is obviously M_J-independent.

[9] Note that in the present context the magnetic quantum number is explicitly given in the characterization of the ASF.

Using the second quantization formalism, the radial operator becomes

$$\hat{\delta}(r) = -\sum_j \sqrt{2j+1} \sum_{n,n',l} \left(\mathbf{a}^\dagger_{n'lj}\ \mathbf{a}_{nlj}\right)^{(0)}_0 \left[P_{n'\kappa}(r)P_{n\kappa}(r) + Q_{n'\kappa}(r)Q_{n\kappa}(r)\right] \ , \tag{3.102}$$

where the irreducible tensor of rank zero $\left(\mathbf{a}^\dagger_{n'lj}\ \mathbf{a}_{nlj}\right)^{(0)}_0$ is built from the $(2j+1)$ components of the creation $a^\dagger_{n'ljm_j}$ and annihilation a_{nljm_j} operators [135]

$$\left(\mathbf{a}^\dagger_{n'lj}\ \mathbf{a}_{nlj}\right)^{(0)}_0 = -\frac{1}{\sqrt{2j+1}} \sum_{m_j} a^\dagger_{n'ljm_j} a_{nljm_j} \ , \tag{3.103}$$

The expectation value of (3.102) provides the spherical density function for any atomic state. The discussion on the electronic densities will be further extended when presenting the natural orbitals in Sec. 4.3.

When evaluating the FS (3.96), the electronic density of the level i is well approximated by an even-power polynomial expansion [148] when $r \to 0$

$$\rho^e_i(\boldsymbol{r}) = \frac{\rho^e_i(r)}{4\pi} \approx b(r) = \sum_{n=0} b_{i,n} r^{2n} \ , \tag{3.104}$$

which is often truncated to $n = 3$. Inserting the relation $(2n+2)(2n+3)r^{2n} = \nabla^2 r^{2n+2}$ in (3.96), integrating by parts, using $\nabla^2 V^A(\boldsymbol{r}) = -4\pi\rho^A(\boldsymbol{r})$, and defining the nuclear mean square radii as

$$\langle r^{2n}\rangle^A = \frac{1}{Z}\int r^{2n}\rho^A(\boldsymbol{r})d\boldsymbol{r} \ , \tag{3.105}$$

where $\rho^A(\boldsymbol{r})$ is the nuclear charge density of the isotope A, the FS becomes

$$\delta\nu^{AA'}_{\mathrm{FS},k} \approx \frac{1}{h}\sum_{n=0}^{3} \Delta F_{k,2n}\ \delta\langle r^{2n+2}\rangle^{A,A'} \ . \tag{3.106}$$

The evaluation of the FS therefore relates the field shift line parameters,

$$\Delta F_{k,2n} = F_{u,2n} - F_{l,2n} = \frac{4\pi Z \Delta b_{k,2n}}{(2n+2)(2n+3)} \ , \tag{3.107}$$

which are electronic quantities and the deviation in nuclear mean square radii,

$$\delta\langle r^{2n+2}\rangle^{A,A'} = \langle r^{2n+2}\rangle^A - \langle r^{2n+2}\rangle^{A'} = \frac{1}{Z}\int r^{2n+2}\left[\rho^A(\boldsymbol{r}) - \rho^{A'}(\boldsymbol{r})\right] d\boldsymbol{r} \ . \tag{3.108}$$

For decades, the approximation of a constant electronic density within the nuclear volume was assumed, limiting the expansion (3.104) to its lowest term (see e.g. [140]). The corresponding FS was therefore simply given by

$$\delta\nu_{\mathrm{FS},k}^{AA'} \approx \frac{\Delta F_{k,0}}{h}\,\delta\langle r^2\rangle^{AA'} \ , \tag{3.109}$$

that accounts for most of the FS. The parameter $\Delta F_{k,0}$ can therefore be computed as

$$\Delta F_{k,0} = \frac{Z}{3}\Delta|\Psi(0)|_k^2 \ , \tag{3.110}$$

where $\Delta|\Psi(0)|_k^2$ is the change of electronic density at the origin. The FS computed using Eq. (3.106) is known as the *reformulated field shift* (rFS) and offers more flexibility than the constant electronic density approximation, allowing to take into account nuclear deformations [149]. Additional details on the rFS are provided in Sec. (5.2) when commenting our papers $\mathrm{B_{III}}$ and B_{IV}.

Finally, it is interesting to mention that the approximation of the constant electronic density is often improved by considering $\lambda^{A,A'}$, the *nuclear parameter*, introduced by Seltzer [150] so that

$$\delta\nu_{\mathrm{FS},k}^{AA'} = \frac{\Delta F_{k,0}}{h}\lambda^{AA'} \ , \tag{3.111}$$

where

$$\lambda^{AA'} = \delta\langle r^2\rangle^{AA'} + \frac{C_2}{C_1}\delta\langle r^4\rangle^{AA'} + \frac{C_3}{C_1}\delta\langle r^6\rangle^{AA'} + \dots \ . \tag{3.112}$$

This parameter could therefore account for isotopic differences in the nuclear charge densities [140, 151] through the coefficients C_i, which are considered configuration-independent, only varying with the atomic number [139, §5.1].

3.5.3 Landé g factors

In this section, we discuss briefly the impact of an external magnetic field on the atomic spectra and give the definition of the Landé g factors. The splitting of the energy levels due to the presence of a homogeneous magnetic field was first observed by Zeeman [152]. For a given atomic level with angular momentum J, the $2J+1$ magnetic components are revealed and the degeneracy removed in the presence of a magnetic field; that is the so-called Zeeman effect. In order to reproduce these experimental observations theoretically, the interaction of the atom with an external magnetic field should be added to the Hamiltonian. In the fully relativistic theory, the replacement

$$\boldsymbol{p}_i \to \boldsymbol{p}_i + \boldsymbol{A} \tag{3.113}$$

should be made in the DC Hamiltonian (3.1). The potential vector $\boldsymbol{A}$ is related, as usual, to the magnetic field as

$$\boldsymbol{B} = \boldsymbol{\nabla} \times \boldsymbol{A} \tag{3.114}$$

where $\boldsymbol{A} = \frac{1}{2}\boldsymbol{B} \times \boldsymbol{r}$ for an homogeneous magnetic field. Inspired by, e.g., the hyperfine structure theory, one can write the magnetic Hamiltonian

$$\mathcal{H}_{\text{mag}} = c \sum_{i=1}^{N_e} \boldsymbol{\alpha}_i \cdot (\frac{1}{2}\boldsymbol{B} \times \boldsymbol{r}_i) \tag{3.115}$$

as the scalar product of two tensor operators or rank 1, explicitly

$$\mathcal{H}_{\text{mag}} = \frac{1}{2}\mathbf{N}^{(1)} \cdot \mathbf{B}^{(1)} \ . \tag{3.116}$$

The latter expression introduces the tensor $\mathbf{N}^{(1)}$ with components

$$N_q^{(1)} = \sum_{i=1}^{N_e} \mu_q^{(1)} = -\frac{1}{\alpha} \sum_{i=1}^{N} \mathrm{i}\sqrt{\frac{8\pi}{3}} r_i \boldsymbol{\alpha}_i \cdot \mathbf{Y}_{1q}^{(0)}(i) \ , \tag{3.117}$$

where $\mathbf{Y}_{1q}^{(0)}(i)$ are the vector spherical harmonics [153] for which the angular variables are omitted, leaving only the symbol i referring to each electron. The latter are defined as [20, §1.5]

$$\mathbf{Y}_{kq}^{(0)}(\theta, \phi) = \frac{1}{\sqrt{k(k+1)}} \boldsymbol{L} Y_k^q(\theta, \phi) \ . \tag{3.118}$$

The definition of the Landé g factors is, however, more natural when considering the magnetic interaction Hamiltonian as

$$\mathcal{H}'_{\text{mag}} = -\boldsymbol{\mu} \cdot \boldsymbol{B} \ , \tag{3.119}$$

where $\boldsymbol{\mu}$, the magnetic moment of the atom, is given by

$$\boldsymbol{\mu} = -\mu_B(\boldsymbol{L} + g_s \boldsymbol{S}) \ , \tag{3.120}$$

and μ_B and g_s are the Bohr magneton and the gyromagnetic factor of the electron, respectively. The expression of the diagonal matrix elements of $\mathcal{H}_{\text{mag}}$ in non-relativistic LS coupling,

$$\langle \Gamma \pi LSJM_J | \mathcal{H}'_{\text{mag}} | \Gamma \pi LSJM_J \rangle = B\mu_B M_J \ g_{LSJ} \ , \tag{3.121}$$

defines the Landé g factor as

$$g_{JLS} = 1 + (g_s - 1)\frac{J(J+1) + S(S+1) - L(L-1)}{2J(J+1)} \ . \tag{3.122}$$

The latter is solely dependent on angular quantities and can therefore be computed easily for any $^{2S+1}L_J$ term. In the case where the external magnetic field is weak, the magnetic interaction can be included perturbatively and hence neglecting off-diagonal elements between states with the same M_J value but different J. In that case, it can be shown that the relativistic LS mixing is taken into account by considering the following weighted sum

$$g_{\gamma J} = \sum_{LS} w(LS) g_{JLS} \, , \tag{3.123}$$

where $w(LS)$ is the weight of the corresponding LS term in the expansion [17, §17.3]. Going back to the fully relativistic case and considering that $\langle \Gamma \pi J M_J | \mathcal{H}_{\rm mag} | \Gamma \pi J M_J \rangle = \langle \Gamma \pi J M_J | \mathcal{H}'_{\rm mag} | \Gamma \pi J M_J \rangle$, one can define the magnetic dipole moment

$$\mu = -\mu_B g_{\gamma J} \boldsymbol{J} \tag{3.124}$$

in analogy with the non-relativistic expression. The $g_{\gamma J}$ is therefore the Landé g factor arising from the relativistic theory and is no longer a pure angular property. Its expression is given by

$$g_{\gamma J} = \frac{1}{2\mu_B} \frac{\langle \Gamma \pi J || \mathbf{N}^{(1)} || \Gamma \pi J \rangle}{\sqrt{J(J+1)(2J+1)}} \, . \tag{3.125}$$

Considerations from QED theory led to introduce a correction to $\mathbf{N}^{(1)}$ known as the Schwinger QED correction, as described and implemented by Andersson and Jönsson [154].

The difference in the radial dependency of the g factor operator between the relativistic expression ($\propto r$) and the non-relativistic expression (independent of r) can be explained by reorganizing Eq. (3.117) in a form that resembles the one given for the magnetic hyperfine interaction (3.90). This can be done by inserting the definition of the vector spherical harmonics (3.118) in (3.117). We find

$$\mathbf{N}^{(1)} = -\frac{\mathrm{i}}{\alpha} \sum_{i=1}^{N} r_i \boldsymbol{\alpha}_i \cdot \boldsymbol{l}_i \mathbf{C}^{(1)}(i) \, , \tag{3.126}$$

which then shows the same $\boldsymbol{\alpha}_i \cdot \boldsymbol{l}_i \mathbf{C}^{(1)}(i)$ spin-angular factor than the magnetic hyperfine operator $\mathbf{T}^{(1)}$ (3.90) and where the renormalized spherical harmonics are such that $\mathbf{C}^{(1)} = \sqrt{4\pi/3}\mathbf{Y}^{(1)}$. Similar spin-angular arguments that were applied to the hyperfine operator $\mathbf{T}^{(1)}$ to explain the r^{-3} radial dependence (see also Sec. 5.1.3) can then be used to explain the vanishing radial dependence of $\mathbf{N}^{(1)}$ in the non-relativistic limit. This relation between the non-relativistic limit of the two operators is rarely discussed, although it was already explicitly mentioned by Pyper *et al.* [155].

3.5.4 Transition rates and lifetimes

Electronic transitions play an important role in atomic physics. The jump of an electron from one electronic state to another, in relation with the absorption or emission of photons, reveals the atomic structure of the atom upon consideration. The spectrum of hydrogen lies partially in the optical region, showing only discrete frequencies, which were the starting point of the quantum theory. Each atomic system emits and absorbs light differently, hence it possesses its own, specific, spectrum which is therefore a signature of the presence of that element in the medium considered. The spectral analysis is used in e.g., the determination of atomic abundances in stellar objects or in plasma diagnostic. Due to significant importance of atomic transition parameters, countless compilations exist (see e.g., the NIST ASD database [9] and references therein) to support experimental and theoretical works.

The mathematics of transitions in the fully relativistic theory were presented by Grant [156]. However, we will rather follow the book by Grant, which precises and develops the already published results [27, §8.2] as well as the book by Johnson [20, §6]. Since transitions are of vast interest and almost essential to a thesis in atomic physics, extensive details were presented in prior theses (see e.g., Refs. [157, 158]). However, our present work focuses mostly on other properties, such as hyperfine structures or isotope shifts, and we will therefore only briefly present the mathematical details of the relativistic radiative transition theory, referring the reader to the above references for more information.

A radiative transition connects an atomic state $|\Gamma_\alpha \pi_\alpha J_\alpha\rangle$ with energy E_α to an other atomic state $|\Gamma_\beta \pi_\beta J_\beta\rangle$ with energy E_β so that for emission we have the transition

$$|\Gamma_\alpha \pi_\alpha J_\alpha\rangle \rightarrow |\Gamma_\beta \pi_\beta J_\beta\rangle + \hbar\omega \ , \tag{3.127}$$

where $\hbar\omega$ corresponds to the energy $\hbar\omega = E_\alpha - E_\beta$ of the photon. One should therefore look for $\mathcal{H}_{\text{int}}$, the Hamiltonian describing the electron-photon interaction. Two equivalent approaches are proposed by Grant [156, §8.1] and Johnson [20, §6], respectively. In the approach taken by Grant, which is in the framework of quantum field theory (see e.g., the book by Mandl and Shaw [159]), $\mathcal{H}_{\text{int}}$ is, using the notations from Sec. 2.3.2, defined as

$$\mathcal{H}_{\text{int}}^{\text{G}} = \frac{1}{c} \int j^\mu(x) a_\mu(x) d^4x \ , \tag{3.128}$$

where x is the four-component spacetime coordinate vector (2.34), j^μ is the electron current density and $a_\mu(x)$, the four-component electromagnetic potential (2.36). Explicitly, the latter is composed of a scalar potential and a vector potential

$$a^\mu(x) = (\Phi(\boldsymbol{r}, t), c\boldsymbol{A}(\boldsymbol{r}, t)) \ . \tag{3.129}$$

The electron current density takes the form

$$j^\mu = -\psi^\dagger(x)\gamma^0 c\gamma^\mu \psi(x) \ , \tag{3.130}$$

where

$$\gamma^0 = \beta, \qquad \gamma^i = \beta\alpha^i, \quad i = 1, 2, 3 \tag{3.131}$$

are the Dirac matrices and $\psi(x)$ is the Dirac field [27, §4].

Johnson [20, §6] on the other hand starts with the description of the electromagnetic field to progressively build the interaction Hamiltonian in the framework of "usual" quantum mechanics (as opposed to quantum field theory). The electric and magnetic fields defined as

$$\boldsymbol{E}(\boldsymbol{r}, t) = -\boldsymbol{\nabla}\Phi(\boldsymbol{r}, t) - \frac{\partial \boldsymbol{A}(\boldsymbol{r}, t)}{\partial t} \tag{3.132}$$

$$\boldsymbol{B}(\boldsymbol{r}, t) = \boldsymbol{\nabla} \times \boldsymbol{A}(\boldsymbol{r}, t) \tag{3.133}$$

satisfy Maxwell's equations

$$\nabla^2\Phi(\boldsymbol{r}, t) - \frac{1}{c^2}\frac{\partial^2\Phi(\boldsymbol{r}, t)}{dt^2} = -\tfrac{1}{\epsilon_0}\rho(\boldsymbol{r}, t) \tag{3.134}$$

$$\nabla^2\boldsymbol{A}(\boldsymbol{r}, t) - \frac{1}{c^2}\frac{\partial^2\boldsymbol{A}(\boldsymbol{r}, t)}{dt^2} = -\mu_0\boldsymbol{J}(\boldsymbol{r}, t) \tag{3.135}$$

where $\rho(\boldsymbol{r}, t)$ and $\boldsymbol{J}(\boldsymbol{r}, t)$ are the charge density and current density, respectively, and providing that the potentials satisfy the Lorentz condition

$$\boldsymbol{\nabla} \cdot \boldsymbol{A} + \frac{1}{c^2}\frac{\partial\Phi(\boldsymbol{r}, t)}{\partial t} = 0\,. \tag{3.136}$$

It is well-known that the electric and magnetic fields remain unchanged under the *gauge transformation*

$$\boldsymbol{A}(\boldsymbol{r}, t) \rightarrow \boldsymbol{A}'(\boldsymbol{r}, t) = \boldsymbol{A}(\boldsymbol{r}, t) + \boldsymbol{\nabla}\chi(\boldsymbol{r}, t) \tag{3.137}$$

$$\Phi(\boldsymbol{r}, t) \rightarrow \Phi'(\boldsymbol{r}, t) = \Phi(\boldsymbol{r}, t) - \frac{\partial\chi(\boldsymbol{r}, t)}{\partial t}\,. \tag{3.138}$$

According to the Lorentz condition (3.136), the gauge function $\chi(\boldsymbol{r}, t)$ satisfies the following wave equation

$$\nabla^2\chi(\boldsymbol{r}, t) - \frac{1}{c^2}\frac{\partial^2\chi(\boldsymbol{r}, t)}{\partial t^2} = 0\,. \tag{3.139}$$

Johnson suggests the use of the *transverse gauge*, which is defined by the condition

$$\boldsymbol{\nabla} \cdot \boldsymbol{A}(\boldsymbol{r}, t) = 0 \tag{3.140}$$

and leads to a vanishing scalar potential $\Phi(\boldsymbol{r}, t) = 0$. Within that choice of gauge, the one-electron interaction Hamiltonian introduced by Johnson reduces to

$$\mathcal{H}^{\mathrm{J}}_{\mathrm{int}} = c\boldsymbol{\alpha} \cdot \boldsymbol{A}(\boldsymbol{r}, t)\,, \tag{3.141}$$

that is easily generalized to N_e electrons as

$$\mathcal{H}_{\text{int}}^{\text{J}} = \sum_{j=1}^{N_e} \left(c\boldsymbol{\alpha}_j \cdot \boldsymbol{A}(\boldsymbol{r}, t) \right) \tag{3.142}$$

while its most general form is given by

$$\mathcal{H}_{\text{int}}^{\text{J}} = \sum_{j=1}^{N_e} \left(c\boldsymbol{\alpha}_j \cdot \boldsymbol{A}(\boldsymbol{r}, t) - \Phi(\boldsymbol{r}, t) I_{4\times 4} \right) \ . \tag{3.143}$$

The link between the two approaches can be made explicit starting from (3.128) and expressing the matrices $-\gamma^0\gamma^\mu$ as

$$(-I_{4\times 4}, -\boldsymbol{\alpha}) \ , \tag{3.144}$$

where $\boldsymbol{\alpha}$ are the matrices appearing in Dirac equation. We can then simply take the inner product of $\gamma^0\gamma^\mu$ with a_μ (3.129)

$$-\gamma^0\gamma^\mu a_\mu = -\Phi(\boldsymbol{r}, t) I_{4\times 4} + c\boldsymbol{\alpha} \cdot \boldsymbol{A}(\boldsymbol{r}, \boldsymbol{t}) \tag{3.145}$$

which resembles the one-electron interaction Hamiltonian of Johnson (3.143). Contrarily to the Hamiltonian of Johnson, that is consistent with the usual interpretation of Hamiltonians developed in this thesis, the Hamiltonian of Grant (3.128) is derived in the QED and Lagrangian field theory frameworks that lead to an equivalent representation of the Hamiltonian operator based on a Hamiltonian density (see e.g. Refs. [27, §4.1] and [34, App. E.3]). Introducing (3.145) in the expression of the matrix element

$$\begin{aligned} \langle \alpha | \mathcal{H}_{\text{int}}^{\text{G}} | \beta \rangle =& \frac{1}{c} \int \langle \alpha | j^\mu | \beta \rangle \, a_\mu d^4x \\ =& -\frac{1}{c} \int \psi_\beta^\dagger(x) \gamma^0 c\gamma^\mu \psi_\alpha(x) a_\mu d^4x \ , \end{aligned} \tag{3.146}$$

we have

$$\langle \alpha | \mathcal{H}_{\text{int}}^{\text{G}} | \beta \rangle = \int \psi_\alpha^\dagger(x) \left[-\Phi(x) I_{4\times 4} + c\boldsymbol{\alpha} \cdot \boldsymbol{A}(x) \right] \psi_\beta(x) d^4x \tag{3.147}$$

that is equivalent to the matrix element $\langle \alpha | \mathcal{H}_{\text{int}}^{\text{J}} | \beta \rangle$.[10]

Up to this point, our focus was mostly on the electromagnetic field and the interaction Hamiltonian. The evaluation of transition properties involved rigorous developments in

[10] Note the difference of a common minus sign compared to Grant [27, §8.2]. However, in the context of radiative transitions the minus sign is irrelevant, as the calculations only involve matrix elements squared. In Sec. 3.5.3, the sign of the magnetic interaction is however important to obtain the correct negative sign of the operator $\mathbf{N}^{(1)}$ (3.117). In order to stay consistent throughout this thesis, we therefore use $-\Phi(x) I_{4\times 4} + c\boldsymbol{\alpha} \cdot \boldsymbol{A}(x)$ as the interaction Hamiltonian in spite of the global sign factor difference with Grant.

the framework of time-dependent perturbation theory, second quantization and quantization of the electromagnetic field. To circumvent these mathematical difficulties and to avoid pages of long and complicated mathematical expressions, we only recall the most important features, accepting that not everything is completely defined being constrained to limit ourselves for the present document.

Both Refs. [27, §8.2] and [20, §6] start with the description of the one-electron atom, generalizing quickly to many-electrons in a second step. A key component of the reasoning is the multipole expansion of the electromagnetic field. Eq. (3.134) accepts plane wave solutions for the scalar potential, i.e.,

$$\Phi(x) = \Phi(\boldsymbol{r}, t) \sim \exp\left[-\mathrm{i}(\omega t - \boldsymbol{k}\cdot\boldsymbol{r})\right] \tag{3.148}$$

with the usual dispersion relation $\omega^2 = c^2|\boldsymbol{k}|^2$. Expanding $\exp\left[-\mathrm{i}\boldsymbol{k}\cdot\boldsymbol{r}\right]$ in terms of Bessel's functions and Legendre polynomials, one can find a complete set of multipole solutions

$$\Phi_{LM}(\boldsymbol{r};\omega) = i^L(2L+1)j_L(\omega r/c)C_{LM}(\theta,\phi) \tag{3.149}$$

where $j_L(\omega r/c)$ and $C_{LM}(\theta,\phi)$ are spherical Bessel and normalized spherical harmonics, respectively. Given that the particular solution of the scalar potential $\Phi(x) = \Phi_{LM}(\boldsymbol{r};\omega)\times \exp\left[-\mathrm{i}\omega t\right]$ verifies the Lorentz condition (3.136), three solutions for the vector potential exist:

$$c\boldsymbol{A}^l_{LM}(\boldsymbol{r};\omega) = \frac{-\mathrm{i}c}{\omega}\nabla\Phi_{LM}(\boldsymbol{r};\omega) \tag{3.150}$$

$$c\boldsymbol{A}^m_{LM}(\boldsymbol{r};\omega) = \frac{\boldsymbol{L}}{\sqrt{L(L+1)}}\Phi_{LM}(\boldsymbol{r};\omega) \tag{3.151}$$

$$c\boldsymbol{A}^e_{LM}(\boldsymbol{r};\omega) = \frac{c\boldsymbol{\nabla}\times\boldsymbol{L}}{\omega\sqrt{L(L+1)}}\Phi_{LM}(\boldsymbol{r};\omega)\ . \tag{3.152}$$

They correspond to the *longitudinal, magnetic* and *electric* types. Note that in the transverse gauge the longitudinal component of the vector potential vanishes. The choice of the gauge function $\chi(\boldsymbol{r},t) = G_L\Phi_{LM}(\boldsymbol{r};\omega)\exp\left[-\mathrm{i}\omega t\right]$ where G_L is the gauge parameter modifies the potentials as

$$\begin{aligned}\Phi_{LM}(\boldsymbol{r};\omega) &\to \left(1-\mathrm{i}\frac{\omega}{c}G_L\right)\Phi_{LM}(\boldsymbol{r};\omega)\\ \boldsymbol{A}^e_{LM}(\boldsymbol{r};\omega) &\to \boldsymbol{A}^e_{LM}(\boldsymbol{r};\omega) + G_L\boldsymbol{A}^l_{LM}(\boldsymbol{r};\omega)\ ,\end{aligned} \tag{3.153}$$

while $\boldsymbol{A}^m_{LM}(\boldsymbol{r};\omega)$ is left unchanged. From these expressions, it appears that setting $G_L = 0$ suppresses the longitudinal components of $\boldsymbol{A}^e_{LM}(\boldsymbol{r};\omega)$, which corresponds to the transverse gauge, also known as the *Coulomb gauge*. The choice $G_L = \sqrt{L(L+1)}$ is known as the *Babushkin gauge*.

Going to second quantization and defining annihilation and creation operators for the electrons and the exchanged photon, the interaction Hamiltonian can be decomposed with emission and absorption contributions as

$$\mathcal{H}_{\rm int} = \sum_{LM} \left\{ [\mathcal{H}^e_{LM}]_{em} + [\mathcal{H}^m_{LM}]_{em} + [\mathcal{H}^e_{LM}]_{abs} + [\mathcal{H}^m_{LM}]_{abs} \right\} \ , \tag{3.154}$$

where e.g.,

$$[\mathcal{H}^{e,m}_{LM}]_{em} = \sum_{\alpha\beta} a^\dagger_\alpha a_\beta c^\dagger_{LM}(\omega) [\mathcal{M}^{e,m}_{LM}(t)]^*_{\alpha\beta} \tag{3.155}$$

with $a^\dagger_\alpha a_\beta$ being the creation and annihilation operators of the active electron, $c^\dagger_{LM}(\omega)$ the creation operator of a photon of energy w (i.e., hence the emission process). $[\mathcal{M}^{e,m}_{LM}(t)]$ is proportional to the *transition amplitude*[11]

$$\langle\alpha|\mathcal{O}^{e,m}_{LM}|\beta\rangle = \langle\alpha| - \Phi^{e,m}_{LM}(\boldsymbol{r}; w) I_{4\times 4} + c\boldsymbol{\alpha}\cdot\boldsymbol{A}^{e,m}_{LM}(\boldsymbol{r};\omega)|\beta\rangle \tag{3.156}$$

where $|\alpha\rangle$ and $|\beta\rangle$ are one-electron wave functions with associated quantum numbers $n_\alpha, \kappa_\alpha, \ldots$. This allows the definition of e.g., the *transition rate* for spontaneous emission of photons by summing over the degeneracy of the initial state $|\alpha\rangle$ and averaging over the final state $|\beta\rangle$ as

$$A^{(L)}_{\alpha\beta} = \frac{2\omega}{c} \frac{1}{(2L+1)(2j_\beta+1)} |\, \langle\alpha||\mathbf{o}^{(L)}||\beta\rangle \,|^2 \tag{3.157}$$

where $\langle\alpha||\mathbf{o}^{(L)}||\beta\rangle$ is defined by using the WE theorem (3.72)

$$\langle\alpha|\mathcal{O}_{LM}|\beta\rangle = (-1)^{j_\alpha - m_\alpha} \begin{pmatrix} j_\alpha & L & j_\beta \\ -m_\alpha & M & m_\beta \end{pmatrix} \langle\alpha||\mathbf{o}^{(L)}||\beta\rangle \ . \tag{3.158}$$

The one-electron reduced matrix elements $\langle\alpha||\mathbf{o}^{(L)}||\beta\rangle$ can be further decomposed into angular and radial contributions. Ultimately, it involves radial integrals with the Bessel functions arising from the multipole expansion of the electromagnetic potential and the large and small radial components of the one-electron orbitals (see Ref. [27, §8.2.1]). The generalization of that result to many-electron systems is derived by Grant using the expansion of the ASF over the CSF basis and the decomposition of the CSFs in one-electron Dirac orbitals using the CFP approach (see Secs. 3.2 and 3.4.4).

[11] As pointed out in the footnote 10, the expression of the transition amplitude (3.156) differs by a minus sign with Grant [27, §8.2] (see Eq. (8.2.6)). The expression of the transition rates (3.157) shows that this global sign factor is irrelevant, as only the square of the transition amplitude is involved.

Transition properties in practice

The mathematical expressions that we summarized in the previous section are needed if one wants to compute transition properties as it was done in A$_{\rm IV}$. However, in the framework of GRASP, theoretical considerations are often hidden due to their complexity and that they have been known for decades. Computations are more result-oriented, trying to provide important transition parameters. Among them, we have the transition rates between levels a and b

$$A^{\lambda(L)}_{a\to b} = \frac{2w}{c}\frac{|\,\langle\Gamma_a\pi_a J_a||\tilde{\mathbf{O}}^{(L)}||\Gamma_b\pi_b J_b\rangle\,|}{(2L+1)(2J_a+1)} \tag{3.159}$$

which is direct generalization of Eq. (3.157) where the tilde simply indicate that $\tilde{\mathbf{O}}^{(L)}$ is the many-electron operator while $\mathbf{o}^{(L)}$ is the corresponding one-electron operator. In that notation, λ indicates the type of transition, i.e., $\lambda = 1$ corresponds to an electric (E) transition while $\lambda = 0$ corresponds to a magnetic (M) transition, and L indicates the polarity $L = 1, 2, 3, \ldots$. The most important ones are the *electric dipole* (E1), *magnetic dipole* (M1) and *electric quadrupole* (E2) transitions. The former are dominant and are usually referred to as *allowed transitions* in connection with the electric dipole approximation (see e.g., [20, §6.2.6] or [17, §14] in the non-relativistic context). Transitions are often accompanied by a set of *selection rules* that connects two atomic states, which can be understood from the Wigner $3j$ symbol arising in the evaluation of the reduced matrix elements. The parity of electric and magnetic transitions is $\Pi^e = (-1)^L$ and $\Pi^m = (-1)^{(L+1)}$, respectively. The states involved in the transition should therefore satisfy $\pi_a\pi_b = \Pi^{e,m}$. The other rule is the triangular relation $\delta(J_a, L, J_b)$. Transitions $J_a = 0 \to J_b = 0$ are then strictly forbidden.

Transition rates are key properties to estimate the lifetime of excited states. Since transition rates provide the number of decays per second, if one consider all possible decay channels from an excited level a, its lifetime is given by

$$\tau_a = \frac{1}{\sum_{b,\lambda L} A^{\lambda(L)}_{a\to b}} \tag{3.160}$$

where the sum runs over all allowed lower levels b and all electric and magnetic multipole transitions.

Non-relativistic limit

For historical reasons, the non-relativistic limit of the transition rates is still often discussed in recent publications. In particular the choice of the gauge can be more easily interpreted. This is one of the foci of A$_{\rm II}$. In the non-relativistic limit, the Coulomb gauge reduces to

the *velocity form* while the Babushkin gauge corresponds to the *length form*. In these forms, the electric dipole reduced matrix elements are

$$\langle \Gamma_a \pi_a J_a || \frac{1}{E_b - E_a} \sum_{i=1}^{N_e} \boldsymbol{\nabla}_i^{(1)} || \Gamma_b \pi_b J_b \rangle \tag{3.161}$$

and

$$\langle \Gamma_a \pi_a J_a || \sum_{i=1}^{N_e} r_i \mathbf{C}^{(1)}(i) || \Gamma_b \pi_b J_b \rangle \ , \tag{3.162}$$

respectively. Due to their different form, they put emphasis onto different spatial localization of the wave function, i.e., the velocity form probes the inner part of the wave function and the length form the outer part. For exact wave functions, it can be shown that the reduced matrix elements in the length and velocity forms are equal [17, §14.14]. However, in real calculations, which always are approximative, the matrix elements depend on the gauge. Also in relativistic calculations the transition matrix elements depend on the gauge, and a small difference is an indication of that the wave functions are accurate. Moreover, the parameter

$$dT = \frac{|A^B - A^C|}{\max(A^B, A^C)} \tag{3.163}$$

has been statistically related to estimated uncerainty of the transition rate for allowed E1 transitions [160, 161].

3.6 Computational aspects

3.6.1 The GRASP computer packages

The methods presented in Sec. 3.4 require numerical procedures whether it is to solve the MCDHF equations or the secular equation in the RCI calculations. Throughout our thesis, we mostly (almost exclusively) used the *General Relativistic Atomic Structure Package* (GRASP) computer programs [107, 162, 30]. The latter are developed within the Computational Atomic Structure (CompAS) group, which is a large international collaboration that aims to provide tools for large-scale atomic structure calculations [163, 164]. The source codes are freely available online, enabling the implementation of additional tools by whoever is interested in performing atomic calculations. The collective efforts led to numerous "side-programs" to the main GRASP routines. Whether they improve the angular integration and our understanding of the optimal coupling scheme [108, 127] or allow us to compute atomic properties such as hyperfine structures [165] with the Zeeman splitting in presence of an external magnetic field [166], isotope shifts [167] including the

relativistic corrections to the recoil operator [140] and a reformulation of the field shift to account for nuclear deformations [141], transition probabilities and Auger parameters for open shell systems with an electron in the continuum [168], radial densities and natural orbitals [146] (see A$_{\text{III}}$) or polarizabilities of nominal one-electron systems [169] (see A$_{\text{V}}$), they are all written to be compatible with the GRASP files system.

It is then obvious that the GRASP package is in constant evolution, as also attests the recent investigations by Froese Fischer and Senchuk [25]. In reality, the difficulty to understand the different programs, beside the understanding of the implemented algorithms, is due to the large number of routines, subroutines, libraries or more simply the number of lines of code. Navigating among GRASP subroutines is indeed a tedious but necessary task for whoever wants to contribute to their developments. This is even more crucial when improving already existing routines. The latest release of the package, GRASP2018, was written in Fortran 95 starting from GRASP2K, written in Fortran 77. Such a substantial change was necessary to maintain the codes accessible with the newest generation of clusters. Moreover, it makes it easier for the younger generation of scientists to get acquainted with the codes' structure. Finally, one should be aware that the GRASP computer package only uses the Fortran programming language with its original features. In the future, GRASP developers might take advantage of the full efficiency of modern computing languages, as it is already in preparation with the recent *object oriented* tests [25] or the recent release of the Jena Atomic Calculator (JAC), implemented in Julia [170].

In the following, we will detail some of GRASP's special features and main numerical methods. We will also provide the reader with the basic workflow of the programs along with their names so that the details of the calculations given in the following will be understood.

The grid

The determination of the $P_{n\kappa}(r)$ and $Q_{n\kappa}(r)$ radial components of the one-electron orbitals (see Eq. (2.54)) is performed by solving numerically the MCDHF equations (see Sec. 3.4.3) based on the SCF procedure. The most basic constituent of the numerical method is therefore to decide on a representation of the radial orbitals. In GRASP, the latter are described on a radial grid spanning the range $[0, +\infty[$. This is however not the only possibility and we will discuss later in Chapter 4 other options.

The grid must then be chosen so that it allows an accurate description of the radial orbitals. Since we already know that their behaviour for $r \to \infty$ is a decreasing exponential, emphasis is given on the inner part of the radial orbitals by defining the following exponential grid,

$$Zr = c_0(\exp[t] - 1) \qquad t_i = ih, \quad i = 0, \ldots, N \,, \tag{3.164}$$

where $c_0 = 2.6 \times 10^{-6}$ and the exponential step $h = 0.05$ by default. Note that the

grid points $\{t_i\}$ are the same for all elements and, although the first non-zero grid point is always $t_1 = 0.05$, the mapping to $r_1 = \frac{c_0}{Z}(\exp[0.05] - 1)$ suggests that the latter is closer to the origin for heavier elements. The use of an exponential grid therefore leads to a higher density of points closer to the origin than toward infinity, which is what is needed for the description of radial orbitals. In their recent paper, Froese Fischer and Senchuk showed that the use of a completely exponential grid such that

$$Zr = c_0 \exp[t] \tag{3.165}$$

could be an alternative to today's grid [25].

The nucleus

The description of the nucleus is also a key feature in atomic structure calculations, especially when considering heavy systems. For light elements, the point-like approximation of the nucleus might be adequate, depending on the targeted atomic properties. Indeed, atomic properties that arise from the interaction between the electron cloud and the nucleus require additional care in the mathematical description of the nucleus. Presently, in GRASP, the common use is to define the nuclear charge distribution as a Fermi distribution

$$\rho^A = \frac{\rho_0^A}{1 + \exp\left(\frac{r-c}{a}\right)} , \tag{3.166}$$

in which ρ_0^A is a normalization constant so that

$$Z = \int_0^\infty 4\pi r^2 \rho^A dr . \tag{3.167}$$

c is the "half-density radius" and a, the diffuseness, is related to the "skin thickness" t by $t/a = 4 \ln 3$ [171]. By default, the skin thickness is set up to $t = 2.3$ fm, while c depends on the choice of the nuclear mean square radius. Recently, the possibility to read a nuclear charge distribution on file was added, allowing a more realistic description of the nucleus. The nuclear charge distribution is then used to e.g. build the nuclear potential V_{nuc}.

Numerical methods

Two main numerical methods are employed in GRASP: finite difference methods [115] and the Davidson diagonalization algorithm [172]. The former are used to solve the radial integro-differential MCDHF equations while the latter is employed to diagonalize the RCI matrix. The choice of a particular method among finite difference methods depends on the number of neighbouring points used to approximate derivatives and integrals, which will

influence the final accuracy as the results (see Ref. [25]). The Davidson algorithm is crucial to speed-up the RCI calculations for which the number of CSFs can reach millions per symmetry (J, π). One of its main advantages is the possibility to compute only targeted eigenvalues, preventing to diagonalize the full matrix.

3.6.2 Computational strategies

The GRASP computer package provides the programs to perform atomic structure calculations on any atomic system from neutral atoms to highly ionized systems, including negative ions. However, even though the chain of programs does not vary much between two calculations, the computational strategies can be drastically different upon the system and property considered. We hereby define useful concepts to discuss computational strategies and ease the understanding of our scientific papers.

Programs workflow

The steps of a calculation are given in GRASP's manual (see e.g., Fig. 3.1). They are summarized as follows, with the name of the corresponding program in parenthesis

1. Generate the nuclear data set (atomic number, mass number, etc.). (RNUCLEUS)
2. Generate the list of CSFs for the ASF expansion. (RCSFGENERATE)
3. Perform the angular integration. (RANGULAR)
4. Generate initial estimates for all radial orbitals. (RWFNESTIMATE)
5. Solve the MCDHF equations in the SCF procedure to obtain radial orbitals and energy parameters. (RMCDHF)
6. Perform RCI calculations to include higher-order effects. (RCI)

These form the simplest succession of actions that could be done. However, as we will see, small changes might occur to use more subtle computational strategies. The more computationally demanding programs such as RANGULAR, RMCDHF and RCI are also available in parallelized version using OpenMPI.

Electron correlation

The ASFs (3.41) are expanded over a set of basis functions, the CSFs. Starting from the targeted configurations, the CSFs are generated by allowing electron substitutions from the spectroscopic occupied orbitals to a set of *correlation orbitals*. The rules to generate the CSFs through electron substitutions are established in a systematic fashion. The difficulty is that the quality of the CSF space otherwise known as the *active space* depends on (i) the system of interest, (ii) the atomic property of interest and (iii) the size of the calculations. The CSF expansion with $N_{\mathrm{CSF}} > 1$ was introduced in section 3.4 to go beyond the DHF approximation and hence include some correlation in the electrons' movement. The latter is composed of two contributions arising from different origins called the *static correlation* and the *dynamic correlation* [28, 173].

Static correlation otherwise known as *nondynamical correlation* is mainly due to the near degeneracies of the (D)HF orbitals, i.e., it is highly dependent on Z, N_e and the symmetry, and is therefore related to a long-range rearrangement of the electron charge distribution. A relatively small subset of configurations is believed to be enough to capture most of the static correlation. This set forms what is known as the *multireference* (MR) space. The choice of the MR is therefore one of the very first steps in any of our calculations, as it is general acknowledged that the MR generates the CSFs with the largest expansion coefficients. However, the size of the MR also has a dramatic influence on the size of the final calculations as the electron substitutions are allowed not only from the targeted configuration (or *singlereference* (SR)) but from the whole group of configurations belonging to the MR. One must then seek for a balance between the numerical accuracy and the computational resources' limits. The choice of the MR is guided by the useful concept of *Layzer complexes*, which arise naturally when analyzing the Hamiltonian eigenvalue with a perturbative expansion based on Z [174]. In the non-relativistic theory, complexes define sets of configurations with the same set of principal numbers and same parity. Indeed, according to the hydrogenic model, the energy of a given configuration is simply $\sum_n = -Z^2/2n^2$, where the sum runs over the principal quantum numbers of all occupied orbitals. In that approximation, the configurations $1s^2 2s^2$ and $1s^2 2p^2$ possess the same total energy; they belong to the complex denoted by $\{1^2 2^2\}$. Layzer later extended his own work to the relativistic theory [175], ultimately demonstrating that the configuration interaction between configurations within a complex is the dominant contribution to the DHF energies. Because Grasp only allows us to generate CSFs following non-relativistic notations, we will often seek the complex that contains the targeted non-relativistic configuration (3.20), which can be written in its most general form as $\{n_1^{\tilde{w}_1} n_2^{\tilde{w}_2} \dots n_{m'}^{\tilde{w}_{m'}}\}$.

The dynamical correlation is related to the 'cusp condition', which derives from the singularities arising from the electron-electron repulsion potential $1/r_{ij}$, and is therefore con-

sidered as a short-range effect [176]. The singularities $r_{ij} = 0$ are not isolated points, but involve hypersurfaces in the entire space. These singularities occur at points that have the highest probability to find a pair of electrons. The concept of pair-correlation is therefore decisive.

It is interesting for the understanding of the static and dynamic correlations in terms of types of electron substitutions or generation of excited configurations, to take an approach based on Z-perturbation theory [175]. As we already discussed, it allows the definition of the Layzer complexes. It is also an efficient tool to categorize correlation effects with respect to the type of electron substitutions. According to Froese Fischer [115, §3.1], the content of the first-order wave function in non-relativistic Z-perturbation theory can be separated into CSFs that differ by one or two electrons from those belonging to the zero-order wave function, i.e., the linear combination of CSFs belonging to the Layzer complex. The CSFs generated by a single electron substitution are of three types (i) the coupling scheme stays the same but one principal quantum number has changed, (ii) one principal quantum number and the coupling scheme have changed and (iii) one angular quantum number has changed, which is then accompanied by a recoupling of the remaining electrons. They are refer to as *radial correlation*, *spin polarization* and *orbital polarization*.

The CSFs generated by double electron substitutions can also be classified [8, §4.2]. Considering the sets of occupied orbitals $\{a, b, c, \cdots\}$ and correlation orbitals $\{x, x', \cdots\}$, then the double substitutions $ab \rightarrow xx'$ are categorized as representing *valence-valence (VV) correlation*, *core-valence (CV) correlation* and *core-core (CC) correlation* if a and b are both outer electrons, a is an outer electron and b is a core electron or a and b are core electrons, respectively. This classification of correlation effects based on the type of electron substitutions was widely used in our manuscripts and articles. This classification relies greatly on the definition of an electronic core. For light elements, the electronic core is identified by looking at the noble gas elements e.g., the $1s^2 2s^2 2p^6 3s$ configuration of sodium is split into the $1s^2 2s^2 2p^6$ neon-like core and the valence $3s$ electron. The orbitals $\{1s,\ 2s,\ 2p\}$ are therefore identified as core orbitals. For heavier systems, however, the core might not be unambiguously defined and extra care must be taken. One might then classify orbitals in three subsets, i.e., inactive core, active core and valence orbitals [28]. A recent example is the study of the Ce^{2+} energies, which led to the identification of the $4d^{10}$ filled subshell as the active core, leaving e.g., $4s^2 4p^6$ as part of the inactive core [107].

The orbital basis set

In the MCDHF method the spectroscopic and correlation orbitals are optimized through the variational process i.e., there is one set of integro-differential equations for each orbital that is occupied in (at least) one CSF. Commonly the spectroscopic orbitals are optimized together and then frozen for the rest of the calculations. The correlation orbitals

are optimized *layer-by-layer* (LBL), where a *correlation layer* contains at most one correlation orbital per symmetry.[12] The *active set* (AS) of orbitals is defined as the set of orbitals, which are either correlation orbitals or spectroscopic orbitals, that are involved in the generation of the active space by electron substitutions. Orbitals belonging to the inactive core are therefore excluded from the AS. Spectroscopic and correlation orbitals are somewhat optimized differently since the former have a specified number of nodes (expected from the hydrogenic one-electron orbitals) while the correlation orbitals are free of this requirement. Correlation orbitals are therefore different, in essence, from spectroscopic orbitals: they are spatially localized depending on the structure of the energetically important CSFs (or equivalently electron substitutions). Consider, for example, double substitutions that are allowed only from the inner core shell, $1s^2$, the corresponding correlation orbitals are localized close to the nucleus. An illustration of how the orbital localization depends on the structure of the substitutions is explicitly given in Ref. [177], in which the authors performed three different MCHF calculations for the ground state of Be. Each calculation includes one correlation effect, i.e., CC, CV or VV correlation, corresponding in the case of the $1s^2 2s^2$ ground configuration of Be to the substitutions $1s^2 \rightarrow xx'$, $1s2s \rightarrow xx'$ and $2s^2 \rightarrow xx'$, respectively. Fig. 1 in the same paper showed how the correlation orbitals are spatially localized depending on type of substitutions that is included. The observed differences motivated the development of the *partitioned correlation function interaction* (PCFI) approach, demonstrating the benefits of describing each correlation effect with its own, well-suited, orbital basis (more discussions on the orbital basis are presented in Chap. 4).

Systematic calculations

The difficulty with large-scale atomic structure calculations is that each system considered possesses its own specificities. Since there is no single recipe we must instead explore a number of correlation models and their relative importance. The calculations are performed in a systematic fashioned so that the we can expect the calculated properties to converge. In their work, Bieroń *et al.* [178] define four "dimensions" that are systematically varied to observe convergence of the targeted atomic properties. They are (1) the substitution multiplicity, i.e., single (S), double (D), triple (T), quadruple (Q), . . . , (2) the number of opened core orbitals, (3) the number of correlation layers and (4) the maximal angular quantum number. A careful, systematic investigation of the dependence of computed atomic properties in each of these dimensions allows to limit the size of the calculations. Extending the calculations in one (or more) of these dimensions can also be used to estimate computational uncertainties, as they probe the sensitivity of the calculated property to the computational model.

[12] Note that the layer-by-layer optimization method is forced due to numerical instabilities arising when all correlation orbitals are optimized together (see A_I).

Part II

Presentation of scientific manuscripts and articles

Chapter 4

Group A: On the orbital basis

In this Chapter, we present the main results of the papers A_I–A_V together, in which we focus on the important choice of the orbital basis in atomic structure calculations. Papers A_I [179] and A_{III} are related to the natural orbitals and their connection with the variational MCDHF orbitals. A_{II} [180] shows the importance of the orbitals in MCDHF calculations and how their localization influence calculated quantities such as transition rates. Papers A_{IV} [181] and A_V [169] present the results of our study of static dipole and quadrupole polarizabilities using a finite basis method. These last two papers are somewhat separate from the others, but are interesting to illustrate alternatives to the MCDHF method. Finally, papers A_{III} and A_V describe computer programs that were developed in connection with A_I and A_{IV}, respectively.

4.1 Complete finite bases

In Sec. 3.6.2, we defined how the GRASP radial orbitals are projected onto an exponential grid and explained that coupled of differential equations are solved using standard finite difference methods to finally obtain one solution for each orbital in the self-consistent field picture. However, besides this numerical approach, other options exist, consisting mostly in expanding the radial orbitals over a finite and complete set of functions,

$$P_{n\kappa}(r) = \sum_{i=1}^{N_f} p_{n\kappa i}\, f_i(r) \tag{4.1}$$

and

$$Q_{n\kappa}(r) = \sum_{i=1}^{N'_f} q_{n\kappa i}\ f'_i(r)\ , \tag{4.2}$$

where the expansion coefficients $\{p_{n\kappa i}, q_{n\kappa i}\}$ are the unknowns to be determined. Multiple choices are available for the basis functions $f_i(r)$ and $f'_i(r)$, each with its own specificities. In the following we discuss two possibilities, one is the orbital basis used in the Lagrange-mesh method (Sec. 4.1.1) and the other is the B-spline orbital basis (Sec. 4.1.2), which appears as the most promising variational alternative to finite-difference MCDHF methods. Other choices of finite bases, each with their advantages and disadvantages, are discussed in e.g., Refs. [27, §5] or [182].

4.1.1 Lagrange-mesh method orbital basis

The Lagrange-mesh method (LMM) exploits the properties of Lagrange-Laguerre functions to generate a basis of functions that form a complete, orthonormal set (for a review see [183]). These functions are associated to a set of mesh points, such that each basis function vanishes at all mesh points except one,

$$f_i(x_j) \propto \delta_{ij}\ . \tag{4.3}$$

The combination of the above property with the Gauss quadrature integration method of a function $g(x)$

$$\int_a^b g(x)dx \approx \sum_{k=1}^{N_f} \lambda_k g(x_k)\ , \tag{4.4}$$

where the λ_k and x_k are the associated weights and mesh points, respectively, allows to efficiently evaluate integrals. Additional considerations about the mesh points, the basis functions or the Gauss quadrature can be found elsewhere [183, 158]. The most important feature is that under specific conditions the Gauss quadrature provides the exact solution to the integral, and not an approximation of it.

The LMM was shown to be particularly effective to solve non-relativistic quantum mechanical problems [184], including three-body systems [185, 186, 187]. Further work in the non-relativistic context showed that the LMM could be used to compute exactly the polarizabilities of the hydrogen-like systems [188] (for a review on polarizabilities, see e.g. Ref. [189]). Later the same method was applied successfully to the one-electron Dirac equation [190], the corresponding hydrogenic polarizabilities [191] and then to hydrogenic two-photon decay rates [192]. This series of paper was extended in A$_{\text{IV}}$, in which we computed polarizabilities and two-photon decay rates of Ca^+, Ba^+ and Sr^+ [181]. However, the passage from the one-electron Dirac equation to the many-electron systems required

the definition of a semiempirical core-polarization potential, that ultimately permitted to recover a one-electron Dirac-like equation for the single valence electron. The focus on polarizabilities and two-photon decay rates is related to the ease of the LMM to include contributions from the negative and positive continua. As an example, the expression of the static polarizability of multipolarity λ for a valence state $v \equiv n_v\kappa_v$ is (see Eq. (14) in A$_{\rm IV}$),

$$\alpha^S_\lambda(v)=\sum_{\kappa'_v} \frac{2[j'_v]}{[\lambda]} \begin{pmatrix} j'_v & \lambda & j_v \\ -1/2 & 0 & 1/2 \end{pmatrix}^2 \sum\!\!\!\!\!\!\int_{n'_v} \frac{\{\int_0^\infty [P_v(r)P_{v'}(r)+Q_v(r)Q_{v'}(r)]\tilde{r}^\lambda\, dr\}^2}{\varepsilon_{v'}-\varepsilon_v}\,, \tag{4.5}$$

involves a summation of all discrete bound states and an integration over both continua, as represented by the symbol $\sum\!\!\!\!\!\!\int$. We leave the definitions of the notations to A$_{\rm IV}$, focusing on the sum-integration requirement.

Because the atomic system with a single valence electron can be described as a closed-shell core plus a valence electron, if one assumes that the core orbitals are known, the problem to solve resumes to

$$\mathcal{H}_{\rm DHFCP}\ \phi_v = \varepsilon_v\ \phi_v\ , \tag{4.6}$$

where $\mathcal{H}_{\rm DHFCP}$ is the Dirac-Coulomb-plus-core-potential (DHFCP) Hamiltonian, ε_v is the individual energy of the valence orbital and $\phi_v = (P_v(r)\ Q_v(r))^T$. Inserting the expansions (4.1) and (4.2), which are based on the same basis functions $f_i(r) = f'_i(r)$ and have the same dimension $N_f = N'_f$, in (4.6), we have

$$\mathbf{H}_{\rm DHFCP}\ \mathbf{p}_v = \varepsilon_v\ \mathbf{p}_v\ , \tag{4.7}$$

where $\mathbf{H}_{\rm DHFCP}$ is a $2N_f \times 2N_f$ square matrix with matrix elements $H_{\rm DHFCP}(i,j) = \int_0^\infty f_i(r)\mathcal{H}_{\rm DHFCP}f_j(r)dr$ and $\mathbf{p}_v = (p_{v1}, p_{v2}, \ldots, p_{vN_f}, q_{v1}, q_{v2}, \ldots, q_{vN_f})^T$. The diagonalization of $\mathbf{H}_{\rm DHFCP}$ returns $2N_f$ eigenvalues and eigenvectors. The eigenvalues correspond to the individual energies and consist of the following spectrum,

$$\mathcal{E}_v = (\varepsilon_v^1, \ldots, \varepsilon_v^{N_f}, \varepsilon_v^{N_f+1}, \ldots, \varepsilon_v^{2N_f})\ , \tag{4.8}$$

ordered by increasing values. To each energy ε_v^i is associated an eigenvector $\mathbf{p}_v^i$. The spectrum $\mathcal{E}_v$ can be separated in three subsets: $\mathcal{C}^- = \{\varepsilon_v^1, \ldots, \varepsilon_v^{N_f}\}$, $\mathcal{B} = \{\varepsilon_v^{N_f+1}, \ldots, \varepsilon_v^{N_f+k}\}$ and $\mathcal{C}^+ = \{\varepsilon_v^{N_f+k+1} \ldots \varepsilon_v^{2N_f}\}$, where k is an integer smaller than N_f. They define the following energy intervals

$$\forall \varepsilon_v^i \in \mathcal{C}^-;\ \varepsilon_v^i \le -2c^2 \quad (i = 1, \ldots, N_f)\ , \tag{4.9}$$

$$\forall \varepsilon_v^i \in \mathcal{B};\ -2c^2 \le \varepsilon_v^i \le 0 \quad (i = N_f+1, \ldots, N_f+k)\ , \tag{4.10}$$

$$\forall \varepsilon_v^i \in \mathcal{C}^+;\ \varepsilon_v^i \ge 0 \quad (i = N_f+k+1, \ldots, 2N_f)\ . \tag{4.11}$$

Among these $2N_f$ states, only the targeted state is 'physical' and its energy belongs to $\mathcal{B}$. The remaining $k-1$ energies of $\mathcal{B}$ are associated to 'unphysical' states that *simulate* the bound-state spectrum. Similarly, states with energies belonging to $\mathcal{C}^-$ and $\mathcal{C}^+$ are also unphysical and are often referred to as *pseudo-states*; they simulate the negative and positive energy continuum, respectively. Thanks to the discretization of the energy spectrum and the completeness property of the basis, sum-integrals such as the one in Eq. (4.5) reduce to a simple sum over the $2N_f$ discrete (pseudo-)states.

The crucial aspect to highlight here is the possibility to describe continuum wave functions easily, which allows to include their contributions to polarizabilities, two-photon transition rates, electric dipole moments, etc.. The determination of these quantities using the MCDHF method is more demanding. It requires to generate continuum wave functions by extrapolating Rydberg series above the ionization limit, enforcing a smooth change between the bound and free wave functions (see e.g., [193]).

However, the LMM method was only successfully applied in the fully relativistic context to nominal one-electron systems. Up to now, it fails to solve systems with two or more electrons. The use of perimetric coordinates in the non-relativistic calculations circumvent some of the difficulties and permit to solve the Schrödinger equation for atomic and molecular systems such as He, H^- or H_2^+ [186]. Nothing similar is yet developed for the Dirac-Coulomb equation, which is why the present method relies on the use of a semiempirical core potential. The latter was theoretically derived by considering the polarization of the core by the electric field of the valence electron, which then acquires an induced dipole moment proportional to the core polarizability $\alpha_1(\text{core})$ [194, 195, 196, 197]

$$V_{\text{CP}}(r) = -\frac{\alpha_1(\text{core})}{2r^4}\left[1-\exp\left(-r^6/\rho_\kappa^6\right)\right] \tag{4.12}$$

where ρ_κ is the cut-off semiempirical parameter (see A_{IV} and A_V for details).

4.1.2 B-splines

The B-spline basis functions have probably become in the past decades the most popular variational alternative to the finite-difference MCDHF method in atomic physics, but also, and mostly, in molecular physics (for a review see e.g., [198, 199] and references therein). The high accuracy obtained from finite-difference methods as introduced by Hartree in atomic physics can be explained by the spherical symmetry of the problem that allows a clean separation of the angular and radial variables, which is not the case for molecular physics, which then developed finite basis set methods faster. Bachau *et al.* [198] argued that the finite basis has to be 'complete enough' so that it becomes competitive with the finite-difference methods. B-splines met this criteria with only a few basis functions, which explains their popularity. Furthermore, the high flexibility of the B-spline functions allows

to generate the grid points to describe bound states and continuum states, i.e., having grid points far away from the nucleus. Finally, the number of B-spline functions can be large without any complications from linear dependences [199]. Numerous applications of B-spline in atomic physics can be found in e.g., Refs. [200, 201, 202, 203, 204, 205, 206].

Contrarily to the Lagrange-Laguerre functions which are defined over the $[0, +\infty[$ range, B-splines are piece-wise polynomial functions defined over finite intervals $[a, b]$. These intervals are determined according to a sequence of grid points or *knot sequence* $[t_i], i = 1, 2, \ldots, n$ [207]. B-splines of order k are then defined recursively from the B-splines $B_{i,k-1}(r)$ and $B_{i+1,k-1}(r)$ as

$$B_{i,k}(r) = \frac{x - t_i}{t_{i+k} - t_i} B_{i,k-1}(r) + \frac{t_{i+k+1} - x}{t_{i+k+1} - t_{i+1}} B_{i+1,k-1}(x) \ , \tag{4.13}$$

with the B-splines of order 1 defined as

$$B_{i,1}(r) = \begin{cases} 1, & t_i \leq r \leq t_{i+1} \\ 0, & \text{otherwise} \end{cases} \ . \tag{4.14}$$

Each $B_{i,k}$ is therefore defined over k intervals generated from $k + 1$ knots. The flexibility of the B-splines functions lies in the numerous possibilities of grid point sequences. Zatsarinny and Froese Fischer [207] illustrate that flexibility by choosing a grid that would be linear with step h_i close to the nucleus, exponential with step $1 + h_e$ in the middle range and then again linear with another step $h_{\max}$ further from the nucleus. One could then tune the grid parameters to obtain a completely logarithmic grid or an equally-spaced grid, instead of the default semi-logarithmic grid. Depending on the application, one grid might then be more suitable than others.

B-splines defined as such are then used to expand the orbital basis as Eqs. (4.1) and (4.2) as

$$P_{n\kappa}(r) = \sum_{i=1}^{n_p} p_{n\kappa i} B_{i,k_p}(r), \quad Q_{n\kappa}(r) = \sum_{i=1}^{n_q} q_{n\kappa i} B_{i,k_q}(r) \ . \tag{4.15}$$

Note that the B-splines orders are different for the large and small component, $k_p \neq k_q$, as suggested by Zatsarinny and Froese Fischer [207] to prevent the apparition of spurious states (for more details about spurious states, see e.g., Ref. [208, 202]). Spurious states, if detected, are however necessary to ensure the completeness of the basis [182]. Recently, Zatsarinny and Froese Fischer [207] developed the program DBSR_HF that solves the DHF equations using B-splines expansions. This appears to be directly in line with the SPHF program, a non-relativistic program to solve the HF equations [209]. Ultimately, the DBSR_HF program builds and diagonalizes one relatively small matrix for each orbital in the SCF procedure.

Bases of B-splines functions, just as bases of Lagrange-Laguerre of functions, take advantage of their completeness property to simulate a complete energy spectrum, including negative (in the relativistic framework only) and positive continua and bound states. They are therefore particularly efficient to deal with infinite summations. Sapirstein and Johnson [199] illustrate this phenomenon by considering the second-order energy correction from perturbation theory. Taking the example of the second-order Stark effect on hydrogen, they explain how the infinite sum over all states reduces to a sum over the pseudospectrum composed of a finite number of states. The contribution from the infinite sum could be taken into account analytically by solving a differential equation. However, the third-order energy correction includes multiple infinite sums and hence a much more complicated differential equation to solve while the B-splines allow to treat these infinite sums as finite. Only the computational time increases, not the complexity.

Finally, because of their high flexibility and practical use, B-splines are very popular to describe continuum processes and collisions. An example is the Spline-Galerkin method that was developed in a series of papers in the autoionization context [210, 211, 212, 213] in connection with the MCHF_AUTO program [214], an extension of the MCHF method developed in the ATSP codes[1] [215] and its earlier releases. Another example is the use of B-splines in R-matrix calculations to describe collisions as implemented in the non-relativistic general suite of codes BSR (B-splines R-matrix code) [216] and its relativistic counterpart DBSR used in e.g. [217], that is the original program on which is based DBSR_HF.

4.2 MCDHF orbitals

The MCDHF orbital basis is usually optimized in three main steps. First, the spectroscopic orbitals are generated by solving the DHF equations of the targeted state. Then, the configuration space is extended to the MR and the corresponding orbitals are optimized (often the spectroscopic orbitals are re-optimized). Finally, correlation orbitals are generated by increasing progressively the CSF space. In this section, we discuss important properties of these orbitals and how the optimization strategy affects the computed atomic quantities.

4.2.1 Brillouin's theorem

Brillouin's theorem is a key concept to explain the success of the HF method, and is often put forward as the main reason why the results obtained with the 'simple' HF method are reasonably good. Since most of the literature on the topic is discussed in the non-relativistic

[1] ATSP is the MCHF atomic-structure package for large-scale calculations, often referred to as the non-relativistic counterpart of GRASP.

context of the HF and MCHF method, we shall do the same since Froese Fischer *et al.* argued that Brillouin's theorem developed for the HF method also applies to the DHF method, providing minor conceptual changes [28].

Brillouin's theorem is intrinsically related to the variational nature of the HF solutions. Following the definition given in Ref. [8, §3.7], we start by considering the perturbation $nl \to n'l$ of an occupied orbital that leaves invariant the angular coupling scheme. Given the (non-relativistic) CSF solution to the HF equation, $\Phi^{\mathrm{HF}}(\gamma LS)$ associated with m occupied orbitals with radial components $P^{\mathrm{HF}}(n_1 l_1; r)$, $P^{\mathrm{HF}}(n_2 l_2; r)$, $\ldots$, $P^{\mathrm{HF}}(n_m l_m; r)$, the perturbation is usually written

$$P(nl; r) = P^{\mathrm{HF}}(nl; r) + \epsilon P(n'l; r) \; . \tag{4.16}$$

Propagating that perturbation to the HF CSF [218, 219, 220] leads us to

$$\Phi(\gamma LS) = \Phi^{\mathrm{HF}}(\gamma LS) + \epsilon F(nl \to n'l) + \mathcal{O}(\epsilon^2) \; , \tag{4.17}$$

where the function $F(nl \to n'l)$ is not always a CSF, as we will discuss later. In turn, the energy functional is also perturbed as

$$\mathcal{F}\big(P(nl; r)\big) = \mathcal{F}\big(P^{\mathrm{HF}}(nl; r)\big) + 2\epsilon \, \langle \Phi^{\mathrm{HF}}(\gamma LS) | \mathcal{H}_{\mathrm{NR}} | F(nl \to n'l) \rangle + \mathcal{O}(\epsilon^2) \; , \tag{4.18}$$

where only the modified radial orbital is explicitly shown as a variable of the energy functional and $\mathcal{H}_{\mathrm{NR}}$ is the non-relativistic Schrödinger Hamiltonian. Because the HF energy functional is stationary to first order to any perturbation, it follows that

$$\langle \Phi^{\mathrm{HF}}(\gamma LS) | \mathcal{H}_{\mathrm{NR}} | F(nl \to n'l) \rangle = 0 \; , \tag{4.19}$$

which is known as the Brillouin theorem. The structure of $F(nl \to n'l)$ is however complicated and only in special cases it is a CSF. These special cases include for example the single substitutions from closed-shell systems, for which $F(nl \to n'l)$ is a well-defined CSF, as described by Bauche and Klapisch [218]. Another presented case is the one of alkali-like systems, where single substitutions from the outermost electron are considered. A well-known example is the ground state of lithium, $1s^2 2s \; {}^2S$, for which the Brillouin theorem holds for any CSF of the form $1s^2 ns \; {}^2S$, i.e.,

$$\langle \Phi^{\mathrm{HF}}(1s^2 2s \; {}^2S) | \mathcal{H}_{\mathrm{NR}} | \Phi(1s^2 ns \; {}^2S) \rangle = 0 \quad \forall n > 2 \; , \tag{4.20}$$

where $F(nl \to n'l)$ is simply $F(2s \to ns) = \Phi(1s^2 ns \; {}^2S)$. In the CI picture, these vanishing matrix elements correspond to non-interacting CSFs and therefore the CSFs $\Phi(1s^2 ns \; {}^2S)$ do not contribute to lower the energy of the ground state by diagonalizing the interaction matrix, i.e., it is already diagonal ! A common argument is to say that the HF solution *already includes* such CSFs, which explain its high quality. One should simply be

aware that in more general cases, $F(nl \rightarrow n'l)$ is not a single CSF, but a linear combination of CSFs weighted by the appropriate coefficients. As it turns out, these coefficients are exactly the CFPs already encountered in Sec. 3.4.4. Taking the example of the $2p^3\ ^2P^{\rm o}$ with the $2p \rightarrow np$ perturbation, Brillouin's theorem holds for a linear combination of the parents $\Phi(2p^2(^3P)np\ ^2P^{\rm o})$, $\Phi(2p^2(^1D)np\ ^2P^{\rm o})$ and $\Phi(2p^2(^1S)np\ ^2P^{\rm o})$. *"Thus the HF solution has included a particular combination of the $2p^2np$ CSFs but not each CSF exactly: adding the three CSFs separately, each with their own expansion coefficient, would lower the energy of the HF wave function."* [28].

An other important case studied in details by Froese Fischer [220] concerns perturbations of a pair of orbitals nl and $n'l$ subject to orthogonality conditions. These perturbations are referred to as *rotations*, since they imply the simultaneous $nl \rightarrow n'l$ and $n'l \rightarrow -nl$ replacements that can be rewritten in matrix form as

$$\begin{pmatrix} P'_{nl}(r) \\ P'_{n'l}(r) \end{pmatrix} = \frac{1}{\sqrt{1+\epsilon^2}} \begin{pmatrix} 1 & -\epsilon \\ \epsilon & 1 \end{pmatrix} \begin{pmatrix} P_{nl}(r) \\ P_{n'l}(r) \end{pmatrix} , \tag{4.21}$$

which is the matrix representation of a rotation of angle θ if $\cos\theta = \epsilon/\sqrt{1+\epsilon^2}$. In such cases, Froese Fischer [220] demonstrated the following relation

$$\langle \Phi^{\rm HF}(nln'l\ LS)|\mathcal{H}|\Phi^{\rm HF}(nl^2\ LS)\rangle = \langle \Phi^{\rm HF}(nln'l\ LS)|\mathcal{H}|\Phi^{\rm HF}(n'l^2\ LS)\rangle\ . \tag{4.22}$$

Therefore if one of the interactions vanishes, the Brillouin theorem holds for both CSFs. To illustrate this last equality, let us take two examples. First, consider again the ground state of Li $1s^22s\ ^2S$, for which the replacements $1s \rightarrow 2s$ and $2s \rightarrow -1s$ lead to the CSFs $\Phi([1s2s]^1S\ 2s\ ^2S)$ and $\Phi([1s1s]^1S\ 1s\ ^2S)$, respectively. However, by the Pauli exclusion principle, the latter is forbidden and therefore its interaction with the ground CSF vanishes and the Brillouin theorem holds also for $\Phi([1s2s]^1S\ 2s\ ^2S) = \Phi(1s2s^2\ ^2S)$. Turning to the case of the first excited state of He, $1s2s\ ^1S$, the replacements $1s \rightarrow 2s$ and $2s \rightarrow -1s$ lead to $\Phi(2s^2\ ^1S)$ and $-\Phi(1s^2\ ^1S)$, respectively. Brillouin's theorem does not apply for each individual CSF but for some average of the two, explicitly,

$$\frac{\Phi(2s^2\ ^1S) - \Phi(1s^2\ ^1S)}{\sqrt{2}}\ . \tag{4.23}$$

The analysis of the effect of a pairwise perturbation (4.21) involving two occupied orbitals belonging to the same l-symmetry has been generalized in the single configuration HF approximation [221]. This paper illustrates the rapid progressive cancellation of the Brillouin matrix element

$$\langle \Phi^{\rm HF}(\gamma LS)|\mathcal{H}_{\rm NR}|F(nl \rightarrow n'l) - F(n'l \rightarrow nl)\rangle = 0\ , \tag{4.24}$$

with the convergence of the HF self-consistent process. Taking into account Brillouin's theorem is an excellent way to reduce the size of the CI expansion by avoiding to include useless CSFs.

The generalization of Brillouin's theorem to the MCHF method comes naturally,

$$\langle \Psi_{nl}^{\mathrm{MCHF}} | \mathcal{H}_{\mathrm{NR}} | \Psi_{nl\to n'l}^{\mathrm{MCHF}} \rangle = 0 \tag{4.25}$$

where $\Psi_{nl}^{\mathrm{MCHF}}$ is the MCHF wave function and $\Psi_{nl\to n'l}^{\mathrm{MCHF}}$ is the perturbed wave function in which each CSF with the orbital nl occupied was subject to the $nl \to n'l$ perturbation. According to Froese Fischer *et al.*, Brillouin's theorem applied to the MCHF method is not nearly as important as for the HF method since *"the included interaction may only apply in a broad average sense"* [28]. The "conceptual changes" needed for discussing Brillouin's theorem in (MC)DHF instead of (MC)HF are the natural adaptation from the l- to κ-symmetry, together with the writing of a rotation matrix identical to (4.21)

$$\begin{pmatrix} P'_{n\kappa}(r)/Q'_{n\kappa}(r) \\ P'_{n'\kappa}(r)/Q'_{n'\kappa}(r) \end{pmatrix} = \frac{1}{\sqrt{1+\epsilon^2}} \begin{pmatrix} 1 & -\epsilon \\ \epsilon & 1 \end{pmatrix} \begin{pmatrix} P_{n\kappa}(r)/Q_{n\kappa}(r) \\ P_{n'\kappa}(r)/Q_{n'\kappa}(r) \end{pmatrix} . \tag{4.26}$$

but applied to the radial functions of both the large and small components.

4.2.2 Non-uniqueness of the wave function

A thorough rotational analysis shows that the (D)HF wave functions might not be unique. Considering the simple $1s^2 2s^2$ case, any unitary transformation of the $1s$ and $2s$ orbitals leaves the energy and wave function invariant. The optimal choice is the one that sets the off-diagonal Lagrange parameters to zero [222]. In multiconfiguration methods, however, non-uniqueness of the wave function is rare and setting the off-diagonal Lagrange multipliers to zero is not always efficient. The most important case of non-uniqueness arises when considering *Complete Active Space* (CAS) expansions, in which all possible substitutions are generated within a set of orbitals. The simplest example is probably the CAS expansion of the He ground state, for which the generation of all CSFs by substitutions from the $1s^2\ {}^1S$ within the $\{1s, 2s\}$ orbital set leads to the $\{1s^2, 1s2s, 2s^2\}\ {}^1S$ CAS. Rotations of the orbitals $1s$ and $2s$ leave the wave function and energy invariant. This degree of freedom can be used to e.g., set one expansion coefficients to zero and hence *reducing* the number of CSFs. The reduced form of a CAS wave function is detailed in all generality in Ref. [8, §5.2]. We shall consider only the case of the He ground state, for which the CAS expansion is, with no limitation on the orbital basis,

$$\begin{aligned} \Psi(1s^2\ {}^1S) = &\sum_{nn'} c_{nn'}^{(ss)} \Phi(nsn's\ {}^1S) + \sum_{nn'} c_{nn'}^{(pp)} \Phi(npn'p\ {}^1S) \\ &+ \sum_{nn'} c_{nn'}^{(dd)} \Phi(ndn'd\ {}^1S) + \dots . \end{aligned} \tag{4.27}$$

Considering only the $l = 0$ part of the expansion as an example, we have

$$\Psi^{l=0}(1s^2\ {}^1S) = \left(\sum_{nn'} c_{nn'}^{(ss)} R_{ns}(r_1) R_{n's}(r_2) \right) |ss\ {}^1S\rangle \ , \tag{4.28}$$

where $R_{ns}(r) = P_{ns}(r)/r$ and $|ss\ ^1S\rangle$ is the spin-angular factor common to all CSFs $\Phi(nsn's\ ^1S)$. The summation over nn' can be rewritten in matrix form, so that

$$\sum_{nn'} c_{nn'}^{(ss)} R_{ns}(r_1) R_{n's}(r_2) = \mathbf{R}(r_1)\mathbf{C}^{(ss)}\mathbf{R}(r_2)^T \ , \tag{4.29}$$

where the matrix elements of $\mathbf{C}^{(ss)}$ are the $c_{nn'}^{(ss)}$ coefficients and $\mathbf{R}(r)$ is the row vector containing the radial parts of all s orbitals. One can then find the unitary transformation that diagonalizes the $\mathbf{C}^{(ss)}$ matrix,

$$\tilde{\mathbf{C}}^{(s)} = \mathbf{O}^{(s)}\mathbf{C}^{(ss)}\mathbf{O}^{(s),T} \ . \tag{4.30}$$

Transforming the orbitals according to $\mathbf{R}'(r) = \mathbf{O}^{(s)}\mathbf{R}(r)$ results in the *reduced form* of the expansion that writes, in the new orbital basis,

$$\Psi^{l=0}(1s^2\ ^1S) = \sum_n d_n^{(s)} \Phi(ns^2\ ^1S) \ . \tag{4.31}$$

The transformed orbitals are known as *natural orbitals* and will be the topic of Sec. 4.3. For more information about the general case, see e.g., Ref. [8, §5.2].

4.2.3 The pair-correlation functions

In the 1970's and 1980's, the removal or relaxation of the orthogonality constraints applied in the MCHF and MCDHF methods was subject to discussions (see e.g., [220, 223, 129, 224]). As shown by Froese Fischer, allowing non-orthogonalities between orbitals of the same angular symmetry considerably simplifies Brillouin's theorem [220]. More importantly, two configurations might require the same nl orbitals to be different, depending on e.g., its occupation number. As an example, the accurate description of the two $^7P^{\rm o}$ states in Cr I and their interaction benefit greatly from non-orthogonalities. Therefore, the corresponding configuration could be denoted as $3d_1^5 4p_1$ and $3d_2^4 4s 4p_2$, where the lower indices emphasize that the $3d$ and $4p$ orbitals are different in the two configurations [223]. The use of two, non-orthogonal, $3d$ and $4p$ orbitals reduces considerably the number of configurations to be included. However, the mathematical treatment of these non-orthogonalities induces more complex equations to solve, in which overlap integrals such as $\langle 4p_1|4p_2\rangle$ must be carried out explicitly [129]. Similar considerations are discussed in $\rm B_{IV}$, in which the $5d^7 6s^2$ and $5d^8 6s$ configurations were found to have very different $5d$ orbitals (see Sec. 5.2).

From Z-perturbation theory, it appears that the most important corrections to the zeroth order wave function are CSFs generated by, at most, double substitutions from the reference (D)HF CSF and that interact with the latter. Take any system with more than

two electrons, then the correlation of the $1s^2$ core leads to substitutions such as $1s^2\ {}^1S \rightarrow nln'l\ {}^1S$. The expansion consisting of all these substitutions is called a *pair-correlation function* (PCF) [115, §3.7]. Ideally, we should then have one PCF by pair of electrons. More recently, Verdebout *et al.* investigated the three PCFs that correlate the three electron pairs of the $1s^22s^2\ {}^1S$ ground state of Be, explicitly, $1s^2$, $1s2s$ and $2s^2$ [177]. Performing individual MCHF calculations for each PCF, they observed that the correlation orbitals are spatially localized very differently, i.e., the correlation orbitals describing the $1s^2$ pair are close to the nucleus, the ones correlating the $2s^2$ are further away while the orbitals optimized for the $1s2s$ pair lie somewhere in between. This is however not surprising, as the correlation orbitals tend to maximize their interaction with the considered pair of electrons occupying the spectroscopic orbitals, i.e., the $1s$, the $1s$ and $2s$, and the $2s$, for each PCF respectively. The authors of Ref. [177] rightfully concluded that to optimize the calculations, each PCF should be described with its own orbital basis. This inevitably leads to non-orthogonalities. The evaluation of any atomic property would then require to compute matrix elements in which the LHS and RHS are described in two different, non-orthogonal orbital bases. The use of biorthogonal transformations and counter-weight transformations of the wave function [225] avoids the increasing complexity of the algebra and allows the application of the original Wigner-Racah-Fano formalism. This gave rise to the *Partition Correlation Function Interaction* (PCFI) method, that was proven to be highly efficient in the case of Be [226]. If non-orthogonal PCFs are built, each with its own basis, one could transform each orbital basis into its reduced form and hence reduce considerably the number of CSFs in each of the PCFs expansion. If, oppositely, non-orthogonalities can not be treated properly, the reduced form of the expansion could only be useful in very limited number of cases.

4.2.4 Smart optimization

In A_{II}, we investigate the role of the optimization strategy for the correlation orbitals on transition rates involving high Rydberg states in C IV and C III. These ions correspond to Li-like and Be-like systems, i.e., with three and four electrons, respectively. Taking the example of C IV, the targeted states belong to configurations of the form $1s^2nl$ for $n = 2$ to 8 and $l = 0$ to 4. The $1s^26h$ configuration is also included. Because of the small number of electrons, the active space is usually generated by allowing all SD substitutions, hence including V, CV and CC correlations effects. Based on such expansions, that we could refer to as normal or conventional expansions, we observe that the correlation orbitals are preferentially localized close to the nucleus, due to the large overlap with the two $1s$ electrons. However, because the targeted states include high Rydberg states for which the external nl orbital lies far away from the nucleus, the orbital basis built in that way might be ill-suited. In order to assess the quality of each ASF, we investigate the gauge dependence of the transition rates through the parameter dT (3.163). Looking for example at the set

of transitions $2p\ ^2P^{\rm o}_{1/2} - ns\ ^2S_{1/2}$ and $np\ ^2P^{\rm o}_{1/2} - 8s\ ^2S_{1/2}$ for increasing value of n (see Fig. 1 in A_{II}), we make the following observations: (i) the gauge difference is close to 0 when two low-lying states are involved (ii) the gauge difference is close to 0 when two high Rydberg states are involved (iii) the gauge difference is large (up to 10%) when the transition involves a low-lying state and a high Rydberg state.

This disagreement was overcome thanks to an alternative method to optimize the correlation orbitals. Because the outermost electron is pushed further away from the core when considering higher Rydberg states, we are looking for an orbital basis that effectively describes both the innermost part of the wave functions, but also the outermost part. In this alternative optimization strategy, the CSFs generated by SD substitutions from the closed $1s^2$ shell were not included, i.e., CC correlation effect was only included through RCI calculations and did not to play any role in the optimization of the orbitals. Table 1 of A_{II} displays the mean radius of the spectroscopic and correlation orbitals. As expected, the alternative optimization strategy generated orbitals that are localized further away from the nucleus. Computing the transitions rates for the same transitions as mentioned above, the dT parameters remain fairly constant and small over the entire set of transitions.

A deeper analysis was performed on the transition rates from which we put in evidence that the large dT values arose from the transition rates computed in the Babushkin gauge. Remembering that the Babushkin gauge emphasizes the outer part of the wave function, we were able to conclude that the original orbital basis was ill-suited to describe higher Rydberg states due to the lack of correlation orbitals at large distances from the nucleus. This was further confirmed by looking at the evolution of the transition rates when the radial integrals involving correlation orbitals are limited to an increasing radius R. This is done in Fig. 4 of A_{II}, from which we observe that the major part of the transition rates computed in the Babushkin gauge comes from the outer part of the wave function. However, the Coulomb gauge, more sensitive to the inner part of the wave function, is almost unaffected by the radial truncation of the integrals, i.e., most of the contributions to the transition rates are captured at small distances from the nucleus. This finally enabled us to recommend the use of the Coulomb gauge instead of the Babushkin gauges for calculations of transition rates involving Rydberg states. The choice of the most appropriate gauge, Babushkin or Coulomb (or equivalently the length or velocity form), can be connected to Brillouin's theorem. Cowan argued that "*The length form weights the integrand toward large r; however this is not an inherent disadvantage when using (D)HF-type radial wavefunctions, which have the correct asymptotic form [...]. Since the length form is calculationally the simplest, it is the only one that we shall consider further.*" [17, §14.3]. In other terms, the Babushkin gauge is well suited for computing transition properties in the single-configuration approximation because the DHF solutions include all single-substitution contributions such as high Rydberg states or continuum states that extend far out from the nucleus: this is the Brillouin theorem (see Sec. 4.2.1). However, when multiple states are targeted simultaneously in

the MCDHF framework, which prevents Brillouin's theorem to hold for each state individually, these single-substitution states should be explicitly added in the calculations. The use of the Babushkin gauge then becomes problematic due to the difficulty to compensate the lack of variational freedom of each individual targeted state usually brought thanks to Brillouin's theorem. The argument made in A_{II} is that the alternative optimization strategy compensates better the lack of Brillouin's theorem that improves the description of the wave function at large r than the traditional optimization strategy.

Finally, we believe that A_{II} is a warning against unthinking computational strategies that would privilege extremely large expansions over a careful choice of the orbital basis. The small cases of C IV and C III already showed that the most obvious optimization strategy can lead to unrecoverable poor quality results. In that context, unrecoverable is meant that even the largest RCI calculations could not compensate the ill-suited orbital basis, as it is commonly thought. One should therefore carefully think about how the orbital basis is optimized. Because different atomic properties are sensitive to different types of electron substitutions due to the form of their respective tensor operator, it also means that two atomic properties might not be adequately described by the same orbital basis.

4.3 Natural orbitals

Natural orbitals (NOs) were first introduced by Löwdin [227] as the orbitals that diagonalize the first-order density matrix. We already discussed a more intuitive way to introduce the NOs in connection with a rotational analysis of the wave function. In the next section, we will discuss briefly how they can be derived using the density matrix formalism. Natural orbitals are mostly used in quantum chemistry, following the work of Kutzelnigg *et al.* [228, 229]. They are known to generate compact active spaces, hence limiting the size of the calculations, and increasing the rate of convergence of CI calculations [230]. More recently, Giesbertz investigates the use of the NOs in his paper *"Are natural orbitals useful for generating an efficient expansion of the wave function?"* [231]: the usefulness of the NOs is still opened to debate. NOs in atomic physics are rarely exploited and their efficiency for many-body methods is still unclear. They were used in pioneer hyperfine structure calculations by e.g., Engels [232] or Lindgren *et al.* [233]. A series of papers in line with the work by Lindgren *et al.* demonstrated how the calculations improved when transforming the orbital basis to NOs or Brueckner orbitals [234, 235, 236, 237, 238]. Brueckner orbitals are the orbitals that maximize the overlap between the exact and approximate wave functions. Note that there is no difference between Brueckner orbitals and NOs when T, Q, . . . , substitutions are neglected, so that the differences between the two sets of orbitals is expected to remain small for many applications [233]. Our results presented in A_I confirm their original conclusions. The use of these orbitals to describe the polarization of the core and the lowest-order correlation effects effectively captures some important higher

order correlation effects. They also observed that for the alkali atoms, the modification of the HF orbitals toward Brueckner or natural orbitals affects considerably the valence orbital, pulling the electron closer to the nucleus, which has substantial effects on hyperfine structures and isotope shifts. We report similar observations for the MCDHF method.

4.3.1 Density matrix formalism

Löwdin defined the density matrix of order p for a many-body wave function of N_e electrons in the non-relativistic context as

$$\Gamma(\boldsymbol{q}'_1, \boldsymbol{q}'_2, \ldots, \boldsymbol{q}'_p | \boldsymbol{q}_1, \boldsymbol{q}_2, \ldots, \boldsymbol{q}_p) = \binom{N_e}{p} \times$$
$$\int \Psi^*(\boldsymbol{q}'_1, \boldsymbol{q}'_2, \ldots, \boldsymbol{q}'_p, \boldsymbol{q}'_{p+1}, \ldots, \boldsymbol{q}_{N_e}) \Psi(\boldsymbol{q}_1, \boldsymbol{q}_2, \ldots, \boldsymbol{q}_p, \boldsymbol{q}_{p+1}, \ldots, \boldsymbol{q}_{N_e}) d\boldsymbol{q}_{p+1} \ldots d\boldsymbol{q}_{N_e} \tag{4.32}$$

where $\binom{N_e}{p}$ is a simple binomial normalization factor [227] and $\boldsymbol{q}$ represents the spatial and spin coordinates.[2] The matrix of interest to us is the matrix of lowest order, i.e.,

$$\gamma(\boldsymbol{q}'_1 | \boldsymbol{q}_1) = N_e \int \Psi^*(\boldsymbol{q}'_1, \boldsymbol{q}_2, \ldots, \boldsymbol{q}_{N_e}) \Psi(\boldsymbol{q}_1, \boldsymbol{q}_2, \ldots, \boldsymbol{q}_{N_e}) d\boldsymbol{q}_2 \ldots d\boldsymbol{q}_{N_e} \tag{4.33}$$

General properties of the density matrices are discussed in the original paper by Löwdin (see Ref. [227]). Note that the diagonal elements, $\gamma(\boldsymbol{q}_1|\boldsymbol{q}_1) = \gamma(\boldsymbol{q}_1)$, have clear physical interpretations: $\gamma(\boldsymbol{q}_1)dv_1$ corresponds to the number of particles times the probability of finding a particle within the volume dv_1 around the point $\boldsymbol{r}_1$ and having the spin s_1. More interesting is the definition of the density matrices in the k-space, i.e., expressing the wave functions in terms of spin-orbitals and Slater determinants.[3]. The mathematical definition is

$$\gamma(l|k) = \sum_K^{(k)} \sum_L^{(l)} C_K^* D_{KL}(k|l) C_L / \sum_K |C_K|^2 \,, \tag{4.34}$$

where C_K and C_L are expansion coefficients and $D_{KL}(k|l)$ is a determinant containing overlap integrals (see Ref. [227] for more information about $D_{KL}(k|l)$ and the associated notations). Using that definition in k-space, the diagonal matrix elements, called the

[2] The use of the coordinate $\boldsymbol{q}$ is directly related to the introduction of spinor wave functions in the non-relativistic theory (see e.g. [115]). Going to the fully relativistic theory, the four-component, spinor character of the relativistic orbitals derives naturally from the structure of the one-electron Dirac-Coulomb equation. The replacement $\boldsymbol{q} \rightarrow \boldsymbol{r}$ should be enough to switch from the non-relativistic framework to the relativistic one, providing to replace the non-relativistic spin-orbitals [115, §1.3] by relativistic orbitals (2.54).

[3] In the context of the original work of Löwdin, basis functions are Slater determinants. When, in the following, we discuss the density matrix in the MCDHF context, the basis functions are CSFs, as usual.

charge order, are *"$\gamma(k)$ = number of particles $\times$ the probability for finding a particle in the spin-orbital k when all other particles occupy arbitrary spin-orbitals"* [227]. The off-diagonal elements $\gamma(l|k)$ are referred to by Löwdin as the *bond order* of the two spin-orbitals k and l. Taking as an example the $c_1\Phi(1s^2\ ^1S) + c_2\Phi(1s2s\ ^1S) + c_3\Phi(2s^2\ ^1S)$ normalized expansion in the MCDHF framework, we have already seen in Sec. 4.2.2 that the natural expansion reduces to $\tilde{c}_1\Phi(\tilde{1s}^2\ ^1S) + \Phi(\tilde{2s}^2\ ^1S)$. Practically, the diagonal elements of the 2×2 density matrix can be readily computed as, e.g., $(c_1^2 \times 1 + c_2^2 \times 1/2) \times 2$ for the $1s$ orbital, where $(c_1^2 \times 1)$ and $(c_2^2 \times 1/2)$ correspond to the probability to have an electron occupying the $1s$ orbital in the CSFs $\Phi(1s^2\ ^1S)$ and $\Phi(1s2s\ ^1S)$, respectively. The third CSF does not contribute as the $1s$ orbital is unoccupied. The global factor two is simply the number of electrons.[4]

This charge- and bond-order matrix is Hermitian, so that a unitary transformation exists that transforms that matrix into its diagonal form

$$\mathbf{U}^\dagger \boldsymbol{\gamma} \mathbf{U} = \tilde{\boldsymbol{\gamma}} \tag{4.35}$$

where $\tilde{\gamma}$ is a diagonal matrix.[5] A new set of spin-orbitals such that

$$\boldsymbol{\chi} = \boldsymbol{\phi}\mathbf{U} \quad \text{or} \quad \chi_\beta = \sum_\alpha \phi_\alpha U_{\alpha\beta} \tag{4.36}$$

are introduced. The χ_b are called the *natural (spin-)orbitals*. In the NO basis, all bond orders vanish and the eigenvalues $\tilde{\gamma}_\beta$ are interpreted as *occupation numbers*. Finally, they fulfil the conditions

$$0 \leq \tilde{\gamma}_\beta \leq 1\ , \quad \sum_\beta \tilde{\gamma}_\beta = N_e\ , \tag{4.37}$$

so that each spin-orbital is occupied by at most one electron. In the limiting case where the wave function is described by a single Slater determinant, each spin-orbital is occupied by an electron ($\tilde{\gamma}_\beta = 1\ \forall\beta$).

In the context of the variational, multiconfiguration methods, the derivation of the natural orbitals is performed in the second quantization formalism and arises naturally when building the electronic density. The mathematical details are given in Ref. [147] for the non-relativistic MCHF method and in A_{III} for the fully relativistic MCDHF method. The steps of the calculations are however similar. We already introduced the radial density in

[4] Note that we consider the $1s$ orbital as being occupied twice. Löwdin, however, refers to spin-orbitals which can only be occupied by a single electron. This implies minor conceptual changes regarding e.g., the range of the eigenvalues of the density matrix (see Eq. 4.45).

[5] Note the use of the conjugate transpose matrix instead of the transpose matrix in Eq. (4.30). In the most general case, the density matrix is Hermitian, as pointed out by Löwdin [227].

Eqs. (3.97–3.101). The density matrix is related to the radial density where the latter is expressed as

$$D(r) = \sum_{ij} c_i D_{ij}(r) c_j = \sum_{ij} c_i \left[\sum_{\kappa} \sum_{nn'} \nu^{ij}_{nn'\kappa} I_\rho(n'\kappa, n\kappa; r) \right] c_j \ , \tag{4.38}$$

where $\nu^{ij}_{nn'\kappa}$ are angular coefficients and

$$I_\rho(n'\kappa, n\kappa; r) \equiv \left[P_{n'\kappa}(r) P_{n\kappa}(r) + Q_{n'\kappa}(r) Q_{n\kappa}(r) \right] \ . \tag{4.39}$$

The angular coefficients $\nu^{ij}_{nn'\kappa}$ and radial factors $I_\rho(n'\kappa, n\kappa; r)$ come from evaluating $D(r)$ as the expectation value of the operator $\delta\hat{(}r)$ (3.102) in the second quantization formalism. Expressing the creation and annihilation operators in their irreducible tensorial form (3.103), one can apply standard Racah algebra and derive the analytical expression of the purely angular coefficients in terms of $3nj$-coefficients and (completely) reduced matrix elements. These angular coefficients can be derived by working out the matrix elements of a one–particle scalar operator between CSFs with u open shells, as explicitly derived by Gaigalas *et al.* [126].

Our interest is to rewrite Eq. (4.38) in such way that the κ-density matrices appear explicitly. Reorganizing the summations in Eq. (4.38), we have

$$D(r) = \sum_{\kappa} \sum_{nn'} \rho^{\kappa}_{nn'} I_\rho(n'\kappa, n\kappa; r) \tag{4.40}$$

where ρ_κ is the density matrix for a specific κ-value with its matrix elements defined as

$$\rho^{\kappa}_{nn'} = \sum_{ij} c_i \nu^{ij}_{nn'\kappa} c_j \ . \tag{4.41}$$

This last equation is in direct connection with expression (4.34) derived by Löwdin using unnormalized determinant sets. Following Löwdin's prescriptions, the orbitals are then transformed to natural orbitals according to

$$\tilde{P}_{m\kappa}(r) = \sum_{n} u^{\kappa}_{n,m} P_{n\kappa}(r) \tag{4.42}$$

and

$$\tilde{Q}_{m\kappa}(r) = \sum_{n} u^{\kappa}_{n,m} Q_{n\kappa}(r) \ , \tag{4.43}$$

where the coefficients $u^{\kappa}_{n,m}$ are the matrix elements of the unitary matrix $\mathbf{U}^\kappa$ that diagonalizes the block $\boldsymbol{\rho}^\kappa$, i.e.,

$$\mathbf{U}^{\kappa,\dagger} \boldsymbol{\rho}^\kappa \mathbf{U}^\kappa = \tilde{\boldsymbol{\rho}}^\kappa \ . \tag{4.44}$$

Finally, note that because we work with *restricted* DHF methods, i.e., the radial components are the same for all orbitals belonging to the same $n\kappa$ shell, the occupation numbers defined as the diagonal elements $\tilde{\rho}^{\kappa}_{nn} = \lambda^{\kappa}_{n}$ are such that

$$0 \leq \lambda^{\kappa}_{n} \leq 2j+1 \quad \text{and} \quad \sum_{\kappa} \sum_{n} \lambda^{\kappa}_{n} = N_e \; . \tag{4.45}$$

A property that follows immediately from these equations, is that if the shell $(n\kappa)^w$ is closed for all CSFs of the MCDHF/RCI expansion, i.e., no substitutions are allowed from that specific shell, then the corresponding matrix elements are $\rho^{\kappa}_{nn'} = \delta_{nn'} w$, i.e., the transformation to the natural orbitals does not affect the original corresponding orbital and its eigenvalue is exactly w, its occupation number.

Finally, it should be pointed out that in the context of the MCHF and MCDHF method, the natural orbitals are computed thanks to the DENSITY [147] and RDENSITY (see A_{III}) programs, which are compatible with ATSP and GRASP, respectively. Up until now, NOs were mostly considered as by-products of the evaluation of the radial density and therefore their properties were not studied in details for many-electron systems. However, for nominal two-electron systems, the *natural expansion* (4.31) of the wave function is well-known (see Sec 4.2.2 or e.g., [115, §3.8]).

4.3.2 Application to the hyperfine structure of Na

In A_I, we investigate the effect of using the NOs on the computed hyperfine structure constants using the non-relativistic MCHF method and the fully relativistic MCDHF method. Following closely the work by Jönsson *et al.* [239], we showed the weaknesses of using a layer-by-layer (LBL) optimization strategy. Starting from non-relativistic considerations, we performed two sets of calculations. One corresponds strictly to the computational strategy of Jönsson *et al.* [239], in which all correlation orbitals and the valence orbital are optimized together at each step, and the other one is a LBL approach in which only the newly introduced correlation orbitals are optimized, keeping the others frozen in the variational process. We were able to show that the computed hyperfine structure constant $A_{1/2}$ of the Na ground state in the LBL and 'full variational' (FV) optimization strategies differ by approximately 1.5%. The value computed in the LBL appears to be ~ 16 MHz too small compared to the experimental value $A_{1/2} = 885.813064\ 4(5)$ MHz [240] while the FV result is much closer to the latter, differing only by ~ 3 MHz. The transformation to NOs for each basis, leading to the LBL_{NO} and FV_{NO} orbital bases, reduced considerably the discrepancy between the two sets of calculations, which became smaller than ~ 2 MHz. The values computed in the NOs bases are also in better agreement with the experimental value than are the values computed in the FV basis. Finally, we see that the FV approach or the LBL approach with transformation to NO gives comparable results. From the point of

computational efficiency the latter approach is to prefer as the simultaneous optimization of a large number of orbitals is very time consuming compared to optimizing one layer at a time. The time for the NO transformation is negligible in comparison.

Strengthened with these observations, we turned to relativistic calculations. Because the GRASP programs do not support simultaneous optimization of multiple layers of correlation orbitals, only the LBL optimization strategy is available. Note also that the LBL optimization strategy is the only strategy adopted by all GRASP users in the last decades. Just as in non-relativistic calculations, the LBL relativistic calculations are far from being in agreement with the experimental value, in spite of adopting the same active space expansions as in the non-relativistic study by Jönsson *et al.* [239]. The transformation to NOs again reduces considerably the discrepancy with the experimental value. It should be mentioned here that the active space is progressively increased. First, only CV correlation effects are taken into account by allowing maximum one hole in the neon-like core of sodium. Then CC correlation is added by allowing all D substitutions, including D substitutions from the core. Finally, higher-order correlation effects are taken into account by allowing T and Q substitutions. The transformation to natural orbitals is performed before the introduction of CC correlation and higher-order electron substitutions. Although the transformation itself leaves almost invariant the energy and the hyperfine structure constant, the subsequent introduction of CC correlation has a drastically different effect on $A_{1/2}$ depending on the orbital basis (LBL or NO), as seen in Table IV of A$_{\text{I}}$.

The effect of the transformation to NOs is to increase the value of the hyperfine structure constants. This was confirmed by performing similar calculations along the Na isoelectronic sequence as well as for the excited $^2P^{\text{o}}_{1/2,3/2}$ states. In A$_{\text{I}}$, we put on evidence that the transformation to the NOs led to a strong spatial rearrangement among the s correlation orbitals. Furthermore, we showed that the spectroscopic $3s$ orbital was more contracted in the NOs than in LBL orbitals and that the mixing coefficient of the DHF reference CSF was increased in the NO basis. Because the ground configuration of Na is $1s^2 2s^2 2p^6 3s$, it is well-known that the unpaired s valence orbital contributes the most to the hyperfine structure constant. Therefore, small changes in its radial shape can strongly affect the value of the computed hyperfine structure constant. A deeper analysis of the role of the spectroscopic $3s$ orbital is conducted in the next sections and should be considered as an unpublished complement of A$_{\text{I}}$.

4.3.2.1 On the crucial role of the spectroscopic $3s$ orbital

Sub-spaces contributions analysis

The unexpected variation of the magnetic dipole hyperfine constant when adding CC correlation to the CV active space incited us to investigate in more details the different con-

Table 4.1: Contributions of the V, CV and C sub-spaces and their combinations to the magnetic dipole hyperfine constant of the ground state of neutral sodium. The effect of CC correlation on $A_{1/2}$ is larger in the LBL basis, leading to a lower $A_{1/2}$-value. Note that its effect is mostly indirect since the decrease in the V-V contribution is much larger than the C-C contribution itself. See text for further discussion.

	$A_{1/2}$ (MHz)			
	CV		CV+CC	
Interaction	LBL	NO	LBL	NO
V-V	775.908	777.888	696.790	727.814
V-CV	150.192	147.442	136.823	139.695
V-C	/	/	0.0	0.0
CV-CV	12.714	11.754	9.206	8.891
CV-C	/	/	−1.894	−1.844
C-C	/	/	14.322	16.098
$\sum$	938.813	937.083	855.247	890.654

tributions to it. The active space based on the $9h$ active set (consisting of all orbitals with $n \leq 9$ and $l \leq 5(h)$) is split into three *sub-spaces*. The first one corresponds to the valence subspace (V) including only CSFs generated from the single substitutions $3s \rightarrow ns$ $(4 \leq n \leq 9)$. The second one is the core-valence subspace (CV) including CSFs generated by all single substitutions from the core and restricted double substitutions (at most one hole in the core). The third one, the core subspace (C), contains all CSFs generated by double substitutions from the core. Each of the sub-space combinations contributes with different weights to the final $A_{1/2}$ value. The *diagonal* (V-V, CV-CV and C-C) and *off-diagonal* (V-CV, V-C and CV-C) contributions are tabulated in Table 4.1. Their sum, corresponding to the total $A_{1/2}$ value, is also given for each basis and each active space. The CV active space calculations, i.e., those performed before including CC correlation, show that the V-V, V-CV and CV-CV contributions provided in both bases are close to each other. In the NO basis, the V-V interaction is slightly stronger than in the LBL basis (by ≈ 2 MHz). This is consistent with the expected property of the NO basis of increasing the mixing coefficient of the leading DHF CSF. In the CV+CC calculations, the difference in the V-V interaction between the two orbital bases is larger (≈ 29 MHz). In addition, the C-C and V-CV interactions are also larger in the NO basis than in the LBL basis by ≈ 3 MHz and ≈ 1.7 MHz, respectively. Independently of the basis, we observe from Table 4.1 that the effect of CC correlation is mainly indirect since the change in the V-V contribution is more than five times larger than the C-C contribution itself (e.g., for the LBL basis the V-V contribution decreases by ≈ 80 MHz while the C-C contribution is only ≈ 14 MHz) as it was already discussed in the analyses of Engels *et al.* [232] and Godefroid *et al.* [241]. The interaction between the valence and core sub-spaces is exactly zero due to the one-body structure of the hyperfine Hamiltonian.

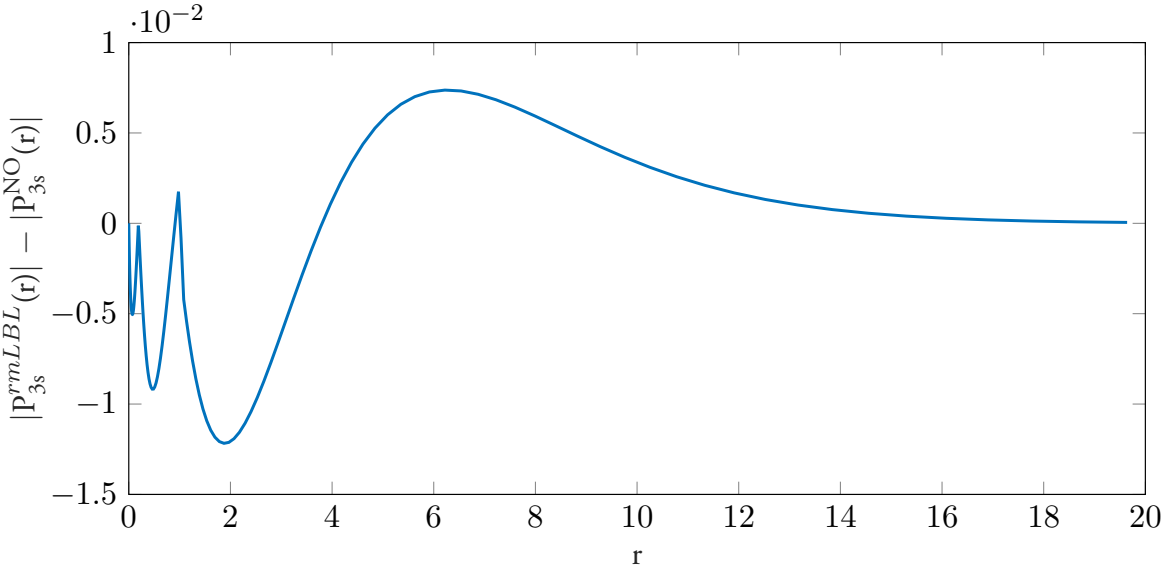

Figure 4.1: Difference between the absolute values of the large component radial function of the spectroscopic $3s$ orbital in the LBL and in NO basis.

Radial functions of the $3s$ orbital: LBL vs. NO

Table V of A_I put in evidence a diffuse $7s$ orbital in the LBL basis as well as a more contracted spectroscopic $3s$ orbital in the NO basis. The purely radial contribution to $\langle 1s^2 2s^2 2p^6 3s\ {}^2S_{1/2}||\mathbf{T}^{(1)}||1s^2 2s^2 2p^6 3s\ {}^2S_{1/2}\rangle$ is -0.026857 and -0.030312 in the LBL basis and in the NO basis, respectively. The small shape difference between the $3s$ and $3s_{\mathrm{NO}}$ orbitals is large enough to create a spectacular $\sim 11\%$ difference in the hyperfine radial expectation value. Fig. 4.1 displays the difference of the absolute values the large components $P(r)$ of the spectroscopic $3s$ orbital in the LBL and NO basis. The $3s$ natural orbital is slightly more contracted than the LBL one, as attested by the three "bumbs" close to the nucleus. This contraction illustrated by a larger transformed $|P^{\mathrm{NO}}_{3s}(r)|$ than the original $|P^{\mathrm{LBL}}_{3s}(r)|$ function in the $r = [0, 4]$ domain, explains its higher value of the radial hyperfine integral in the calculations of the $\langle 1s^2 2s^2 2p^6 3s\ {}^2S_{1/2}||\mathbf{T}^{(1)}||1s^2 2s^2 2p^6 3s\ {}^2S_{1/2}\rangle$ reduced matrix element. The contraction of the spectroscopic valence orbital is a direct effect of core-valence correlation. This becomes obvious when looking the results of the non-relativistic FV optimization strategy of Jönsson *et al.* [239] is analyzed. We reproduced their computations by allowing all correlation orbitals to vary simultaneously with the valence $3s$ orbital for which the mean radius was computed after each layer. In Fig. 4.2 is plotted the mean radius of the $3s$ orbital along the expansion of the active space characterized by its maximum principal quantum number. For comparison, the relativistic LBL and natural $3s$ orbitals mean radii are also shown on the figure. The black line, corresponding to the non-relativistic calculations, clearly illustrates the progressive contraction with the active space expansion, i.e., the core-valence correlation has the direct effect of

contracting the valence orbital (see e.g., [233]). In the LBL optimization strategy the $3s$ orbital is frozen after the optimization of the $n = 3$ layer and therefore lacks of variational freedom, which is partially recovered when computing the natural-orbital basis. Indeed the radial re-organization caused by the diagonalization of the density matrix mixes correlation orbitals and spectroscopic orbitals leading to a more contracted natural $3s$ orbital.

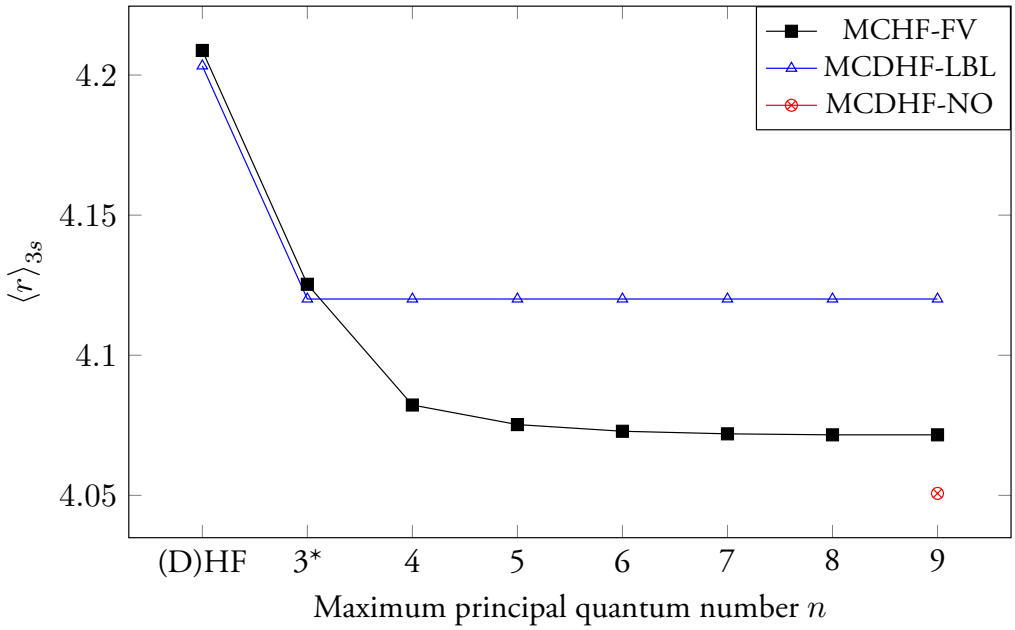

Figure 4.2: Mean radii of the $3s$ orbital in the LBL basis, NO basis and the non-relativistic FV scheme in which all orbitals are optimized together. The layer star next to the $n = 3$ value is there as a reminder that the spectroscopic $3s$ orbitals was varied along with the correlation $3p$ and $3d$ orbitals.

Artificial contractions

According to the previous section, the $3s$ orbital is not contracted enough in the LBL approach. The introduction of correlation should compensate for a too diffuse DHF $3s$ orbital. However it is frozen in a layer-by-layer approach. To confirm the strong link between the contraction of the $3s$ orbital (through its mean radius) and a larger hyperfine structure constant value, two artificial ways of contracting the $3s$ orbital are explored in the MCDHF framework:

(i) Mixing with a diffuse orbital
The first layer, corresponding to the $n = 3$ active space, optimizes together the

$3s, 3p-, 3p, 3d-, 3d$ orbitals. An additional (artificial) hydrogenic $6s$ orbital is added to the set of optimized orbitals so that the interaction between the diffuse $6s$ orbital and the spectroscopic $3s$ orbital results in a contraction of the latter. Only the $n = 3$ orbitals are kept while the $6s$ orbital is removed and the optimization of layers $n = 4, 5, 6, 7, 8, 9$ is performed as described in A_I. The corresponding orbital basis is labelled LBL-$6s$.

(ii) Extented optimal level optimization (EOL)
The first layer, corresponding to the $n = 3$ active space, optimizes together the $3s, 3p-, 3p, 3d-, 3d$ orbitals by minimizing simultaneously the two $J = 1/2$ lowest levels. Relative weights between the lowest and second lowest levels are chosen to be (20,1) or (15,1) in two separate calculations. Such weight partitions affect only slightly the results obtained by optimizing on the lowest level only. These two sets of calculations are labelled LBL-W20 and LBL-W15, respectively.

The $A_{1/2}$ hyperfine constants computed with these different optimization strategies are reported in Table 4.2 along with the active space expansion. Since these strategies were not built on rational arguments - except for the need of a more contracted $3s$ orbital - computations do not include the two core-core correlation layers nor the triple excitations in RCI. A single, smaller, RCI calculation is performed for each strategy to include CC correlation which is already enough to appreciate the difference between the LBL and NO bases. The mean radii of the $3s$ orbital are also given in Table 4.2. A high correlation is observed between the change in the mean radius and the hyperfine structure constants. Indeed, going from left to right, the mean radius of the $3s$ orbital decreases, corresponding to a contraction of the orbital, while the $A_{1/2}$ RCI CV+CC value increases. It is remarkable that the NO approach provides similar values for all four bases in both the CV and CV+CC active spaces.

4.3.2.2 Assessing the reliability of NOs ...

While orbital rotations within each kappa symmetry in complete active spaces leave the wave function and energy invariant, rotations in incomplete active spaces perturb the wave function and can, therefore, lead to disastrous results as shown in Sec. IV C 3 and the appendix in A_I. Since the negative impact of rotations in incomplete active spaces has been established, it is important to assess the reliability of the NO basis. The small example presented in the Appendix of A_I already shows that the NO corresponds to rotations with small angles and therefore only slightly perturb the wave function.

In sodium, due to the single valence electron, core-valence correlation had to be included from the very beginning. The $2p3s \rightarrow nln'l'$ and $2s3s \rightarrow nln'l'$ classes of substitutions

Table 4.2: Hyperfine constant $A_{1/2}$ and mean radius of the spectroscopic $3s$ orbital for different optimization processes (see text).

	$A_{1/2}$(MHz)			
Active set	LBL	LBL-6s	LBL-W20	LBL-W15
DHF	633.698	633.698	633.698	633.698
MCDHF+CI CV				
3	691.693	692.023	723.437	736.966
4	837.150	844.857	856.808	862.500
5	870.354	879.427	887.737	895.054
6	895.195	903.684	915.213	920.594
7h	906.639	912.244	935.625	941.586
8h	939.435	938.593	938.594	941.357
9h	938.813	938.034	938.041	938.617
9h-NO	937.083	936.320	936.394	936.833
CI CV+CC:				
9h	855.247	860.768	876.257	883.897
9h-NO	890.654	889.932	890.486	890.390
			$\langle r \rangle$	
3s	4.12007	4.10243	4.06620	4.04693
3s-NO	4.05068	4.05484	4.04769	4.04951

generate an incomplete active space. The opening of the $n = 2$ shell would require the simultaneous excitations of nine electrons (two from the $2s$, six from the $2p$ and one from the $3s$) to recover completeness. Fortunately, the LBL orbital basis is 'not so far' from the natural-orbital basis, i.e., the corresponding rotations have small angles. Indeed, all spectroscopic orbitals are only slightly perturbed as shown by the leading contribution of their vector composition (at least 99.995 % in their analogous orbital in the LBL basis). Nevertheless, it is important to assess the quality of the natural-orbital basis, proving that the change due to the NO rotations in our specific incomplete active space remains small.

…through overlaps

Since the wave function is not invariant, the relation

$$|\Psi\{\phi\}\rangle = |\tilde{\Psi}\{\tilde{\phi}\}\rangle + |\tilde{\Gamma}\{\tilde{\phi}\}\rangle \tag{4.46}$$

defines $|\tilde{\Gamma}\{\tilde{\phi}\}\rangle$ as the gap between the wave function $|\Psi\{\phi\}\rangle$ built on the LBL orbital basis $\{\phi\}$ and the transformed wave function $|\widetilde{\Psi}\{\widetilde{\phi}\}\rangle$ built on the NO orbital basis $\{\widetilde{\phi}\}$. The

projection of $|\Psi\{\phi\}\rangle$ on itself,

$$\underbrace{\langle\Psi\{\phi\}|\Psi\{\phi\}\rangle}_{=1} = \langle\Psi\{\phi\}|\tilde{\Psi}\{\tilde{\phi}\}\rangle + \underbrace{\langle\Psi\{\phi\}|\tilde{\Gamma}\{\tilde{\phi}\}\rangle}_{:=\gamma_1}$$

allows to introduce

$$\gamma_1 = 1 - \langle\Psi\{\phi\}|\tilde{\Psi}\{\tilde{\phi}\}\rangle \ , \tag{4.47}$$

as a measure of the gap, as a function of the overlap between the LBL and transformed wave functions. Since the two orbital bases are nonorthogonal, the biorthogonalization method [225] is employed to evaluate the overlap $\langle\Psi\{\phi\}|\tilde{\Psi}\{\tilde{\phi}\}\rangle$. The biorthogonalization provides two additional bases, $\{\phi'\}$ and $\{\tilde{\phi}'\}$ such that $\langle\phi'_i|\tilde{\phi}'_j\rangle = \delta_{ij}$. The counter-transformation [225] acts on the mixing coefficients so that the total wave functions are invariant. If c'_i and $\tilde{c}'_i$ are the mixing coefficients resulting from the counter-transformations for the LBL and NO wave functions respectively, then

$$\begin{cases} |\Psi\{\phi\}\rangle = \sum_{i=1}^{N} c_i \, |\Phi_i\{\phi\}\rangle = \sum_{i=1}^{N} c'_i \, |\Phi'_i\{\phi'\}\rangle \\ |\tilde{\Psi}\{\tilde{\phi}\}\rangle = \sum_{i=1}^{N} \tilde{c}_i \, |\tilde{\Phi}_i\{\tilde{\phi}\}\rangle = \sum_{i=1}^{N} \tilde{c}'_i \, |\tilde{\Phi}'_i\{\tilde{\phi}'\}\rangle \ . \end{cases} \tag{4.48}$$

Starting from Eq. (4.47) and using the relations of Eq. (4.48) together with the biorthogonality conditions, γ_1 resumes to

$$\gamma_1 = 1 - \sum_{i=1}^{N} c'_i \tilde{c}'_i \ . \tag{4.49}$$

The overlap represents a measure of the change induced by transforming the LBL basis to the NO basis. It is therefore necessary to ensure that atomic properties converge with respect to the NO transformation. The natural orbitals are the orbitals that diagonalize the density matrix. If the active space was complete, re-computing the natural orbitals would be trivial since the density matrix would already be diagonal by definition. If the active space is incomplete, the density matrix re-calculated in the NO basis is no longer diagonal. The diagonalization of this new density matrix provides another NO basis. It is crucial to show that an iterative transformation to NO converges to a diagonal density matrix. Applying iteratively Eq. (4.46), the wave function is written

$$|\Psi\{\phi\}\rangle = |\tilde{\tilde{\Psi}}\{\tilde{\tilde{\phi}}\}\rangle + |\tilde{\tilde{\Gamma}}\{\tilde{\tilde{\phi}}\}\rangle + |\tilde{\Gamma}\{\tilde{\phi}\}\rangle \ . \tag{4.50}$$

The "second-order" overlap is therefore related to both γ_1 and γ_2 by the relation

$$\gamma_2 + \gamma_1 = 1 - \langle\Psi\{\phi\}|\tilde{\tilde{\Psi}}\{\tilde{\tilde{\phi}}\}\rangle \tag{4.51}$$

which is easily generalized for a number x of transformations as

$$\langle \Psi\{\phi\}|\Psi^{(x)}\{\phi^{(x)}\}\rangle = 1 - \sum_{j=1}^{x} \gamma_x \ . \tag{4.52}$$

…through iterative transformations

Iterative transformations to the natural orbitals are applied to the sodium ground state to assess the validity of the results presented in A_I. Each iteration consists in the following two-step procedure:

(i) For a given orbital basis, $\{\phi^{(i)}\}$ with $0 \leq i \leq x-1$ where x is the total number of iterations, the ASF expansion coefficients are determined through CI calculation.

(ii) A density matrix is computed using the mixing coefficients of step (i) and diagonalized. Its eigenvectors provide the rotations coefficients to build the new orbital basis, $\{\phi^{(i+1)}\}$, as linear combinations of $\{\phi^{(i)}\}$ with $0 \leq i \leq x-1$.

Table 4.3 presents the energy, the hyperfine constant and the overlap with the LBL wave function for an increasing number of transformations to the NOs. Each quantity is computed for two different active spaces, one based on CV correlation alone and another based on CV+CC correlation. These three properties seem to converge fast with the number of iterations, x. This result is reassuring and leads to the conclusion that performing small rotations in an incomplete active space only slightly perturb the wave function.

Table 4.3: Energy and hyperfine constant as a function of the number of times the NOs are computed. The effect of core-core correlation is also shown.

	Energy		$A_{1/2}$		$\lvert\langle\Psi\lvert\Psi^{(x)}\rangle - 1\rvert$	
x	CV	CV+CC	CV	CV+CC	CV	CV+CC
0	−162.0480429	−162.4106111	938.813	855.247	8.88[−16]	4.33[−15]
1	−162.0480373	−162.4105571	937.083	890.654	3.82[−7]	5.51[−5]
2	−162.0480354	−162.4105655	937.523	890.140	1.66[−7]	5.32[−5]
3	−162.0480356	−162.4105632	937.391	890.284	2.22[−7]	5.38[−5]
4	−162.0480356	−162.4105639	937.429	890.242	2.05[−7]	5.36[−5]
5	−162.0480356	−162.4105637	937.418	890.254	2.10[−7]	5.36[−5]
6	−162.0480356	−162.4105637	937.421	890.250	2.08[−7]	5.36[−5]
7	−162.0480356	−162.4105637	937.420	890.252	2.09[−7]	5.36[−5]
8	−162.0480356	−162.4105637	937.421	890.251	2.09[−7]	5.36[−5]
9	−162.0480356	−162.4105637	937.420	890.251	2.09[−7]	5.36[−5]
10	−162.0480356	−162.4105637	937.420	890.251	2.09[−7]	5.36[−5]

4.4 Concluding remarks

In this chapter, we investigated different possibilities of orbital basis for variational atomic structure calculations. We showed that complete finite orbital basis set methods are a real alternative to finite-difference MCDHF methods and have the advantage of describing continuum states easily. Focusing on the MCDHF orbital optimization strategy, we discussed the intrinsic quality of the HF orbitals inherited from verifying the so-called Brillouin theorem. We further showed that for multiconfiguration systems, one should pay attention to the spatial localization of correlation orbitals. As it turns out, small differences in radial orbitals can lead to huge effects on the computed property. We discussed the efficiency of using the natural orbitals for hyperfine structure calculations in neutral sodium. Our study showed the limitations of the current LBL strategy commonly adopted in all GRASP calculations. However, further work on the natural orbitals should be conducted to evaluate and understand fully their potential. Investigations on the transition rates of Na-like Si ($Z = 14$) following the work of Atalay *et al.* [242] are ongoing [243]. Preliminary results are promising. The computed gauge-discrepancy is reduced in the NO basis. Considering for example the [Ne]$7p\ ^2P^{\rm o}_{3/2} \rightarrow$ [Ne]$3s\ ^2S_{1/2}$ transition, Atalay *et al.* report a transition rate of $A^B = 1.046 \times 10^8$ s^{-1} in the Babushkin gauge with $dT = 0.071$, corresponding to $A^C = 1.126 \times 10^8$ s^{-1}. The values computed in the NO basis are $A^B_{\rm NO} = 1.205 \times 10^8$ s^{-1} and $A^C_{\rm NO} = 1.161 \times 10^8$ s^{-1}, corresponding to $dT = 0.036$. We observe an improvement by a factor two compared to the original results. Furthermore, this seems to confirm our findings in A$_{\rm II}$ that the Coulomb gauge would be more reliable, as the transition rate computed in the Coulomb gauge is less affected by the transformation to the NO basis. Similar analyses over the entire range of computed transition rates should be done before drawing any conclusion, but this small example motivates further studies.

Chapter 5

Group B: Nuclear physics applications

In this Chapter, we present the results of our published works with applications to nuclear physics. The first two papers (B_I and B_{II}) result from the joint theoretical and experimental studies on the hyperfine structure of tin while in the last two (B_{III} and B_{IV}) we focus on the isotope field shift in neutral iridium. The two papers of each subgroup are presented simultaneously as they are complementary, i.e., oriented to nuclear physics and to computational atomic physics, respectively.

5.1 Hyperfine structure of tin

The theory of hyperfine structure was presented in Sec. 3.5.1. The present section introduces the two papers B_I [61] and B_{II} [244] on the hyperfine structure of tin ($Z = 50$) that were recently published. They should be considered as complementary. B_I focuses mostly on the nuclear physics and relies on the calculated electronic factors to extract nuclear properties while B_{II} is dedicated to the details of the many-body atomic structure calculations. From the perspective of a thesis on computational atomic structures, the complementarity of these two papers is a perfect example of how atomic physics connects to other research fields and their challenges. Papers like B_I provide the larger context in which the atomic calculations are performed, which gives an easy and understandable purpose for the calculations while papers like B_{II} are essential for the development and improvements of the current computational tools for large-scale atomic calculations.

The variety of research fields involved, i.e., experimental and theoretical atomic physics, nuclear physics, and search for "new physics" leads to large international collaborations and networks gathering researchers from all around the world. B_I, for example, is the product

of the collaboration of 41 scientists spread over 23 different universities. Amongst them, 8 were responsible for the atomic structure calculations reported in B_{II}. The ability to communicate results and objectives along with a realist time line is a difficult and challenging task. From our computational perspective, the calculations were performed in the fall of 2018 and the papers published in the spring 2020 for B_I and early in 2021 for B_{II}. Two years and half were needed to ultimately communicate one number to the nuclear physics community and publish the details of the calculations. In the next sections, we will present both papers simultaneously from the atomic structure point of view, outlining the most important results as well as providing insightful materials that did not fit into the papers.

5.1.1 Computational strategies

One of the interesting features of the present study is the plurality of the computational strategies employed to calculate the electronic factors A_{el} and B_{el} (see Eq. 3.92) of the [Kr]$4d^{10}5s^2 5p6s\ ^{1,3}P_1^o$ excited states of neutral tin. In direct line with a previous study on the hyperfine structure of Zn [63, 245] different methodologies based on the same theoretical approach (the MCDHF+RCI method) and using the same computer program (Grasp) were performed in parallel with no or little communication between the different research groups. In a way, we show the complexity of performing large-scale calculations, which is (at least partially) due to the high flexibility that offers Grasp. A fourth independent set of calculations based on the configuration interaction Dirac-Fock-Sturm (CI-DFS) method [246, 247, 248, 249, 250] was also performed, allowing to validate the MCDHF+RCI results. Focusing on the Grasp calculations, the computational strategies differ in three major aspects: the choice of the multireference, the optimization of the correlation orbitals and the active space of the RCI calculations. Each of these aspects will be detailed. Practically, they are related to how CSFs-expansions are generated, whether used for the MCDHF step or the RCI step. The differences in the computational strategies are made explicit by referring to the three sets of calculations as S-MR-MCDHF, SrD-SR-MCDHF and SrD-MR-MCDHF.

Multireferences

The choice of the MR is guided by the concept of the Layzer complexes (see Sec. 3.6.2) or by previous experimental and theoretical studies. Table 5.1 presents the MR for each computational strategy. The case where the number of configurations is one trivially reduces to a SR. In the S-MR-MCDHF strategy, the choice of the MR is guided by a previous study, which showed the importance to include the $5s5p^3$ configuration[1] [251]. The fourth configuration, $5s^2 5p7s$, is included to account for the LS-term dependence between the

[1] The [Kr]$4d^{10}$ is common to all configurations and is therefore omitted.

$5s^2 5p6s\ {}^3P_1^o$ and $5s^2 5p6s\ {}^1P_1^o$ levels [8, §3.8]. Finally, the third MR is chosen by performing small calculations to identify the configurations with the highest mixing coefficient and includes three configurations that belong to the $\{5^3 6^1\}$ Layzer complex defined by the reference configuration.

Table 5.1: Multireference configurations for the S-MR-MCDHF, SrD-SR-MCDHF and SrD-MR-MCDHF computational strategies. The configurations in parenthesis are not included in the calculations but were used to probe the sensitivity of the hyperfine structure factors to the MR.

m	S-MR-MCDHF	SrD-SR-MCDHF	SrD-MR-MCDHF
1	$5s^2 5p6s$	$5s^2 5p6s$	$5s^2 5p6s$
2	$5s^2 5p5d$		$5p^3 6s$
3	$5s5p^3$		$5s5p5d6s$
4	$5s^2 5p7s$		$(5s^2 5p6d)$
5			$(5s5p^2 6p)$
6			$(5s^2 6s6p)$
7			$(5s^2 5d6p)$

Further investigations are performed to assess the quality of the chosen MR. This is done by progressively enlarging the MR set by additional configurations according to column 4 of Table 5.1. Note that all configurations but the sixth one belong to the complex. The same orbital basis is used for all calculations and includes 5 correlation layers. The optimization of the orbitals targets VV correlation for which the CSFs are generated by allowing SD substitutions from the valence orbitals with $n \geq 5$. Using this orbital basis set, RCI calculations are performed, enlarging progressively the number of configurations in the MR and including CV correlation by allowing SrD substitutions from the $4d$ orbital. Fig. 5.1 shows $A_{\text{el}}[{}^3P_1^o]$ as a function of the number of CSFs in the MR for both correlation models, i.e., VV and VV+CV($4d$) where the $4d$ in parenthesis emphasizes that only the $4d$ subshell was opened to SrD substitutions. The cases for which $m = 1$ and $m = 2$ are added for the VV correlation model to show the smooth convergence of $A_{\text{el}}[{}^3P_1^o]$. We observe that the VV calculations converge for $m = 3$, which justifies the choice of the MR of the SrD-MR-MCDHF calculations. However the VV+CV($4d$) calculations demonstrate that additional configurations are required to reach convergence within that correlation model. Furthermore, its convergence is irregular and the difference between the VV and VV+CV calculations increases for an increasing number of configurations. Unfortunately, enlarging the MR is computationally costly since the number of CSFs in the subsequent calculations that describe different correlation effects increases more rapidly as a function of the increasing orbital set. This is shown in Fig. 5.2 that displays the number of CSFs generated for each calculation for an increasing number of configurations. On the left figure only the VV calculations are shown while on the right both VV and VV+CV calculations appear. Note first that the introduction of CV leads to active spaces ~ 20 times larger. Second, going from $m = 3$ to $m = 7$ at least doubles the number of CSFs. One should therefore limit the size of the MR so that additional correlation layers can be included before reaching the limit of the available computational resources.

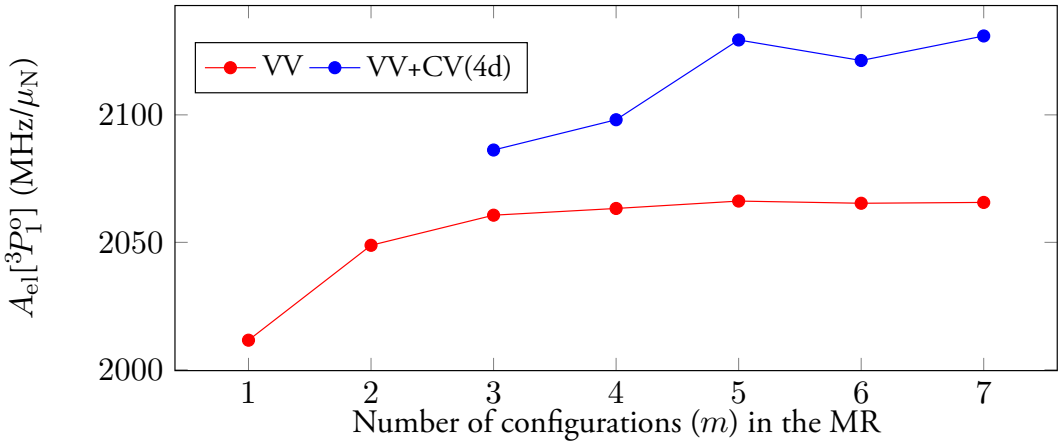

Figure 5.1: Convergence of the A[$^3P_1^o$] value as a function of the number of configurations in the MR according to the SrD-MR-MCDHF column of Table 5.1. Two sets of calculations are presented. They both include the same 5 correlations layers that are optimized on VV correlation. One includes part of CV correlation by allowing SrD substitutions from the $4d$ orbital.

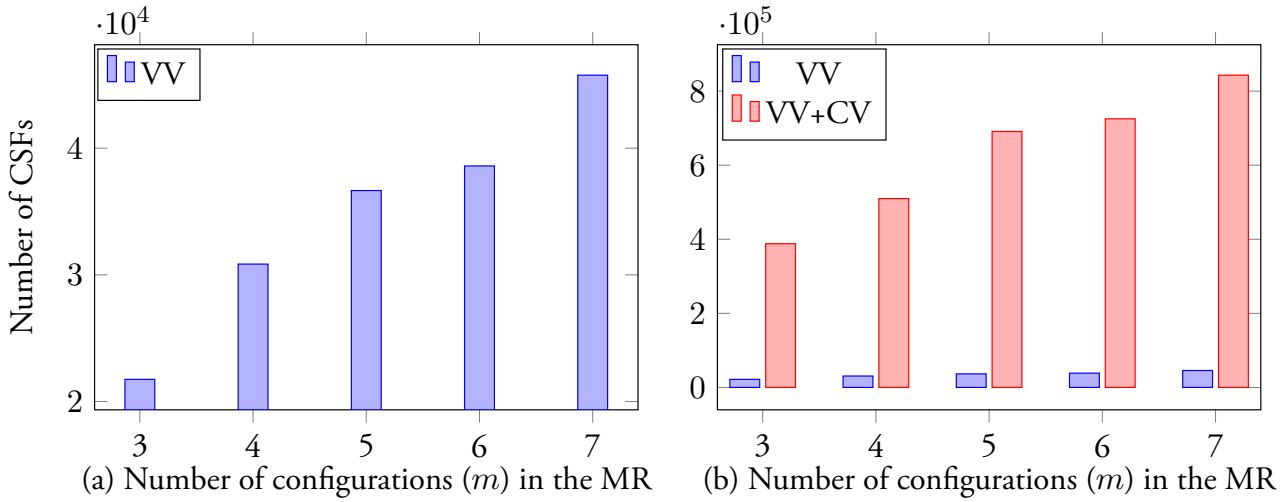

Figure 5.2: Number of CSFs for an increasing number of configurations in the MR. (a) shows only the VV calculations while (b) presents both the VV and the VV+CV calculations. The orbital set includes all spectroscopic orbitals and five correlation orbitals per symmetry (s, p, d, and f).

Optimization of the correlation orbitals

The optimization of the orbital basis is performed layer by layer. Prior to the optimization of the correlation orbitals, the spectroscopic orbitals, i.e., the orbitals occupied in at least one CSF belonging to the MR, are optimized together. An analysis of the spectroscopic orbitals in terms of their individual energy and/or their spatial localization helps to determine the type of electron substitutions to be included. Fig. 5.3 displays the large components of all spectroscopic orbitals with $\kappa < 0$, i.e., $1s_{1/2}$, $2s_{1/2}$, $2p_{3/2}$, . . . , showing only one rela-

tivistic orbital per l-symmetry to lighten the graph. We identify three spatial areas denoted A, B, C in Fig. 5.3 that are approximately delimited by the dashed lines. A is the closest to the nucleus and expectedly all orbitals lying dominantly in that area are the core orbitals. C is the furthest away from the nucleus and the corresponding orbitals ($5s$, $5p$, $5d$ and $6s$) are the valence orbitals. The last region, B, lies between the core and the valence and includes the $4s$, $4p$ and $4d$ orbitals. A refined analysis shows that $\langle r\rangle_{4s} < \langle r\rangle_{4p} < \langle r\rangle_{4d}$, which, combined with that there are 10 d electrons, led us to open the $4d$ orbital to substitutions in the optimization of the correlation orbitals. This corresponds to the optimization strategy employed in the SrD-MR-MCDHF, where the SrD explicitly refers to the allowed SrD substitutions from the $4d$ orbital. In the other approaches, different considerations were taken into account to define the optimization strategy. The SrD-SR-MCDHF approach allows SrD substitutions from all spectroscopic orbitals but the $1s$. The choice of a SR indeed reduces the number of CSFs generated and allows electrons to be correlated deeper in the core. Finally, the S-MR-MCDHF procedure optimizes the correlation orbitals allowing solely S substitutions. Although this last strategy lacks of energetically important CSFs generated from D substitutions, the use of S substitutions for hyperfine structures can be justified from perturbation theory (see Sec. 5.1.2 for a dedicated discussion).

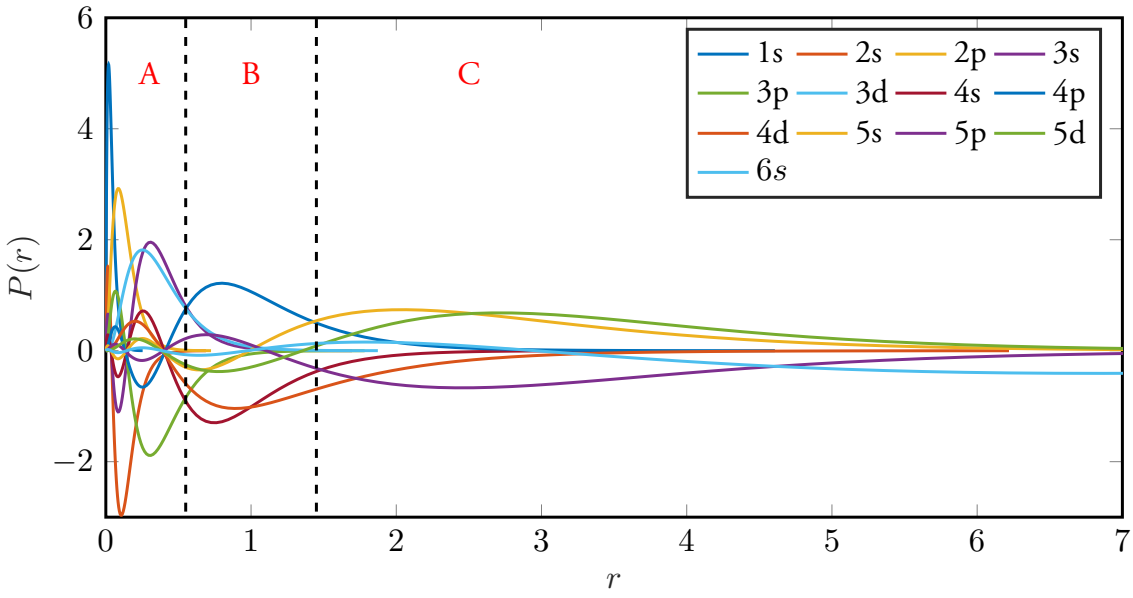

Figure 5.3: Large radial components of the spectroscopic orbitals belonging to the MR. Only orbitals with $\kappa < 0$ are shown (those with $j = l + 1/2$). The straight dashed lines separate the different spatial regions A, B and C (see text for details).

RCI active space

As explained in Sec. 3.6.2, the MCDHF optimization of the orbitals is followed by RCI calculations. Breit interaction and leading QED corrections are included and the active

space is further enlarged. Leaving the details to B_{II}, it is nevertheless worth mentioning some specificities of each strategy, in line with the analyses presented above. The S-MR-MCDHF approach adds CSFs generated by D substitutions from the valence orbitals, which are energetically dominant. The SrD-SR-MCDHF approach allows further SD substitutions from the core orbitals. Because of the use of a SR, important T substitutions need to be included explicitly, which increase tremendously the size of the active space. Nevertheless we showed that the effect of T substitutions is to counterbalance the effect of the D substitutions (see Fig. 2 of B_{II}) and thus they must be taken into account. Regarding the SrD-MR-MCDHF approach, the RCI calculations included S substitutions from all orbitals and SrD substitutions from the $4p$ orbitals as motivated by the spatial localization analysis of the spectroscopic orbitals. Similar substitutions from the $4s$ were considered but the computational resources at our disposal did not allow us to include them.

5.1.2 Perturbative approach

In this section, we investigate the role of the S substitutions through a perturbative analysis to justify their importance when computing electronic hyperfine structure factors. We follow the work by Verdebout *et al.* [226] who employed a non-relativistic perturbative approach to efficiently target the configurations that contribute the most to the expectation value of a given operator. Their analysis is reinvestigated here to justify the inclusion of single substitutions. Consider that the DC Hamiltonian can be rewritten as $\mathcal{H}_{\mathrm{DC}} = \mathcal{H}_0 + \lambda V$, where $\mathcal{H}_0$ is the zero-order Hamiltonian consisting of the sum of one-electron Hamiltonians for which the eigen-solutions are known

$$\mathcal{H}_0 \left|n^{(0)}\right\rangle = E_n^{(0)} \left|n^{(0)}\right\rangle \tag{5.1}$$

and λ is the expansion parameter related to the perturbation V, which is the electron-electron repulsion potential. Perturbation theory leads us to build the eigenfunction of $\hat{\mathcal{H}}_{\mathrm{DC}}$ as

$$\begin{aligned} \left|n\right\rangle = &\left|n^{(0)}\right\rangle + \lambda \sum_{k\neq n} \left|n^{(0)}\right\rangle \frac{V_{kn}}{E_n^{(0)} - E_k^{(0)}} \\ &+ \lambda^2 \left(\sum_{k\neq n} \sum_{k'\neq n} \left|n^{(0)}\right\rangle \frac{V_{kn}V_{k'n}}{\left(E_n^{(0)} - E_k^{(0)}\right)\left(E_n^{(0)} - E_{k'}^{(0)}\right)} \right. \\ &\left. - \sum_{k\neq n} \left|n^{(0)}\right\rangle \frac{V_{nn}V_{kn}}{\left(E_n^{(0)} - E_k^{(0)}\right)^2} \right) \end{aligned} \tag{5.2}$$

to second order of λ^2. In this expansion $V_{ij} = \langle i^{(0)}|V|j^{(0)}\rangle$ is the matrix elements of the perturbation V between two eigenfunctions belonging to the zero-order space. The

expectation value of any operator $\langle n|X|n\rangle$ can then also be expanded in power of λ. To the second order, it gives

$$\begin{aligned}\langle n|X|n\rangle = &\langle n^{(0)}|X|n^{(0)}\rangle \\ &+ \lambda \left(\sum_{k\neq n} \frac{X_{nk}V_{kn}}{E_n^{(0)} - E_k^{(0)}} + \sum_{k\neq n} \frac{X_{kn}V_{kn}}{E_n^{(0)} - E_k^{(0)}} \right) \\ &+ \lambda^2 \left(\sum_{k\neq n}\sum_{k'\neq n} \frac{X_{kk'}V_{kn}V_{k'n}}{\left(E_n^{(0)} - E_k^{(0)}\right)\left(E_n^{(0)} - E_{k'}^{(0)}\right)} \right. \\ &+ \sum_{k\neq n}\sum_{k'\neq n} \frac{X_{nk}V_{kk'}V_{k'n}}{\left(E_n^{(0)} - E_k^{(0)}\right)\left(E_n^{(0)} - E_{k'}^{(0)}\right)} - \sum_{k\neq n} \frac{X_{nk}V_{nn}V_{kn}}{\left(E_n^{(0)} - E_k^{(0)}\right)^2} \\ &\left. + \sum_{k\neq n}\sum_{k'\neq n} \frac{X_{kn}V_{kk'}V_{k'n}}{\left(E_n^{(0)} - E_k^{(0)}\right)\left(E_n^{(0)} - E_{k'}^{(0)}\right)} - \sum_{k\neq n} \frac{X_{kn}V_{nn}V_{kn}}{\left(E_n^{(0)} - E_k^{(0)}\right)^2} \right)\end{aligned} \tag{5.3}$$

The terms of first order in λ are known as the 'crossed second-order' corrections [252] since they require the evaluation of V_{nk} and X_{nk} and therefore the CSFs that contribute the most to $\langle n|X|n\rangle$ are those that interact with the reference CSF through the Coulomb repulsion perturbation and the operator of interest, here the hyperfine structure operators. Note that the zero-order space is composed of the CSFs belonging to the Layzer complex, i.e., leading to a degeneracy of the energies $E_i^{(0)}$, $E_j^{(0)}$ while the first-order space is composed of the CSFs that interact with the MR through the perturbation V_{nk}. However, one can show that treating the non-degenerate case is enough and the results are easily generalized [115, §3.3]. The first-order correction to the hyperfine expectation value is exclusively dependent on the first-order wave function. However the second-order contribution arises from both

$$\langle n^{(1)}|X|n^{(1)}\rangle \tag{5.4}$$

and

$$\langle n^{(0)}|X|n^{(2)}\rangle \tag{5.5}$$

types of matrix elements. One should therefore look for CSFs that are energetically important and will constitute the first-order space, i.e., SD substitutions from the reference and then CSFs that are important for the hyperfine structure in the second-order space. Since the hyperfine operators are one-body operators, only the CSFs generated by S substitutions are of interest. Going one step further could be to consider the energetically first-order space as the 'hyperfine-structure zero-order space' and then generating the important CSFs by allowing S substitutions from this new zero-order space. In this way, the generated CSFs could be T substitutions from the reference configurations, hence confirming the importance of T substitutions.

5.1.3 Correlation between electronic factors

A key argument to assess the reliability of the calculations of hyperfine electron factors is the empirically-observed correlation between A_{el} and B_{el} when looking at their convergence with an increasing number of correlation layers or with the increasing size of the RCI active space (see e.g., [253, 254]). In B_{II} we rely greatly on this argument to impose a shift on B_{el} by considering that

$$\frac{|B - B_{\text{expt}}|}{B_{\text{expt}}} \approx \frac{|A - A_{\text{expt}}|}{A_{\text{expt}}} \,. \tag{5.6}$$

It is often assumed that the radial behaviour of A_{el} and B_{el} is proportional to r^{-3}, which explains the correlation between the two quantities and justify the use of (5.6). Although this is obvious from non-relativistic considerations (see e.g., the non-relativistic hyperfine operators in Ref. [8, §8.8]), the relativistic operators $\mathbf{T}^{(1)}$ (3.90) and $\mathbf{T}^{(2)}$ (3.91) show at first sight a radial dependency of r^{-2} and r^{-3}, respectively. Following Johnson [20, §5.2] we will demonstrate how the magnetic dipole and electric quadrupole operators ultimately have the same radial dependence. The proof is given in the DHF approximation for a system with a single valence electron outside a closed shell core. In that specific case, the core electrons do not contribute to the hyperfine electronic factors which then reduce to

$$\langle n_v \kappa_v j_v m_v | t_0^{(1)} | n_v \kappa_v j_v m_v \rangle = 2\kappa_v \, \langle -\kappa_v j_v m_v | C_0^{(1)} | \kappa_v j_v m_v \rangle \left(\frac{1}{r^2} \right)_{vv} \,, \tag{5.7}$$

and

$$\langle n_v \kappa_v j_v m_v | t_0^{(2)} | n_v \kappa_v j_v m_v \rangle = - \langle \kappa_v j_v m_v | C_0^{(2)} | \kappa_v j_v m_v \rangle \left\langle \frac{1}{r^3} \right\rangle_{vv} \,, \tag{5.8}$$

where $t_0^{(k)}$ (k=1,2) are the one-electron hyperfine operators. Focusing only on the radial integrals, they are defined, in all generality, as

$$\left(\frac{1}{r^2} \right)_{vw} = \int_0^\infty \frac{dr}{r^2} \left(P_v(r) Q_v(r) + Q_w(r) P_w(r) \right) \tag{5.9}$$

and

$$\left\langle \frac{1}{r^3} \right\rangle_{vw} = \int_0^\infty \frac{dr}{r^3} \left(P_v(r) P_w(r) + Q_w(r) Q_v(r) \right) \,. \tag{5.10}$$

Observe how the magnetic dipole operator mixes the small and large components while the electric dipole operators does not. Consider the non-relativistic limit with the usual Pauli approximation discussed in Sec. 2.3.6, which is such that

$$Q_v \approx -\frac{1}{2c} \left(\frac{d}{dr} + \frac{\kappa}{r} \right) P_v \,, \tag{5.11}$$

according to Eqs. (2.83) and (2.84). The radial expectation values $\left(\frac{1}{r^2}\right)_{vw}$ and $\left\langle\frac{1}{r^3}\right\rangle_{vw}$ are related to each other by [20, §5.2]

$$\left(\frac{1}{r^2}\right)_{vw} = \frac{1}{2c}\left(\frac{P_v P_w}{r^2}\right)_{r=0} - \frac{\kappa_v + \kappa_w + 2}{2c}\left\langle\frac{1}{r^3}\right\rangle_{vw} . \tag{5.12}$$

Note that in the above expression P_v, P_w and $\left\langle\frac{1}{r^3}\right\rangle_{vw}$ must be computed using non-relativistic wave functions. The first term can be seen as an offset due to the contribution of s electrons while the second term demonstrates the proportionality between the radial expectation value of the magnetic dipole operator and electric quadrupole operator.

5.1.4 Uncertainties

The variational MCDHF+RCI method lacks, just as other many-body methods such as MBPT, an efficient procedure to estimate uncertainties. Furthermore, the origin of the theory–experiment discrepancies is a mix between numerical, computational and theoretical errors. Numerical inaccuracy arises from, e.g., the numerical integration algorithms and could therefore be improved or, at least, tested, as suggested in Ref. [25]. Computational uncertainties are hard to assess, they are related to the computational strategy employed to perform the calculations. The present example of the hyperfine structure of tin illustrates perfectly how results obtained with the same theoretical model are dependent on the computational strategy. In order to provide realistic uncertainties, one should therefore perform a careful investigation that compares the orbital bases, the active spaces, the computed energies etc. Finally, errors can also arise from the theoretical model that is used. As an example, if the Breit interaction is not taken into account, the model is not complete and one should therefore try to estimate its effect. Fortunately the influence of the Breit interaction can be measured by performing calculations with and without adding it to the Hamiltonian, which might not be the case for other interactions.

In the present work, extra care was put into the estimation of reliable uncertainties. Different means were employed e.g., considering the results from the four sets of calculations as a statistical sample or using the correlation between the electronic factors (see Sec. 5.1.3). This is particularly important when the atomic structure quantities are later combined with experiments to extract information about e.g., nuclear properties. We ultimately estimate the uncertainty on $B_{\mathrm{el}}[^1P_1^{\mathrm{o}}]$ to be 50 MHz/μ_{N}, which corresponds to a relative uncertainty of $\sim 7\%$ on our final value, $B_{\mathrm{el}}[^1P_1^{\mathrm{o}}] = 706$ MHz/μ_{N}. Although this uncertainty could be considered as being large, we are convinced that to further use $B_{\mathrm{el}}[^1P_1^{\mathrm{o}}]$, a reliable uncertainty is mandatory to prevent falsely (in)accurate results for e.g., nuclear quadrupole moments. The accuracy of the nuclear moments is therefore limited by both the experimental measurements of B and the theoretical predictions of B_{el}, as it should. Recent calculations using the relativistic Fock-space couple-cluster method were recently performed to

determine the hyperfine structure factors for the same $B_{\mathrm{el}}[^1P_1^{\mathrm{o}}]$ level, showing reasonable agreement with our value [255].

5.1.5 Nuclear physics outcomes

The hyperfine structure provides information about the nuclear structure. Indeed, it arises from the coupling of the electron cloud with the electromagnetic field of the nucleus. Calculations of hyperfine structure electronic factors are therefore often realized in the ultimate goal to extract the relevant nuclear information. This was done in $\mathrm{B_I}$ by combining the computed $B_{\mathrm{el}}[^1P_1^{\mathrm{o}}]$ factor with experimental measurements of the hyperfine quadrupole coupling constant $B[^1P_1^{\mathrm{o}}]$. In the context of nuclear physics, tin is of particular importance as it is the element with the largest number of stable isotopes. The experiment was performed over a long series of odd-N isotopes with a nucleon number ranging from 117 to 131. Due to the fact that all its proton shells are closed, tin only acquires quadrupole moments because of the unpaired, valence neutron, which polarizes the protons. Since the remaining valence neutrons have the opposite parity and lower angular momenta, isomeric states were also detected in the experiment. Therefore changes in the nuclear structure between the ground and isomeric state are also investigated in addition to the evolution of the nuclear structure along the isotopic chain. The experiment was performed at the CERN-ISOLDE laboratory [256] at which the atomic tin beam was produced by uranium fission. A tunable laser was used to excite the tin atoms to their $^3P_1^{\mathrm{o}}$ and $^1P_1^{\mathrm{o}}$ excited states using two complementary transitions from the ground state (see Fig. 1b of $\mathrm{B_I}$).

The experiment ultimately provided information on the nuclear quadrupole moments and the difference in mean square radii between the nuclear ground and isomeric states. Trends were found and compared to the cadmiun isotones, which have only two protons less than tin. Observations are listed in $\mathrm{B_I}$ (see the section on experimental trends) and we hereby highlight the most important ones. First, there is a significant attenuation of the quadrupole moments going from cadmium ($Z = 48$) to tin ($Z = 50$), which is due to the closing of the proton shell and second, all trends follow simple polynomials, sometimes linear and at most quadratic.

The experiment was followed by nuclear structure calculations in the framework of the nuclear density functional theory (for more information about nuclear density functional theory, see e.g. [257]). The comparison between the experimental results and the *ab initio* nuclear calculations provides insight into the nuclear models. The results are satisfactory in the sense that they reproduce well the observed linear or quadratic trends for both Cd and Sn. Another interesting feature is that the quadrupole moment should vanish at mid (neutron) shell, which is, according to the seniority coupling scheme, happening at $N = 75$. Experimentally, this zero crossover point is at $N = 73$, which should alert us that some of our parameters e.g., the single-particle energy of the valence neutron, might not be opti-

mal. Hence, reproducing the experimental results using *ab initio* calculations is an efficient way to refine our theoretical models. This stresses the need for accurate measurements.

5.2 Isotope shift of iridium

The mathematical definition of the isotope shift was succinctly presented in Sec. 3.5.2. The present section aims to comment our two published papers B_{III} [258] and B_{IV} [259] on the isotope shifts and nuclear properties of ^{196,197,198}Ir ($Z = 77$). The IS determination is primarily of interest in nuclear physics as it is an efficient mean to extract information about the nucleus (size, shape, deformations, ...). This transpires clearly from Eq. (3.111), from which one could extract the difference in mean square radii along an isotope chain, providing that the FS were previously measured. The determination of the FS from first principles is a complex task, requiring atomic calculations for the FS line parameter(s) and nuclear modelling for the mean square radii. In the context of GRASP, the root mean square (rms) radii are either taken from available compilations or computed according to the formula

$$\sqrt{\langle r^2 \rangle^A} = 0.836 A^{1/3} + 0.570 \qquad \text{(in fm)} \; . \tag{5.13}$$

Then, the nuclear potential is built by adjusting the Fermi distribution (3.166) so that the corresponding rms radius matches the one computed with the above formula.

5.2.1 Mass shifts and King plots

In the context of atomic structure calculations, 'FS calculations' more commonly refer to the *ab initio* determination of the field shift parameters, which are then combined with measured FS to extract nuclear mean square radii. We already argued in Sec. 3.5.2 that the FS becomes dominant over the MS for heavy systems, allowing us to neglect the latter so that $\delta\nu_{\text{IS},k} \approx \delta\nu_{\text{FS},k}$. From non-relativistic considerations the MS can be estimated using the "scaling law approximation" as

$$\delta\nu_{\text{MS},k} = \delta\nu_{\text{NMS},k} + \delta\nu_{\text{SMS},k} \approx -\frac{(1 \pm 0.5)}{1836.1} \nu_0 \frac{M' - M}{M M'} \; , \tag{5.14}$$

where ν_0 is the frequency of the line and assuming the following crude estimation of the specific mass shift: $|\delta\nu_{\text{SMS},k}| < 1/2 |\delta\nu_{\text{NMS},k}|$. Considering the case of interest in our paper with e.g., the 193–197 isotope pair and the transition line at 247.587 nm (or 1 210 857 GHz), the MS is approximated by $35 \leq \delta\nu_{\text{MS},k} \leq 100$ MHz, which is below the experimental uncertainty of 0.7 GHz (see B_{III}).

For light(er) systems, the MS must be included and the corresponding atomic parameters computed, which increases the complexity of the calculations and is therefore often accompanied by a decrease in accuracy. To overcome this issue, one can separate experimental MS and FS using the King plot technique [139, §6.1] (see e.g., [260, 261, 262, 263] for recent applications).

The basic idea is to combine the IS measurements for multiple isotope pairs and (at least) two electronic transitions. Consider the modifying factor for the isotope pair (A,A')

$$\mu_{(AA')} = \frac{(M_R - M_{R'})M_A M_{A'}}{(M_A - M_{A'})M_R M_{R'}} \tag{5.15}$$

where R, R' refer to the isotope pair of reference.[2] The modified shifts for the atomic transitions k and k' are

$$\mu_{(AA')}\delta\nu^{AA'}_{\mathrm{IS},k} = \delta\nu^{RR'}_{\mathrm{MS},k} + \mu_{(AA')}\delta\nu^{AA'}_{\mathrm{FS},k} \tag{5.16}$$

and

$$\mu_{(AA')}\delta\nu^{AA'}_{\mathrm{IS},k'} = \delta\nu^{RR'}_{\mathrm{MS},k'} + \mu_{(AA')}\delta\nu^{AA'}_{\mathrm{FS},k'} \tag{5.17}$$

respectively. Plotting the modified IS of the transition k' against that of the transition k for multiple isotope pairs should exhibit a linear behaviour. The corresponding straight line passes through $(\delta\nu^{RR'}_{\mathrm{MS},k}, \delta\nu^{RR'}_{\mathrm{MS},k'})$ and its gradient is $\delta\nu^{AA'}_{\mathrm{FS},k'}/\delta\nu^{AA'}_{\mathrm{FS},k}$ (see Fig. 6.1 in Ref. [139]). Therefore, providing information for one given isotope pair, the FS and/or MS can be retrieved, hence allowing the determination of the nuclear parameters of interest.

However, since the 1960's non-linearities in the King plots were detected. One example occurred when King himself analyzed the spectrum of Sm ($Z = 62$) [264] which shook one of his fundamental hypothesis, that is *" the isotope shift due to the finite nuclear volume can be split into an electronic factor E (different for Lines A and B) multiplied by a nuclear volume factor V (different for the pairs of isotopes 1, 2, 3)"* [264]. Although he concluded that his assumption holds, the existence of non-linearities in King plots are nowadays established. Furthermore, the recent years saw an increasing number of publications on the topic, considering these non-linearities as potential sources of new physics, e.g., the signature of a new boson [78, 79]. Further investigations in the IS of Yb^+ ($Z = 70$) however rather showed that these non-linearities are most probably due to nuclear deformations [265], using a slightly different formalism than the one developed in RIS4 [141]. Examples of non-lineraties in King plots were recently found in Sr [266, 267] or ionized Ar [268], stressing the need for improving the accuracy of the measurements and/or the atomic calculations [269].

[2] The modified factor sometimes takes the simpler form $\mu_{(AA')} = (M_A - M_{A'})/M_A M_{A'}$ which present some advantages and disadvantages (see [139, §6.1] for details).

5.2.2 Variational approach

The details of the computational strategy applied to determine the FS in iridium isotopes are already given in B_{IV}. Nevertheless, it is worth extending our analysis. In particular, we performed isotope-dependent calculations, for which the computational model was simplified by choosing a single-reference picture over the more common multireference approach adopted in the two published papers. The former has the advantage of reducing the number of CSFs and hence the size of the calculations and the corresponding computational time. We were then able to perform separate calculations for isotopes with mass numbers 191, 193, 196, 197 and 198. Since the MS operators are not included in the Hamiltonian, the isotopic change in the theoretical transition energy only depends on the different nuclear potentials, i.e., it is not contaminated by MS contributions and strictly reflects the level FS. Because the isotope dependence is embedded in the variational process, we refer to this method as a "variational approach", in opposition to the perturbative approach used in B_{III} and B_{IV}.

The isotope field shift is therefore simply given as

$$\delta\nu_{\mathrm{IS},k}^{AA'} = \frac{\Delta E_k^A - \Delta E_k^{A'}}{h} \,, \tag{5.18}$$

where ΔE_k^A is the transition energy associated to the spectral line k and isotope with mass number A. Then, one could be tempted to use Eq. (3.111) to extract $\Delta F_{k,0}$ as

$$\Delta F_{k,0} = \frac{h\delta\nu_{\mathrm{IS},k}^{AA'}}{\delta\langle r^2\rangle^{AA'}} \tag{5.19}$$

where the $\delta\langle r^2\rangle^{AA'}$ values are simply taken from GRASP.[3] In our calculations, we have, in fm^2,

$$\delta\langle r^2\rangle^{198,197} = 0.09 \leq \delta\langle r^2\rangle^{198,A'} \leq 0.63 = \delta\langle r^2\rangle^{198,191} \,. \tag{5.20}$$

for the considered range $A' = 197 - 191$. The difference in mean square radius $\delta\langle r^2\rangle^{AA'}$ is given for each isotopic pair in Table 5.2. Using Eq. (5.19) can lead to strong discrepancies between isotope pairs due to the non-linear behaviour that is expected from the rFS (3.106). An alternative picture inspired by the King plots is to display $\delta\nu_k^{AA'}$ as a function of $\delta\langle r^2\rangle^{AA'}$ as it is done in Fig. 5.4 for the transition at 247 nm. Although the SR calculations are slightly different than the MR calculations presented in B_{III} and B_{IV}, they rely on the same strategy, i.e. they include VV correlation in the MCDHF optimization process and part of CV correlation in RCI calculations. We present here only the last two

[3] Note that one could chose "manually" $\langle r^2\rangle^{A'}$ so that $\delta\langle r^2\rangle^{AA'}$ is exactly one, i.e., the choice of the mean square radii does not play any role.

RCI steps, which both include SD substitutions from the $5d$ orbital but only the largest calculations include S substitutions from all orbitals with $n \geq 4$. The Breit interaction and QED corrections are included in all RCI calculations. Assuming in a first approximation that the linear relation (5.19) holds, one can extract $\Delta F_{247,0}$ using a linear regression. Fig. 5.4 displays the FS as a function of the variation in mean square radii for all pairs of isotopes. A linear fit, which crosses the origin, is performed on the data points and shown on the figure to guide the eyes.

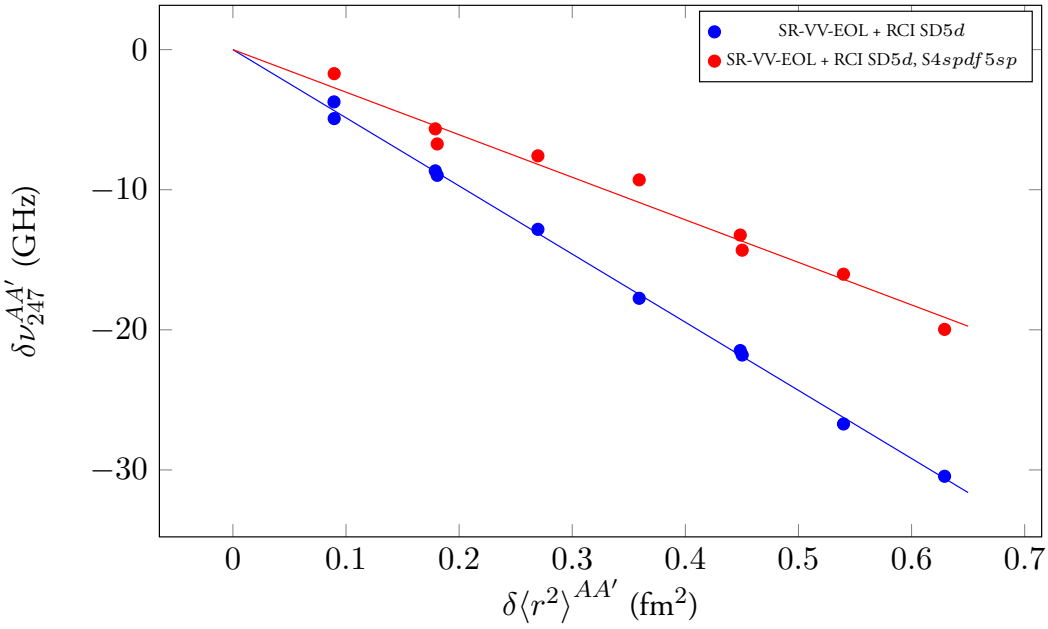

Figure 5.4: Field shifts as a function of the difference in mean radii for pairs of isotopes for different correlation models. The $\delta\langle r^2\rangle^{AA'}$ value is given for each isotopic pair in Table 5.2.

Table 5.2: Difference in nuclear mean square radius $\delta\langle r^2\rangle^{AA'}$ extracted from the GRASP package for the range $A, A' = 198, 197, 196, 193, 191$ with $A' < A$ in fm^2.

$A \setminus A'$	198	197	196	193	191
198		+0.09	+0.18	+0.45	+0.63
197			+0.09	+0.36	+0.54
196				+0.27	+0.45
193					+0.18

Analyzing first the calculations that do not include S substitutions, we extract $\Delta F_{247,0} = -48.6$ GHz/fm^2. Interestingly, if we extract $\Delta F_{247,0}$ for each isotope pair according to Eq. (5.19), the values range from -55.0 to -41.7 GHz/fm^2 for the 198–197 and 197–196 isotope pairs, respectively. This confirms that the FS parameter should not be extracted from a single isotope pair when using this variational approach, especially when considering small $\delta\langle r^2\rangle^{AA'}$.

Comments on the reformulated field shift

According to Ref. [141], the rFS (3.106) can be rewritten in terms of two new FS parameters that account for a varying electron density (ved) inside the nucleus, namely $\Delta F_{k,0}^{(0)\text{ved}}$ and $\Delta F_{k,0}^{(1)\text{ved}}$, such that

$$\delta\nu_{\text{IS},k}^{AA'} \approx \frac{1}{h}\left(\Delta F_{k,0}^{(0)\text{ved}} + \Delta F_{k,0}^{(1)\text{ved}}\delta\langle r^2\rangle^{AA'}\right)\delta\langle r^2\rangle^{AA'} \quad . \tag{5.21}$$

Taking advantage of the Fermi distribution (3.166) that models the nuclear charge density, it is possible to demonstrate that (5.21) is a rather good approximation of (3.106). This new expression of the rFS has the advantage of hiding the dependence in higher nuclear momenta into the FS parameters. The disadvantage is, obviously, that the FS is now quadratic in $\delta\langle r^2\rangle^{AA'}$. Nevertheless, it is interesting to evaluate $\Delta F_{k,0}^{(0)\text{ved}}$, as it contributes the most to the FS and includes the largest part of the correction that arises from a varying electron density (the contribution from $\Delta F_{k,0}^{(1)\text{ved}}$ is usually much smaller). Since the variational calculations described above include the effect of a varying electron density through the different nuclear potentials in the Hamiltonians, one could use a fit of the type $y = ax^2 + bx$ instead of a linear fit as it is done in Fig. 5.4 so that the coefficients extracted from the fit compare to $\Delta F_{k,0}^{(0)\text{ved}}$ and $\Delta F_{k,0}^{(1)\text{ved}}$. The latter parameters are computed, in the SR picture, to be -43.3 GHz/fm^2 and -0.0427729 GHz/fm^4, respectively while the extracted coefficients from the quadratic fit are $a = -48.5$ GHz/fm^2 and $b = -0.232$ GHz/fm^4. The second coefficient, b, is, however, highly sensitive to the fitting procedure and should not be considered as reliable before any additional investigation. Note that in our published papers, the aim was to extract nuclear deformations, and hence we needed to compute the $\Delta F_{k,0}$, $\Delta F_{k,2}$, $\Delta F_{k,4}$ and $\Delta F_{k,6}$ parameters. The evaluation of $\Delta F_{k,0}^{(0)\text{ved}}$ and $\Delta F_{k,0}^{(1)\text{ved}}$ helps to measure the importance of the effect of a varying electron density and the determination of reliable theoretical error bars. According to our published results, this effect is of the order of 7%, which stresses the need taking a varying electron density into account. This is confirmed in the SR picture by considering the relative discrepancy between the computed values of $\Delta F_{k,0} = -46.4$ GHz/fm^2 and $\Delta F_{k,0}^{(0)\text{ved}} = -43.3$ GHz/fm^2.

5.2.3 Multireference, single substitutions and root flipping

The dominant configurations in the low-lying part of the Ir spectrum are [Xe]$4f^{14}5d^76s^2$, [Xe]$4f^{14}5d^86s$ and [Xe]$4f^{14}5d^9$ for the even parity and [Xe]$4f^{14}5d^76s6p$, [Xe]$4f^{14}5d^86p$ and [Xe]$4f^{14}5d^66s^26p$ for the odd parity. The opened $5d$ shell is one of the difficulties

explaining why *ab initio* calculations for the elements belonging to the group VIII of the periodic table are rare. Nevertheless, we demonstrated in B_{IV} that the density at the origin, and hence the $F_{0,i}$ parameter, was essentially proportional to the occupation number of the $6s$ orbital. It is indeed well known that s orbitals contribute the most to the FS as they have a non-vanishing radial density at the origin. In relativistic theory, the $p_{1/2}$ orbitals also contribute to the density at the origin. However, the latter contribute much less. The ratio of electron densities from the $p_{1/2}$ orbitals to the $s_{1/2}$ orbitals is estimated to remain small, although increasing with the atomic numbers. It reaches 13% for Fr I (see e.g., [139, §4.4]).

Using the "sharing rule", we separated the contributions from the leading configurations to the FS and established the relation between FS values and configuration compositions. Having the 'correct' configuration compositions is therefore critical to evaluate accurately the FS parameters. We therefore consider the configurations given above as the multireference. Note that they are all generated from substitutions that modify the occupation of the $6s$ orbital. The size of the calculations, however, is known to grow rapidly with the number of reference configurations and therefore higher-order correlation effects could be only included partially. Single substitutions were included with similar arguments than those developed in our study on tin HFS based on considerations from perturbation theory. The latter are related to the one-electron character of the density operator.

The introduction of single substitutions from close orbitals was performed in RCI calculations. We would expect, according to the HUM theorem (see Sec 3.4.2), to improve the excitation energy of all targeted states and hence the quality of our RCI expansions. We demonstrated that single substitutions, on the contrary, perturb considerably the computed energy spectrum. These perturbations led to the observation of a "root flipping", which consists of the inversion of two roots of the Hamiltonian with respect to the experimental energy-ordered spectrum [270]. Due to the high sensitivity of the FS parameters to the configuration composition, root flipping, if undetected, can be dramatic. In the present case, the sixth and seventh roots are in reverse order and exhibit strong differences in their configuration composition and hence in their respective FS values. This root flipping was confirmed by computing the Landé g factors (see Sec. 3.5.3), which are highly composition-dependent properties, and changes in phases of the dominant CSFs (see B_{IV} for more explanations). Both demonstrated that the sixth and seventh levels are not correctly positioned in the spectrum and that the experimentally targeted sixth level was computed as the seventh level in our calculations. This is visible already in Fig. 5.4 as we observed a radical change in the slopes of the two straight lines. The red one corresponds to the largest calculations, that include single substitutions, and deviates strongly from the calculations excluding these substitutions. It is interesting to note that the root flipping can already be detected when performing simpler, computationally faster calculations in the SR picture.

5.2.4 Nuclear physics outcomes

B_{IV} focuses solely on the atomic structure calculations for evaluating the FS parameters, which therefore addresses the computational challenges of using *ab initio* methods. However, atomic structure calculations are often a piece in larger studies, e.g., in nuclear physics. Collaborations between nuclear and atomic physicists are frequent, as attest the present work and our hyperfine study of tin (see Sec. 5.1). Iridium is one of the element of importance in the understanding of the *rapid neutron capture process* (r process), as part of the third-peak elements, which are often used to constrain the r process abundances. The nuclear simulations depend on the shapes, deformations, β decays, etc. of a large variety of nuclei, which, in turn, influence greatly the computed abundances used in e.g., cosmochronometry [271]. These theoretical developments therefore constantly require updated values of nuclear parameters either from measurements or calculations from first principles.

The computed FS parameters described in B_{IV} are combined with laser spectroscopy measurements in B_{III} to extract nuclear properties. Emphasis is put on the determination of mean square radii deviations and the corresponding nuclear deformations. However, B_{III} also discusses the complex hyperfine structure of Ir and determine the associated μ_I, I and Q. From the definition of the hyperfine constants A and B in Eq. (3.89), it appears that theoretical calculations of the isotope-independent hyperfine factors $A_{\rm el}$ and $B_{\rm el}$ can be avoided if μ_I, I and Q are known for a reference isotope. We have

$$\begin{aligned} \mu_I &= \frac{I}{I_{\rm ref}} \frac{A}{A_{\rm ref}} \mu_{I,\rm ref} \ , \\ Q &= \frac{B}{B_{\rm ref}} Q_{\rm ref} \ , \end{aligned} \tag{5.22}$$

which were used in B_{III} to resolve the hyperfine structures of iridium isotopes. $\mu_{I,\rm ref}$ and $Q_{\rm ref}$ were determined from precision measurements involving atomic beam magnetic resonance [272] and muonic x-rays [273], respectively. Both techniques do not require the calculations of electronic quantities. The theoretical calculations of the $A_{\rm el}$ and $B_{\rm el}$ hyperfine factors are, however, direct. Indeed, with the knowledge of the ASF for the ground and excited states, one can evaluate the associated $A_{\rm el}$ and $B_{\rm el}$ factors as described in Sec. 3.5.1. Furthermore, because of the similar one-body nature of the HFS and density operators, one could argue that a single ASF could be suitable for FS and HFS calculations.[4] In B_{IV}, we

[4] This would be somewhat 'accidental' because the HFS operators are sensitive to spin- and orbital-polarizations (see e.g., Ref. [8, §8.14]) while the density operator is sensitive to radial correlation (see Sec. 3.6.2 for the definitions). However, in the framework of GRASP calculations, single substitutions describing spin- and orbital-polarizations and radial correlation are included simultaneously without the possibility of easily identifying their different contributions.

exploit the Landé g factors to identify the root flipping. The latter are computed using the RHFS program, hence providing the hyperfine factors alongside the Landé g factors. However, for a meaningful comparison, one should conduct a more thorough analysis to determine relevant theoretical uncertainties.

The determination of the FS parameters are used subsequently to extract nuclear mean square radii and deformations. The rFS was demonstrated to enable the extraction of nuclear deformations by using two different atomic transitions for the same pair of isotopes and orthogonalized nuclear moments [149]. Another approach was used in the present work by considering the deformation parameter β_2^A, which modifies the Fermi distribution (3.166) as

$$\rho^A(r,\theta) = \frac{\rho_0^A}{1+\exp\left(\frac{r-c_{\rm def}^A[1+\beta_2^A Y_{20}(\theta)]}{a}\right)} \,. \tag{5.23}$$

The parameter $c_{\rm def}^A$ has an analytical expression that is derived by considering the conservation of the nuclear density. It depends on β_2^A and the mean square radii computed from the spherical droplet model. The determination of β_2^A has to be performed iteratively and relies on the assumption that β_2^A is known for the reference isotope, i.e., $\beta_2^{191} = +0.140(2)$ [273]. Then, by varying arbitrarily β_2^A for another isotope, $\delta\nu_{\rm FS,k}^{A,191}$ can be estimated according to Eq. (3.106), in which the nuclear moments are evaluated from the modified Fermi distribution, until it matches the experimental value. One should have in mind that for each β_2^A value, the Fermi distribution should be rescaled accordingly to conserve the nuclear density. This last step is performed by recomputing the parameter $c_{\rm def}^A$.

5.3 Conclusion

The studies on tin hyperfine structures ($B_{\rm I}$ and $B_{\rm II}$) and iridium isotope shifts ($B_{\rm III}$ and $B_{\rm IV}$) are excellent examples of what multidisciplinary research can lead to. In this chapter, we focused in particular on the close link between atomic and nuclear physics and how the electronic structure of an atom can be used to probe the properties of the nucleus. Whether it is for hyperfine structures or field shifts, we highlighted the challenges faced in the atomic calculations and emphasized the importance of their accuracy to extract nuclear quantities. We also put forward the crucial role of choosing appropriately the MR configurations and their influence on the resulting atomic properties and on the size of the calculations. It is particularly impressive, to our opinion, that large-scale atomic structure calculations are required to provide a single (or a few) atomic quantity(ies) for discussing nuclear shapes, trends, deformations, ... From the nuclear physics point of view, one could summarize the input from atomic physics by two single numbers: $B_{\rm el}[^1P_1] = 706(50)$ MHz/$\mu_{\rm N}$ and $\Delta F_{247,0} = -48.1(3.0)$ GHz/fm^2 for the hyperfine structure of tin and the isotope shift

of iridium, respectively. However, we hope that we succeeded to show the complexity of the calculations hidden behind these single numbers in our two 'technical' papers B_{II} and B_{IV}. The details provided in those papers were extended in this chapter to incorporate unpublished material that should clarify some assumptions made in the papers, such as the importance of S substitutions, the correlation between A_{el} and B_{el} or the 'variational approach' for FS calculations. Finally, the collaborative nature of these works stresses the need of atomic calculations to support other research fields and should encourage nuclear and atomic physicists to pursue collaborations.

Chapter 6

Group C: Astrophysics applications

After presenting applications of atomic physics to nuclear physics, this Chapter discusses applications of computational atomic structure calculations for astrophysics. Theoretical calculations of wavelengths, energy levels, transitions rates or Landé g factors over sequences of highly charged ions of specific interest in e.g., astrophysics, solar physics or plasma diagnosis, is probably the area in which the atomic community is the most productive. A recent review by Jönsson *et al.* [274] shows the efficiency of the MCDHF method to compute atomic properties of astrophysical interest (see references therein). There is an urgent need for atomic data to support experimental determination of e.g., elemental abundances in stellar objects or plasma properties [275, 276, 277]. Although atomic properties of low-lying states of many highly ionized systems of astrophysical interest are known experimentally, the lack of reliable data for higher excited states prevent experimental physicists to build the complete corresponding atomic spectrum. They therefore rely on theoretical calculations (see e.g., [70, 69, 278, 279, 280, 281]).

Over the last decades, the computational methodology for evaluating simultaneously atomic quantities of hundreds of states evolved considerably. Using, for example, the comparison between the computed relative energies of the low-lying excited states and their experimental value that are known with high accuracy or the comparison between MCDHF and MBPT methods over the entire spectrum allows to estimate the reliability of the results. According to Jönsson *et al.* *"calculations can give transition energies of spectroscopic accuracy, i.e., with an accuracy comparable to the one obtained from observations, as well as transition rates with estimated uncertainties of a few percent for a broad range of ions"* [274].

For this Chapter, we chose to focus on features of our calculations that are, to our opinion, key aspects for astrophysical purposes: how we technically produce large data sets and how we motivate and interpret these calculations. Through the papers C_I and C_{II}, we will

provide examples of large-scale calculations and give an interesting context related to the determination of magnetic fields in the solar corona. In C_I, special care is taken to make the analysis understandable for astro- or solar physicists who are not experts in atomic structure calculations. Interestingly, we could have chosen to include A_{II} in this chapter rather than in Chap. 4, since it is also of interest for the determination of the carbon solar abundances, as shown in Ref. [282] that extends the results of A_{II}. However, the two sets of studied systems, the S-like ions and the C ions considered in C_{II} and A_{II}, respectively, target different spectral ranges, illustrating the ability of the MCDHF method to provide accurate transition data over a wide frequency range. Indeed, the study of S-like ions concerns the UV and XUV domains [276, 277], which are typical for spectra of highly charged ions, while calculations on C ions focus on the near-infrared region (see e.g., [283, 284]), involving transitions between highly excited states with small energy separations.

6.1 Production of large data sets

C_{II} is an excellent example of what is possible to achieve with state-of-the-art methods in spectrum calculations. We considered the isoelectronic sequence of S I ($N_e = 16$), including Cr IX, Mn X, Fe XI, Co XII, Ni XIII and Cu XIV ($24 \leq Z \leq 29$). For each ion, hundreds of atomic energy levels are targeted simultaneously, over both parities and multiple J-values. Taking Fe XI as an example, we considered the lowest 236 levels belonging to the $3s^2 3p^4$, $3p^6$, $3s 3p^4 3d$, $3s^2 3p^2 3d^2$ even and $3s 3p^5$, $3s^2 3p^3 3d$, and $3s 3p^3 3d^2$ odd configurations (omitting the neon-like core), spanning $0 \leq J \leq 6$. In the largest RCI calculations the CSF basis consisted of approximately 13 000 000 and 17 000 000 CSFs for the even and odd parities, respectively. To the knowledge of the authors, together they are one of the largest calculations ever conducted in the framework of the MCDHF method. Fig. 6.1 displays the number of CSFs per (J, π)-block symmetry. For most J values, the number of CSFs per parity is over one million, reaching 4 millions for the $(5, -)$-block symmetry. Even though the calculations for each block are performed separately thanks to the block-diagonal form of the matrix, a few millions of CSFs per block is at the limit of what is achievable with modern clusters. Each calculation takes days or even weeks, depending on the number of cores that are used in parallel.

Fortunately, possibilities exist to reduce the computational time with little loss in accuracy. Inspired from perturbation theory [36, 285], the following method is known as *CI combined with second-order Brillouin–Wigner perturbation theory* [286], but has been renamed recently [287] the *zero-first order method* (ZF). In that approach, the active space is split into two subspaces P and Q. The P subspace contains the most important CSFs and corresponds to the zero-order space while the Q subspace is the first-order space. The choice of the P subspace is left to the user and it conventionally contains at the very least the MR CSFs. It is usually augmented by CSFs based on the previous layer calculation or, in the

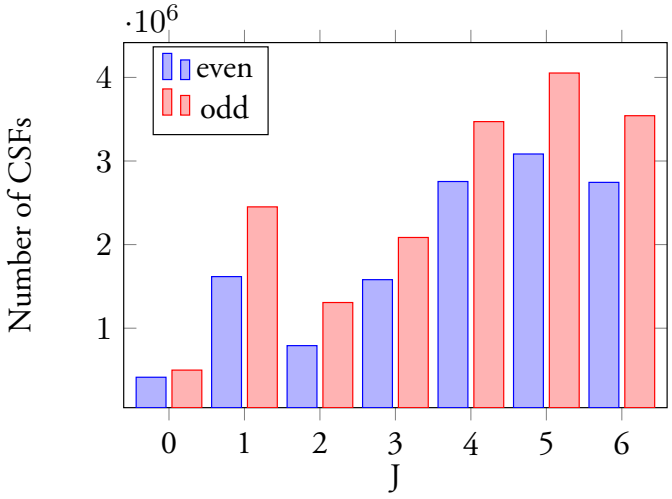

Figure 6.1: Number of CSFs for each (J, π)-block symmetry in the Fe XI largest RCI calculations.

case of RCI calculations, the contributions of CSFs that accumulate to a certain percentage of the wave function generated after the SCF procedure. The interaction matrix is then partitioned as

$$\begin{pmatrix} H^{(PP)} & H^{(PQ)} \\ H^{(QP)} & H^{(QQ)} \end{pmatrix} , \tag{6.1}$$

where $H^{(PP)}$ and $H^{(QQ)}$ are the submatrices corresponding to the interaction of CSFs within the P subspace and Q subspace, respectively, and $H^{(PQ)}$ is the interaction matrix between the P and Q spaces. The general idea of the method is to approximate $H_{ij}^{(QQ)} = \delta_{ij} E_i^Q$, which then takes a diagonal form. Typically, the number of CSFs in the Q space is much larger than in the P space, and therefore the diagonal form of $H^{(QQ)}$ prevents us from computing numerous off-diagonal elements. Because CC correlation is known to generate tremendous number of CSFs, this method was proven to be particularly efficient to capture that effect in spectrum calculations of Mg-like ions, allowing to open shells deep in the core [286].

One difficulty of calculations targeting hundreds of states together is to ensure a correct balance in the electron correlation between e.g., low-lying states and high excited states. If such a balance is not reached, one might observe energy shifts between the lower and higher parts of the spectrum i.e., the computed excitation energies of the low-lying levels are in good agreement with experiments while those for higher excited levels are not. To assess the overall quality of the spectrum, we evaluate a *mean level deviation* (MLD) defined as

$$\text{MLD} = \frac{1}{n_L} \sum_{i=1}^{n_L} |E_{\text{NIST}}(i) - E_{\text{MCDHF}}(i) - ES| , \tag{6.2}$$

in which n_L is the number of targeted levels, $E_{\text{NIST}}(i)$ and $E_{\text{MCDHF}}(i)$ are the experimen-

tal (usually taken from the NIST ASD DATABASE [9]) and the theoretical energy of level i, and ES is an *energy shift* that minimizes the MLD. ES is therefore computed assuming a systematic error and could be interpret as a correction for the ground state energy. For example, we obtained the values $ES = 547$ cm^{-1} and MLD$= 458$ cm^{-1} for Fe XI.

The analysis of the results is a tedious task. As it can be seen in C$_{\rm II}$, the spectrum of each ion is carefully analyzed and compared to experiments and other methods. Besides the energy, the label of each level is also discussed by looking at the LS composition of each atomic level. The LS composition of each state is computed using the program developed by Gaigalas and co-workers [108, 30] that transforms wave functions from their jj coupling representation to their LS-coupling representation (see Sec. 3.2). Further work is also needed to assess the quality of the radiative rates, usually by using the gauge dependence of the results through the parameter dT (3.163) as an accuracy indicator. Such careful analyses are useful to highlight spectral lines and energy levels misidentifications in experimental spectra. One such examples were found for Fe XI, as discussed in C$_{\rm II}$. According to our calculations the levels involved in misidentified transitions have energy differences with NIST reaching over 5 000 cm^{-1}, far beyond the MLD parameter.

6.2 Motivation and interpretation of the results

After describing how the calculations were performed, it is worth discussing the motivations behind the production of these large tables of energies and transition parameters. For that purpose, C$_{\rm I}$ is a good example. In C$_{\rm I}$ indeed, we estimated the Landé g factors (see Sec. 3.5.3) of multiple states of S-like ions. We took advantage of the availability of the wave functions determined in C$_{\rm II}$ to evaluate the Landé g factors. Since the wave functions are already known, i.e., the orbitals and expansion coefficients are known, one can 'simply' compute the Landé g factors with the HFSZEEMAN95 program [166]. Two main reasons motivated C$_{\rm I}$. First, in close collaboration with solar physicists, we have an interest in determining magnetic fields in the solar corona. As described in C$_{\rm I}$ (see Sec. 2), the method proposed by Judge [288] and extended by Plowman [289] to use a pair of M1 transitions suffers from undeterminations when a certain factor F,

$$F = \frac{3}{4}\left\{J(J+1) - J'(J'+1) - 2\right\}\left(g_J - g_{J'}\right), \tag{6.3}$$

is zero for both lines. For each transition $J - J'$ involved in such a pair of lines, g_J and $g_{J'}$ are the Landé g factors of the two levels J and J', respectively. This F factor is zero for transitions for which $J = 1$ and $J' = 0$ and for transitions with $g_J = g_{J'}$. Such a case arises for Si-like systems when considering the astrophysically important forbidden M1 transitions within the ground [Ne]$3s^2 3p^2\ {}^3P$ term. Indeed, the ${}^3P_1 \rightarrow {}^3P_0$ has $F = 0$ because of the first factor on the RHS of Eq. (6.3) while the ${}^3P_2 \rightarrow {}^3P_1$ transition has $F = 0$

due to the equality $g_{J=2} = g_{J'=1}$ in the same equation. Indeed, in pure LS coupling, according to Eq. (3.122), all fine structure levels of an LS term with $L = S$ have the same Landé g factors, i.e. $g_{JLS} \cong 1.5012$ for all J.[1] This is the case for a ^3P term ($L = S = 1$), at least in the non relativistic picture. Although from the atomic structure calculations perspective, it is well known that substantial deviations from pure LS-coupling values exist, it might not be as evident for astro- and solar physicists. Our goal is therefore *"to perform accurate atomic structure calculations of departures from LS coupling along several isoelectronic sequences, for ions of interest in astrophysics and highlighting solar corona applications."* (C_I). The second goal is to provide basic analyses with pedagogical intentions for readers that are not experts in atomic structure calculations.

We focused mostly on two systems, i.e., the fine structure levels of the $3s^23p^2$ configuration in Si-like ions and those of the $3s^23p^4$ configuration in S-like ions. These two systems are identical, in a single-configuration picture, except for the the fine structure of the lowest term being inverted in S-like ions. Performing simple calculations in the MCHF+BP approximation, we showed that the Landé g factor of the $^3P_2$ states deviates from its LS-coupling value mostly due to the $^1D_2$–$^3P_2$ relativistic mixing. In the single-configuration case, small transformations matrices can be used to switch from LS coupling to jj coupling. These transformations are written explicitly in Sec. 4.3 of C_I using the notations $^{2S+1}L_J$ and $(jj')_J$ to refer to states in LS coupling and jj coupling, respectively. Term mixing within the configuration cannot occur for the $^3P_1$ level, since it is the only $J = 1$ level arising from the $3s^23p^2$ or $3s^23p^4$ configurations. We therefore demonstrated that the Landé g factor of the $^3P_1$ level remains fairly close to its pure LS value of 1.5. We further showed that the $^1D_2$–$^3P_2$ relativistic mixing perturbs the Landé g factor of the $^3P_2$ level in direct proportion of the ^1D weight of the wave function, as expected from Eq. (3.123). Nevertheless, its deviation from the pure LS-coupling value remains small. This can be explained by the fact that a substantial relativistic mixing is needed to lead to a significant deviation from LS-coupling values due to the relative closeness of $g_{J=2}(^3P) = 1.5$ and $g_{J=2}(^1D) = 1$.

Deviations from LS coupling can be dramatic for other properties. According to the Landé interval rule, in LS coupling , we have

$$\frac{E(^3P_2) - E(^3P_1)}{E(^3P_1) - E(^3P_0)} = 2\ . \tag{6.4}$$

Because the $^3P_1$ is almost unaffected by LS mixing while the $^3P_2$ and $^3P_0$ strongly interact with the $^1D_2$ and $^1S_0$, respectively, this energy ratio takes unexpectedly large values. The latter are easily explained by looking at Fig. 6 in C_I, in which the crossing of the $^3P_1$ and $^3P_0$ levels along the S-like ions leads to unusually large wavelengths. We have in this

[1] This is not true in the case $J = 0$ for which Eq. (3.122) is undetermined due to a $0/0$ factor.

way pointed out to the astrophysics community that large deviations of energy difference ratios from the Landé interval rule values such as (6.4) can occur for cases showing small deviations of the Landé factors from the pure LS g factors, an *a priori* counter-intuitive observation.

Finally, the large-scale calculations allowed us to show how often the Landé g factors differ from the analytically computed LS values. As we could expect, these deviations due to LS-term mixings are larger and more frequent for heavier ions, as the relativistic effects are known to increase with the nuclear charge Z. C_I ultimately provides the Landé g factors for ions of interest along the S-like isoelectronic sequence, alerting solar physicists to the risk of getting unreliable analytical g factors when assuming pure LS coupling.

Chapter 7

Group D: Negative ions

7.1 Introduction

Negative ions are exotic systems that provide incomparable insight into the collective behaviour of the electrons (for a review, see e.g. [290, 291]). The overall neutral charge of the atom is disturbed when an extra electron passes at its vicinity, polarizing its electronic cloud and inducing an electric dipole moment. The short-range interaction between the incoming electron and the atomic dipole moment might be strong enough for the atom to capture the electron, hence acquiring an overall negative charge. However, the effective screening of the nuclear charge by the atomic electrons makes the negative ions highly sensitive to electron correlation. They are therefore excellent systems for understanding the role of electron correlation in the binding energy and offer interesting insight into the many-body problem.

Over 80% of naturally occurring atoms may form negative ions. These are of particular interest in weakly ionized gases or plasmas. They can be found in astrophysical environment and in planetary atmospheres, in which they play a crucial role in the low-energy collisions with neutral atoms. An example is the associative attachment process $\mathrm{H}^- + \mathrm{H} \rightarrow \mathrm{H}_2 + e^-$ that is the main production mechanism of hydrogen molecules in interstellar media.

Due to the short-range of the induced potential, the extra electron in negative ions is loosely bound, which makes negative ions unstable and fragile systems. Most negative ions are found to have a few bound states, often belonging to the same ground configuration and the same LS term. Many only possess a single bound state, i.e., their ground state. The sensitivity of these bound states to electron correlation is illustrated by looking at the evolution of the number of bound states along the nitrogen homologous sequence [292]. Calculations predict no bound state in N^-, three in P^- and As^- (corresponding to the ^3P fine

structure), four in Sb^- and two in Bi^-, highlighting the unpredictability character of the spectra of negative ions [292]. Very few negative ions have been shown to have excited states of opposite parity to that of the ground state. Such observations were made recently in La^-, Os^-, Ce^- and Th^- [293, 294, 295, 296, 297]. These anions are excellent candidates for laser cooling, a process during which they absorb a laser photon and undergo E1 transitions from the ground state to an excited state of opposite parity. Precooled anions are of great interest in the formation of antihydrogen, for which the antiprotons and positrons need to be cooled below 1 K [298]. In most negative ions, however, excited states have the same parity as the ground state and decay through weaker, higher-order multipole transitions such as M1 or E2, i.e. they are metastable states. The longest lifetime measurement of a negative ion excited state was performed at the Double ElectroStatic Ion Ring Experiment (DESIREE) facility at Stockholm University [299]. The $^2P_{1/2}$ excited states of $^{32}S^-$ was measured to be 503 ± 54 s [300] following the method proposed by Andersson *et al.* [301]. As we will discuss later, our joint theory-experiment study of Ir^- suggests that the $J = 2$ first excited state has a lifetime longer than the storage time of ~ 1230 s (see D_I).

7.2 Detachment processes

Since the negative ions are fragile systems, the extra electron might be detached by even low-energetic processes. Various processes are competing and their relative probabilities depend on the relative positioning of the energy levels of the negative ion and the atom, as well as the possible incoming energy, either of a photon or an electron. A review of the different processes is given in Refs. [290, 291, 302]. Experimentally, attosecond (10^{-18} s) pulses are used to study detachment processes of negative ions and photoionizations of neutral atoms. However processes that emit photons are subject to a time delay that should be taken into account in the analyzes [303]. In neutral atoms, two contributions make that time delay, one of which arises from the interaction between the laser and the long-range ionic field. In negative ions, however, because the detachment process produces the neutral atom (and not a positive ion), the long-range potential vanishes and the corresponding contribution to the time delay is essentially zero[1] [303]. This allows the access to other contributions experimentally. In the following, we will not focus on the time characterization of attosecond pulses, although this is of prime importance in the study of resonances in photoinonization studies [304, 305].

First, it is necessary to define the *electron affinity* (EA) of an atom A as

$$\mathrm{EA(A)} = E_{\mathrm{g.s}}(\mathrm{A}) - E_{\mathrm{g.s}}(\mathrm{A}^-) \tag{7.1}$$

[1] According to Lindroth and Dahlström this time delay is not exactly zero but decreases exponentially [303].

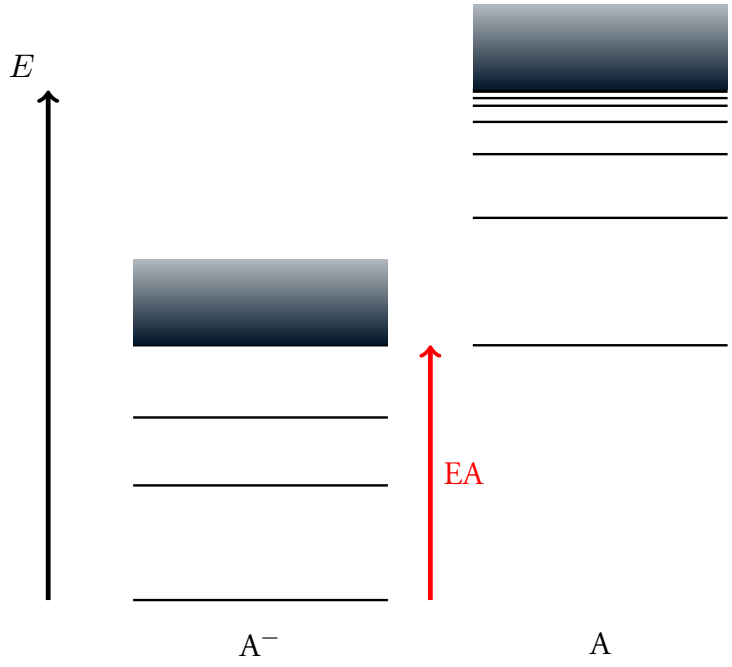

Figure 7.1: Schematic spectra of an atom A and its negative ions A^- inspired by Fig. 1 of Ref. [290]. The gradient blocks represent the continua. The electron affinity is defined as the energy difference between the ground states.

where $E_{\mathrm{g.s}}$ is the energy of the ground state. With that definition, a positive EA(A) means that the corresponding negative ion, A^-, has at least one bound state. Fig. 7.1 presents the schematic energy spectrum of the A/A^- system, with the explicit definition of the EA. The continua are represented by block gradients. Note that a lower number of bound states in the negative ion spectrum is voluntarily shown to present a realistic situation. Indeed, negative ions only have a finite number of bound states while atoms have an infinite number.

Discarding the collisional detachment processes, Brage identifies four decay modes of an excited bound state of a negative ion, namely, through optical transitions, autodetachments, radiative autodetachments and photodetachments, as represented in Fig. 3 of Ref. [302]. Optical transitions refer to radiative transitions in which an excited state decays toward a lower-energy state via the emission of a photon. It corresponds to the transitions already encountered in this work, with the noticeable characteristic of negative ions that most of the detected excited bound states share parity with the ground state and hence can not decay through E1 transitions, i.e., they are metastable. The autodetachment process describes the process in which an excited state of the negative ion interacts with the continuum and an electron is ejected. This decay channel is therefore opened only if the excited state is above the ionization limit, i.e., degenerate to a continuum state. This decay can be represented as

$$A^{-*} \rightarrow A + e^- \tag{7.2}$$

where the asterisk indicates that the negative ion is in an excited state. It is required that

such states lying in the continuum involve a pair of excited electrons, for which one can easily imagine an energy transfer between the two electrons resulting in the ejection of one of them and the deexcitation of the other; the autodetachment is induced by the repulsive force between these two electrons. The corresponding lifetimes are typically of the order of $10^{-13} - 10^{-15}$ s. In rare cases such as Li^- [306] or Be^- [307], autodetaching and radiative decay rates are comparable and we can observe radiative transitions between two metastable states. If the detachment is allowed, i.e., it follows the non-relativistic selection rules, it is fast, but sometimes the direct decay is forbidden. Then it is metastable against autodetachment. The radiative autodetachment process is fairly similar to the autodetachment process (7.2). The difference comes from the additional emission of a photon. The process can be represented as

$$A^{-*} \rightarrow A + e^- + \gamma \, . \tag{7.3}$$

Finally, the photodetachment process, which will be the focus of the next section, corresponds to the ejection of an electron following the absorption of a photon, i.e.,

$$A^{-*} + \gamma \rightarrow A + e^- \, . \tag{7.4}$$

Resonances: the case of Ce^-

The case of the Ce^- negative ion is particularly interesting because of the existence of excited bound states of opposite parity than the ground state close to the detachment limit. A series of experimental and theoretical papers detected some resonances in its photodetachment spectrum [308, 295]. Resonances arise when an atom and an electron are transiently associated into a state induced by bound-free transitions between a bound state of the negative ion and the excited states, which are in the continua above the detachment limit. Traditionally these autodetaching excited states are classified as being either Feshbach or shape resonances [309, 291]. Feshbach resonances lie energetically below the parent state of the neutral atom and have longer autodetachment lifetimes than shape resonances. Oppositely shape resonances lie above the parent state of the atom, they have shorter lifetime and are therefore wider than Feshbach resonances. The analysis of the observed spectrum is, however, extremely complicated due to the large number of possible transitions toward the continuum (see e.g. [310] on La^-). Computations of autodetachment processes involve treating both the bound negative ion and the continuum of the atom + a free electron, where the latter may include a large number of channels through different coupling possibilities. In the case of doubly excited negative ions, an interesting method is to use complex rotations [311, 312].[2] Attempting to identify the transitions and resonances observed in the measured spectrum with the energy level structure of the negative ion and the atom is

[2] Note that the two Refs. [311, 312] use B-splines for their calculations, confirming the B-splines interesting properties.

a difficult task. It depends crucially on the relative positioning of the bound states of the negative ion, but also on the atom [295] .

7.3 The iridium case: a collaboration with DESIREE

In this section we present D_I, which resulted from the joint experiment-theory work in collaboration with the DESIREE facility.

7.3.1 Supporting experiments with theoretical predictions

Negative ions are interesting from both experimental and theoretical points of views. Often, the experiment relies on theoretical predictions, at least to allow clear identifications of the observed bound states, sometimes to perform the measurement itself (see e.g., the joint theory-experiment work on Th^- [297] or the pair of theoretical and experimental papers on La^- [313, 293]). The photodetachment measurement is described in D_I and we limit ourselves to present the basics of the experiment. The general idea is to use a tunable laser to photodetach the bound states of the negative ions. By choosing the energy of the laser source, only certain bound states can photodetach according to their respective energy threshold, i.e., the energy at which photodetachment becomes possible. The choice of the laser energy is guided by prior experiments and theoretical studies.

We performed atomic structure calculations for the iridium negative ion and found that four states should be bound, i.e., Ir^- should have three excited bound states. The ground state was already identified to be $5d^86s^2\ ^3F_4$. The two first excited states were identified to $5d^86s^2\ ^3P_2$ and $5d^86s^2\ ^3F_3$, respectively. However, our calculations showed that the $J = 2$ state exhibited strong LS mixing, refuting the prior identification to a $^3P_2$. Furthermore, we predicted the existence of a third bound state with $J = 2$ closer to the detachment limit. Because of the large mixing that prevents a clear LS identification of the energy levels, a nomenclature inspired from molecular spectroscopy was used, in which the ground state is refer to as X and the excited states as A, B and C (see Fig. 1 in D_I). The photodetachment experiment was repeated for four different photon energies (arrows 1,2,3,4 in D_I), supposedly detaching (1) all bound states, (2) states A, B and C, (3) states B and C, and (4) state C only, as shown on Fig. 3 of D_I. For each of these possibilities, the count of photodetached electrons decreases exponentially over time, allowing the determination of the radiative lifetimes. Table II of D_I shows the relatively good agreement between the measured and computed lifetimes. Both states B and C are found to be metastable with lifetimes longer than 100 s. State A, however, was found to be even more long-lived with a lifetime larger than the storage time, hence a precise measurement was not doable.

The measurement of the binding energy of an excited state is performed by slowly varying the laser energy in the range around the threshold energy. Plotting the yield as a function of the photon energy can be fitted according to a Wigner law. This relationship gives the behaviour of the photodetachment cross section around the energy threshold as [314]

$$\sigma = (E - E_t)^l + 1/2 \qquad E \geq E_t \,, \tag{7.5}$$

where $E - E_t$ is the excess energy above the threshold. The angular quantum number l corresponds of the allowed partial waves describing the outgoing free electron. In the case of iridium, in which the photodetachment

$$5d^8 6s^2 + \gamma \rightarrow 5d^7 6s^2 + e^-(l) \tag{7.6}$$

is observed, the allowed values for l are $l = 1, 3$, corresponding to partial p-wave and f-wave, respectively. However, it is well-known that close to the detachment threshold, the centrifugal barrier suppresses the f-wave, leaving the p-wave to dominate the photodetachment cross section [314]. Although the validity of the Wigner law close to the energy threshold is well established, the range of that validity is not definite [294]. However, the fitting of the data to a Wigner law with $l = 1$ enabled the determination of the binding energy of state A to be 1.045 ± 0.002 eV, in good agreement with the recent value of 1.04788 ± 0.00002 eV [315].

7.3.2 On photodetachment intensities

Referring to the numbering of the vertical arrows of Fig. 3 in D_I, the methodology employed to determine the lifetimes of the excited states relies on the fact that the signals obtained with the photon energies (2), (3) and (4) originate from a single bound state, i.e., that the signal can be fitted to a single exponential. For the determination of the lifetime of state A, using the photon energy (2), the signal is registered for a time much longer than the lifetimes of states B and C, avoiding its contamination by the decay of states B and C. The situation is unfortunately different when performing the experiment with the photon energy (3) that can photodetach both states B and C, which have lifetimes of similar order of magnitude. One would usually fit the corresponding data to two exponentials arising from the decay of both states B and C, where the lifetime of C can be inferred from the measurement (4). However, the signal from the state C was too weak to enable this method.

To circumvent these experimental difficulties, one could try to predict the relative photodetachment intensities arising from the A, B and C states theoretically. Following Scharf

and Godefroid [316], a single-shell photodetachment reaction of a single electron can be written as,

$$X^-[n_i l_i^N\ (S_i L_i) J_i] + (\hbar\omega) \rightarrow X[n_i l_i^{N-1}\ (S_a L_a) J_a] + e^-[(s l_c) j_c] \qquad (7.7)$$

in SL(J) coupling, where the labels i, a and c refer to the negative ion, the atom and the continuum electron, respectively. The ejected electron is represented by the s, l_c and j_c quantum numbers. Under the assumption that the photodetachment can be described as a direct one-electron process in which a laser beam instantaneously promotes an electron in the active $n_i l_i^N$ shell to the continuum, the relative intensities of various channels can be determined from standard Wigner-Racah algebra using a fractional parentage approach via the Cox-Engelking-Lineberger (CEL) formula,

$$\mathcal{I}(J_a, J_i) = \sum_{j_i} [J_a, J_i, j_i] \begin{Bmatrix} S_a & L_a & J_a \\ s & l_i & j_i \\ S_i & L_i & J_i \end{Bmatrix}^2 \quad , \qquad (7.8)$$

using the notation $[j] = (2j+1)$ [317].

In the case of Ir^-, detachment occurs from either of four predicted bound $5d^8\,6s^2$ anion states with $J = 4, 2, 3$ and 2, in increasing energy order, corresponding to states X, A, B and C. The dominant detachment channel at threshold energy is likely the release of a p-electron. The two lowest final atomic states both have $^4F_{9/2}$ terms and belong to either $5d^8\,6s$ or $5d^7\,6s^2$ configurations indicating configuration interaction effects. Similarly as in the paper by Scheer *et al.* [318], we provide the relative photodetachment intensities computed according to Eq. (7.8), assuming that the ions are in local thermal equilibrium and thus described by the Boltzman distribution $\exp(-E_J/k_B T)$.

The normalization still remains an interesting question. One solution is to consider all fine-structure transitions between all possible LS terms of the negative ion (i.e., all terms appearing in the composition mixing of at least one bound state) to the ground term of the atom as 100% of the signal. This is done in Table 7.1, considering an infinite temperature following the normalization by Scheer *et al.* in their study of Ni^- [318]. The level structure of Ir^- is however quite different, since the lower $J = 2$ state is the only one to present a component of a ^3P fine structure level appearing as a bound state. Moreover, the B state, commonly identified as a $^3P_2$ level is highly mixed with the $^3F_2$ and $^1D_2$ levels, perturbing the fine structure of the ^3F term. The evaluation of intensities using Eq. (7.8), however, assumes pure LS coupling and is not able to treat relativistic mixing. Therefore, a normalized signal can only be recovered if all fine-structure transitions between two fully-resolved LS terms are considered, as shown in Table 7.2. This normalization is directly related to the properties of the $9j$-coefficients. Note that the dominant contributions always involve the atomic ground state.

Table 7.1: Relative photodetachment intensities computed according to Eq. (7.8) for all transitions between fine structure levels of the ion ground and (potential) excited states and the atomic ground state (see text for details).

^3F		^3P		^1D	
Thresholds	Intensities	Thresholds	Intensities	Thresholds	Intensities
$^3F_4 \rightarrow {}^4F_{9/2}$	29.23	$^3P_2 \rightarrow {}^4F_{9/2}$	35.71	$^1D_2 \rightarrow {}^4F_{9/2}$	0.0
$\rightarrow {}^4F_{7/2}$	10.63	$\rightarrow {}^4F_{7/2}$	14.29	$\rightarrow {}^4F_{7/2}$	0.0
$\rightarrow {}^4F_{5/2}$	2.79	$\rightarrow {}^4F_{5/2}$	4.6	$\rightarrow {}^4F_{5/2}$	0.0
$\rightarrow {}^4F_{3/2}$	0.20	$\rightarrow {}^4F_{3/2}$	0.95	$\rightarrow {}^4F_{3/2}$	0.0
$^3F_3 \rightarrow {}^4F_{9/2}$	6.20	$^3P_1 \rightarrow {}^4F_{9/2}$	0		
$\rightarrow {}^4F_{7/2}$	13.29	$\rightarrow {}^4F_{7/2}$	14.29		
$\rightarrow {}^4F_{5/2}$	9.55	$\rightarrow {}^4F_{5/2}$	12.38		
$\rightarrow {}^4F_{3/2}$	4.29	$\rightarrow {}^4F_{3/2}$	6.67		
$^3F_2 \rightarrow {}^4F_{9/2}$	0.28	$^3P_0 \rightarrow {}^4F_{9/2}$	0		
$\rightarrow {}^4F_{7/2}$	4.65	$\rightarrow {}^4F_{7/2}$	0		
$\rightarrow {}^4F_{5/2}$	9.08	$\rightarrow {}^4F_{5/2}$	4.44		
$\rightarrow {}^4F_{3/2}$	9.80	$\rightarrow {}^4F_{2/2}$	6.67		

Another possibility is to consider the signal from the following 3 detected channels, X $\rightarrow {}^4F_{9/2}$, A $\rightarrow {}^4F_{9/2}$ and B $\rightarrow {}^4F_{9/2}$ as representing 100% of the photodetachment signal, where the X and B are unambiguously identified as the $^3F_4$ and $^3F_3$ levels, respectively. The fourth channel that involves the fourth computationally predicted bound state, C $\rightarrow {}^4F_{9/2}$, is neglected as its population is much lower, due to its higher excitation energy. It will therefore be impossible to discriminate the signals from the photodetachment of the B and C states. However, the discussion about photodetachment intensities is still interesting to understand the relative strengths of the other channels.

In order to discuss the strong relativistic mixing observed in the B state (see Table I of $\mathrm{D_I}$), three different scenarios are presented in Table 7.2, in which the the three LS components ($^3F_2$, $^3P_2$ or $^1D_2$) of the B state are consider individually as potential candidates for the identification of the lowest $J = 2$ state. The $^1D_2$, however can not decay to any of the ^4F_J levels of the atomic ground state, due to the selection rules embedded in the $9j-$coefficient. The first state to which the $^1D_2$ could photodetach is one of the ^2P_J levels that has an excitation energy larger than 1 eV. In conclusion, the relativistic mixing observed among the $J = 2$ levels complicates considerably the calculation of photodetachment intensities, especially when they are performed using LS-coupling formulas. One could be tempted to weight the intensities according to the LS composition. However, in doing so, important off-diagonal contributions are neglected that can not be computed with the present computational tools.

Table 7.2: Relative photodetachment intensities and states population of Ir^- for different temperatures considering the three possible channels X($= {}^3F_4$) $\rightarrow {}^4F_{9/2}$, A $\rightarrow {}^4F_{9/2}$ and B($= {}^3F_3$) $\rightarrow {}^4F_{9/2}$ as representing 100% of the signal. Three scenarios are presented in which the lowest $J = 2$ level, commonly identified as a $^3P_2$ level, is arbitrarily considered to be a $^3F_2$, a $^3P_2$ or a $^1D_2$ level.

Thresholds	Intensities			Population
	$T = \infty$	$T = 650$ K	$T = 1300$ K	$T = 1300$ K
Scenario 1				
${}^3F_4 \rightarrow {}^4F_{9/2}$	81.85	100.00	99.98	9.0
${}^3F_2 \rightarrow {}^4F_{9/2}$	0.79	$< 10^{-4}$	0.004	0.019
${}^3F_3 \rightarrow {}^4F_{9/2}$	17.36	$< 10^{-5}$	0.01	0.0029
Scenario 2				
${}^3F_4 \rightarrow {}^4F_{9/2}$	41.09	100.00	99.53	9.0
${}^3P_2 \rightarrow {}^4F_{9/2}$	50.20	0.02	0.01	0.46
${}^3F_3 \rightarrow {}^4F_{9/2}$	8.72	$< 10^{-5}$	0.01	0.0029
Scenario 3				
${}^3F_4 \rightarrow {}^4F_{9/2}$	82.5	100.00	99.99	9.0
${}^1D_2 \rightarrow {}^4F_{9/2}$	0	0	0	0.019
${}^3F_3 \rightarrow {}^4F_{9/2}$	17.50	$< 10^{-5}$	0.01	0.0029

7.4 Theoretical study on heavy negative ions

In D_{II}, we carried multiconfiguration calculations to compute atomic properties of the homologous In ($Z = 49$) and Tl ($Z = 81$) atoms and their negative ion. We focus on the evaluation of EAs, as well as the isotope shift on the EAs, and radiative properties of the bound excited states of In^-. No excited states were found to be bound in Tl^-. Working with a pair (or more) of homologous atoms presents the advantage of validating a computational strategy using a less complicated system, hence computationally cheaper. This was done e.g., along the N^- homologous sequence [292] or the Cl^- homologous sequence to estimate the EA of At ($Z = 85$) [319]. The In/In^- and Tl/Tl^- ground configurations are ns^2np and ns^2np^2 for the neutral and anionic systems, respectively, with $n = 5$ for In and $n = 6$ for Tl (closed shells besides ns^2 were omitted). The energy levels are shown in Fig 2 of D_{II}, in which the grounds states are identified as ${}^2P^o_{1/2}$ and ${}^3P_0$ for the neutral and anionic systems, respectively. Before turning to the radiative properties and excitation energies of the bound excited states, it is interesting to discuss the determination of the EAs.

As explained in Sec. 7.1, the role of electron correlation is enhanced in negative ions, which makes it difficult to balance adequately the calculations in the negative ion and in the neutral system. This is exemplified when summarizing the various theoretical predictions of EA(Tl), that range from 270 meV [320] to 2415 meV [321]. The extreme value obtained by Felfi *et al.* is intriguing, as it is far from all other theoretical predictions (see Table III in D_{II}). Nevertheless, the authors argued that "*the theoretical and the experimental EAs for Tl in the published literature actually correspond to the binding energy of the first excited state*

of the Tl^- negative ion" [321] and call for experimental verification. Recently, Walter *et al.* measured an EA(Tl) of 320.053(19), hence thereby confirming the order of magnitude of the available values found in the literature. They argued "*While our experiment cannot rule out the existence of a more strongly bound ground state of Tl as predicted by Felfli et al., several pieces of evidence support the assignment of the present photodetachment threshold value of* $320.053(19)$ *meV*" [322], leaving room for some uncertainty that motivated the present study.

The calculations of the EAs are, as we already stated, difficult. One would like to balance correlation between the negative ion and the neutral atom. If this balance is not reached, unrealistic values can be obtained. In practice, we are tempted to include in both MRs configurations generated from similar electron substitutions. For example, in Tl/Tl^-, the $5d^{10} \rightarrow 5d^8 5f^2$ is found to be important, henceforth we included the configurations $5d^8 5f^2 6s^2 6p$ and $5d^8 5f^2 6s^2 6p^2$ in the MR set of Tl and Tl^-, respectively. However, because correlation is known to play a more important role in the negative ion, we might need to enlarge its MR compare to the neutral system. This is done by adding the configuration $5d^9 5f 6s 6p^2 7p$. Furthermore some electron substitutions are allowed to a larger active set of orbitals in the negative ion calculations (see D_{II} for details). One should also note that calculations for the atom and the anions are performed separately, i.e., their respective orbital bases are different and therefore include orbital relaxation.

To monitor that correlation is properly included, two sets of EAs are computed, denoted EA($\Delta n = 0$) and EA($\Delta n = 1$), as suggested originally in calculations of the boron's EA [323, 324]. They are defined as

$$\text{EA}(\Delta n = 0) = E_n(\text{Tl}) - E_n(\text{Tl}^-) \quad \text{and} \quad \text{EA}(\Delta n = 1) = E_n(\text{Tl}) - E_{n+1}(\text{Tl}^-) \,, \tag{7.9}$$

where E_n is the ground state energy computed after n layer of correlation orbitals. These values provide a lower and upper bound for the EA, respectively. Both sets of EAs are then extrapolated for $n \rightarrow \infty$ and their intersection provides a realistic estimation of the EA. We estimated the EA of In and Tl to be 383.4(7.7) meV and 322.8(6.5) meV, respectively, which are both in excellent agreement with the recent experimental values of 382.92(6) meV [325] and 320.053(19) [322].

In and Tl both have more than one stable isotopes. For example, Tl has two stable isotopes ^{205}Tl and ^{203}Tl with natural abundances of 70% and 30%, respectively. It is therefore interesting to study the isotope shift on the EA. We already argued in Sec. 5.2 that the relative weight of the MS over the FS decreases for increasing Z. This is confirmed by computing explicitly the MS and the FS on the EA for In and Tl. Fig. 1 of D_{II} shows the MS, FS and their sum on the same graph for In (left) and Tl (right). From In to Tl, the MS goes from being comparable to the FS to completely negligible (approximately two orders of magnitude smaller), which confirms the dominance of the FS for heavy nuclei.

This observation is of great interest, since the calculations of the atomic MS parameters require to evaluate the matrix elements of two-body operators, while the FS only requires the knowledge of the electron density inside the nuclear volume. Therefore, for the latter one can expect to reach acceptable accuracy with smaller calculations.

Finally, we investigated the potential existence of excited bound states. We confirmed the existence of two bound excited states in In, the $^3P_1$ and $^3P_2$ states, i.e., the three fine structure levels of the ^3P are found to be bound. Their excitation energies with respect to the anionic $^3P_0$ ground state is in agreement with the previous measurements [325, 326]. In addition to the excitation energy, we also computed the transition rates of all inter-term transitions within the fine structure of the ^3P. Such transitions are E1-forbidden, and hence dominant contributions arise from M1 and/or E2 transitions. For both excited bound states, M1 transitions are found to be dominant over E2 transitions. Therefore the computed radiative lifetimes are believed to be reliable.[3] For Tl, however, the first excited state is found to lie above the detachment limit by $\approx$ 60 meV, i.e., it is unbound. The second excited state lies even higher in energy so that the $^3P_0$ is found to be the only bound state in Tl^-.

7.5 Conclusion

Negative ions are rich and fascinating atomic systems from computational and experimental perspectives. The loosely bound extra electron makes the variational calculations numerically unstable. In many cases, the DHF method alone is not enough to reach convergence of the variational solutions and one must include electron correlation to stabilize the SCF procedure. However, theoretical studies of negative ions might not require high accuracy of the computed atomic properties. Theoretical calculations can indeed be useful as rough predictions to support experiments in choosing e.g., the laser's energy for photodetachment, or identifying the observed levels. Such support was successfully provided to the photodetachment measurements of Ir^-, which allowed the clear identification of four bound states including one additional excited bound state in addition to the three initially detected. The calculations of binding energies and radiative lifetimes allowed to discriminate the different photodetachment signals and hence, enabling with certainty the identification of the measured lifetimes of each metastable state. A fairly similar study is currently engaged to explore the atomic structure of the Rh negative ion, that is homologous to Ir. Preliminary calculations show a similar structure to the one observed in Ir^-, including also four bound states with the same angular symmetries. However, the mixing among $J = 2$ levels is found to be considerably less important, which allows a clear LS-term identification of

[3] In the Breit-Pauli approximation the M1 line strength $S_{ab} = \langle \Gamma_a \pi_a J_a || \mathbf{O}^{\mathrm{M1}} || \Gamma_b \pi_b J_b \rangle$ is entirely determined by the LS composition [17, §15.1], which is less sensitive to electron correlation. Note also that contrarily to electric transitions, magnetic transitions are gauge-independent.

the detected levels. Values from the calculations are still under analyzed but the results are promising, demonstrating the real need of theoretical support for photodetachment studies of negative ions.

Finally, our theoretical study of In and Tl confirmed the importance of balancing electron correlation effects between the anion and atom. It confirmed the experimental value of the EA of Tl and contradicted the large theoretical value of Felfli *et al.* [321]. It also allowed us to highlight the increasing importance of the FS with respect to the MS when considering heavier atoms. From In to Tl (i.e., going down one row in the periodic table), the MS:FS relative weight went from approximately 1:1 to 1:100. The dominance of the FS over the MS has positive consequences, as the former is known to be easier to compute accurately and one could hope to obtain accurate IS theoretical predictions for heavy systems. Lastly, the parallel investigations in In and Tl demonstrated the sensitivity of the negative ions to electron correlation, simply by looking at the number of bound states of each system. Indeed, In^- was predicted to have 3 bound states, all belonging to the fine structure of the ground ^3P term whereas calculations anticipated the existence of a single bound state in Tl^-, that is the lowest fine structure level of the ^3P term.

Chapter 8

Conclusions and perspectives

We reported the results of our four years of research work in computational atomic structures, employing mostly the MCDHF method combined with the RCI approach. Throughout this thesis, we have shown the capabilities of the MCDHF/RCI method as implemented in GRASP, to accurately predict a diverse range of atomic properties (excitation energies, transition rates, radiative lifetimes, hyperfine and isotope shift electronic parameters, Landé g factors, etc.) for various complex atomic systems, on the road to heavy elements. We pointed out the weaknesses and limitations of the theoretical approach that should encourage further methodological and computational developments. The interested reader is referred to the different conclusion sections associated with each chapter of Part II.

One key aspect that we emphasized is the role of the orbital basis in many-body atomic structure calculations (see Chap. 4). The comparison of the MCDHF numerical orbital basis with the Lagrange-Laguerre finite complete basis associated with the Lagrange-mesh method that we used for nominal one-electron systems was particularly interesting. It illustrated the inability of the finite difference MCDHF method to include contributions from states lying in the positive or negative continua to atomic properties such as polarizabilities or two-photon decay rates. Besides the obvious advantage of (judiciously) selected finite basis set inherited from their completeness, finite basis set methods generate a multitude of orbitals corresponding to pseudo-states that could be used to enrich the MCDHF numerical orbital basis and expand the configuration space of the subsequent RCI calculations. In B_{II}, we already pointed out the common confusion between the *correlation* orbitals, that optimize the interaction with the orbitals of the MR configuration and that are necessarily occupied at the end of the variational SCF procedure process, and the virtual orbitals that result, as a "by-product", from the resolution of the matrix equations in finite basis set methods. Although the two terminologies are often confounded (even in our own papers !), we were very careful to only refer in this thesis to correlation orbitals when working in the

MCDHF framework. Thanks to the program developed in AV for nominal one-electron systems using the LMM method, one could retrieve the LMM virtual orbitals, project them onto the GRASP radial grid and use them to enrich the orbital basis set used in a following extended RCI calculations and hence avoiding the time-consuming SCF procedure.

Another aspect that we developed in the same chapter is the use of natural orbitals (NOs) in many-electron variational calculations. Their efficiency for computing hyperfine structure constants of nominal one-electron systems is undeniable. A natural, interesting follow up could therefore be to investigate their relevance in higher-order hyperfine interactions, especially for the octupole magnetic interaction [327, 328]. Nevertheless, little is known about their properties and how the transformation to NOs influences the ASF expansion. In nominal two-electron systems, it is well known, as we discussed in Sec. 4.2.2, that the CSF expansion is considerably reduced in the NO basis thanks to vanishing mixing coefficients. Such a spectacular compactness of the wave function is however no longer observed for more complex systems, for which the value of some mixing coefficients decrease but are not exactly zero. Further investigations are needed to understand the mechanisms behind the decrease of the weight of certain CSFs but, still, this empirical observation could be a starting point. Two main ideas are interesting to develop in that direction. First, one could take advantage of the NO basis to generate a more compact MR set of CSFs. This could be done by computing the NOs *before optimizing correlation orbitals,* and so "cleaning" the MR set by removing the CSFs with mixing coefficient below a given arbitrary cutoff treshold. As we repeatedly pointed out in this thesis, the size of the MR space crucially impacts the size of the RCI matrices, and substantial reductions of the CSF space could be obtained for the RCI by reducing the MR CSF list. Second, and following the same idea, the diagonalization of the density matrix at each step of the SCF procedure would allow us to suppress from the variational process the CSFs that are less important. Omitting these CSFs could also be useful to ensure the uniqueness of the wave function, preventing unnecessary orbital rotations. It is not rare that for very heavy systems such as lanthanides, 99% of the wave function is accounted for by $\sim$ 1000 CSFs, while the expansion of the ASF reaches millions of CSFs. Why then spend so much effort on the remaining small contributions ?

This is directly in line with the conclusions developed in Chap. 4, in which we argued that choosing the most appropriate optimization scheme for the orbital basis would be more efficient than having to compensate for an orbital basis of poor quality by generating extremely large CSFs expansions.

New developments in the GRASP community are always on-going, having in mind to improve the efficiency of the method. The most promising idea is probably the *relativistic Partition Correlation Function* (PCFI) method (see Refs. [226, 329] for its non-relativistic counterpart), in which non-orthogonal orbital basis sets capture different correlation effects. The orbital bases could therefore be tailored accurately for the atomic property of

interest. The non-relativistic PCFI approach has already demonstrated its potential for neutral Be. In particular, it showed a faster convergence of the energy and hyperfine structure constants. However, the current version of the non-relativistic program suffers from the lack of a parallelized version. Improvements in the data structure and algorithms would also be needed for making the approach more efficient, hence rendering the PCFI method competitive for more complex systems.

Another interesting idea under development focuses the use of *symmetry ordered primals* (SOPs) [330]. The continuous increase in the size of RCI calculations goes along with longer computational times and more coefficients to store. One quickly realizes that the evaluation of angular coefficients is often redundant, i.e., the same set of angular coefficients is computed explicitly too many times. Taking the simplest example of He ground state $1s^2\ ^1S_0$, the ASF expansion includes CSFs such as $|ns^2\ ^1S_0\rangle$ with $n \geq 1$. The angular part of the CSF is entirely determined by the angular quantum number $l = s$ and is independent of the principal quantum number n that only differentiates the s orbitals according to their number of nodes. Therefore the diagonal matrix elements $\langle ns^2\ ^1S_0|\mathcal{H}|ns^2\ ^1S_0\rangle$ generates the same angular coefficients for all values of n. By grouping all CSFs with the same angular structure in SOPs such as e.g., $|n_{max}s^2\ ^1S_0\rangle$ where n_{max} is the maximum n-value in the CSFs space, the CSF-like SOP written as $|n_{max}s^2\ ^1S_0\rangle$ spans all CSFs with $n \leq n_{max}$. The interaction submatrix $\langle ns^2\ ^1S_0|\mathcal{H}|n's^2\ ^1S_0\rangle$, that is a square matrix of dimension $(n_{max}) \times (n_{max})$, only requires to evaluate 2 sets of angular coefficients: those for diagonal matrix elements $n = n'$ and those for off-diagonal matrix elements $n \neq n'$. Taking a realistic numerical example, $n_{max} = 10$, angular coefficients would be computed twice instead of $(10 \times 9/2) = 45)$ times ! Furthermore, only the SOP $|10s^2\ ^1S_0\rangle$ would appear in the CSFs list, reducing the size of the corresponding file and hence speeding up its processing. Note that for extreme expansions the CSFs list file can reach few GBs of disk space. We conducted exploratory work in this direction that showed promising results. However, due to the lack of time, one can only consider these results as a proof of principle that the efficiency of the method would be improved following the use of SOPs.

Turning to more practical applications, we successfully applied the MCDHF method to compute atomic properties such as hyperfine structures or isotope shifts. In Chap. 5, we presented the results of our calculations for Sn ($Z = 50$) and Ir ($Z = 77$), that led ultimately to the extraction of nuclear quadrupole moments, nuclear mean square radii and nuclear deformations. Besides illustrating the usefulness and relevance of atomic structure calculations to nuclear physics, we put forward the difficulties arising in large-scale calculations. In B_{II} and B_{IV}, we carefully provided extensive details to illustrate how challenging computational atomic structures can be for heavy elements. In particular, the observation of a root-flipping in the isotope shift calculations of Ir is a perfect example of the thoroughness that is required when analyzing the results. A more superficial investigation might

have led to miss the root-flipping, and therefore to erroneous field shift parameters and, more importantly, to meaningless nuclear mean square radii and deformations. We also addressed, in B_{II}, the question of theoretical accuracy and how to estimate meaningful uncertainties in *ab initio* methods. It is indeed hard to separate the contributions arising from numerical procedures, computational strategies and theoretical models. The solution presented in B_{II} is a reasonable alternative. However, it requires to perform separate, independent calculations, which then tremendously increase the needed computer resources and manpower. Contrarily to experiments, a large part of assessing theoretical uncertainties in atomic structure calculations comes from experience and comparison with previous calculations, which lack of a rigorous procedure.

The range and diversity of systems studied in this thesis also highlighted the differences that exist in calculations that target very few atomic states (as is the case in the nuclear applications) or hundreds of atomic states (as in the case of the astrophysics applications). Extended studies of hundreds of states over multiple ions along isoelectronic sequences allow us to deduce interesting trends. It is the case in our study of Landé g factors, in which we have shown how these factors deviate from their LS-coupling values and how these deviations evolve along the isoelectronic sequence upon consideration.

Finally, the last chapter on negative ions illustrated the variety of domains in which theoretical atomic physics can provide support to experiments. Indeed, we have shown how the theoretical prediction of a third excited bound state in Ir^- led to its experimental detection: it is definitely easier to find something when we know where to look. To conclude, we have shown that combining theoretical and experimental work provides interesting insights in our understanding of some of the most fundamental interactions. The need from experimental physics for high-accuracy theoretical data continuously motivates further developments of state-of-the-art *ab initio* methods and we believe that the work presented in this thesis constitutes an original contribution to these improvements.

References

[1] J. J. McDonnell. *The concept of an atom from Democritus to John Dalton*. The Edwin Mellen Press, 1991.

[2] B. Pullman. *The Atom in the History of Human Thought*. Oxford University Press, 1998.

[3] J. Dalton. *A New System of Chemical Philosophy*. Number vol. 1 in A New System of Chemical Philosophy. Weale, 1842.

[4] A. van Melsen. From atomos to atom. *Revue des Sciences Religieuses*, 28(3), 1954.

[5] W. H. E. Schwarz. *Relativistic Methods for Chemists*. Springer Netherlands, 2010.

[6] S.-G. Wang and E. W. H. Schwarz. Icon of Chemistry: The Periodic System of Chemical Elements in the New Century. *Angewandte Chemie International Edition*, 48(19):3404–3415, 2009.

[7] P. Pyykkö and J.-P. Desclaux. Relativity and the periodic system of elements. *Accounts of Chemical Research*, 12(8):276–281, 1979.

[8] C. Froese Fischer, T. Brage, and P. Jönsson. *Computational atomic structure: an MCHF approach*. Institute of Physics Publ, Philadelphia, Penn; Bristol, UK, 1997.

[9] A. Kramida, Yu. Ralchenko, J. Reader, and and NIST ASD Team. NIST Atomic Spectra Database (ver. 5.7), [Online]. Available: `https://physics.nist.gov/asd` [2019, October]. National Institute of Standards and Technology, Gaithersburg, MD., 2019.

[10] J. C. Slater. The Theory of Complex Spectra. *Physical Review*, 34:1293–1322, 1929.

[11] E. U. Condon and G. H. Shortley. *The Theory of Atomic Spectra*. Cambridge University Press, Cambridge, UK, 1935.

[12] G. Racah. Theory of Complex Spectra. I. *Physical Review*, 61:186–197, 1942.

[13] G. Racah. Theory of Complex Spectra. II. *Physical Review*, 62:438–462, 1942.

[14] G. Racah. Theory of Complex Spectra. III. *Physical Review*, 63:367–382, 1943.

[15] G. Racah. Theory of Complex Spectra. IV. *Physical Review*, 76:1352–1365, 1949.

[16] B. Edlén. *Atomic Spectra*. Springer Berlin Heidelberg, Berlin, Heidelberg, 1964.

[17] R. D. Cowan. *The theory of atomic structure and spectra*. University of California Press, Berkeley, 1981.

[18] Z. Rudzikas. *Theoretical Atomic Spectroscopy*. Cambridge Monographs on Atomic, Molecular and Chemical Physics. Cambridge University Press, 1997.

[19] B. R. Judd. *Operator Techniques In Atomic Spectroscopy*. Princeton University Press, 1998.

[20] W. R. Johnson. *Atomic Structure Theory: Lectures on Atomic Physics*. Springer-Verlag, Berlin, Heidelberg, 2007.

[21] S. Gamrath, M. R. Godefroid, P. Palmeri, P. Quinet, and K. Wang. Spectral line list of potential cosmochronological interest deduced from new calculations of radiative transition rates in singly ionized thorium (Th II). *Monthly Notices of the Royal Astronomical Society*, 496(4):4507–4516, 2020.

[22] B. G. C. Lackenby, V. A. Dzuba, and V. V. Flambaum. Calculation of atomic spectra and transition amplitudes for the superheavy element Db ($Z = 105$). *Physical Review A*, 98:022518, 2018.

[23] C. Froese Fischer and G. Gaigalas. The Effect of Correlation on Spectra of the Lanthanides: Pr^{3+}. *Atoms*, 6(1):8, 2018.

[24] W. Li, R. Casini, T. Alemán, and P. Judge. Solar Spectral Lines with Special Polarization Properties for the Calibration of Instrument Polarization. *The Astrophysical Journal*, 848:82, 10 2017.

[25] C. Froese Fischer and A. Senchuk. Numerical Procedures for Relativistic Atomic Structure Calculations. *Atoms*, 8(4), 2020.

[26] V. A. Dzuba, V. V. Flambaum, and B. M. Roberts. Calculations of the atomic structure for the low-lying states of actinium. *Physical Review A*, 100:022504, 2019.

[27] I. P. Grant. *Relativistic Quantum Theory of Atoms and Molecules: Theory and Computation (Springer Series on Atomic, Optical, and Plasma Physics)*. Springer-Verlag, Berlin, Heidelberg, 2006.

[28] C. Froese Fischer, M. Godefroid, T. Brage, P. Jönsson, and G. Gaigalas. Advanced multiconfiguration methods for complex atoms: I. Energies and wave functions. *Journal of Physics B: Atomic, Molecular and Optical Physics*, 49(18), 2016.

[29] C. Froese Fischer, G. Gaigalas, P. Jönsson, and J. Bieroń. GRASP2018−Fortran 95 version of the General Relativistic Atomic Structure Package. *Computer Physics Communications*, 237:184 – 187, 2019.

[30] P. Jönsson, G. Gaigalas, J. Bieron, C. Froese Fischer, and I.P. Grant. New version: GRASP2K relativistic atomic structure package. *Computer Physics Communications*, 184(9):2197 – 2203, 2013.

[31] J. P. Desclaux. A multiconfiguration relativistic DIRAC-FOCK program. *Computer Physics Communications*, 9(1):31 – 45, 1975.

[32] P. Indelicato. Effects of the Breit interaction on the 1s binding energy of superheavy elements. *Journal of Physics B: Atomic and Molecular Physics*, 19(12):1719–1730, 1986.

[33] P. Indelicato, J. Bieroń, and P. Jönsson. Are MCDF calculations 101% correct in the super-heavy elements range? *Theoretical Chemistry Accounts*, 129(3):495–505, 2011.

[34] I. Lindgren. *Relativistic many-body theory: a new field-theoretical approach*, volume 63. Springer-Verlag New York, 2011.

[35] P. Cársky J. Paldus and J. Pittne. *Recent Progress in Coupled Cluster Methods*, volume 11 of *Challenges and Advances in Computational Chemistry and Physics*. Springer Netherlands, 2010.

[36] I. Lindgren and J. Morrison. *Atomic Many-Body Theory*. Springer-Verlag Berlin Heidelberg, 1986.

[37] M. F. Gu. The flexible atomic code. *Canadian Journal of Physics*, 86(5):675–689, 2008.

[38] A. S. P. Gomes, T. Saue, L. Visscher, H. J. Aa. Jensen, R. Bast, and et al. DIRAC, a relativistic ab initio electronic structure program Release DIRAC19 (2019). http://www.diracprogram.org.

[39] M. G. Kozlov, S. G. Porsev, M. S. Safronova, and I. I. Tupitsyn. CI-MBPT: a package of programs for relativistic atomic calculations based on a method combining configuration interaction and many-body perturbation theory. *Computer Physics Communications*, 195:199–213, 2015.

[40] E. V. Kahl and J. C. Berengut. AMBiT: A programme for high-precision relativistic atomic structure calculations. *Computer Physics Communications*, 238:232 – 243, 2019.

[41] B. K. Mani, S. Chattopadhyay, and D. Angom. RCCPAC: A parallel relativistic coupled-cluster program for closed-shell and one-valence atoms and ions in FORTRAN. *Computer Physics Communications*, 213:136–154, 2017.

[42] M. Schädel. Chemistry of the superheavy elements. *Philosophical Transactions of the Royal Society A: Mathematical, Physical and Engineering Sciences*, 373(2037):20140191, 2015.

[43] E. Eliav, S. Fritzsche, and U. Kaldor. Electronic structure theory of the superheavy elements. *Nuclear Physics A*, 944:518–550, 2015.

[44] S. A. Giuliani, Z. Matheson, W. Nazarewicz, E. Olsen, P.-G. Reinhard, J. Sadhukhan, B. Schuetrumpf, N. Schunck, and P. Schwerdtfeger. Colloquium: Superheavy elements: Oganesson and beyond. *Review of Modern Physics*, 91:011001, 2019.

[45] Yu. Ts. Oganessian and V. K. Utyonkov. Super-heavy element research. *Reports on Progress in Physics*, 78(3):036301, 2015.

[46] P. Quinet. Overview of recent advances performed in the study of atomic structures and radiative processes for the lowest ionization stages of heavy elements. *Canadian Journal of Physics*, 95(9):790–804, 2017.

[47] P. Indelicato and E. Lindroth. Relativistic effects, correlation, and QED corrections on Kα transitions in medium to very heavy atoms. *Physical Review A*, 46:2426–2436, 1992.

[48] F.-K. Thielemann, A. Arcones, R. Käppeli, M. Liebendörfer, T. Rauscher, C. Winteler, C. Fröhlich, I. Dillmann, T. Fischer, G. Martinez-Pinedo, K. Langanke, K. Farouqi, K.-L. Kratz, I. Panov, and I. K. Korneev. What are the astrophysical sites for the r-process and the production of heavy elements? *Progress in Particle and Nuclear Physics*, 66(2):346–353, 2011.

[49] O. Dorvaux, A. Lopez-Martens, K. Hauschild, A. V. Yeremin, A. Khouaja, A. V. Belozerov, Ch. Briançon, M. L. Chelnokov, V. I. Chepigin, D. Curien, P. Désesquelles, B. Gall, V. A. Gorshkov, M. Guttormsen, F. Hanappe, A. P. Kabachenko, F. Khalfallah, A. Korichi, A. C. Larsen, O. N. Malyshev, A. Minkova, Yu. Ts. Oganessian, A. G. Popeko, M. Rousseau, N. Rowley, R. N. Sagaidak, S. Sharo, A. V. Shutov, S. Siem, V. I. L. Stuttgé, A. I. Svirikhin, N. U. H. Syed, and Ch. Theisen. Spectroscopy of heavy elements at Dubna. *AIP Conference Proceedings*, 1012(1):64–68, 2008.

[50] V. M. Shabaev, A. N. Artemyev, D. A. Glazov, I. I. Tupitsyn, A. V. Volotka, and V. A. Yerokhin. Quantum Electrodynamics of Heavy Ions and Atoms. *AIP Conference Proceedings*, 869(1):52–59, 2006.

[51] S. Fritzsche. On the accuracy of valence–shell computations for heavy and super–heavy elements. *The European Physical Journal D - Atomic, Molecular, Optical and Plasma Physics*, 33(1):15–21, 2005.

[52] P. J. Indelicato. QED tests with highly charged ions. *Journal of Physics B: Atomic, Molecular and Optical Physics*, 52:232001, 2019.

[53] M. C. Li, R. Si, T. Brage, R. Hutton, and Y. M. Zou. Proposal of highly accurate tests of Breit and QED effects in the ground state $2p^5$ of the F-like isoelectronic sequence. *Physical Review A*, 98:020502, 2018.

[54] G. Plunien, B. Müller, W. Greiner, and G. Soff. Nuclear polarization contribution to the Lamb shift in heavy atoms. *Physical Review A*, 39:5428–5431, 1989.

[55] V. A. Yerokhin and V. M. Shabaev. Lamb Shift of $n = 1$ and $n = 2$ States of Hydrogen-like Atoms, $1 \leq Z \leq 110$. *Journal of Physical and Chemical Reference Data*, 44(3):033103, 2015.

[56] B. G. C. Lackenby, V. A. Dzuba, and V. V. Flambaum. Atomic structure calculations of superheavy noble element oganesson ($Z = 118$). *Physical Review A*, 98:042512, 2018.

[57] S. O. Allehabi, J. Li, V. A. Dzuba, and V. V. Flambaum. Theoretical study of electronic structure of erbium and fermium. *Journal of Quantitative Spectroscopy and Radiative Transfer*, 253:107137, 2020.

[58] V. A. Dzuba and V. V. Flambaum. Electron structure of superheavy elements Uut, Fl and Uup (Z =113 to 115). *Hyperfine Interactions*, 237(1):1–17, 2016.

[59] S. Gamrath, P. Palmeri, and P. Quinet. Calculated oscillator strengths for the strongest lines of cosmochronological interest in the visible spectrum of singly ionized uranium (U II). *Monthly Notices of the Royal Astronomical Society*, 480(4):4754–4760, 2018.

[60] M. Laatiaoui, W. Lauth, H. Backe, M. Block, D. Ackermann, B. Cheal, P. Chhetri, C. E. Düllmann, P. Van Duppen, J. Even, R. Ferrer, F. Giacoppo, S. Götz, F. P. Hessberger, M. Huyse, O. Kaleja, J. Khuyagbaatar, P. Kunz, F. Lautenschläger, A. K. Mistry, S. Raeder, E. M. Ramirez, T. Walther, C. Wraith, and A. Yakushev. Atom-at-a-time laser resonance ionization spectroscopy of nobelium. *Nature*, 538(7626):495–498, 2016.

[61] D. T Yordanov, L. V. Rodríguez, D. L. Balabanski, J. Bieroń, M. L. Bissell, K. Blaum, B. Cheal, J. Ekman, G. Gaigalas, R. F. Garcia Ruiz, G. Georgiev, W. Gins, M. R. Godefroid, C. Gorges, Z. Harman, H. Heylen, P. Jönsson, A. Kanellakopoulos, S. Kaufmann, C. H. Keitel, V. Lagaki, S. Lechner, B. Maa, S. Malbrunot-Ettenauer, W. Nazarewicz, R. Neugart, G. Neyens, W. Nörtershäuser, N. S. Oreshkina, A. Papoulia, P. Pyykkö, P.-G. Reinhard, S. Sailer, R. Sánchez, S. Schiffmann, S. Schmidt, L. Wehner, C. Wraith, L. Xie, Z. Xu, and X. Yang. Structural trends in atomic nuclei from laser spectroscopy of tin. *Communications Physics*, 3(1):107, 2020.

[62] A. E. Barzakh, D. Atanasov, A. N. Andreyev, M. Al Monthery, N. A. Althubiti, B. Andel, S. Antalic, K. Blaum, T. E. Cocolios, J. G. Cubiss, P. Van Duppen, T. Day Goodacre, A. de Roubin, G. J. Farooq-Smith, D. V. Fedorov, V. N. Fedosseev, D. A. Fink, L. P. Gaffney, L. Ghys, R. D. Harding, M. Huyse, N. Imai, S. Kreim, D. Lunney, K. M. Lynch, V. Manea, B. A. Marsh, Y. Martinez Palenzuela, P. L. Molkanov, D. Neidherr, M. Rosenbusch, R. E. Rossel, S. Rothe, L. Schweikhard, M. D. Seliverstov, S. Sels, C. Van Beveren, E. Verstraelen, A. Welker, F. Wienholtz, R. N. Wolf, and K. Zuber. Shape coexistence in ^{187}Au studied by laser spectroscopy. *Physical Review C*, 101:064321, 2020.

[63] C. Wraith, X. F. Yang, L. Xie, C. Babcock, J. Bieroń, J. Billowes, M. L. Bissell, K. Blaum, B. Cheal, L. Filippin, R. F. G. Ruiz, W. Gins, L. K. Grob, G. Gaigalas, M. Godefroid, C. Gorges, H. Heylen, M. Honma, P. Jönsson, S. Kaufmann, M. Kowalska, J. Krämer, S. Malbrunot-Ettenauer, R. Neugart, G. Neyens, W. Nörtershäuser, F. Nowacki, T. Otsuka, J. Papuga, R. Sánchez, Y. Tsunoda, and D. T. Yordanov. Evolution of nuclear structure in neutron-rich odd-Zn isotopes and isomers. *Physics Letters B*, 771:385–391, 2017.

[64] B. A. Marsh, T. Day Goodacre, S. Sels, Y. Tsunoda, B. Andel, A. N. Andreyev, N. A. Althubiti, D. Atanasov, A. E. Barzakh, J. Billowes, K. Blaum, T. E. Cocolios, J. G. Cubiss, J. Dobaczewski, G. J. Farooq-Smith, D. V. Fedorov, V. N. Fedosseev, K. T. Flanagan, L. P. Gaffney, L. Ghys, M. Huyse, S. Kreim, D. Lunney, K. M. Lynch, V. Manea, Y. Martinez Palenzuela, P. L. Molkanov, T. Otsuka, A. Pastore, M. Rosenbusch, R. E. Rossel, S. Rothe, L. Schweikhard, M. D. Seliverstov, P. Spagnoletti, C. Van Beveren, P. Van Duppen, M. Veinhard, E. Verstraelen, A. Welker, K. Wendt, F. Wienholtz, R. N. Wolf, A. Zadvornaya, and K. Zuber. Characterization of the shape-staggering effect in mercury nuclei. *Nature Physics*, 14(12):1163–1167, 2018.

[65] T. Day Goodacre, A. V. Afanasjev, A. E. Barzakh, B. A. Marsh, S. Sels, P. Ring, H. Nakada, A. N. Andreyev, P. Van Duppen, N. A. Althubiti, B. Andel, D. Atanasov, J. Billowes, K. Blaum, T. E. Cocolios, J. G. Cubiss, G. J. Farooq-Smith, D. V. Fedorov, V. N. Fedosseev, K. T. Flanagan, L. P. Gaffney, L. Ghys,

M. Huyse, S. Kreim, D. Lunney, K. M. Lynch, V. Manea, Y. Martinez Palenzuela, P. L. Molkanov, M. Rosenbusch, R. E. Rossel, S. Rothe, L. Schweikhard, M. D. Seliverstov, P. Spagnoletti, C. Van Beveren, M. Veinhard, E. Verstraelen, A. Welker, K. Wendt, F. Wienholtz, R. N. Wolf, A. Zadvornaya, and K. Zuber. Laser spectroscopy of neutron-rich ^{207,208}Hg isotopes: Illuminating the kink and odd-even staggering in charge radii across the $n = 126$ shell closure. *Physical Review Letters*, 126:032502, 2021.

[66] K. Wang, C. X. Song, P. Jönsson, J. Ekman, M. Godefroid, C. Y. Zhang, R. Si, X. H. Zhao, C. Y. Chen, and J. Yan. Large-scale Multiconfiguration Dirac-Hartree-Fock and Relativistic Configuration Interaction Calculations of Transition Data for B-like S XII. *The Astrophysical Journal*, 864(2):127, 2018.

[67] K. Wang, P. Jönsson, G. Gaigalas, L. Radžiūtė, P. Rynkun, G. Del Zanna, and C. Y. Chen. Energy Levels, Lifetimes, and Transition Rates for P-like Ions from Cr X to Zn XVI from Large-scale Relativistic Multiconfiguration Calculations. *The Astrophysical Journal Supplement Series*, 235(2):27, 2018.

[68] K. Wang, C. X. Song, P. Jönsson, G. Del Zanna, S. Schiffmann, M. Godefroid, G. Gaigalas, X. H. Zhao, R. Si, C. Y. Chen, and J. Yan. Benchmarking Atomic Data from Large-scale Multiconfiguration Dirac–Hartree–Fock Calculations for Astrophysics: S-like Ions from Cr IX to Cu XIV. *The Astrophysical Journal Supplement Series*, 239(2):30, 2018.

[69] K. Wang, X. H. Zhang, C. Y. Zhang, W. Dang, X. H. Zhao, Z. B. Chen, R. Si, C. Y. Chen, and J. Yan. Extended calculations of energy levels, radiative properties, and lifetimes for P-like Ge XVIII. *Journal of Quantitative Spectroscopy and Radiative Transfer*, 261:107512, 2021.

[70] C. X. Song, C. Y. Zhang, K. Wang, R. Si, M. Godefroid, P. Jönsson, W. Dang, X. H. Zhao, J. Yan, and C. Y. Chen. Extended calculations with spectroscopic accuracy: Energy levels and radiative rates for O-like ions between Ar XI and Cr XVII. *Atomic Data and Nuclear Data Tables*, 138:101377, 2021.

[71] W. Li, H. Hartman, K. Wang, and P. Jönsson. Theoretical investigation of oscillator strengths and lifetimes in Ti. *Astronomy and Astrophysics*, 643:A156, 2020.

[72] J. Grumer, T. Brage, M. Andersson, J. Li, P. Jönsson, W. Li, Y. Yang, R. Hutton, and Y. Zou. Unexpected transitions induced by spin-dependent, hyperfine and external magnetic-field interactions. *Physica Scripta*, 89(11):114002, 2014.

[73] W. Li, J. Grumer, Y. Yang, T. Brage, K. Yao, C. Chen, T. Watanabe, P. Jönsson, H. Lundstedt, R. Hutton, and Y. Zou. A Novel Method to Determine Magnetic

Fields in Low-density Plasma Facilitated through Accidental Degeneracy of Quantum States in Fe^{9+}. *The Astrophysical Journal*, 807(1):69, 2015.

[74] J. Li, M. Godefroid, and J. Wang. Atomic parameters for the $2p^5 3p\ ^2[3/2]_2 - 2p^5 3s\ ^2[3/2]^o_2$ transition of Ne I relevant in nuclear physics. *Journal of Physics B: Atomic, Molecular and Optical Physics*, 49(11), 2016.

[75] P. G. Judge, R. Hutton, W. Li, and T. Brage. On the Fine Structure Splitting of the $3p^4 3d\ ^4D_{5/2}$ and $3p^4 3d\ ^4D_{7/2}$ Levels of Fe X. *The Astrophysical Journal*, 833(2):185, 2016.

[76] R. Si, W. Li, T. Brage, and R. Hutton. Proposal for observation of transitions induced by external magnetic fields mixing in the lower states: with an example from Fe X. *Journal of Physics B: Atomic, Molecular and Optical Physics*, 53(9):095002, 2020.

[77] R. Si, T. Brage, W. Li, J. Grumer, M. Li, and R. Hutton. A First Spectroscopic Measurement of the Magnetic-field Strength for an Active Region of the Solar Corona. *The Astrophysical Journal*, 898(2):L34, 2020.

[78] C. Delaunay, R. Ozeri, G. Perez, and Y. Soreq. Probing atomic Higgs-like forces at the precision frontier. *Physical Review D*, 96:093001, 2017.

[79] J. C. Berengut, D. Budker, C. Delaunay, V. V. Flambaum, C. Frugiuele, E. Fuchs, C. Grojean, R. Harnik, R. Ozeri, G. Perez, and Y. Soreq. Probing New Long-Range Interactions by Isotope Shift Spectroscopy. *Physical Review Letters*, 120:091801, 2018.

[80] V. A. Dzuba, S. O. Allehabi, V. V. Flambaum, J. Li, and S. Schiller. Time keeping and searching for new physics using metastable states of Cu, Ag, and Au. *Physical Review A*, 103:022822, 2021.

[81] M. S. Safronova, D. Budker, D. DeMille, D. F. Jackson Kimball, A. Derevianko, and C. W. Clark. Search for new physics with atoms and molecules. *Review of Modern Physics*, 90:025008, 2018.

[82] B. H. Bransden and C. Joachain. *Quantum mechanics (Second Edition)*. Prentice Hall-Pearson, 01 2007.

[83] C. Cohen-Tannoudji, B. Diu, and F. Laloë. *Mécanique quantique*, volume 2. EDP Sciences, 1973.

[84] B. Bransden and C. Joachain. *Physics of Atoms and Molecules*. Prentice Hall-Pearson, 10 2014.

[85] E. Schrödinger. An Undulatory Theory of the Mechanics of Atoms and Molecules. *Physical Review*, 28:1049–1070, 1926.

[86] W. Gerlach and O. Stern. Der experimentelle Nachweis der Richtungsquantelung im Magnetfeld. *Zeitschrift für Physik*, 9(1):349–352, 1922.

[87] W. Pauli. Über den Zusammenhang des Abschlusses der Elektronengruppen im Atom mit der Komplexstruktur der Spektren. *Zeitschrift für Physik*, 31(1):765–783, 1925.

[88] W. Pauli. Zur Quantenmechanik des magnetischen Elektrons. *Zeitschrift fur Physik*, 43(9-10):601–623, 1927.

[89] O. Klein. Quantentheorie und fünfdimensionale relativitätstheorie. *Zeitschrift für Physik*, 37(12):895–906, 1926.

[90] W. Gordon. Der comptoneffekt nach der schrödingerschen theorie. *Zeitschrift für Physik*, 40(1):117–133, 1926.

[91] W. Greiner. *Relativistic Quantum Mechanics*. Springer-Verlag Berlin, 1990.

[92] P. A. M. Dirac and R. H. Fowler. On the theory of quantum mechanics. *Proceedings of the Royal Society of London. Series A, Containing Papers of a Mathematical and Physical Character*, 112(762):661–677, 1926.

[93] I. P. Grant. Variational methods for Dirac wave equations. *Journal of Physics B: Atomic and Molecular Physics*, 19(20):3187, 1986.

[94] W. E. Lamb and R. C. Retherford. Fine Structure of the Hydrogen Atom by a Microwave Method. *Physical Review*, 72:241–243, 1947.

[95] T. A. Welton. Some Observable Effects of the Quantum-Mechanical Fluctuations of the Electromagnetic Field. *Physical Review*, 74:1157–1167, 1948.

[96] P. A. M. Dirac. A theory of electrons and protons. *Proceedings of the Royal Society of London. Series A, Containing Papers of a Mathematical and Physical Character*, 126(801):360–365, 1930.

[97] L. L. Foldy and S. A. Wouthuysen. On the Dirac Theory of Spin 1/2 Particles and Its Non-Relativistic Limit. *Physical Review*, 78:29–36, 1950.

[98] E. J. Baerends, W. H. E. Schwarz, P. Schwerdtfeger, and J. G. Snijders. Relativistic atomic orbital contractions and expansions: magnitudes and explanations. *Journal of Physics B: Atomic, Molecular and Optical Physics*, 23(19):3225–3240, 1990.

[99] P. Jerabek, B. Schuetrumpf, P. Schwerdtfeger, and W. Nazarewicz. Electron and Nucleon Localization Functions of Oganesson: Approaching the Thomas-Fermi Limit. *Physical Review Letters*, 120:053001, 2018.

[100] J. H. Hamilton, S. Hofmann, and Y. T. Oganessian. Search for Superheavy Nuclei. *Annual Review of Nuclear and Particle Science*, 63(1):383–405, 2013.

[101] S. Hofmann, S. Heinz, R. Mann, J. Maurer, G. Münzenberg, S. Antalic, W. Barth, H. G. Burkhard, L. Dahl, K. Eberhardt, R. Grzywacz, J. H. Hamilton, R. A. Henderson, J. M. Kenneally, B. Kindler, I. Kojouharov, R. Lang, B. Lommel, K. Miernik, D. Miller, K. J. Moody, K. Morita, K. Nishio, A. G. Popeko, J. B. Roberto, J. Runke, K. P. Rykaczewski, S. Saro, C. Scheidenberger, H. J. Schött, D. A. Shaughnessy, M. A. Stoyer, P. Thörle-Pospiech, K. Tinschert, N. Trautmann, J. Uusitalo, and A. V. Yeremin. Review of even element super-heavy nuclei and search for element 120. *The European Physical Journal A*, 52(6):180, 2016.

[102] K. Morita. SHE research at RIKEN/GARIS. *Nuclear Physics A*, 944:30–61, 2015. Special Issue on Superheavy Elements.

[103] J. D. Jackson. *Classical electrodynamics*. Wiley, New York, NY, 3rd edition, 1999.

[104] H. A. Bethe. The Electromagnetic Shift of Energy Levels. *Physical Review*, 72:339–341, 1947.

[105] H. A. Bethe and E. E. Salpeter. *Quantum Mechanics of One- and Two-electron Atoms*. Springer, Berling, Heidelberg, 1957.

[106] P. J. Mohr. Self-energy radiative corrections in hydrogen-like systems. *Annals of Physics*, 88(1):26–51, 1974.

[107] C. Froese Fischer and M. R. Godefroid. Electron correlation in the lanthanides: $4f^2$ spectrum of Ce^{2+}. *Physical Review A*, 99:032511, 2019.

[108] G. Gaigalas, T. Zalandauskas, and Z. Rudzikas. LS-jj transformation matrices for a shell of equivalent electrons. *Atomic Data and Nuclear Data Tables*, 84(2):99 – 190, 2003.

[109] D. R. Hartree. *The Calculation of Atomic Structures*. John Wiley & Sons, New York, 1957.

[110] P.-O. Löwdin. Quantum Theory of Many-Particle Systems. II. Study of the Ordinary Hartree-Fock Approximation. *Physical Review*, 97:1490–1508, 1955.

[111] J. Sucher. Foundations of the relativistic theory of many-electron atoms. *Physical Review A*, 22:348–362, 1980.

[112] H. M. Quiney, I. P. Grant, and S. Wilson. The Dirac equation in the algebraic approximation. *Physica Scripta*, 36(3):460–463, 1987.

[113] C. Froese. Hartree-Fock Procedure for Some ns^2 ^1S Configurations. *Physical Review*, 150:1–6, 1966.

[114] R. McWeeny and B. T. Sutcliffe. *Methods of molecular quantum mechanics*. London, New York, Academic Press, 1969.

[115] C. Froese Fischer. *The Hartree-Fock Method for Atoms, A numerical method*. Wiley, New York, 1977.

[116] P.-O. Löwdin. Quantum Theory of Many-Particle Systems. III. Extension of the Hartree-Fock Scheme to Include Degenerate Systems and Correlation Effects. *Physical Review*, 97:1509–1520, 1955.

[117] E. A. Hylleraas and B. Undheim. Numerische Berechnung der 2S-Terme von Ortho- und Par-Helium. *Zeitschrift für Physik*, 65(11-12):759–772, 1930.

[118] J. K. L. MacDonald. Successive Approximations by the Rayleigh-Ritz Variation Method. *Physical Review*, 43:830–833, 1933.

[119] I. P. Grant, B. J. McKenzie, P. H. Norrington, D. F. Mayers, and N. C. Pyper. An atomic multiconfigurational Dirac-Fock package. *Computer Physics Communications*, 21(2):207 – 231, 1980.

[120] U. Fano. Interaction between Configurations with Several Open Shells. *Physical Review*, 140:A67–A75, 1965.

[121] D. M. Brink and G. R. Satchler. *Angular momentum*. Oxford science publications. Clarendon Press, Oxford, 1993.

[122] G. Gaigalas and Z. Rudzikas. On the secondly quantized theory of the many-electron atom. *Journal of Physics B: Atomic, Molecular and Optical Physics*, 29(15):3303, 1996.

[123] G. Gaigalas, Z. Rudzikas, and C. Froese Fischer. An efficient approach for spin - angular integrations in atomic structure calculations. *Journal of Physics B: Atomic, Molecular and Optical Physics*, 30(17):3747, 1997.

[124] G. Gaigalas, A. Bernotas, Z. Rudzikas, and C. Froese Fischer. Spin-other-orbit Operator in the Tensorial Form of Second Quantization. *Physica Scripta*, 57(2):207–212, 1998.

[125] G. Gaigalas, S. Fritzsche, and Z. Rudzikas. Reduced Coefficients of Fractional Parentage and Matrix Elements of the Tensor $W^{(k_q k_j)}$ in jj-Coupling. *Atomic Data and Nuclear Data Tables*, 76(2):235 – 269, 2000.

[126] G. Gaigalas, S. Fritzsche, and I. P. Grant. Program to calculate pure angular momentum coefficients in jj-coupling. *Computer Physics Communications*, 139(3):263 – 278, 2001.

[127] G. Gaigalas. Coupling: The program for searching optimal coupling scheme in atomic theory. *Computer Physics Communications*, 247:106960, 2020.

[128] M. Godefroid and C. Froese Fischer. Isotope shift in the oxygen electron affinity. *Physical Review A*, 60:R2637–R2640, 1999.

[129] A. Hibbert, C. Froese Fischer, and M. R. Godefroid. Non-orthogonal orbitals in MCHF or configuration interaction wave functions. *Computer Physics Communications*, 51(3):285 – 293, 1988.

[130] A. P. Jucys, I. Levinson, and V. Vanagas. *Mathematical Apparatus of the Angular Momentum Theory*. Israel Program for Scientific Translations, Jerusalem, 1963.

[131] J. S. Briggs. Evaluation of Matrix Elements from a Graphical Representation of the Angular Integral. *Review of Modern Physics*, 43:189–230, 1971.

[132] D. A. Varshalovich, A. N. Moskalev, and V. K. Khersonskii. *Quantum Theory of Angular Momentum*. World Scientific, 1988.

[133] U. Fano and G. Racah. *Irreducible tensorial sets*. Pure and applied physics ; v. 4. Academic Press, New York, 1959.

[134] Godefroid, M. R. and Gaigalas, G. On the different versions of the Wigner-Eckart reduced matrix elements. Work in progress (private communication), 2021.

[135] B. R. Judd. *Second Quantization and Atomic Spectroscopy*. The Johns Hopkins Press, Baltimore, MD, 1967.

[136] I. Lindgren and A. Rosén. Relativistic self-consistent-field calculations with application to atomic hyperfine interaction. II. Relativistic theory of atomic hyperfine interaction. *Case Studies in Atomic Physics*, 4(3):150–196, 1974.

[137] J. Grumer, M. Andersson, and T. Brage. Hyperfine induced intensity redistribution in In. *Journal of Physics B: Atomic, Molecular and Optical Physics*, 43(7):074012, 2010.

[138] M. Andersson, J. Grumer, T. Brage, Y. Zou, and R. Hutton. Analysis of the competition between forbidden and hyperfine-induced transitions in Ne-like ions. *Physical Review A*, 93:032506, 2016.

[139] W. H. King. *Isotope Shifts in Atomic Spectra*. Plenum Press, NY, 1984.

[140] C. Nazé, E. Gaidamauskas, G. Gaigalas, M. Godefroid, and P. Jönsson. RIS3: A program for relativistic isotope shift calculations. *Computer Physics Communications*, 184(9):2187–2196, 2013.

[141] J. Ekman, P. Jönsson, M. Godefroid, C. Nazé, G. Gaigalas, and J. Bieroń. RIS4: A program for relativistic isotope shift calculations. *Computer Physics Communications*, 235(433 - 446), 2019.

[142] V. M. Shabaev. Mass corrections in a strong nuclear field. *Theoretical and Mathematical Physics*, 63(3):588–596, 1985.

[143] V. M. Shabaev and A. N. Artemyev. Relativistic nuclear recoil corrections to the energy levels of multicharged ions. *Journal of Physics B: Atomic, Molecular and Optical Physics*, 27(7):1307–1314, 1994.

[144] C. W. P. Palmer. Reformulation of the theory of the mass shift. *Journal of Physics B: Atomic and Molecular Physics*, 20(22):5987–5996, 1987.

[145] I. P. Grant. Many-Electron Effects in the Theory of Nuclear Volume Isotope Shift. *Physica Scripta*, 21(3-4):443–447, 1980.

[146] S. Schiffmann, J. G. Li, J. Ekman, G. Gaigalas, M. Godefroid, and P. Jönsson. Relativistic Multiconfiguration Electron Density Functions and Natural Orbitals from Grasp2018. To be submitted, 2021.

[147] A. Borgoo, O. Scharf, G. Gaigalas, and M. Godefroid. Multiconfiguration electron density function for the ATSP2K-package. *Computer Physics Communications*, 181(2):426 – 439, 2010.

[148] S. A. Blundell, P. E. G. Baird, C. W. P. Palmer, D. N. Stacey, and G. K. Woodgate. A reformulation of the theory of field isotope shift in atoms. *Journal of Physics B: Atomic and Molecular Physics*, 20(15):3663–3681, 1987.

[149] A. Papoulia, B. G. Carlsson, and J. Ekman. Effect of realistic nuclear charge distributions on isotope shifts and progress towards the extraction of higher-order nuclear radial moments. *Physical Review A - Atomic, Molecular, and Optical Physics*, 94(4), 2016.

[150] E. C. Seltzer. *K* X-Ray Isotope Shifts. *Physical Review*, 188:1916–1919, 1969.

[151] D. Verney, L. Cabaret, J. E. Crawford, H. T. Duong, B. Fricke, J. Genevey, G. Huber, F. Ibrahim, M. Krieg, F. Le Blanc, J. K. P. Lee, G. Le Scornet, D. Lunney, J. Obert, J. Oms, J. Pinard, J. C. Puteaux, K. Rashid, B. Roussière, J. Sauvage, V. Sebastian, and the ISOLDE Collaboration. Deformation change in light iridium nuclei from laser spectroscopy. *The European Physical Journal A - Hadrons and Nuclei*, 30(3):489–518, 2006.

[152] P. Zeeman. The effect of magnetisation on the nature of light emitted by a substance. *Nature*, 55(1424):347–347, 1897.

[153] K. T. Cheng and W. J. Childs. Ab initio calculation of $4f^N 6s^2$ hyperfine structure in neutral rare-earth atoms. *Physical Review A*, 31:2775–2784, 1985.

[154] M. Andersson and P. Jönsson. HFSZEEMAN—A program for computing weak and intermediate field fine and hyperfine structure Zeeman splittings from MCDHF wave functions. *Computer Physics Communications*, 178(2):156–170, 2008.

[155] N.C. Pyper, I.P. Grant, and N. Beatham. A new program for calculating matrix elements of one-particle operators in jj-coupling. *Computer Physics Communications*, 15(5):387–400, 1978.

[156] I. P. Grant. Gauge invariance and relativistic radiative transitions. *Journal of Physics B: Atomic and Molecular Physics*, 7(12):1458–1475, 1974.

[157] J. Grumer. *Theoretical Atomic Spectroscopy of Earthbound and Stellar Plasma*. PhD thesis, Lund University, 2016.

[158] L. Filippin. *Relativistic study of electron correlation effects on polarizabilities, two-photon decay rates, and electronic isotope-shift factors in atoms and ions*. PhD thesis, École polytechnique de Bruxelles, Université libre de Bruxelles, 2017.

[159] F. Mandl and G. Shaw. *Quantum Field Theory*. 2nd Edition, Wiley, Chichester., 1985.

[160] C. Froese Fischer. Evaluating the accuracy of theoretical transition data. *Physica Scripta Volume T*, 134:014019, 2009.

[161] J. Ekman, M. Godefroid, and H. Hartman. Validation and Implementation of Uncertainty Estimates of Calculated Transition Rates. *Atoms*, 2(2):215–224, 2014.

[162] P. Jönsson, X. He, C. Froese Fischer, and I. P. Grant. The GRASP2K relativistic atomic structure package. *Computer Physics Communications*, 177(7):597 – 622, 2007.

[163] Compas collaboration webpage: *https://ddwap.mah.se/tsjoek/compas/*. last checked: Dec. 2020.

[164] Compas collaboration github page: *https://compas.github.io/*. last checked: Dec. 2020.

[165] P. Jönsson, F. A. Parpia, and C. Froese Fischer. HFS92: A program for relativistic atomic hyperfine structure calculations. *Computer Physics Communications*, 96(2):301–310, 1996.

[166] W. Li, J. Grumer, T. Brage, and P. Jönsson. HFSZEEMAN95–program for computing weak and intermediate magnetic-field- and hyperfine-induced transition rates. *Computer Physics Communications*, 253:107211, 2020.

[167] P. Jönsson and C. Froese Fischer. SMS92: a program for relativistic isotope shift calculations. *Computer Physics Communications*, 100(1):81–92, 1997.

[168] S. Fritzsche. The RATIP program for relativistic calculations of atomic transition, ionization and recombination properties. *Computer Physics Communications*, 183(7):1525 – 1559, 2012.

[169] S. Schiffmann, L. Filippin, D. Baye, and M. Godefroid. POLALMM: a program to compute polarizabilities for nominal one-electron systems using the lagrange-mesh method. *Computer Physics Communications*, 256:107452, 2020.

[170] S. Fritzsche. A fresh computational approach to atomic structures, processes and cascades. *Computer Physics Communications*, 240:1 – 14, 2019.

[171] F. A. Parpia and A. K. Mohanty. Relativistic basis-set calculations for atoms with fermi nuclei. *Physical Review A*, 46:3735–3745, 1992.

[172] A. Stathopoulos and C. Froese Fischer. A Davidson program for finding a few selected extreme eigenpairs of a large, sparse, real, symmetric matrix. *Computer Physics Communications*, 79(2):268–290, 1994.

[173] O. Sinanoğlu and I. Öksüz. Theory of Atomic Structure Including Electron Correlation. *Physical Review Letters*, 21:507–511, 1968.

[174] D. Layzer. On a screening theory of atomic spectra. *Annals of Physics*, 8(2):271 – 296, 1959.

[175] D. Layzer and J. Bahcall. Relativistic Z-dependent theory of many-electron atoms. *Annals of Physics*, 17(2):177 – 204, 1962.

[176] T. Kato. On the eigenfunctions of many-particle systems in quantum mechanics. *Communications on Pure and Applied Mathematics*, 10(2):151–177, 1957.

[177] S. Verdebout, P. Jönsson, G. Gaigalas, M. Godefroid, and C. Froese Fischer. Exploring biorthonormal transformations of pair-correlation functions in atomic structure variational calculations. *Journal of Physics B: Atomic, Molecular and Optical Physics*, 43(7):074017, 2010.

[178] J. Bieroń, C. Froese Fischer, P. Indelicato, P. Jönsson, and P. Pyykkö. Complete-active-space multiconfiguration Dirac-Hartree-Fock calculations of hyperfine-structure constants of the gold atom. *Physical Review A*, 79(5), 2009.

[179] S. Schiffmann, M. Godefroid, Jörgen Ekman, P. Jönsson, and C. Froese Fischer. Natural orbitals in multiconfiguration calculations of hyperfine-structure parameters. *Physical Review A*, 101:062510, 2020.

[180] A. Papoulia, J. Ekman, G. Gaigalas, M. Godefroid, S. Gustafsson, H. Hartman, W. Li, L. Radžiūtė, P. Rynkun, S. Schiffmann, K. Wang, and P. Jönsson. Coulomb (Velocity) Gauge Recommended in Multiconfiguration Calculations of Transition Data Involving Rydberg Series. *Atoms*, 7(4):106, 2019.

[181] L. Filippin, S. Schiffmann, J. Dohet-Eraly, D. Baye, and M. Godefroid. Relativistic semiempirical-core-potential calculations in Ca^+, Ba^+ and Sr^+ ions on Lagrange meshes. *Physical Review A*, 97:012506, 2018.

[182] P. Amaro, A. Surzhykov, F. Parente, P. Indelicato, and J. P. Santos. Calculation of two-photon decay rates of hydrogen-like ions by using B-polynomials. *Journal of Physics A: Mathematical and Theoretical*, 44(24):245302, 2011.

[183] D. Baye. The Lagrange-mesh method. *Physics Reports*, 565:1–107, 2015.

[184] D. Baye and P. Heenen. Generalised meshes for quantum mechanical problems. *Journal of Physics A: Mathematical and General*, 19(11):2041–2059, 1986.

[185] M. Hesse and D. Baye. Lagrange-mesh calculations of three-body atoms and molecules. *Journal of Physics B: Atomic, Molecular and Optical Physics*, 32(23):5605–5617, 1999.

[186] M. Hesse and D. Baye. Lagrange-mesh calculations of excited states of three-body atoms and molecules. *Journal of Physics B: Atomic, Molecular and Optical Physics*, 34(8):1425, 2001.

[187] M. Hesse and D. Baye. Lagrange-mesh calculations of the ground-state rotational bands of the H_2^+ and D_2^+ molecular ions. *Journal of Physics B: Atomic, Molecular and Optical Physics*, 36(1):139–154, 2003.

[188] D. Baye. Exact nonrelativistic polarizabilities of the hydrogen atom with the Lagrange-mesh method. *Physical Review A*, 86(6), 2012.

[189] J. Mitroy, M. S. Safronova, and C. W. Clark. Theory and applications of atomic and ionic polarizabilities. *Journal of Physics B: Atomic, Molecular and Optical Physics*, 43(20):202001, 2010.

[190] D. Baye, L. Filippin, and M. Godefroid. Accurate solution of the Dirac equation on Lagrange meshes. *Physical Review E*, 89(4):043305, 2014.

[191] L. Filippin, M. Godefroid, and D. Baye. Relativistic polarizabilities with the Lagrange-mesh method. *Physical Review A*, 90(5), 2014.

[192] L. Filippin, M. Godefroid, and D. Baye. Relativistic two-photon decay rates with the Lagrange-mesh method. *Physical Review A*, 93(1), 2016.

[193] P. Syty, J. E. Sienkiewicz, L. Radžiūtė, G. Gaigalas, P. Rynkun, and J. Bieroń. Continuum wave functions for estimating the electric dipole moment: Calculation based on a multiconfiguration Dirac-Hartree-Fock approximation. *Physical Review A*, 99:012514, 2019.

[194] S. Hameed, A. Herzenberg, and M. G. James. Core polarization corrections to oscillator strengths in the alkali atoms. *Journal of Physics B: Atomic and Molecular Physics*, 1(5):822–830, 1968.

[195] D. W. Norcross and M. J. Seaton. Energy levels for Be I calculated using a model potential and cores approximations. *Journal of Physics B: Atomic and Molecular Physics*, 9(17):2983, 1976.

[196] A. Hibbert. Model potentials in atomic structure. volume 18 of *Advances in Atomic and Molecular Physics*, pages 309 – 340. Academic Press, 1982.

[197] J. Mitroy and D. W. Norcross. Electron-impact excitation of the resonance transition in Be^+. *Physical Review A*, 37:3755–3764, 1988.

[198] H. Bachau, E. Cormier, P. Decleva, J. E. Hansen, and F. Martín. Applications of B-splines in atomic and molecular physics. *Reports on Progress in Physics*, 64(12):1815–1943, 2001.

[199] J. Sapirstein and W. R. Johnson. The use of basis splines in theoretical atomic physics. *Journal of Physics B: Atomic, Molecular and Optical Physics*, 29(22):5213–5225, 1996.

[200] J. P. Santos, F. Parente, and P. Indelicato. Application of B-splines finite basis sets to relativistic two-photon decay rates of $2s$ level in hydrogenic ions. *The European Physical Journal D*, 3(1):43–52, 1998.

[201] P. Amaro, F. Fratini, L. Safari, J. Machado, M. Guerra, P. Indelicato, and J. P. Santos. Relativistic evaluation of the two-photon decay of the metastable $1s^2 2s2p\ ^3P_0$ state in berylliumlike ions with an effective-potential model. *Physical Review A*, 93(3):032502, 2016.

[202] I. P. Grant. B-spline methods for radial Dirac equations. *Journal of Physics B: Atomic, Molecular and Optical Physics*, 42(5):055002, 2009.

[203] S. S. Tayal and O. Zatsarinny. Transition Probabilities and Collision Strengths for Fine-structure Levels Excitation of Ti II. *The Astrophysical Journal*, 905(2):101, 2020.

[204] Y.-B. Tang, B.-Q. Lou, and T.-Y. Shi. Relativistic multireference coupled-cluster theory based on a B-spline basis: Application to atomic francium. *Physical Review A*, 96:022513, 2017.

[205] M. Kozlov and I. Tupitsyn. Mixed Basis Sets for Atomic Calculations. *Atoms*, 7(3), 2019.

[206] Z. Lai, S. Zhang, Q. Gou, and Y. Li. Polarizabilities of Rydberg states of Rb atoms with n up to 140. *Physical Review A*, 98:052503, 2018.

[207] O. Zatsarinny and C. Froese Fischer. DBSR-HF: A B-spline Dirac-Hartree-Fock program. *Computer Physics Communications*, 202:287–303, 2016.

[208] C. Froese Fischer and O. Zatsarinny. A B-spline Galerkin method for the Dirac equation. *Computer Physics Communications*, 180(6):879 – 886, 2009.

[209] C. Froese Fischer. A B-spline Hartree–Fock program. *Computer Physics Communications*, 182(6):1315 – 1326, 2011.

[210] T. Brage, C. Froese Fischer, and G. Miecznik. Non-variational, spline-Galerkin calculations of resonance positions and widths, and photodetachment and photoionization cross sections for H^- and He. *Journal of Physics B: Atomic, Molecular and Optical Physics*, 25(24):5289–5314, 1992.

[211] T. Brage, C. Froese Fischer, and N. Vaeck. MCHF calculations of autoionization widths in two- and three-electron systems. *Journal of Physics B: Atomic, Molecular and Optical Physics*, 26(4):621–640, 1993.

[212] T. Brage and C. Froese Fischer. Spline-Galerkin methods for Rydberg series, including Breit-Pauli effects. *Journal of Physics B: Atomic, Molecular and Optical Physics*, 27(22):5467–5484, 1994.

[213] T. Brage and C. Froese Fischer. Spline-Galerkin methods applied to Rydberg series between the $4s$ ^{2}S and 3d ^{2}D limits of calcium. *Physical Review A*, 50:2937–2947, 1994.

[214] C. Froese Fischer and T. Brage. A program for computing autoionization properties. *Computer Physics Communications*, 74(3):381 – 398, 1993.

[215] C. Froese Fischer, G. Tachiev, G. Gaigalas, and M. R. Godefroid. An MCHF atomic-structure package for large-scale calculations. *Computer Physics Communications*, 176(8):559–579, 2007.

[216] O. Zatsarinny. BSR: B-spline atomic R-matrix codes. *Computer Physics Communications*, 174(4):273 – 356, 2006.

[217] O. Zatsarinny and K. Bartschat. Relativistic B-spline R-matrix method for electron collisions with atoms and ions: Application to low-energy electron scattering from Cs. *Physical Review A*, 77:062701, 2008.

[218] J. Bauche and M. Klapisch. Remarks on Brillouin's theorem in the atomic variational approach. *Journal of Physics B: Atomic and Molecular Physics*, 5(1):29–36, 1972.

[219] J. J. Labarthe. Brillouin's theorem for inter-shell correlations in the atomic Hartree-Fock method. *Journal of Physics B: Atomic and Molecular Physics*, 5(9):L181–L182, 1972.

[220] C. Froese Fischer. Brillouin's theorem for excited $(nl)^q(n'l)^{q'}$ configurations. *Journal of Physics B: Atomic and Molecular Physics*, 6(10):1933–1941, 1973.

[221] M. Godefroid, J. Lievin, and J. Y. Metz. Brillouin's theorem for complex atomic configurations. *Journal of Physics B: Atomic and Molecular Physics*, 20(14):3283–3296, 1987.

[222] C. Froese Fischer. Self-consistent-field (SCF) and multiconfiguration (MC) Hartree-Fock (HF) methods in atomic calculations: Numerical integration approaches. *Computer Physics Reports*, 3(5):274–325, 1986.

[223] C. Froese Fischer, J. E. Hansen, and M. Barwell. Ab initio results for V I and Cr I. *Journal of Physics B: Atomic and Molecular Physics*, 9(11):1841–1848, 1976.

[224] M. Godefroid and C. Froese Fischer. The Mg^+ 3s $^2S_{1/2}$ -4p $^2P^o_{3/2,1/2}$ weak transition probabilities revisited. *Journal of Physics B: Atomic, Molecular and Optical Physics*, 32(18):4467, 1999.

[225] J. Olsen, M. R. Godefroid, P. Jönsson, P. Å. Malmqvist, and C. Froese Fischer. Transition probability calculations for atoms using nonorthogonal orbitals. *Physical Review E*, 52:4499–4508, 1995.

[226] S. Verdebout, P. Rynkun, P. Jönsson, G. Gaigalas, C. Froese Fischer, and M. Godefroid. A partitioned correlation function interaction approach for describing electron correlation in atoms. *Journal of Physics B: Atomic, Molecular and Optical Physics*, 46(8), 2013.

[227] P.-O. Löwdin. Quantum Theory of Many-Particle Systems. I. Physical Interpretations by Means of Density Matrices, Natural Spin-Orbitals, and Convergence Problems in the Method of Configurational Interaction. *Physical Review*, 97:1474–1489, 1955.

[228] W. Kutzelnigg. Direct Determination of Natural Orbitals and Natural Expansion Coefficients of Many-Electron Wavefunctions. I. Natural Orbitals in the Geminal Product Approximation. *The Journal of Chemical Physics*, 40(12):3640–3647, 1964.

[229] R. Ahlrichs and W. Kutzelnigg. Direct Calculation of Approximate Natural Orbitals and Natural Expansion Coefficients of Atomic and Molecular Electronic Wavefunctions. II. Decoupling of the Pair Equations and Calculation of the Pair Correlation Energies for the Be and LiH Ground States. *The Journal of Chemical Physics*, 48(4):1819–1832, 1968.

[230] L. Bytautas, J. Ivanic, and K. Ruedenberg. Split-localized orbitals can yield stronger configuration interaction convergence than natural orbitals. *The Journal of Chemical Physics*, 119(16):8217–8224, 2003.

[231] K. J. H. Giesbertz. Are natural orbitals useful for generating an efficient expansion of the wave function? *Chemical Physics Letters*, 591:220 – 226, 2014.

[232] B. Engels, S. D. Peyerimhoff, and E. R. Davidson. Calculation of hyperfine coupling constants. *Molecular Physics*, 62(1):109–127, 1987.

[233] I. Lindgren, J. Lindgren, and A.-M. Mårtensson. Many-body calculations of the hyperfine interaction of some excited states of alkali atoms, using approximate Brueckner or natural orbitals. *Zeitschrift für Physik A Hadrons and Nuclei*, 279:113–125, 1976.

[234] S. Hörbäck, A.-M. Pendrill, L. Pendrill, and M. Pettersson. Experimental and theoretical investigation of the isotope shift of the $4D$ level in atomic potassium. *Zeitschrift für Physik A Atoms and Nuclei*, 318(3):285–290, 1984.

[235] A.-M. Mårtensson-Pendrill and S. Salomonson. Hyperfine structure of the $4s$, $4p$, and $3d$ states in Ca^+ evaluated by many-body perturbation theory. *Physical Review A*, 30:712–721, 1984.

[236] S. Salomonson. Ab-initio calculations of pair-correlation effects on the hyperfine structure of the $4s\ 4p$ and $4s\ 3d$ configurations of Ca. *Zeitschrift für Physik A Atoms and Nuclei*, 316(2):135–148, 1984.

[237] E. Lindroth, A.-M. Mårtensson-Pendrill, and S. Salomonson. Specific mass shift of the (4s4p) $^{1,3}P$ states in calcium studied with many-body perturbation theory. *Physical Review A*, 31:58–66, 1985.

[238] J.-L. Heully and A.-M. Mårtensson-Pendrill. The Hyperfine Structure in the Alkaline-Earth Ions. *Physica Scripta*, 31(3):169, 1985.

[239] P. Jönsson, A. Ynnerman, C. Froese Fischer, M. R. Godefroid, and J. Olsen. Large-scale multiconfiguration Hartree-Fock and configuration-interaction calculations of the transition probability and hyperfine structures in the sodium resonance transition. *Physical Review A*, 53(6):4021–4030, 1996.

[240] A. Beckmann, K. D. Böklen, and D. Elke. Precision measurements of the nuclear magnetic dipole moments of ^{6}Li, ^{7}Li, ^{23}Na, ^{39}K and ^{41}K. *Zeitschrift für Physik*, 270(3):173–186, 1974.

[241] M. R. Godefroid, G. Van Meulebeke, P. Jönsson, and C. Froese Fischer. Large-scale MCHF calculations of hyperfine structures in nitrogen and oxygen. *Zeitschrift für Physik D Atoms, Molecules and Clusters*, 42(3):193–201, 1997.

[242] B. Atalay, T. Brage, P. Jönsson, and H. Hartman. MCDHF and RCI calculations of energy levels, lifetimes, and transition rates in Si III and Si IV. *Astronomy and Astrophysics*, 631:A29, 2019.

[243] S. Schiffmann *et al.* Work in progress, 2021.

[244] A. Papoulia, S. Schiffmann, J. Bieroń, G. Gaigalas, M. Godefroid, Z. Harman, P. Jönsson, NN.atalia S. Oreshkina, P. Pyykkö, and I. I. Tupitsyn. Ab initio electronic factors of the A and B hyperfine structure constants for the $5s^2 5p 6s\,^{1,3}P_1^o$ states in Sn I. *Physical Review A*, 103:022815, 2021.

[245] J. Bieroń, L. Filippin, G. Gaigalas, M. Godefroid, P. Jönsson, and P. Pyykkö. Ab initio calculations of the hyperfine structure of zinc and evaluation of the nuclear quadrupole moment $Q(^{67}\mathrm{Zn})$. *Physical Review A*, 97:062505, 2018.

[246] I. I. Tupitsyn and A. V. Loginov. Use of Sturmian expansions in calculations of the hyperfine structure of atomic spectra. *Optics and Spectroscopy*, 94(3):319–326, 2003.

[247] I. I. Tupitsyn, V. M. Shabaev, J. R. Crespo López-Urrutia, I. Draganić, R. Soria Orts, and J. Ullrich. Relativistic calculations of isotope shifts in highly charged ions. *Physical Review A*, 68:022511, 2003.

[248] I. I. Tupitsyn, A. V. Volotka, D. A. Glazov, V. M. Shabaev, G. Plunien, J. R. Crespo López-Urrutia, A. Lapierre, and J. Ullrich. Magnetic-dipole transition probabilities in B-like and Be-like ions. *Physical Review A*, 72:062503, 2005.

[249] R. Soria Orts, Z. Harman, J. R. Crespo López-Urrutia, A. N. Artemyev, H. Bruhns, A. J. González Martínez, U. D. Jentschura, C. H. Keitel, A. Lapierre, V. Mironov, V. M. Shabaev, H. Tawara, I. I. Tupitsyn, J. Ullrich, and A. V. Volotka. Exploring Relativistic Many-Body Recoil Effects in Highly Charged Ions. *Physical Review Letters*, 97:103002, 2006.

[250] I.I. Tupitsyn. *Dirac-Fock-Sturm method in relativistic calculations for atoms and two-atomic molecules*. PhD thesis, Saint-Petersburg State University, Saint-Petersburg, 12 2008. in Russian.

[251] J. Dembczyński and H. Rebel. Perturbation of the configurations $5s^2 5pn's$ and $5s^2 5pn''d$ by the configuration $5s5p^3$ in the spectrum Sn I. *Physica C*, 125(3):341 – 352, 1984.

[252] J. Bauche and R.-J. Champeau. Recent progress in the theory of atomic isotope shift. volume 12 of *Advances in Atomic and Molecular Physics*, pages 39 – 86. Academic Press, 1976.

[253] N. Frömmgen, D. L. Balabanski, M. L. Bissell, J. Bieroń, K. Blaum, B. Cheal, K. Flanagan, S. Fritzsche, C. Geppert, M. Hammen, M. Kowalska, K. Kreim, A. Krieger, R. Neugart, G. Neyens, M. M. Rajabali, W. Nörtershäuser, J. Papuga, and D. T. Yordanov. Collinear laser spectroscopy of atomic cadmium. *The European Physical Journal D*, 69(6):164, 2015.

[254] J. Bieroń and P. Pyykkö. Nuclear Quadrupole Moments of Bismuth. *Physical Review Letters*, 87:133003, 2001.

[255] F. P. Gustafsson, C. M. Ricketts, M. L. Reitsma, R. F. Garcia Ruiz, S. W. Bai, J. C. Berengut, J. Billowes, C. L. Binnersley, A. Borschevsky, T. E. Cocolios, B. S. Cooper, R. P. de Groote, K. T. Flanagan, Á. Koszorús, G. Neyens, H. A. Perrett, A. R. Vernon, Q. Wang, S. G. Wilkins, and X. F. Yang. Tin resonance-ionization schemes for atomic- and nuclear-structure studies. *Physical Review A*, 102:052812, 2020.

[256] R. Neugart, J. Billowes, M. L. Bissell, K. Blaum, B. Cheal, K. T. Flanagan, G. Neyens, W. Nörtershäuser, and D. T. Yordanov. Collinear laser spectroscopy at ISOLDE: new methods and highlights. *Journal of Physics G: Nuclear and Particle Physics*, 44(6):064002, 2017.

[257] P. Klüpfel, P.-G. Reinhard, T. J. Bürvenich, and J. A. Maruhn. Variations on a theme by Skyrme: A systematic study of adjustments of model parameters. *Physical Review C*, 79:034310, 2009.

[258] M. Mukai, Y. Hirayama, Y. X. Watanabe, S. Schiffmann, J. Ekman, M. Godefroid, P. Schury, Y. Kakiguchi, M. Oyaizu, M. Wada, S. C. Jeong, J. Y. Moon, J. H. Park, H. Ishiyama, S. Kimura, H. Ueno, M. Ahmed, A. Ozawa, H. Watanabe, S. Kanaya, and H. Miyatake. In-gas-cell laser resonance ionization spectroscopy of ^{196,197,198}Ir. *Physical Review C*, 102:054307, 2020.

[259] S. Schiffmann and M. Godefroid. Electronic isotope shift factors for the Ir $5d^7 6s^2\ ^4F_{9/2} \rightarrow$ (odd,$J = 9/2$) line at 247.587 nm. *Journal of Quantitative Spectroscopy and Radiative Transfer*, 258:107332, 2021.

[260] Y. Ishida, H. Iimura, S. Ichikawa, and T. Horiguchi. Isotope shifts of optical transitions in Ce II by collinear laser - ion-beam spectroscopy. *Journal of Physics B: Atomic, Molecular and Optical Physics*, 30(11):2569–2579, 1997.

[261] C. Gorges, K. Blaum, N. Frömmgen, Ch. Geppert, M. Hammen, S. Kaufmann, J. Krämer, A. Krieger, R. Neugart, R. Sánchez, and W. Nörtershäuser. Isotope shift of ^{40,42,44,48}Ca in the $4s\ ^2S_{1/2} \rightarrow 4p\ ^2P_{3/2}$ transition. *Journal of Physics B: Atomic, Molecular and Optical Physics*, 48(24):245008, 2015.

[262] B. Cheal, T. E. Cocolios, and S. Fritzsche. Laser spectroscopy of radioactive isotopes: Role and limitations of accurate isotope-shift calculations. *Physical Review A*, 86:042501, 2012.

[263] J. S. Schelfhout and J. J McFerran. Isotope shifts for $^1S_0$–$^3P^o_{0,1}$ Yb lines from multiconfiguration Dirac-Hartree-Fock calculations. arXiv 2102.08657, 2021.

[264] W. H. King. Comments on the article "peculiarities of the isotope shift in the samarium spectrum". *Journal of the Optical Society of America*, 53(5):638–639, 1963.

[265] S. O. Allehabi, V. A. Dzuba, V. V. Flambaum, and A. V. Afanasjev. Nuclear deformation as a source of the non-linearity of King plot in the Yb^+ ion. *Physical Review Letters*, 103:L030801, 2021.

[266] T. Manovitz, R. Shaniv, Y. Shapira, R. Ozeri, and N. Akerman. Precision Measurement of Atomic Isotope Shifts Using a Two-Isotope Entangled State. *Physical Review Letters*, 123:203001, 2019.

[267] H. Miyake, N. C. Pisenti, P. K. Elgee, A. Sitaram, and G. K. Campbell. Isotope-shift spectroscopy of the $^1S_0 \rightarrow^3 P_1$ and $^1S_0 \rightarrow^3 P_0$ transitions in strontium. *Physical Review Research*, 1:033113, 2019.

[268] V. A. Yerokhin, R. A. Müller, A. Surzhykov, P. Micke, and P. O. Schmidt. Nonlinear isotope-shift effects in Be-like, B-like, and C-like argon. *Physical Review A*, 101:012502, 2020.

[269] J. C. Berengut, C. Delaunay, A. Geddes, and Y. Soreq. Generalized King linearity and new physics searches with isotope shifts. *Physical Review Research*, 2:043444, 2020.

[270] N. Vaeck, M. Godefroid, and J. E. Hansen. MCHF oscillator strength and lifetime calculations in neutral calcium. *Journal of Physics B: Atomic, Molecular and Optical Physics*, 24(2):361–381, 1991.

[271] S. Goriely and M. Arnould. Actinides: How well do we know their stellar production? *Astronomy and Astrophysics*, 379(3):1113–1122, 2001.

[272] K. H. Bürger, S. Büttgenbach, R. Dicke, G. Gölz, and F. Träber. Direct measurement of the nuclear magnetic dipole moments of ^{191}Ir and ^{193}Ir by high-precision atomic beam magnetic resonance. *Physics Letters B*, 140(1):17 – 21, 1984.

[273] Y. Tanaka, R. M. Steffen, E. B. Shera, W. Reuter, M. V. Hoehn, and J. D. Zumbro. Systematics of ground-state quadrupole moments of odd-A deformed nuclei determined with muonic M x rays. *Physical Review C*, 29:1830–1838, 1984.

[274] P. Jönsson, G. Gaigalas, P. Rynkun, L. Radžiūtė, J. Ekman, S. Gustafsson, H. Hartman, K. Wang, M. Godefroid, C. Froese Fischer, I. Grant, T. Brage, and G. Del Zanna. Multiconfiguration Dirac-Hartree-Fock Calculations with Spectroscopic Accuracy: Applications to Astrophysics. *Atoms*, 5(2), 2017.

[275] S. Buder, M. Asplund, L. Duong, J. Kos, K. Lind, M. K. Ness, S. Sharma, J. Bland-Hawthorn, A. R. Casey, G. M. De Silva, V. D'Orazi, K. C. Freeman, G. F. Lewis, J. Lin, S. L. Martell, K. J. Schlesinger, J. D. Simpson, D. B. Zucker, T. Zwitter, A. M. Amarsi, B. Anguiano, D. Carollo, L. Casagrande, K. Čotar, P. L. Cottrell, G. Da Costa, X. D. Gao, M. R. Hayden, J. Horner, M. J. Ireland, P. R. Kafle, U. Munari, D. M. Nataf, T. Nordlander, D. Stello, Y.-S. Ting, G. Traven, F. Watson, R. A. Wittenmyer, R. F. G. Wyse, D. Yong, J. C. Zinn, M. Žerjal, and GALAH collaboration. The GALAH Survey: second data release. *Monthly Notices of the Royal Astronomical Society*, 478(4):4513–4552, 2018.

[276] G. Del Zanna and H. E. Mason. Solar UV and X-ray spectral diagnostics. *Living Reviews in Solar Physics*, 15(1):5, 2018.

[277] N. Hell, P. Beiersdorfer, G. V. Brown, M. E. Eckart, R. L. Kelley, C. A. Kilbourne, M. A. Leutenegger, T. E. Lockard, F. S. Porter, and J. Wilms. Highly charged ions in a new era of high resolution X-ray astrophysics. *X-Ray Spectrometry*, 49(1):218–233, 2020.

[278] L. Zhou, S.Gamrath, P. Palmeri, P. Quinet, M. Zhang, and Z. Dai. Experimental and Theoretical Radiative Lifetimes, Branching Fractions, Transition Probabilities,

and Oscillator Strengths of Some Highly Excited Odd-parity Levels in Ir I. *The Astrophysical Journal Supplement Series*, 238(1):3, 2018.

[279] Y. Li, S. Gamrath, P. Palmeri, P. Quinet, Q. Li, Q. Yu, M. Zhang, L. Zhou, and Z. Dai. Radiative lifetimes, branching fractions, and oscillator strengths of high-lying levels in Re I. *Monthly Notices of the Royal Astronomical Society*, 491(2):2953–2958, 2019.

[280] E. Bokamba Motoumba, S. Enzonga Yoca, P. Quinet, and P. Palmeri. Calculations of transition rates in erbium-like ions Lu IV, Hf V and Ta VI using the Ab initio MCDHF-RCI and semi-empirical HFR methods. *Atomic Data and Nuclear Data Tables*, 133-134:101340, 2020.

[281] A. Papoulia, J. Ekman, and P. Jönsson. Extended transition rates and lifetimes in Al I and Al II from systematic multiconfiguration calculations. *Astronomy and Astrophysics*, 621:A16, 2019.

[282] W. Li, A. M. Amarsi, A. Papoulia, J. Ekman, and P. Jönsson. Extended theoretical transition data in C I−IV. *Monthly Notices of the Royal Astronomical Society*, 502(3):3780–3799, 2021.

[283] E. T. Young, E. E. Becklin, P. M. Marcum, T. L. Roellig, J. M. De Buizer, T. L. Herter, R. Güsten, E. W. Dunham, P. Temi, B.-G. Andersson, D. Backman, M. Burgdorf, L. J. Caroff, S. C. Casey, J. A. Davidson, E. F. Erickson, R. D. Gehrz, D. A. Harper, P. M. Harvey, L. A. Helton, S. D. Horner, C. D. Howard, R. Klein, A. Krabbe, I. S. McLean, A. W. Meyer, J. W. Miles, M. R. Morris, W. T. Reach, J. Rho, M. J. Richter, H.-P. Roeser, G. Sandell, R. Sankrit, M. L. Savage, E. C. Smith, R. Y. Shuping, W. D. Vacca, J. E. Vaillancourt, J. Wolf, and H. Zinnecker. Early science with sofia, the stratospheric observatory for infrared astronomy. *The Astrophysical Journal*, 749(2):L17, 2012.

[284] H.-U. Käufl, P. Ballester, P. Biereichel, B. Delabre, R. Donaldson, R. Dorn, E. Fedrigo, G. Finger, G. Fischer, F. Franza, D. Gojak, G. Huster, Y. Jung, J.-L. Lizon, L. Mehrgan, M. Meyer, A. Moorwood, J.-F. Pirard, J. Paufique, E. Pozna, R. Siebenmorgen, A. Silber, J. Stegmeier, and S. Wegerer. CRIRES: a high-resolution infrared spectrograph for ESO's VLT. In Alan F. M. Moorwood and Masanori Iye, editors, *Ground-based Instrumentation for Astronomy*, volume 5492 of *Society of Photo-Optical Instrumentation Engineers (SPIE) Conference Series*, pages 1218–1227, 2004.

[285] D. Kato, X.-M. Tong, H. Watanabe, T. Fukami, T. Kinugawa, C. Yamada, S. Ohtani, and T. Watanabe. Fine-structure in $3d^4$ States of Highly Charged Ti-like Ions. *Journal of the Chinese Chemical Society*, 48(3):525–529, 2001.

[286] S. Gustafsson, P. Jönsson, C. Froese Fischer, and I. Grant. Combining Multiconfiguration and Perturbation Methods: Perturbative Estimates of Core-Core Electron Correlation Contributions to Excitation Energies in Mg-Like Iron. *Atoms*, 5(1):3, 2017.

[287] G. Gaigalas, P. Rynkun, L. Radžiūtė, D. Kato, M. Tanaka, and P. Jönsson. Energy Level Structure and Transition Data of Er^{+2}. *The Astrophysical Journal Supplement Series*, 248(1):13, 2020.

[288] P. G. Judge. Spectral Lines for Polarization Measurements of the Coronal Magnetic Field. V. Information Content of Magnetic Dipole Lines. *The Astrophysical Journal*, 662(1):677–690, 2007.

[289] J. Plowman. Single-point inversion of the coronal magnetic field. *The Astrophysical Journal*, 792(1):23, 2014.

[290] D. J. Pegg. Structure and dynamics of negative ions. *Reports on Progress in Physics*, 67(6):857–905, 2004.

[291] T. Andersen. Atomic negative ions: structure, dynamics and collisions. *Physics Reports*, 394(4):157 – 313, 2004.

[292] Y. Su, R. Si, K. Yao, and T. Brage. The structure and radiative lifetimes of negative ions homologous to N^-. *Journal of Physics B: Atomic, Molecular and Optical Physics*, 52(12):125002, 2019.

[293] C. W. Walter, N. D. Gibson, D. J. Matyas, C. Crocker, K. A. Dungan, B. R. Matola, and J. Rohlén. Candidate for Laser Cooling of a Negative Ion: Observations of Bound-Bound Transitions in La^-. *Physical Review Letters*, 113:063001, 2014.

[294] R. C. Bilodeau and H. K. Haugen. Experimental Studies of Os^-: Observation of a Bound-Bound Electric Dipole Transition in an Atomic Negative Ion. *Physical Review Letters*, 85:534–537, 2000.

[295] C. W. Walter, N. D. Gibson, Y.-G. Li, D. J. Matyas, R. M. Alton, S. E. Lou, R. L. Field, D. Hanstorp, Lin Pan, and Donald R. Beck. Experimental and theoretical study of bound and quasibound states of Ce^-. *Physical Review A*, 84:032514, 2011.

[296] A. Kellerbauer, A. Fischer, and U. Warring. Measurement of the Zeeman effect in an atomic anion: Prospects for laser cooling of Os^-. *Physical Review A*, 89:043430, 2014.

[297] R. Tang, R. Si, Z. Fei, X. Fu, Y. Lu, T. Brage, H. Liu, C. Chen, and C. Ning. Candidate for Laser Cooling of a Negative Ion: High-Resolution Photoelectron Imaging of Th^-. *Physical Review Letters*, 123:203002, 2019.

[298] L. Pan and D. R. Beck. Candidates for laser cooling of atomic anions: La^- versus Os^-. *Physical Review A*, 82:014501, 2010.

[299] H. T. Schmidt, R. D. Thomas, M. Gatchell, S. Rosén, P. Reinhed, P. Löfgren, L. Brännholm, M. Blom, M. Björkhage, E. Bäckström, J. D. Alexander, S. Leontein, D. Hanstorp, H. Zettergren, L. Liljeby, A. Källberg, A. Simonsson, F. Hellberg, S. Mannervik, M. Larsson, W. D. Geppert, K. G. Rensfelt, H. Danared, A. Paál, M. Masuda, P. Halldén, G. Andler, M. H. Stockett, T. Chen, G. Källersjö, J. Weimer, K. Hansen, H. Hartman, and H. Cederquist. First storage of ion beams in the Double Electrostatic Ion-Ring Experiment: DESIREE. *Review of Scientific Instruments*, 84(5):055115, 2013.

[300] E. Bäckström, D. Hanstorp, O. M. Hole, M. Kaminska, R. F. Nascimento, M. Blom, M. Björkhage, A. Källberg, P. Löfgren, P. Reinhed, S. Rosén, A. Simonsson, R. D. Thomas, S. Mannervik, H. T. Schmidt, and H. Cederquist. Storing keV Negative Ions for an Hour: The Lifetime of the Metastable $^2P^o_{1/2}$ level in $^{32}S^-$. *Physical Review Letters*, 114:143003, 2015.

[301] P. Andersson, K. Fritioff, J. Sandström, G. Collins, D. Hanstorp, A. Ellmann, P. Schef, P. Lundin, S. Mannervik, P. Royen, C. Froese Fischer, F. Österdahl, D. Rostohar, D. J. Pegg, N. D. Gibson, H. Danared, and A. Källberg. Radiative lifetimes of metastable states of negative ions. *Physical Review A*, 73:032705, 2006.

[302] T. Brage. Atomic negative ions. *AIP Conference Proceedings*, 260(1):94–108, 1992.

[303] E Lindroth and J. M. Dahlström. Attosecond delays in laser-assisted photodetachment from closed-shell negative ions. *Physical Review A*, 96:013420, 2017.

[304] M. Isinger, R. J. Squibb, D. Busto, S. Zhong, A. Harth, D. Kroon, S. Nandi, C. L. Arnold, M. Miranda, J. M. Dahlström, E. Lindroth, R. Feifel, M. Gisselbrecht, and A. L'Huillier. Photoionization in the time and frequency domain. *Science*, 358(6365):893–896, 2017.

[305] M. Kotur, D. Guénot, Á. Jiménez-Galán, E. W. Kroon, D .and Larsen, M. Louisy, S. Bengtsson, M. Miranda, J. Mauritsson, C. L. Arnold, S. E. Canton, M. Gisselbrecht, T. Carette, J. M. Dahlström, E. Lindroth, A. Maquet, L. Argenti, F. Martín, and A. L'Huillier. Spectral phase measurement of a Fano resonance using tunable attosecond pulses. *Nature Communications*, 7(1):10566, 2016.

[306] S. Mannervik, G. Astner, and M. Kisielinski. An optical transition in the negative lithium ion. *Journal of Physics B: Atomic and Molecular Physics*, 13(14):L441–L444, 1980.

[307] J. O. Gaardsted and T. Andersen. Observation of an optical transition in the negative beryllium ion. *Journal of Physics B: Atomic, Molecular and Optical Physics*, 22(3):L51–L55, 1989.

[308] C. W. Walter, N. D. Gibson, C. M. Janczak, K. A. Starr, A. P. Snedden, R. L. Field III, and P. Andersson. Infrared photodetachment of Ce^-: Threshold spectroscopy and resonance structure. *Physical Review A*, 76:052702, 2007.

[309] Stephen J. Buckman and Charles W. Clark. Atomic negative-ion resonances. *Review of Modern Physics*, 66:539–655, 1994.

[310] M. S. Safronova, C. Cheung, M. G. Kozlov, S. E. Spielman, N. D. Gibson, and C. W. Walter. Predicting quasibound states of negative ions: La^- as a test case. *Physical Review A*, 103:022819, 2021.

[311] E. Lindroth and J. Luis Sanz-Vicario. Photodetachment of few-electron negative ions. *Radiation Physics and Chemistry*, 70(1):387–405, 2004. Photoeffect: Theory and Experiment.

[312] M.A. Albert, S. Laulan, and S. Barmaki. Accurate numerical method for the calculation of doubly excited states in atoms. *Canadian Journal of Physics*, 97(3):317–320, 2019.

[313] S. M. O'Malley and D. R. Beck. Lifetimes and branching ratios of excited states in La^-, Os^-, Lu^-, Lr^-, and Pr^-. *Physical Review A*, 81:032503, 2010.

[314] E. P. Wigner. On the Behavior of Cross Sections Near Thresholds. *Physical Review*, 73:1002–1009, 1948.

[315] Y. Lu, J. Zhao, R. Tang, X. Fu, and C. Ning. Measurement of electron affinity of iridium atom and photoelectron angular distributions of iridium anion. *The Journal of Chemical Physics*, 152(3):034302, 2020.

[316] O. Scharf and M. R. Godefroid. On the fine structure photodetachment intensities using the irreducible tensorial expression of second quantization operators. https://arxiv.org/abs/0808.3529v1, 2008.

[317] P. C. Engelking and W. C. Lineberger. Laser photoelectron spectrometry of Fe^-: The electron affinity of iron and the "nonstatistical" fine-structure detachment intensities at 488 nm. *Physical Review A*, 19:149–155, 1979.

[318] M. Scheer, C. A. Brodie, R. C. Bilodeau, and H. K. Haugen. Laser spectroscopic measurements of binding energies and fine-structure splittings of Co^-, Ni^-, Rh^-, and Pd^-. *Physical Review A*, 58:2051–2062, 1998.

[319] R. Si and C. Froese Fischer. Electron affinities of At and its homologous elements Cl, Br, and I. *Physical Review A*, 98:052504, 2018.

[320] F. Arnau, F. Mota, and J. J. Novoa. Accurate calculation of the electron affinities of the group-13 atoms. *Chemical Physics*, 166(1):77 – 84, 1992.

[321] Z. Felfli, A. Z. Msezane, and D. Sokolovski. Slow electron elastic scattering cross sections for In, Tl, Ga and At atoms. *Journal of Physics B: Atomic, Molecular and Optical Physics*, 45(4):045201, 2012.

[322] C. W. Walter, N. D. Gibson, and S. E. Spielman. Electron affinity of thallium measured with threshold spectroscopy. *Physical Review A*, 101:052511, 2020.

[323] C. Froese Fischer, A. Ynnerman, and G. Gaigalas. Multiconfiguration-Hartree-Fock calculations for the electron affinity of boron. *Physical Review A*, 51:4611–4616, 1995.

[324] C. Froese Fischer and G. Gaigalas. The electron affinity of $2s2p^2\ ^4P$ in boron. *Journal of Physics B: Atomic, Molecular and Optical Physics*, 29(6):1169–1173, 1996.

[325] C. W. Walter, N. D. Gibson, D. J. Carman, Y.-G. Li, and D. J. Matyas. Electron affinity of indium and the fine structure of In^- measured using infrared photodetachment threshold spectroscopy. *Physical Review A*, 82:032507, 2010.

[326] J. F. Williams. Resonance structure in inelastic scattering of electrons from atomic hydrogen. *Journal of Physics B: Atomic, Molecular and Optical Physics*, 21(11):2107, 1988.

[327] D. Xiao, J. Li, W. C. Campbell, T. Dellaert, P. McMillin, A. Ransford, C. Roman, and A. Derevianko. Hyperfine structure of $^{173}Yb^+$: Toward resolving the ^{173}Yb nuclear-octupole-moment puzzle. *Physical Review A*, 102:022810, 2020.

[328] J. Li *et al.* New Version of HFS92. private communication, 2021.

[329] S. Verdebout. *On the use of non-orthogonal partition correlation functions in atomic physics: theory and applications*. PhD thesis, Université libre de Bruxelles, 2012.

[330] P. Jönsson. Fast implementation of the deconstrained PCFI method in GRASP. *Private communication*, 2017.